HYBRIDS PART A: HYBRIDS FOR TISSUE REGENERATION

EDITED BY: Kai Zheng, Jonathan Lao and Antonio Jesus Salinas
PUBLISHED IN: Frontiers in Bioengineering and Biotechnology

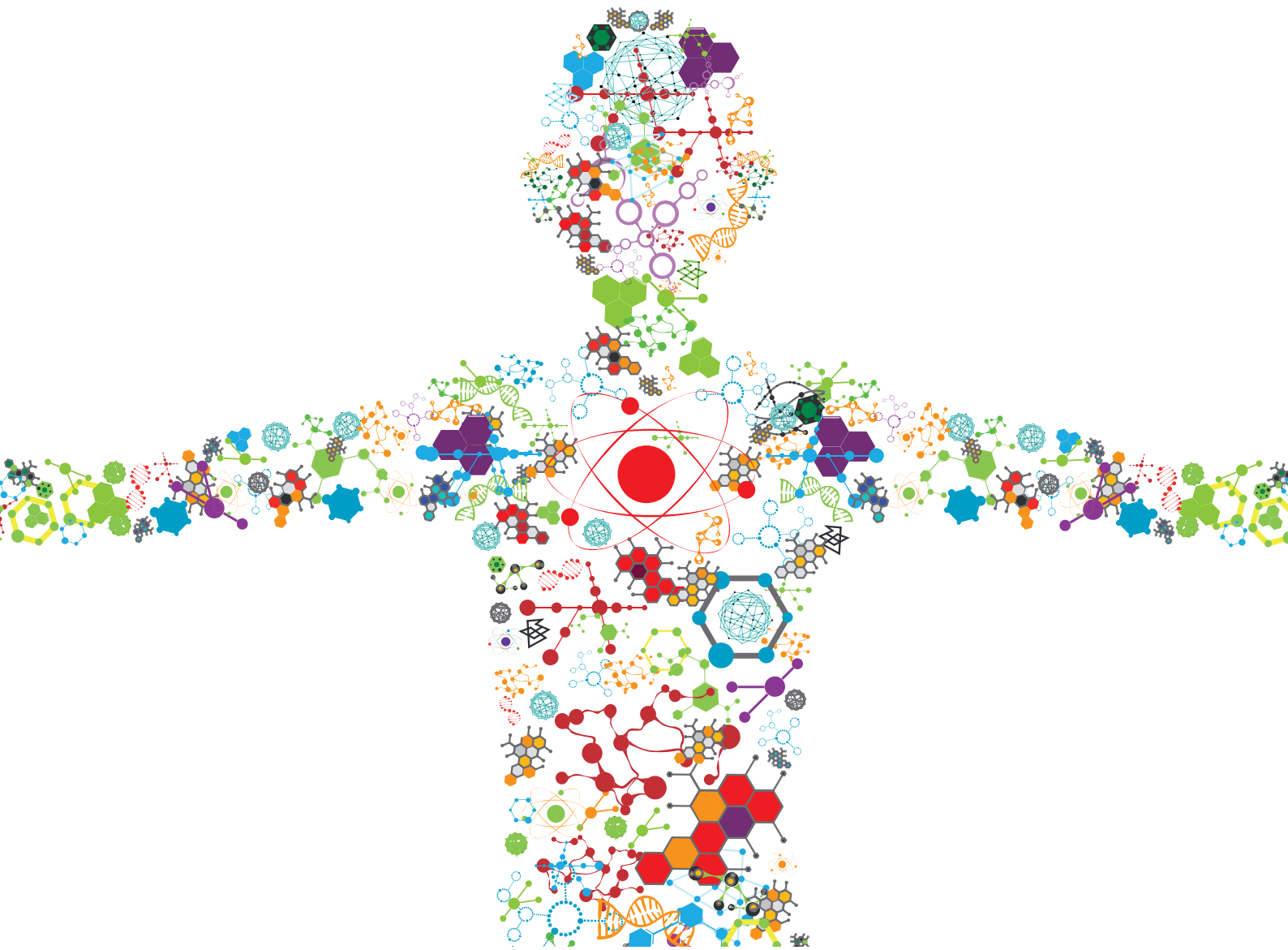

frontiers Research Topics

ISSN 1664-8714
ISBN 978-2-88971-451-3
DOI 10.3389/978-2-88971-451-3

About Frontiers

Frontiers is more than just an open-access publisher of scholarly articles: it is a pioneering approach to the world of academia, radically improving the way scholarly research is managed. The grand vision of Frontiers is a world where all people have an equal opportunity to seek, share and generate knowledge. Frontiers provides immediate and permanent online open access to all its publications, but this alone is not enough to realize our grand goals.

Frontiers Journal Series

The Frontiers Journal Series is a multi-tier and interdisciplinary set of open-access, online journals, promising a paradigm shift from the current review, selection and dissemination processes in academic publishing. All Frontiers journals are driven by researchers for researchers; therefore, they constitute a service to the scholarly community. At the same time, the Frontiers Journal Series operates on a revolutionary invention, the tiered publishing system, initially addressing specific communities of scholars, and gradually climbing up to broader public understanding, thus serving the interests of the lay society, too.

Dedication to Quality

Each Frontiers article is a landmark of the highest quality, thanks to genuinely collaborative interactions between authors and review editors, who include some of the world's best academicians. Research must be certified by peers before entering a stream of knowledge that may eventually reach the public - and shape society; therefore, Frontiers only applies the most rigorous and unbiased reviews.
Frontiers revolutionizes research publishing by freely delivering the most outstanding research, evaluated with no bias from both the academic and social point of view. By applying the most advanced information technologies, Frontiers is catapulting scholarly publishing into a new generation.

What are Frontiers Research Topics?

Frontiers Research Topics are very popular trademarks of the Frontiers Journals Series: they are collections of at least ten articles, all centered on a particular subject. With their unique mix of varied contributions from Original Research to Review Articles, Frontiers Research Topics unify the most influential researchers, the latest key findings and historical advances in a hot research area! Find out more on how to host your own Frontiers Research Topic or contribute to one as an author by contacting the Frontiers Editorial Office: frontiersin.org/about/contact

HYBRIDS PART A: HYBRIDS FOR TISSUE REGENERATION

Topic Editors:
Kai Zheng, University of Erlangen Nuremberg, Germany
Jonathan Lao, Université Clermont Auvergne, France
Antonio Jesus Salinas, Complutense University of Madrid, Spain

Citation: Zheng, K., Lao, J., Salinas, A. J., eds. (2021). Hybrids Part A: Hybrids for Tissue Regeneration. Lausanne: Frontiers Media SA. doi: 10.3389/978-2-88971-451-3

Table of Contents

frontiers in Bioengineering and Biotechnology

EDITORIAL
published: 17 August 2021
doi: 10.3389/fbioe.2021.746641

Editorial: Hybrids Part A: Hybrids for Tissue Regeneration

Kai Zheng[1]*, *Antonio Jesus Salinas*[2,3]* and *Jonathan Lao*[4]*

[1]Institute of Biomaterials, University of Erlangen-Nuremberg, Erlangen, Germany, [2]Departamento de Química en Ciencias Farmacéuticas, Instituto de Investigación Sanitaria Hospital 12 de Octubre, Universidad Complutense de Madrid, Madrid, Spain, [3]CIBER-BBN, Madrid, Spain, [4]Laboratoire de Physique de Clermont, Université Clermont Auvergne, Clermont-Ferrand, France

Keywords: wound healing, bone regeneration, scaffolds, hybrids, periodontal tissue regeneration

Editorial on the Research Topic

Hybrids Part A: Hybrids for Tissue Regeneration

Numerous tissue engineering and regenerative medicine strategies have been applied in the past two decades to regenerate and reconstruct injured or diseased tissues. Many promising tissue regeneration strategies involve biomaterials (e.g., tissue engineering scaffolds, injectable formulations) (Gaharwar et al., 2020). Biomaterials can provide mechanical support and biochemical signals to encourage cell recruitment, attachment, growth, and differentiation and consequently guide tissue regeneration. Numerous organic (e.g., natural or synthetic polymers) or inorganic (e.g., bioceramics, bioactive glasses) materials have been successfully applied in various tissue regeneration scenarios (Gaharwar et al., 2020; Koons et al., 2020). Hybrids, commonly defined as consisting of components intimately mixed at the nanometer or molecular level—meaning that at least one of the components is circumscribed to areas ranging from several angstroms to a few hundred nanometers (Sanchez and Soler-Illia, 2006). Hybrids can be obtained by the homogeneous dispersion of nanoparticles inside a matrix or preferably by the entanglements or interpenetration of at least two different networks at the nanoscale—usually an organic one and an inorganic one. Since the nano dimension of the inorganic units and/or organic building blocks leads to more homogeneous materials and possible synergistic effects, hybrids exhibit unique physical, chemical, mechanical, and biological properties compared to their constituting phases. Hybrids have recently emerged as advanced biomaterials and are attracting increasing attention in tissue regeneration applications (Granel et al., 2019; Zhou et al., 2021).

This Research Topic entitled "*Hybrids for Tissue Regeneration*" shows the potential of hybrids in tissue regeneration. This topic invited researchers to contribute studies on recent advances in hybrid systems for tissue regeneration, including also (nano)composites since there are no clear borderlines between these materials (Kickelbick, 2006). We have collected one review article and nine original research articles, highlighting several emerging trends of hybrids and (nano)composites in the field of hard and soft tissue repair and regeneration.

Hybrids have shown impressive therapeutic effects in wound healing applications. Fu et al. reviews the recent development of metal-organic frameworks (MOFs) based hybrid systems as antibacterial agents, therapeutic delivery vehicles, and dressing systems for wound healing. They highlight the importance of surface engineering of MOFs with unique ligands in developing multifunctional hybrid systems. Cheng et al. developed freeze-dried hybrid dressings composed of epidermal growth factor and recombinant human-like collagen. Such a hybrid dressing significantly accelerated the healing of cutaneous wounds, as evidenced in a rat model. Yang et al. developed a hybrid delivery system composed of silk

Edited and reviewed by:
Hasan Uludag,
University of Alberta, Canada

***Correspondence:**
Kai Zheng
kai.zheng@fau.de
Antonio Jesus Salinas
salinas@farm.ucm.es
Jonathan Lao
jonathan.lao@clermont.in2p3.fr

Specialty section:
This article was submitted to Biomaterials, a section of the journal Frontiers in Bioengineering and Biotechnology

Received: *24 July 2021*
Accepted: *03 August 2021*
Published: *17 August 2021*

Citation:
Zheng K, Salinas AJ and Lao J (2021) Editorial: Hybrids Part A: Hybrids for Tissue Regeneration. Front. Bioeng. Biotechnol. 9:746641. doi: 10.3389/fbioe.2021.746641

fibroin microparticles and insulin. This hybrid platform could release insulin in a sustained manner and consequently enhanced the healing of diabetic wounds.

Hybrids have also shown great potential in bone, cartilage, and periodontal tissue regeneration. Li et al. developed a gold nanoparticle/L-cysteine hybrid system to alleviate periodontal destruction by enhancing osteogenic differentiation of human periodontal ligament cells. Another important application of hybrids in implant dentistry, particularly in improving the resistance against bacterial infections around oral implants, was proposed by Wei et al. by using titanium reinforced with nanosized aggregates of graphene to enhance soft tissue sealing. Artificial ligaments for anterior cruciate ligament based on polyethylene terephthalate (PET) can also be improved by applying hybrid materials. Wu et al. show that PET artificial ligaments can be improved by coating them with antibacterial polydopamine and using this interlayer to introduce nano-hydroxyapatite and silver atoms to the PET surface, obtaining materials susceptible of further functionalization suitable for more advanced applications. In addition, Han et al. demonstrated that the cellular behavior of bone marrow mesenchymal stem cells (BMSCs), chondrocytes, and tendon stem cells could be modulated by controlling the pore size of melt electrowritten scaffolds based on polycaprolactone that is one of the most frequently used polymers for 3D printing. The results from Han et al. suggest that the biological properties of polycaprolactone-based hybrids and nanocomposites can be improved by modulating their morphology in addition to the composition optimization. Guided tissue regeneration (GTR) is a widely used clinical strategy for treating periodontal tissue defects. In this strategy, a membrane is applied to build a mechanical barrier from the gingival epithelium and hold space for periodontal regeneration. Zhou et al. (2021) developed fish collagen and polyvinyl alcohol (Col/PVA) dual-layer membranes for GTR. The collagen layer could enhance the osteogenic differentiation of BMSCs, while the PVA layer had the potential to prevent gingival epithelium ingrowth.

Hybrids based on bioceramics and bioactive glasses (BGs) are attractive biomaterials for hard tissue repair and regeneration, considering their bioactivity and osteogenic activity. Karbowniczek et al. successfully produced electrospun hybrid poly(3-hydroxybutyric acid-co-3-hydrovaleric acid) (PHBV)/HA fibrous scaffolds to biomimetic bone tissue. The combination of PHBV with HA significantly enhanced cell proliferation and filopodia formation responsible for cell anchoring within the created 3D environment. The obtained results show great potential in the development of hybrid scaffolds stimulating bone tissue regeneration. Han et al. developed BGs-modified hybrid dental resins. BGs enhanced the mechanical properties, biocompatibility, antibacterial and remineralizing activities due to the release of active ions from BGs. Hybridization with BGs or bioceramics provides an effective strategy to enhance the mineralization and osteogenic activity of polymeric matrices.

In summary, the Research Topic "*Hybrids Part A: Hybrids for Tissue Regeneration*" covers the recent development of hybrids for tissue regeneration. The editors hope this Research Topic will contribute to the progress in the field of hybrids for tissue regeneration and inspire researchers with sparkling ideas to further advance this field. Last but not least, we would like to thank all the authors, reviewers, and the development team for their efforts in producing this Research Topic.

AUTHOR CONTRIBUTIONS

All authors listed have made a substantial, direct, and intellectual contribution to the work, and approved it for publication.

FUNDING

KZ acknowledges financial support from DFG (German Science Foundation, BO1191/23). AS acknowledges financial support from IIS Carlos III through Research project PI20/01384.

REFERENCES

Gaharwar, A. K., Singh, I., and Khademhosseini, A. (2020). Engineered Biomaterials for *In Situ* Tissue Regeneration. *Nat. Rev. Mater.* 5, 686–705. doi:10.1038/s41578-020-0209-x

Granel, H., Bossard, C., Collignon, A. M., Wauquier, F., Lesieur, J., Rochefort, G. Y., et al. (2019). Bioactive Glass/Polycaprolactone Hybrid with a Dual Cortical/Trabecular Structure for Bone Regeneration. *ACS Appl. Bio Mater.* 2, 3473–3483. doi:10.1021/acsabm.9b00407

Kickelbick, G. (2006). "Introduction to Hybrid Materials," in *Hybrid Materials. Synthesis, Characterization, and Applications*. Editor G. Kickelbick (Weinheim: Wiley-VCH Verlag), 1–48.

Koons, G. L., Diba, M., and Mikos, A. G. (2020). Materials Design for Bone-Tissue Engineering. *Nat. Rev. Mater.* 5, 584–603. doi:10.1038/s41578-020-0204-2

Sanchez, C., and Soler-Illia, G. (2006). "Hybrid Materials (Organic–Inorganic)," in *Encyclopedia of Chemical Processing*. Editor S. Lee (Oxfordshire: Taylor & Francis), 1267–1280.

Zhou, L., Fan, L., Zhang, F. M., Jiang, Y., Cai, M., Dai, C., et al. (2021). Hybrid Gelatin/oxidized Chondroitin Sulfate Hydrogels Incorporating Bioactive Glass Nanoparticles with Enhanced Mechanical Properties, Mineralization, and Osteogenic Differentiation. *Bioactive Mater.* 6, 890–904. doi:10.1016/j.bioactmat.2020.09.012

Conflict of Interest: The authors declare that the research was conducted in the absence of any commercial or financial relationships that could be construed as a potential conflict of interest.

Publisher's Note: All claims expressed in this article are solely those of the authors and do not necessarily represent those of their affiliated organizations, or those of the publisher, the editors and the reviewers. Any product that may be evaluated in this article, or claim that may be made by its manufacturer, is not guaranteed or endorsed by the publisher.

frontiers in Bioengineering and Biotechnology

ORIGINAL RESEARCH
published: 15 July 2020
doi: 10.3389/fbioe.2020.00742

Hybrid Freeze-Dried Dressings Composed of Epidermal Growth Factor and Recombinant Human-Like Collagen Enhance Cutaneous Wound Healing in Rats

*Yating Cheng[1†], Yangfan Li[1†], Shiyi Huang[1], Fenglin Yu[1], Yu Bei[2], Yifan Zhang[2], Jianzhong Tang[2], Yadong Huang[1,2] and Qi Xiang[1,2]**

[1] Institute of Biomedicine and Guangdong Provincial Key Laboratory of Bioengineering Medicine, Jinan University, Guangzhou, China, [2] Biopharmaceutical R&D Center of Jinan University, Guangzhou, China

Epidermal growth factor (EGF) is important for promoting skin repair and remodeling. Native collagen is also widely used as a scaffold for skin tissue engineering. The limitations of EGF include easy decomposition or inactivation, whereas native collagen is immunogenic and has poor solubility. Therefore, we constructed a freeze-dried dressing based on the recombinant human-like collagen (RHC) to act as a carrier for EGF (RHC/EGF freeze-dried dressing) and promote skin wound closure. Here, the freeze-dried dressing that combined EGF and RHC significantly enhanced the proliferation, adhesion, and spreading of NIH/3T3 fibroblasts and migration of HaCaT keratinocytes at the wound site. The physicochemical characteristics of the RHC/EGF freeze-dried dressing investigated using scanning electron microscopy, Fourier transform infrared (FTIR) spectroscopy, and differential scanning calorimetry revealed that it was a loose and porous cake that redissolved quickly. The molecular mechanisms involved in cell proliferation and angiogenesis were also assessed. The expression levels of the markers Ki-67, proliferating cell nuclear antigen, vascular endothelial growth factor, and cluster of differentiation 31 were significantly increased after treatment with the RHC/EGF freeze-dried dressing ($P < 0.01$, vs. RHC or EGF alone). This increase indicated that the RHC/EGF freeze-dried dressing significantly accelerated wound closure, re-epithelialization, and the orderly arrangement and deposition of collagen in the Sprague–Dawley rats with full-thickness skin defects. This work describes a significant step toward the development of wound environments conducive to healing, and the RHC/EGF freeze-dried dressing is a potential therapeutic strategy in wound management.

Keywords: full-thickness skin defects, cell proliferation, angiogenesis, freeze-dried dressing, recombinant human-like collagen, epidermal growth factor

OPEN ACCESS

Edited by:
Kai Zheng,
Friedrich–Alexander University Erlangen–Nürnberg, Germany

Reviewed by:
Baolin Guo,
Xi'an Jiaotong University, China
Samit Kumar Nandi,
West Bengal University of Animal and Fishery Sciences, India

****Correspondence:***
Qi Xiang
txiangqi@jnu.edu.cn

† These authors have contributed equally to this work

Specialty section:
This article was submitted to Tissue Engineering and Regenerative Medicine, a section of the journal Frontiers in Bioengineering and Biotechnology

Received: *02 May 2020*
Accepted: *10 June 2020*
Published: *15 July 2020*

Citation:
Cheng Y, Li Y, Huang S, Yu F, Bei Y, Zhang Y, Tang J, Huang Y and Xiang Q (2020) Hybrid Freeze-Dried Dressings Composed of Epidermal Growth Factor and Recombinant Human-Like Collagen Enhance Cutaneous Wound Healing in Rats. Front. Bioeng. Biotechnol. 8:742. doi: 10.3389/fbioe.2020.00742

INTRODUCTION

Chronic wounds that are labeled as complex and hard-to-heal, as well as those leading to amputations, are health problems that have devastating consequences for patients, healthcare systems, and societies (Olsson et al., 2019). Consequently, enhancing the wound healing process and increasing efficacy of treatments are a major research focus (Ying et al., 2019). Zhao et al. (2020) prepared physical double-network removable hydrogel adhesives with both increased wound healing efficiency and photothermal antibacterial activities. This was achieved via catechol–Fe^{3+} coordination with quadruple hydrogen-bonding cross-linked amphiphilic polyester and gelatin (Zhao et al., 2020). The use of wound dressings to protect the wound and provide an optimal environment for wound repair is common practice within burn clinics. Although traditional wound healing dressings have improved significantly, wound healing complications remain a significant healthcare challenge (Aljghami et al., 2019). Various types of wound dressing materials including biomimetic extracellular matrices (ECMs) and biomaterials containing growth factors (GFs) are some of the advancements in tissue engineering and biomaterial sciences that have been widely adopted to accelerate wound healing (Choi et al., 2018; Thönes et al., 2019). Epidermal growth factor (EGF) plays a critical role in initiating and sustaining the different phases of wound healing (Hardwicke et al., 2008). Collagen, the most abundant ECM structural protein, has excellent biocompatibility and degradability. Thus, it is considered to be a top candidate for wound dressing preparations (Evan et al., 2019). We constructed a freeze-dried dressing based on recombinant human-like collagen (RHC) and EGF to generate a multifunctional product that can improve cell–biomaterial interactions and promote wound healing.

Numerous studies have examined the potential of EGF for wound repair. Epidermal growth factor not only promotes the proliferation and migration of keratinocytes, but it also improves collagen construction and stimulates the formation and synthesis of the ECM (Chin et al., 2019). However, the proteolytic environment of the wound is one of the major limitations of using EGF. This is because the delivered proteins are effectively degraded in these environments. To overcome the degradation challenge and improve EGF bioavailability, different drug delivery methods have been explored, including sprays, nanoparticle conjugation, and incorporation within dressings. In the future, the main focus will be on developing more patient-friendly and efficient delivery systems through polymer modification and carrier systems (Garg and Goyal, 2014).

Collagen and collagen-based materials have been successfully used in regenerative medicine for over 50 years (Gontijo et al., 2019). Collagen is suitable for tissue engineering because it is a biocompatible and stable structure that forms a large portion of the ECM. In addition, it also provides a physical barrier that is involved in exudate management (Ramanathan et al., 2018). Within the collagen family, type I collagen is widely used as a biological material because it forms fibrils via heterogeneous self-assembly unlike types II and III collagen, which do not (Aljghami et al., 2019). However, natural type I collagen from animal sources can be immunogenic, while at the same time, problems related to the processing techniques, degradation rate, and the disinfection process of type I collagen limit its application. With the development of genetic engineering, a series of RHC, which are highly hydrophilic, safe, and effective, have attracted extensive attention worldwide. Many reports have demonstrated the expression of recombinant truncated type I human-like collagen peptides in *Escherichia coli* (Yang et al., 2004; Guo et al., 2010). In some of these studies, the use of codon optimization allowed for the expression of recombinant type I human-like collagen peptides that contained multiple identical motifs (Yao et al., 2004; Olsen et al., 2005). Some of these motifs are ligands for specific types of integrin receptors. Recombinant type I human-like collagen peptides are not only expected to enhance cell activity through specific integrin-binding receptors but are also extensible and can be used in various fibrous structural materials, including dressings (Grab et al., 1996; Mashiko et al., 2018).

In this study, a new type of RHC was designed and constructed using genetic engineering technology. This RHC contained cell adhesion domains derived from native type I collagen, and this overcame the limitations of native animal-derived collagen. In addition, EGF is capable of controlling biological processes by regulating the proliferation and migration of keratinocytes and epithelial cells. In this study, we sought to determine whether the combination of these two materials would result in a more efficient skin wound dressing. Traditional wound dressings are made of dry gauze, require regular changes, and are prone to secondary injury. In contrast, the ideal characteristics of an improved wound dressing include non-adherence, cost-effectiveness, and the ability to maintain a moist environment for wound healing. To address the limitations described above, we prepared an RHC/EGF (1:1) freeze-dried dressing. Unlike other passive moist wound dressings, the RHC/EGF freeze-dried dressing not only keeps the surrounding wound environment moist but also actively accelerates the wound repair process. Finally, in the model of full-thickness skin defects *in vivo*, RHC/EGF freeze-dried dressings demonstrated strong potential for application in wound healing and repair.

MATERIALS AND METHODS

Reagents

Escherichia coli BL21 (DE3) and plasmids containing pET-3c, an ampicillin resistance gene, and isopropyl β-D-1-thiogalactopyranoside (IPTG) were provided by Invitrogen (Carlsbad, CA, United States). Plasmid extraction and gel recovery kits, as well as restriction enzymes and ligase, were purchased from Guangzhou Tianjin Biotechnology Co., Ltd. (Guangzhou, China). Epidermal growth factor was supplied by Jinan University Biopharmaceutical R&D Center (Guangzhou, China). All other reagents were provided by GBCBIO Technologies Inc. (Guangdong, China).

NIH/3T3 (ATCC CRL-7724) cells were purchased from the Chinese Academy of Sciences (Shanghai, China) and cultured in RPMI 1640 supplemented with 10% fetal bovine serum (FBS) (Gibco, Grand Island, NY, United States). HaCaT

cells (ATCC CRL-2310) were purchased from the Chinese Academy of Sciences and cultured in Dulbecco modified eagle medium supplemented with 10% FBS. All cell culture plates and bottles were obtained from Corning Company (Corning, NY, United States).

Construction and Identification of RHC

The gene encoding RHC was cloned into the pET-3c expression vector to generate a recombinant plasmid named pET3c-hlcollagen, which was transformed into *E. coli* BL21 (DE3). After screening for ampicillin resistance and induction by IPTG, the best expression condition was selected. Larger-scale production of RHC was performed using a 50-L fermenter. Moreover, RHC protein was purified using affinity chromatography on a Ni Sepharose 6 Fast Flow column combined with gel filtration Sephadex G-25. Polymerase chain reaction, Western blot, and gel electrophoresis were used for the identification of RHC.

Interaction Between EGF and RHC

The interaction between EGF and RHC was demonstrated using cell proliferation, migration, and adhesion assays. Proliferation of cells on EGF, RHC, porcine skin collagen, type III collagen, RHC/EGF(0.25:1), RHC/EGF(0.5:1), RHC/EGF(1:1), RHC/EGF(2:1), and RHC/EGF(4:1) was assessed using an MTT assay. Absorbance for each cell culture plate (at 570 nm) was measured in a microplate reader (MK3; Thermo, Waltham, MA, United States). Each assay was performed in triplicate. An *in vitro* scratch wound-healing model was used to assess cell migration. Images of the cells at the beginning of migration and after regular intervals were captured and used to quantify the cellular migration rate. The crystal violet assay was used to measure cell adhesion activity. Images were then captured with an MF53 microscope (Mshot, Guangzhou, China). The experiment was performed in quintuplicate, and the number of adherent cells was calculated from the average of images captured at five positions per well. To investigate cell lysis, a 1% sodium dodecyl sulfate (SDS) solution was added to the culture plate, and the absorbance was measured using a microplate reader at 570 nm (Yuan et al., 2016).

Cytoskeleton Staining Assays

Coating of 12-well plates with 1 nmol/mL of EGF, RHC, and RHC/EGF was performed at 4°C (overnight). After washing with phosphate-buffered saline (PBS), the wells were blocked with 1% (wt/vol) bovine serum albumin (BSA) for 30 min. NIH/3T3 cells were seeded in the same plates at 4×10^4 cells per well in FBS-free medium. After 4 h, the cells were washed with PBS and fixed with a 4% paraformaldehyde solution for 10 min. Next, phalloidin (1:200; Solarbio, Beijing, China) was used for staining at 37°C for 30 min in the dark, and the cells were washed with PBS (three times). The cells were stained with DAPI (1:1,000; Beyotime, Beijing, China) at room temperature for 5 min and washed with PBS (three times). LSM 700 confocal laser scanning microscope (Zeiss, Wetzlar, Germany) was used for image acquisition, with excitation wavelengths of 488 and 561 nm. The images were analyzed with ImageJ (National Institutes of Health, United States) to calculate the cell adhesion area.

Preparation of RHC, EGF, and RHC/EGF Freeze-Dried Dressings

Recombinant human-like collagen, EGF, and RHC/EGF (1:1) were lyophilized separately to obtain the freeze-dried dressings. In short, the configured RHC, EGF, and RHC/EGF solutions were subjected to gradient cooling. This involved placing the solutions at 4°C for 1 h, then at −20°C for 6 h, and finally at −80°C overnight. Next, the frozen RHC, EGF, and RHC/EGF were vacuum freeze-dried at −50°C for 24 h. The freeze-dried dressing was sterilized using cobalt-60 gamma irradiation and stored in a sterile dry-sealed EP tube for future experiments.

Characterization of the RHC and RHC/EGF Freeze-Dried Dressings

The morphologies and structural properties of the freeze-dried dressings were characterized by scanning electron microscopy (SEM, XL30; Philips, Amsterdam, Netherlands), Fourier transform infrared (FTIR, model 8400; Shimadzu, Kyoto, Japan), and differential scanning calorimetry (DSC; Mettler Toledo, Columbus, OH, United States). The micromorphology of RHC and the freeze-dried dressings were observed using SEM after applying gold sputtering on samples using a gold spray carbonator. Fourier transform infrared spectroscopy measurements (in attenuated total reflectance mode) were carried out using a Nicolet iS50 FTIR Spectrometer (Thermo Scientific, Waltham, MA, United States) at room temperature. All the film samples were obtained using the conventional KBr disk method. The samples were scanned in the 400 and 4,000 cm^{-1} range. Thermal curves of RHC, EGF, and RHC/EGF, as well as a physical mixture of RHC and EGF, were obtained using DSC (Mettler Toledo).

The Rehydration Time of RHC and RHC/EGF Freeze-Dried Dressings

The resolubility tests of RHC and RHC/EGF freeze-dried dressings were performed using physiological saline. In short, we dissolved RHC and RHC/EGF freeze-dried dressings in 300 μL of physiological saline and determined whether the liquid could be sufficiently dissolved (by the degree of liquid clarification) and recorded the dissolution time. All these physical measurements were made in triplicate at 25°C.

In vivo Studies in Full-Thickness Skin Defect SD Rat Model

All SD rats (60 days postnatal) used in this study were purchased from the Animal Centre of Guangdong Province (no. 44007200069979) and caged in a suitable and controlled environment. The experimental protocols used in this study were approved by the Institutional Animal Care and Use Committee of Jinan University (approval 2019228). All experiments were conducted according to the guidelines for animal care and use of China, and the animal ethics committee of the Chinese Academy of Medical Sciences approved them. A full-thickness skin defect model was established to evaluate the role of the RHC, EGF, and RHC/EGF freeze-dried dressings in wound healing. Female SD rats, 200 ± 20 g (n = 20 per group) were assigned randomly

to three groups: (1) EGF, (2) RHC, and (3) RHC/EGF. Briefly, rats were anesthetized with an intraperitoneal injection of chloral hydrate (10%), and their backs were shaved and cleaned with ethanol. A whole-skin defect model was prepared with a 1.8-cm-diameter ring drill to compress a circular mark on both sides of the rat's back (2.54 cm^2), and then the skin was cut off along the mark. One of the wounds was treated with physiological saline as the control group, and the experimental groups on the other side were treated with EGF, RHC, or RHC/EGF freeze-dried dressings, respectively. Postoperatively, antibiotics were administered for 3 days to prevent wound infection. After the respective treatments, the wounds were covered with gauze, which was fixed in place with a sterile bandage. On days 3, 7, 14, and 21, five mice were randomly selected from each group, anesthetized, and sacrificed.

Macroscopic Evaluation of Wounded Tissues

To measure percent wound closure, the wounds were photographed at 0, 3, 7, 10, 14, and 21 days after wounding and analyzed by ImageJ software. The limits of grossly evident epithelialization were used to measure the wound area. The percent wound closure at each time point was calculated using the following formula: [((initial wound size – current wound size)/initial wound size) × 100].

Microscopic Evaluation of Hematoxylin and Eosin–Stained Skin Samples

The rats were sacrificed on days 3, 7, 14, and 21 after surgery, and wound tissue was collected. The sample was fixed in 4% neutral buffered paraformaldehyde, dehydrated with ethanol, and exposed to xylene. Then the samples were embedded in paraffin, sectioned at a thickness of 8.0 μm, and placed onto glass slides. Finally, they were examined with hematoxylin and eosin (H&E) as well as Masson trichrome staining. Sections were analyzed, and images were captured by microscopy (Olympus IX71, Tokyo, Japan). Hematoxylin and eosin–stained samples were used to measure the epithelial thickness at 14 and 21 days after wounding.

Immunohistochemical Analysis

On days 3 and 14, wound tissue specimens harvested from the rat model were used for immunohistochemical (IHC) evaluation. Immunohistochemical staining of vascular endothelial growth factor (VEGF) and cluster of differentiation 31 (CD31) was performed using the streptavidin–biotin method. In brief, sections were dewaxed and microwaved for 10 min to retrieve antigens, and then endogenous peroxidase was blocked by incubation in hydrogen peroxide (3%) for 30 min in the dark. Sections were permeabilized with Triton X-100 (1%) solution and blocked in BSA (5%). Next, sections were incubated with antibodies against VEGF (1:300 dilution, GB14165; Google Biotechnology, Wuhan, China) and CD31 (1:200 dilution, GB11063-3; Google Biotechnology) overnight. After rinsing with PBS, the sections were incubated with rabbit secondary antibody for 40 min. After washing four times with PBS, the DAB and hematoxylin were applied for coloration and redyeing the nucleus, respectively. Finally, sections were dehydrated and sealed with Permount^{TM} Mounting Medium for microscopic observation (Olympus IX71).

Immunofluorescence Analysis

On days 7 and 14, wound tissue specimens harvested from the rat model were used for IHC fluorescence evaluation. To visualize immunofluorescence, sections were incubated with antibodies against Ki-67 (1:300 dilution, GB13030-2; Google Biotechnology) and proliferating cell nuclear antigen (PCNA, 1:200 dilution, GB11010; Google Biotechnology) overnight. After rinsing with PBS, sections were incubated with a fluorescent rabbit secondary antibody for 40 min. After washing four times with PBS, cell nuclei were stained with DAPI, and images were acquired with a confocal laser scanning microscope (Olympus LSM 700).

Statistical Analysis

All data were expressed as the mean ± standard deviation (SD) of at least three independent experiments and were analyzed using one-way analysis of variance with a Tukey honestly significant difference comparison test, where $P < 0.05$ was considered statistically significant. GraphPad Prism 6 software (GraphPad Software Inc., La Jolla, CA, United States) was used for statistical analysis.

RESULTS

Construction and Identification of RHC

Using genetic engineering technology, we constructed RHC according to the construction schematic shown for the recombinant plasmid of pET3c-hlcollagen (**Figure 1A**). The results from nucleic acid electrophoresis showed that the RHC gene was successfully ligated into the expression vector (**Figure 1B**). After induction of the *E. coli* BL21 that contained recombinant plasmid RHC with IPTG (at either 30°C or 37°C) for 4 h, or 20°C overnight, soluble RHC expression was highest at 37°C (**Figure 1C**). Subsequently, the RHC protein was purified using affinity chromatography on a Ni Sepharose 6 Fast Flow column combined with gel filtration Sephadex G-25. The purity of RHC was detected by SDS–polyacrylamide gel electrophoresis (PAGE) gel electrophoresis (**Figure 1D**) and Western blot (**Figure 1E**), and in both of them, a single band was obtained. Identity was confirmed by matrix-assisted laser desorption/ionization–time of flight mass spectrometry and High-performance liquid chromatography–based peptide mapping (data not shown). We conducted at least three consecutive batches of 50-L fermentation process tests, and the mean of RHC protein expression accounted for 48% of the total protein in the bacterial cell supernatant (data not shown).

Combined RHC With EGF Promotes Proliferation and Migration Synergistically

The proliferation of NIH/3T3 cells cultured on RHC, EGF, porcine skin collagen, type III collagen, and RHC/EGF substrates

was assessed. These experiments demonstrated that RHC, porcine skin collagen, and type III collagen did not promote the proliferation of NIH/3T3 cells (**Supplementary Figure 1A**).

When the cells were cultured on substrates containing various freeze-dried combinations of RHC and EGF (ratio of RHC/EGF = 0.25:1, 0.5:1, 1:1, 2:1, and 4:1), our results showed that the RHC/EGF (1:1) freeze-dried dressing had the strongest effect on proliferation (**Supplementary Figure 3**). In addition, EGF also significantly promoted cell proliferation (**Figure 2A**).

HaCaT cells are considered to be a good *in vitro* model of the skin epidermal layer and can be used to assess the therapeutic effects of different compounds on tissue regeneration. The *in vitro* scratch wound healing assay using HaCaT cells shows that, in the RHC and RHC/EGF group, wound closure by cell migration in HaCaT cells is significantly enhanced when compared with those of untreated or EGF groups (**Figure 2B**). After a 12- or 24-h incubation with HaCaT cells, markedly higher percent wound closures were observed. The migration characteristics of HaCaT cells on RHC, EGF, and RHC/EGF were examined by the scratch wound assay (**Figure 2B**). After a 24-h incubation, a significantly higher ($P < 0.01$) percent wound closure is observed in RHC (78% $\pm$ 3.12%) and RHC/EGF (91.6% $\pm$ 1.62%) compared with that in control (46.3% $\pm$ 1.82%) and EGF (62.3% $\pm$ 2.12%) (**Figure 2C**).

The Joint Application of RHC and EGF Promotes NIH/3T3 Cell Adhesion and Spreading

To investigate the effect of RHC, EGF, porcine skin collagen, type III collagen, or RHC/EGF on cell adhesion, NIH/3T3 cells were cultured in serum-free medium and plated on 96-well plates coated with RHC, EGF, or RHC/EGF for 2 h. The cell adhesion activity of the NIH/3T3 cells was then evaluated using the crystal violet assay. Recombinant human-like collagen and RHC/EGF groups significantly promoted cell adhesion compared with the control and EGF groups (**Figure 2D**). In addition, compared with porcine skin and type III collagen, the RHC group significantly enhanced cell adhesion ($P < 0.001$, **Supplementary Figure 1B**). Among all the groups, RHC/EGF had the highest number of attached cells that were well-spread and exhibited a typical fibroblast cell morphology. We also determined the average number of cells attached to monolayers representing the control, RHC, EGF, and RHC/EGF groups (**Figure 2E**). The largest number of cells was attached to RHC/EGF, with approximately 130 cells attached per field of view. When compared with the control and EGF, cell attachment was significantly lower at 20–30 cells per field.

To further analyze the adhesion activity, we assessed NIH/3T3 cell adhesion to RHC/EGF. Cells were allowed to adhere for 4 h to each of the monolayer substrates, and then samples were fixed and stained to allow for the comparison of cytoskeletal development (**Figure 2F**). We observed that cells on the RHC/EGF surfaces displayed an organized actin cytoskeleton. In contrast, cells on the control and EGF surfaces lacked an organized actin structure. To quantify the spread of the attached cells, we calculated the cell area using ImageJ (**Figure 2G**). The results showed that the spread area of the NIH/3T3 cells cultured on the RHC/EGF substrates was significantly larger than the spread area of cells cultured on the control and EGF substrates. These results indicate that compared with the other groups tested, RHC/EGF has the best NIH/3T3 cell adhesion activity.

Characterization of the RHC/EGF Freeze-Dried Dressings

Recombinant human-like collagen and RHC/EGF (1:1) freeze-dried dressings have a noticeable but irregular pore structure and self-assemble by lyophilization to form a distinct fibrous structure (**Figure 3**). In addition, solubility experiments showed that both RHC and RHC/EGF freeze-dried dressings could be completely dissolved in physiological saline within a short period (3–5 s), to form a transparent and uniform aqueous solution.

The structural characteristics of the RHC/EGF freeze-dried dressing were examined using FTIR spectroscopy (**Figure 3B**). The presence of the characteristic bands of collagen in RHC, porcine skin collagen, type III collagen, and RHC/EGF freeze-dried dressings at approximately 1,640, 1,535, and 1,260 cm^{-1} is attributed to the absorption bands of amide I, II, and III, respectively, and exhibits with a hydrogen-bonded amine group (**Figure 3B** and **Supplementary Figure 2A**). The carbonyl group with the absorption peak ranging from 1,700 to 1,600 cm^{-1} reveals the presence of a main structural protein in the RHC/EGF freeze-dried dressing. The peak ranging from 3,600 to 3,000 cm^{-1} represents the stretching vibration of -NH bonds. There was no difference seen in the FTIR spectra of these three groups.

The amino acid denaturation temperature of collagen dressings is an essential parameter to consider for biomaterials used in tissue engineering applications. The results of both the DSC and TG (thermogravimetric analysis) indicated that the denaturation temperature of porcine skin and type III collagen was approximately 78 and 73°C, respectively (**Figure 3C** and **Supplementary Figure 2B**). The denaturation temperature of EGF was 157.6°C, whereas the denaturation temperature of the RHC/EGF freeze-dried dressing was 224.2°C, which demonstrated that RHC combined with EGF had improved thermal stability. The RHC/EGF freeze-dried dressing had a weight loss of 6.3% in the transition temperature range of 150–250°C compared to 27.3 and 35.6% for native collagen and EGF, respectively (**Figure 3C**). This result indicates that EGF had a strong interaction with RHC, which increased the thermal stability of RHC/EGF freeze-dried dressings.

The RHC/EGF Freeze-Dried Dressings Improve Wound Healing of Sprague–Dawley Rats With Full-Thickness Skin Defects

After establishing the full-thickness skin defects model, the wounds were treated with EGF, RHC, and RHC/EGF freeze-dried dressings. Wounds treated with EGF served as the positive control group, whereas physiological saline was administered to the negative control group. Wound closure at each time point for all the experimental groups was measured. The healing time of the RHC/EGF group was reduced compared with that of

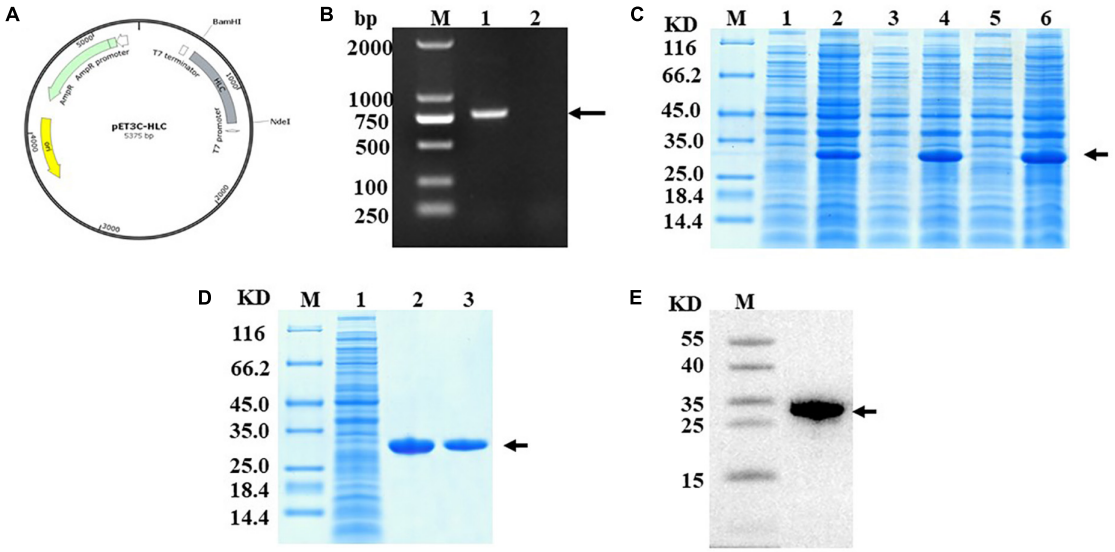

FIGURE 1 | Construction and identification of RHC. **(A)** Construction schematic of the recombinant pET3c-hlcollagen plasmid. **(B)** Nucleic acid electrophoresis of recombinant plasmid pET3C-HLC. M: DNA Ladder 2000; lane 1: monoclone of recombinant plasmid pET3C-HLC; lane 2: negative control. **(C)** Effect of temperature on RHC expression, as analyzed by SDS-PAGE. Recombinant human-like collagen was induced by IPTG for 4 h at either 37 or 30°C or overnight at 20°C. M: middle molecular weight protein markers; lanes 2, 4, and 6: RHC after induction at 20, 30, or 37°C; lanes 1, 3, and 5: RHC before induction. **(D)** Sodium dodecyl sulfate–PAGE analysis of proteins during purification. M: middle molecular weight protein markers; lane 1: broken by PBS; lane 2: Ni-NTA spin columns; lane 3: washed protein through 80 mM imidazole. **(E)** Western blotting analysis. M: middle molecular weight protein markers; lane 1: RHC with an anti-His antibody.

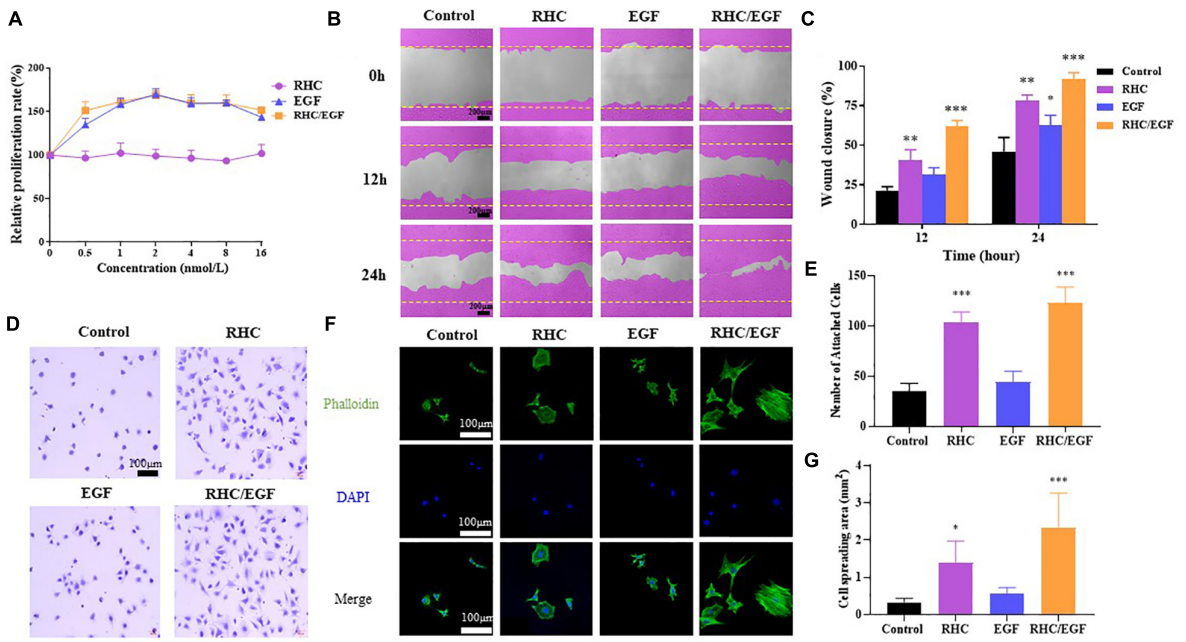

FIGURE 2 | Cell biological activity of RHC/EGF (1:1). **(A)** MTT assay of NIH/3T3 cell proliferation rates on RHC, EGF, or RHC/EGF. **(B)** Images obtained at 0, 12, and 24 h after wound creation *in vitro* migration assay on RHC, EGF, or RHC/EGF. **(C)** Quantitative analysis of gap area of HaCaT cells cultured on RHC, EGF, or RHC/EGF. **(D)** Optical micrographs of crystal violet–stained NIH/3T3 cells adhering to monolayers. **(E)** Quantitative detection of the number of adherent NIH/3T3 cells. **(F)** Cytoskeleton staining. **(G)** Quantitative calculation of cell spread area. $n = 3$, means ± SD, $^{*}P < 0.05$, $^{**}P < 0.01$, $^{***}P < 0.001$ vs. control group.

the other groups, and the wound closure rate of the RHC/EGF group was much higher than that of the other two groups (**Figure 4A**). At 10 days after wounding, a significantly higher ($P < 0.01$) percent wound closure is observed in the EGF (88.39% ± 4.13%) and RHC/EGF (90.33% ± 7.47%) groups compared with the RHC (69.32% ± 6.18%) and control groups

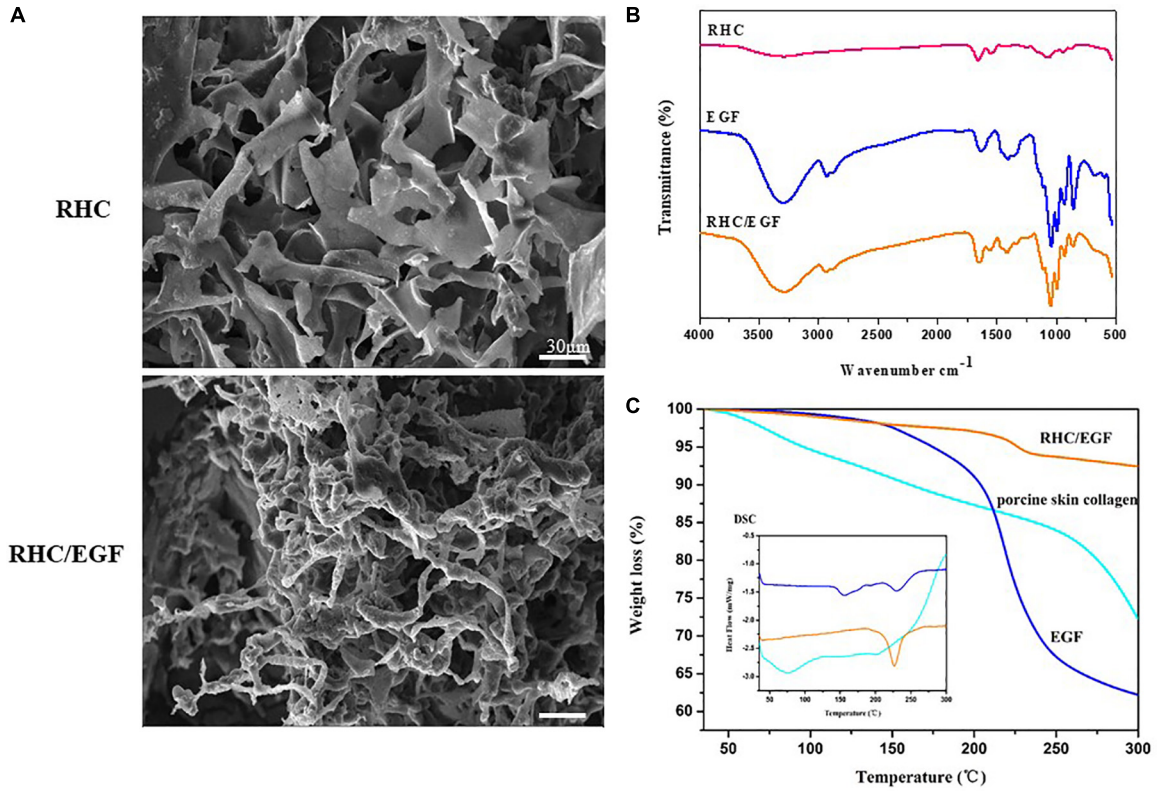

FIGURE 3 | Characteristics of RHC and RHC/EGF. **(A)** Scanning electron micrographs of RHC and RHC/EGF freeze-dried dressings. **(B)** Fourier transform infrared spectra of RHC, EGF, and RHC/EGF freeze-dried dressings. **(C)** Differential scanning calorimetry spectrum of EGF, porcine skin collagen, RHC/EGF freeze-dried dressing.

(65.79% ± 9.48%) (**Figure 4B**). The appearances of the wounds indicated that RHC/EGF freeze-dried dressings improved wound healing, whereas non-treatment resulted in noticeable large and elongated scars.

Next, a histological analysis (via H&E staining) was performed to assess the quality of the newly formed skin tissue (**Figure 4C**). Hematoxylin and eosin staining results indicated that on day 3, there was a decrease in wound inflammation and significant capillary growth in the RHC/EGF freeze-dried dressing group. In the control group, a large number of inflammatory cells infiltrated the upper layer of the dermis, but there was negligible capillary growth. Evaluation of the skin-injury model after treatment for 14 or 21 days (**Figure 4D**) indicates a significant increase in epithelial thickness in the RHC/EGF group (41.66 ± 4.62 μM, $P < 0.01$) compared with the control (26.83 ± 3.58 μM) and RHC group (32.33 ± 3.18 μM).

The RHC/EGF Freeze-Dried Dressing Promotes Skin Collagen Regeneration and Orderly Arrangement

Masson trichrome staining can be used to assess the overall quality of the scar area by measuring collagen deposition and morphology. Masson trichrome staining results showed that the wound treated with RHC exhibited deposition of ECM on day 7, especially for blue-stained collagen (**Figure 4E**). In addition, at day 21, wound surfaces treated with RHC/EGF had enhanced collagen deposition, as well as highly compact and arranged collagen fibers compared with those in the control group.

The RHC/EGF Freeze-Dried Dressing Accelerates Both Cell Proliferation and Neovascularization in Skin Defects

Ki-67 and PCNA are important protein biomarkers for measuring cell proliferation. On days 7 and 14, damaged skin tissues were collected to examine the expression of two cell proliferation–specific proteins, Ki-67 and PCNA (**Figure 5**). After treatment with RHC/EGF for 7 days, there is a significant increase in the expression of Ki-67 and PCNA (**Figures 5A,C**). Statistical results showed that there is a significant difference between the RHC/EGF group and the control group (**Figures 5B,D**; $P < 0.001$). On day 14, the expression of Ki-67 and PCNA is significantly decreased in all groups. Neovascularization is required for normal tissue development, and both CD31 and VEGF are widely used as markers of angiogenesis. Damaged skin was collected on days 3 and 14, and the expression of CD31 and VEGF in the vascular network was assessed by IHC (**Figure 6**). After treatment for 3 or 14 days, the expression of CD31 is significantly increased in the EGF and RHC/EGF groups

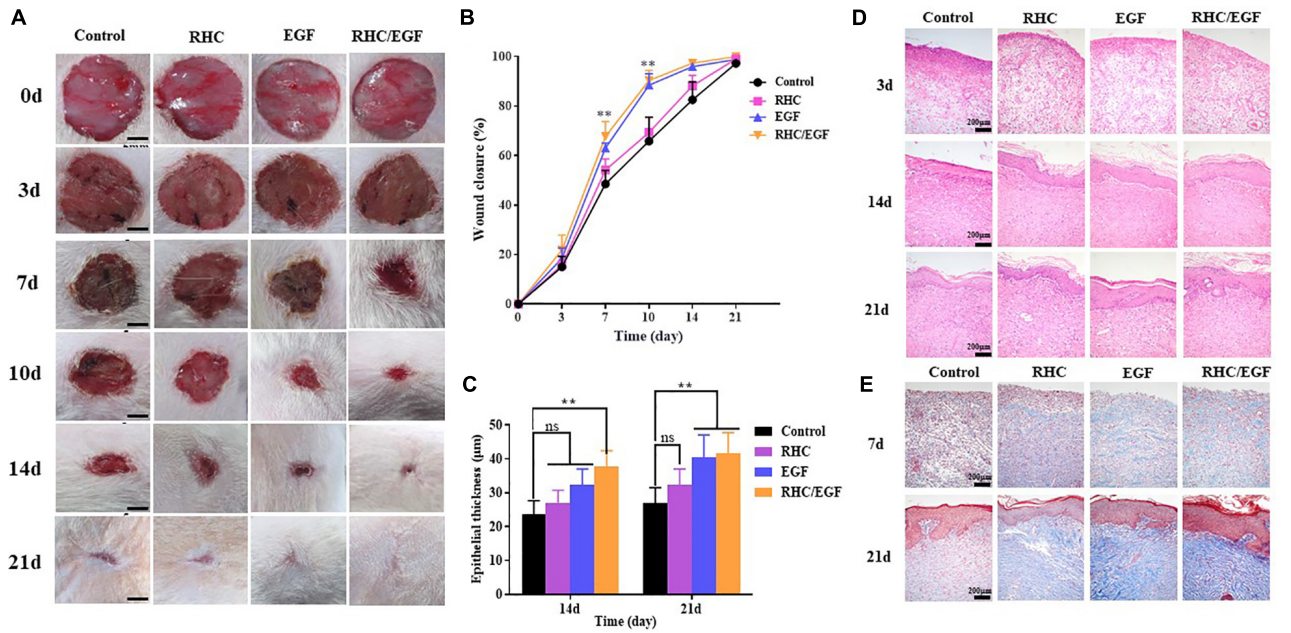

FIGURE 4 | Experimental study of rat wound-healing model after treatment with physiological saline, RHC, EGF, or RHC/EGF. **(A)** Wounds were photographed at days 0, 3, 5, 7, 10, 14, and 21. **(B)** Quantitative analysis of epithelial thickness at days 14 and 21 using ImageJ software. **(C)** Hematoxylin and eosin staining of rat wound-healing model after treatment for 3, 14, and 21 days. **(D)** Quantitative analysis of wound closure rate. **(E)** Masson trichrome staining of rat wound-healing model after treatment for 7 and 21 days. $n = 5$, means ± SD, $^{**}P < 0.01$ vs. control group, ns means no significant difference vs. control group, $P > 0.05$.

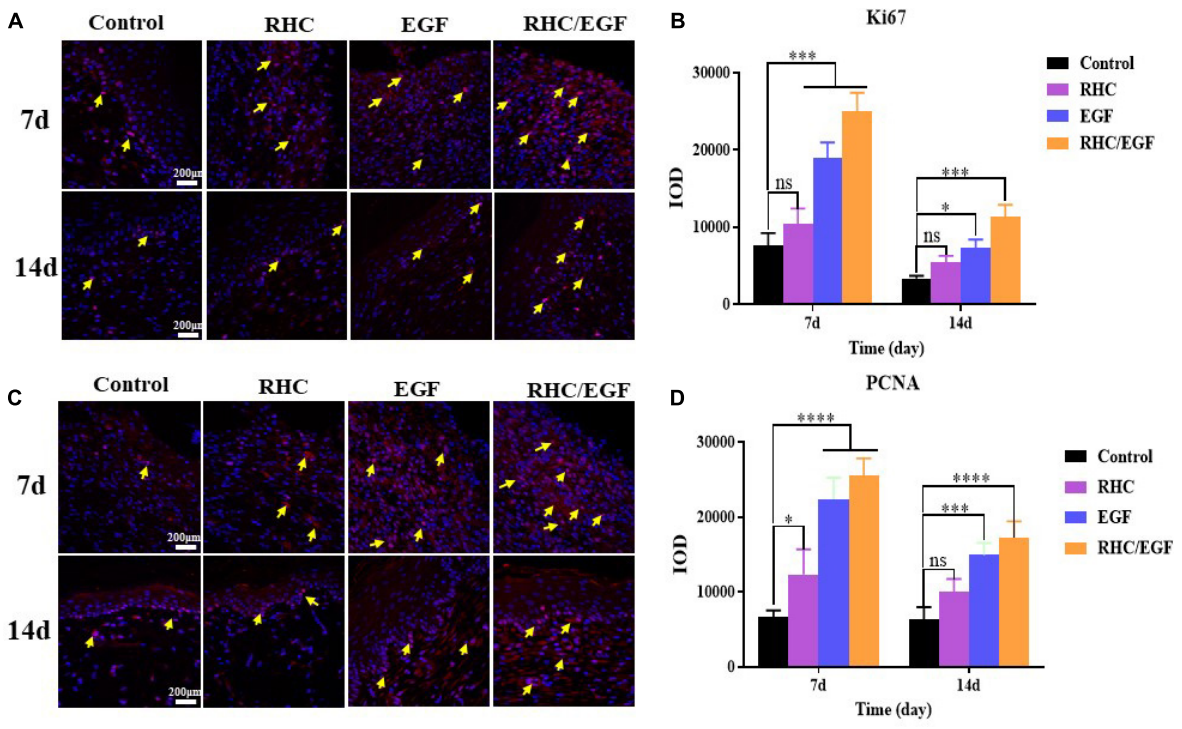

FIGURE 5 | Immunofluorescence examination of Ki-67 and PCNA expression. **(A)** Immunofluorescence examination of Ki-67–positive cells after treatment for 7 and 14 days. Arrows indicate Ki-67 expression. **(B)** Quantitative analysis of Ki-67–expressing cells at 7 and 14 days measured using ImageJ software. **(C)** Immunofluorescence examination of PCNA-positive cells after treatment for 7 and 14 days. Arrows indicate PCNA expression. **(D)** Quantitative analysis of PCNA-expressing cells at 7 and 14 days measured using ImageJ software. $n = 3$, means ± SD, $^{*}P < 0.05$, $^{***}P < 0.001$, $^{****}P < 0.0001$ vs. control group, ns means no significant difference *vs.* control group, $P > 0.05$.

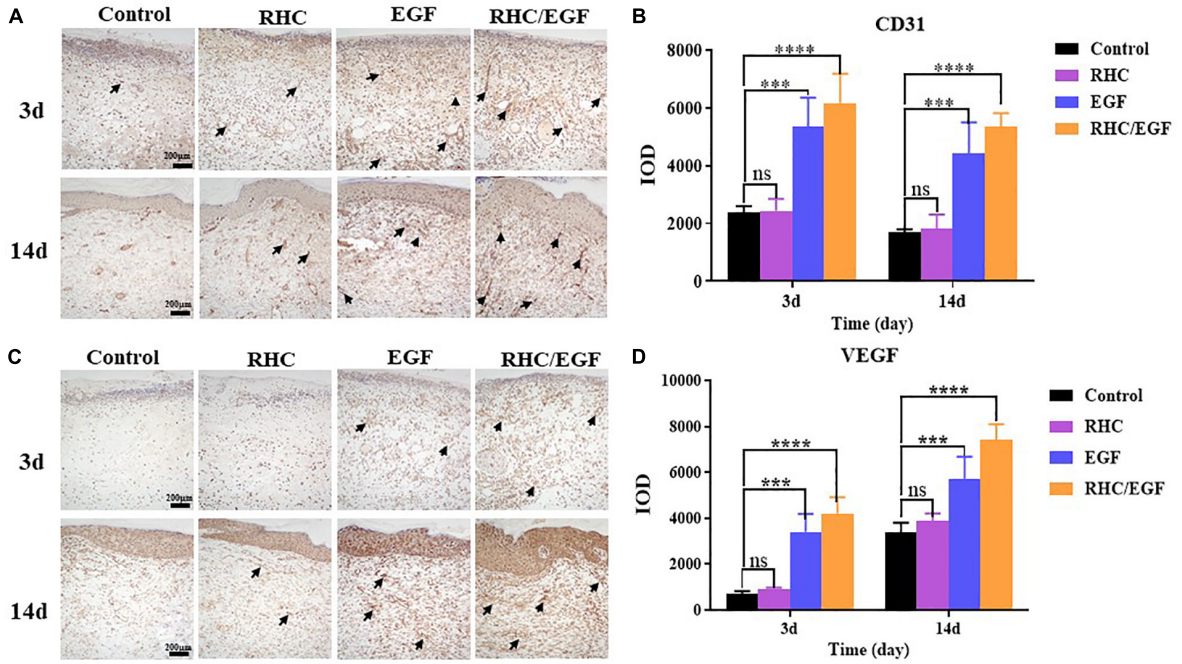

FIGURE 6 | Immunohistochemical examination of CD31 and VEGF expression. **(A)** Immunohistochemical labeling of CD31-positive cells after treatment for 3 and 14 days. Arrows indicate CD31 expression. **(B)** Quantitative analysis of CD31-expressing cells at 3 and 14 days measured using ImageJ software. **(C)** Immunohistochemical labeling of VEGF-positive cells after treatment for 3 and 14 days. Arrows indicate VEGF expression. **(D)** Quantitative analysis of VEGF-expressing cells measured at 3 and 14 days using ImageJ software. $n = 3$, means ± SD, $^{***}P < 0.001$, $^{****}P < 0.0001$ vs. control group, ns means no significant difference *vs.* control group, $P > 0.05$.

compared with the control and RHC groups. Vascular endothelial growth factor expression also exhibited a similar trend at the same time points.

DISCUSSION AND CONCLUSION

The wound healing process is a dynamic and relatively lengthy process. At present, various interventions, including external dressings, biotherapy, physical therapy, and surgical skin grafts, are used for clinical treatment. Numerous research studies have focused on the development of dressings for wound repair. Zhao et al. (2017) developed a series of injectable and conductive self-healed hydrogels. These were based on the quaternized chitosan-*g*-polyaniline (QCSP), and the benzaldehyde group–functionalized poly(ethylene glycol)-co-poly(glycerol sebacate) (PEGS-FA) used as self-healing wound dressings, which significantly promoted the *in vivo* wound healing process (Zhao et al., 2017). Qu et al. (2018) prepared a series of hydrogels by mixing quaternized chitosan (QCS) and benzaldehyde-terminated Pluronic®F127 (PF127-CHO) under physiological conditions as a wound dressing for joint skin wound healing, which were biocompatible and promoted efficient hemostasis (Qu et al., 2018). Wound dressings based on collagen are practical and easily remodeled because of their simple structure, relative uniformity, and abundance. Various wound healing products developed using native collagen (with or without other bioactive compounds) have been available on the market for many years. However, the application of native collagen is limited because of its poor solubility and immunogenicity. Native collagen consists of multiple molecular weight components, and this affects wound dressing consistency and quality. With the improvements in recombinant protein techniques, the research on high-quality and contaminant-free RHC has been growing by leaps and bounds. The RHC may produce a suitable biological dressing for burn wounds as an alternative to native collagen (Shilo et al., 2013; Udhayakumar et al., 2017; Cheng and Hu, 2019). Rutschmann et al. (2014) coexpressed human type III collagen with virus-derived proline 4-hydroxylase in the *E. coli* expression system to obtain RHC with hydroxylated structure (Rutschmann et al., 2014). Many researchers have successfully attempted to produce recombinant type III human-like collagen peptides (Xu et al., 2011; Zhang et al., 2017; Suarez Muñoz et al., 2018). On the wound surface, type I collagen promotes wound healing by providing structural support for cell attachment and migration. Nevertheless, type I collagen is composed of two different peptide chains, and it is more difficult to recombinantly express it compared with type III collagen. Pawelec et al. (2017) recombinantly expressed type I human-like collagen peptides to serve as a scaffold to promote hMSC differentiation (Pawelec et al., 2017). Tye et al. (2005) constructed recombinant type I human-like collagen with a high affinity for the bone sialoprotein and promoted the combination of bone sialoprotein and hydroxyapatite as a

scaffold (Tye et al., 2005). We succeed in constructing an RHC composed of type I collagen-derived cell adhesion domains in the *E. coli* expression system and realized the Modern Scale Production. Because of its safety, reliability, good water solubility, and ease of mass production, it is suitable for use as a tissue-material component in the field of skin repair in the future.

According to the SEM results, the RHC has a nanofibrous structure similar to natural collagen, which can keep the skin lesion moist, as well as retain GFs. The FTIR results indicate that there are no significant structural differences between the RHC and RHC/EGF freeze-dried dressings owing to their similar amino acid or polypeptide composition. This finding does not indicate whether there is a chemical bond between EGF and RHC. With regard to the thermal stability, the results from DSC and TG demonstrated that the RHC and RHC/EGF freeze-dried dressings exhibited higher denaturation temperatures when compared with porcine skin collagen or EGF. We designed the RHC/EGF freeze-dried dressing based on the assumptions that (1) RHC has binding sites for fibroblasts and has a chemotactic effect on these cells; (2) EGF promotes proliferation and migration of keratinocytes; and (3) the combination of RHC/EGF has synergistic effects on the process of skin repair and skin remodeling. The feasibility and efficiency were verified by experiments both *in vivo* and *in vitro*. After treating NIH/3T3 cells (fibroblast-like cell) for 48 h, both EGF alone (69.76% $\pm$ 5.14%, $P < 0.01$, vs. control group) and together with RHC (68.39% $\pm$ 4.55%) significantly enhanced fibroblast cell proliferation compared with RHC alone, suggesting that RHC alone only has the ability to improve adsorption.

In addition, the combination of RHC and EGF accelerates the migration of keratinocytes and significantly promotes the adhesion of NIH/3T3 cells (**Figure 2B**, $P < 0.01$). The cells spread well, and the organized actin cytoskeleton is found throughout the entire cell (**Figures 2D,F**). The results of both the scratch wound assay and immunofluorescence staining showed that the RHC/EGF freeze-dried dressing could promote the migration of cells into the wound area. Recombinant human-like collagen acts as a scaffold to retain EGF and facilitate its long-term function. Recombinant human-like collagen and EGF are mutually interdependent and interact to achieve a wide variety of wound repair functions.

To demonstrate the effects of our RHC/EGF freeze-dried dressing on wound healing *in vivo*, a full-thickness rat skin excisional model was used. In the early process of wound healing, tissue defects are gradually filled with migrating and proliferating fibroblasts, keratinocytes, vascular endothelial cells, and macrophages (Rippa et al., 2019). Granulation tissue formation marks the completion of early wound repair, and its rate of formation is directly related to the rate of wound healing. At 7 days after wounding, there are significant differences between the groups. At 10 days after wounding, the percent wound closure of the RHC/EGF freeze-dried dressing group is greater than 90% ($P < 0.01$), and the wound is generally healed (**Figure 4B**). This phenomenon can be explained by the fact that RHC/EGF promotes the proliferation of fibroblasts and the formation of tiny blood vessels, thus accelerating the formation of granulation tissue and shortening the time for wound healing. In fact, our experiments confirmed the results. When treated with the RHC/EGF freeze-dried dressing, the angiogenic markers CD31 and VEGF in the wound site are significantly upregulated ($P < 0.01$). This indicated to us that the capillary number increased significantly. Wound healing involves the spatiotemporal synchronization of multiple cell types in the hemostasis, inflammation, growth, re-epithelialization, and remodeling phase. The upregulation of cell proliferation biomarkers Ki-67 and PCNA on the third day suggested that the RHC/EGF dressing enhanced cell proliferation in the early stages of wound healing significantly. We observed that the RHC/EGF dressing group healed without scarring, 21 days after wounding. As the healing process continues, regenerative scarless healing greatly depends on the well-controlled reestablishment of normal ECM during the remodeling phase. To assess the quality of the newly formed skin tissue, we used both H&E and Masson trichrome staining. After treatment with the RHC/EGF dressing, histological staining demonstrated that the newly deposited collagen at the wound site had a more orderly arrangement compared with the control group, and the wound area had more collagen fibers and deposition, as well as a significantly increased epithelial thickness.

The primary focus of burn care is the optimization of functional and cosmetic outcomes so that survivors can return to a normal life. Zhao et al. (2018) reported injectable antibacterial conductive cryogels based on carbon nanotubes and glycidyl methacrylate-functionalized quaternized chitosan, which enhanced hemostasis in rabbit liver defects (Zhao et al., 2018). A large number of burns are relatively small and do not affect the quality of life, but even minor burns, if not handled properly, can result in scarring. This can limit function and result in a decreased quality of life. Although many paramedics are skilled at handling small wounds, they are not well-equipped to provide the care that prevents the occurrence of scarring (Greenhalgh, 2016). Epidermal growth factor has a strong effect on wound repair (acute, chronic or large-area burn), and it has also been employed for clinical interventions such as diabetic foot ulcer management (Park et al., 2018). To continually improve the EGF-carrier vector structure and maximize therapeutic effects against pathological processes, we also need to perform rigorous exploration. Based on the results of the full-thickness rat skin excisional model, we speculate that the RHC/EGF dressing can be extensively used in burn and chronic dermal ulcers (such as diabetic ulcers). In addition, whether the RHC/EGF dressing can act as a stem cell attractant is of great interest to us and will form the basis of future studies.

In this study, we constructed an RHC with better cell adhesion properties and also achieved our goal to produce relatively large quantities of RHC. Compared with NIH/3T3 cells cultured on RHC or EGF alone, cells on RHC/EGF demonstrated better adhesion, viability, and migration characteristics ($P < 0.01$). The freeze-dried RHC/EGF dressings are more like the natural collagen fibrous structure when compared with the RHC dressing alone. Consequently, we investigated its potential application in wound healing and repair via full-thickness skin defect SD rats. At 7 days after wounding, the percent wound closure in the RHC/EGF group (67.72% $\pm$ 4.91%) was significantly

higher than the control groups. At 10 days after wounding, the RHC/EGF-treated group recovered. At 21 days after wounding, the RHC/EGF group healed without scarring, whereas non-treatment developed some scars. The wound treated with the RHC/EGF dressing had more collagen fibers and deposition, and the arrangement was denser and more orderly than the control group. Moreover, the wound treated by RHC/EGF upregulated expression of the angiogenesis biomarkers VEGF and CD31, as well as the cell proliferation–specific proteins Ki-67 and PCNA. Collectively, these results support the therapeutic value of the RHC freeze-dried dressing as a topical biomaterial dressing and EGF carrier for regenerative therapies. Because the RHC/EGF freeze-dried dressing is easy to prepare, can be produced on a large scale, and has a clear mechanism of action, we believe that it has great potential for clinical application in the treatment of skin wounds.

DATA AVAILABILITY STATEMENT

The datasets presented in this study can be found in online repositories. The names of the repository/repositories and accession number(s) can be found in the article/ **Supplementary Material**.

ETHICS STATEMENT

The experimental protocols used in this study were approved by the Institutional Animal Care and Use Committee of Jinan University (Approval number: 2019228). All experiments were conducted according to the guidelines for animal care and use of China, and they were approved by the animal ethics committee of the Chinese Academy of Medical Sciences.

AUTHOR CONTRIBUTIONS

QX and YH contributed to the study conception and design. YC and YL contributed to the acquisition of data and study conduct. YL, FY, and SH contributed to the analysis of data. YB and JT contributed to the materials. YB, SH, and YZ helped perform the analysis with constructive discussions. YC and YL wrote the manuscript. QX and YH modified the manuscript. All the authors contributed to the article and approved the submitted version.

FUNDING

This work was supported by grants from the Guangzhou Science and Technology Program Key Project (Grant No. 201803010044), the Major Scientific and Technological Special Project of the Administration of Ocean and Fisheries of Guangdong Province (GDME-2018C013), and the Special Innovation Projects of Universities in Guangdong Province (Grant No. 2019KTSCX011).

ACKNOWLEDGMENTS

The authors would like to acknowledge the faculty and staff at the Biopharmaceutical R&D Center of Jinan University.

SUPPLEMENTARY MATERIAL

The Supplementary Material for this article can be found online at: https://www.frontiersin.org/articles/10.3389/fbioe.2020.00742/full#supplementary-material

REFERENCES

Aljghami, M. E., Saboor, S., and Amini-Nik, S. (2019). Emerging innovative wound dressings. *Ann. Biomed. Eng.* 47, 659–675. doi: 10.1007/s10439-018-02186-w

Cheng, Y., and Hu, Z. (2019). Sponges of carboxymethyl chitosan grafted with collagen peptides for wound healing. *Int. J. Mol. Sci.* 20:3890. doi: 10.3390/ijms20163890

Chin, J. S., Madden, L., Chew, S. Y., and Becker, D. L. (2019). Drug therapies and delivery mechanisms to treat perturbed skin wound healing. *Adv. Drug Deliv. Rev.* 14, 2–18. doi: 10.1016/j.addr.2019.03.006

Choi, S. M., Lee, K. M., Kim, H. J., Park, I. K., Kang, H. J., Shin, H. C., et al. (2018). Effects of structurally stabilized EGF and bFGF on wound healing in type I and type II diabetic mice. *Acta Biomater.* 66, 325–334. doi: 10.1016/j.actbio.2017.11.045

Evan, D.-K., Willian, S. M., and Elena, G.-G. (2019). Sources of collagen for biomaterials in skin wound healing. *Bioengineering* 6:56. doi: 10.3390/bioengineering6030056

Garg, T., and Goyal, A. K. (2014). Biomaterial-based scaffolds–current status and future directions. *Expert. Opin. Drug Deliv.* 11, 767–789. doi: 10.1517/17425247.2014.891014

Gontijo, V. S., Viegas, F. P. D., Ortiz, C. J. C., de Freitas Silva, M., Damasio, C. M., Rosa, M. C., et al. (2019). Molecular hybridization as a tool in the design of multi-target directed drug candidates for neurodegenerative diseases. *Curr. Neuropharmacol.* 18, 348–440. doi: 10.2174/1385272823666191021124443

Grab, B., Miles, A. J., Furcht, L. T., and Fields, G. B. (1996). Promotion of fibroblast adhesion by triple-helical peptide models of type I collagen-derived sequences. *J. Biol. Chem.* 271, 12234–12240. doi: 10.1074/jbc.271.21.12234

Greenhalgh, G. D. (2016). *Burn Care for General Surgeons and General Practitioners*. Germany: Springer Nature.

Guo, J., Luo, Y. E., Fan, D., Yang, B., and Zhu, C. (2010). Medium optimization based on the metabolic-flux spectrum of recombinant *Escherichia coli* for high expression of human-like collagen II. *Biotechnol. Appl. Biochem.* 57, 55–62. doi: 10.1042/BA20100081

Hardwicke, J., Schmaljohann, D., Boyce, D., and Thomas, D. (2008). Epidermal growth factor therapy and wound healing — past, present and future perspectives. *Surgeon* 6, 172–177. doi: 10.1016/s1479-666x(08)80114-x

Mashiko, T., Takada, H., Wu, S. H., Kanayama, K., Feng, J., Tashiro, K., et al. (2018). Therapeutic effects of a recombinant human collagen peptide bioscaffold with human adipose-derived stem cells on impaired wound healing after radiotherapy. *J. Tissue Eng. Regen. Med.* 12, 1186–1194. doi: 10.1002/term.2647

Olsen, D., Jiang, J., Chang, R., Duffy, R., Sakaguchi, M., Leigh, S., et al. (2005). Expression and characterization of a low molecular weight recombinant human gelatin: development of a substitute for animal-derived gelatin with superior features. *Protein Expr. Purif.* 40, 346–357. doi: 10.1016/j.pep.2004.11.016

Olsson, M., Järbrink, K., Divakar, U., Bajpai, R., Upton, Z., Schmidtchen, A., et al. (2019). The humanistic and economic burden of chronic wounds: a systematic review. *Wound Repair Regen.* 27, 114–125. doi: 10.1111/wrr.12683

Park, K. H., Han, S. H., Hong, J. P., Han, S. K., Lee, D. H., Kim, B. S., et al. (2018). Topical epidermal growth factor spray for the treatment of chronic diabetic foot

ulcers: a phase III multicenter, double-blind, randomized, placebo-controlled trial. *Diabetes Res. Clin. Pract.* 142, 335–344. doi: 10.1016/j.diabres.2018.06.002

Pawelec, K. M., Confalonieri, D., Ehlicke, F., van Boxtel, H. A., Walles, H., and Kluijtmans, S. G. J. M. (2017). Osteogenesis and mineralization of mesenchymal stem cells in collagen type I-based recombinant peptide scaffolds. *J. Biomed. Mater. Res. A* 105, 1856–1866. doi: 10.1002/jbm.a.36049

Qu, J., Zhao, X., Liang, Y., Zhang, T., Ma, P. X., and Guo, B. (2018). Antibacterial adhesive injectable hydrogels with rapid self-healing, extensibility and compressibility as wound dressing for joints skin wound healing. *Biomaterials* 183, 185–199. doi: 10.1016/j.biomaterials.2018.08.044

Ramanathan, G., Thyagarajan, S., and Sivagnanam, U. T. (2018). Accelerated wound healing and its promoting effects of biomimetic collagen matrices with siderophore loaded gelatin microspheres in tissue engineering. *Mater. Sci. Eng. C Mater. Biol. Appl.* 93, 455–464. doi: 10.1016/j.msec.2018.08.026

Rippa, A. L., Kalabusheva, E. P., and Vorotelyak, E. A. (2019). Regeneration of dermis: scarring and cells involved. *Cells* 8:607. doi: 10.3390/cells8060607

Rutschmann, C., Baumann, S., Cabalzar, J., Luther, K. B., and Hennet, T. (2014). Recombinant expression of hydroxylated human collagen in *Escherichia coli*. *Appl. Microbiol. Biotechnol.* 98, 4445–4455. doi: 10.1007/s00253-013-5447-z

Shilo, S., Roth, S., Amzel, T., Harel-Adar, T., Tamir, E., Grynspan, F., et al. (2013). Cutaneous wound healing after treatment with plant-derived human recombinant collagen flowable gel. *Tissue Eng. Part. A* 19, 1519–1526. doi: 10.1089/ten.TEA.2012.0345

Suarez Muñoz, M., Confalonieri, D., Walles, H., van Dongen, E., and Dandekar, G. (2018). Recombinant collagen I peptide microcarriers for cell expansion and their potential use as cell delivery system in a bioreactor model. *J. Vis. Exp.* 7:57363. doi: 10.3791/57363

Thönes, S., Rother, S., Wippold, T., Blaszkiewicz, J., Balamurugan, K., Moeller, S., et al. (2019). Hyaluronan/collagen hydrogels containing sulfated hyaluronan improve wound healing by sustained release of Heparin-Binding EGF-like growth factor. *Acta Biomater.* 86, 135–147. doi: 10.1016/j.actbio.2019.01.029

Tye, C. E., Hunter, G. K., and Goldberg, H. A. (2005). Identification of the type I collagen-binding domain of bone sialoprotein and characterization of the mechanism of interaction. *J. Bio.Chem.* 280, 13487–13492. doi: 10.1074/jbc.M408923200

Udhayakumar, S., Shankar, K. G., Sowndarya, S., and Rose, C. (2017). Novel fibrous collagen-based cream accelerates fibroblast growth for wound healing applications: *in vitro* and *in vivo* evaluation. *Biomater. Sci.* 5, 1868–1883. doi: 10.1039/c7bm00331e

Xu, X., Gan, Q., Clough, R. C., Pappu, K. M., Howard, J. A., Baez, J. A., et al. (2011). Hydroxylation of recombinant human collagen type I alpha 1 in transgenic maize co-expressed with a recombinant human prolyl 4-hydroxylase. *BMC Biotechnol.* 11:69. doi: 10.1186/1472-6750-11-69

Yang, C., Hillas, P. J., Báez, J. A., Nokelainen, M., Balan, J., Tang, J., et al. (2004). The application of recombinant human collagen in tissue engineering. *Biodrugs* 18, 103–119. doi: 10.2165/00063030-200418020-00004

Yao, J., Yanagisawa, S., and Asakura, T. (2004). Design, expression and characterization of collagen-like proteins based on the cell adhesive and crosslinking sequences derived from native collagens. *J. Biochem.* 136, 643–649. doi: 10.1093/jb/mvh172

Ying, H., Zhou, J., Wang, M., Su, D., Ma, Q., Lv, G., et al. (2019). In situ formed collagen-hyaluronic acid hydrogel as biomimetic dressing for promoting spontaneous wound healing. *Mater. Sci. Eng. C Mater. Biol. Appl.* 101, 487–498. doi: 10.1016/j.msec.2019.03.093

Yuan, Y., Wu, L., Shen, S., Wu, S., and Burdick, M. M. (2016). Effect of alpha 2,6 sialylation on integrin-mediated adhesion of breast cancer cells to fibronectin and collagen IV. *Life Sci.* 149, 138–145. doi: 10.1016/j.lfs.2016.02.071

Zhang, Z., Zhang, C., Guo, Q., Ma, G., Shen, L., Yu, H., et al. (2017). Application of recombinant collagen type I combined with polyaspartic acid in biomimetic biomineralization. *Acta Acad. Med. Sin.* 39, 318–323. doi: 10.3881/j.issn.1000-503X.2017.03.004

Zhao, X., Guo, B., Wu, H., Liang, Y., and Ma, P. X. (2018). Injectable antibacterial conductive nanocomposite cryogels with rapid shape recovery for noncompressible hemorrhage and wound healing. *Nat. Commun.* 9:2784.

Zhao, X., Liang, Y., Huang, Y., He, J., Han, Y., and Guo, B. (2020). Physical double-network hydrogel adhesives with rapid shape adaptability, fast self-healing, antioxidant and NIR/pH stimulus-responsiveness for multidrug-resistant bacterial infection and removable wound dressing. *Adv. Funct. Mater.* 30:1910748. doi: 10.1002/adfm.201910748

Zhao, X., Wu, H., Guo, B., Dong, R., Qiu, Y., and Ma, P. X. (2017). Antibacterial anti-oxidant electroactive injectable hydrogel as self-healing wound dressing with hemostasis and adhesiveness for cutaneous wound healing. *Biomaterials* 122, 34–47. doi: 10.1016/j.biomaterials.2017.01.011

Conflict of Interest: The authors declare that the research was conducted in the absence of any commercial or financial relationships that could be construed as a potential conflict of interest.

frontiers in Bioengineering and Biotechnology

REVIEW
published: 17 September 2020
doi: 10.3389/fbioe.2020.576348

Surface Engineered Metal-Organic Frameworks (MOFs) Based Novel Hybrid Systems for Effective Wound Healing: A Review of Recent Developments

Luo-Qin Fu[1†], Xiao-Yi Chen[2,3†], Mao-Hua Cai[1], Xiao-Hua Tao[4†], Yi-Bin Fan[4] and Xiao-Zhou Mou[2,3*]*

[1] Department of General Surgery, Chun'an First People's Hospital (Zhejiang Provincial People's Hospital Chun'an Branch), Hangzhou, China, [2] Key Laboratory of Tumor Molecular Diagnosis and Individualized Medicine of Zhejiang Province, Zhejiang Provincial People's Hospital, People's Hospital of Hangzhou Medical College, Hangzhou, China, [3] Clinical Research Institute, Zhejiang Provincial People's Hospital, People's Hospital of Hangzhou Medical College, Hangzhou, China, [4] Department of Dermatology, Zhejiang Provincial People's Hospital, People's Hospital of Hangzhou Medical College, Hangzhou, China

Wounds present serious medical complications and their healing requires strategies that promote angiogenesis, deposition of collagen as well as re-epithelialization of wounds. Currently used conventional wound healing strategies have become less effective due to various issues associated with them. Thus, novel strategies are needed to be developed for early and effective healing of wounds. Metal-organic frameworks (MOFs), formed by linking of metal ions through organic bridging ligands, are highly tunable hybrid materials and have attracted more considerable scientific attention due to their charming and prominent properties, such as abundant pore structures and multiple functionalities. Surface engineering of MOFs with unique ligands can overcome issues associated with conventional wound healing methods, thus resulting in early and effective wound healing. This review has been undertaken to elaborate wound healing, and the use of surface engineered MOFs for effective and rapid wound healing. The process of wound healing will be discussed followed by a detailed review of recent literature for summarizing applications of surface engineered MOFs for wound healing. MOFs wound healing will be discussed in terms of their use as antibacterial agents, therapeutic delivery vehicles, and dressing systems in wound healing.

Keywords: metal-organic frameworks, surface modification, wounds healing, bactericidal, dressings

OPEN ACCESS

Edited by:
Kai Zheng,
University of Erlangen Nuremberg, Germany

Reviewed by:
Xin Zhao,
Hong Kong Polytechnic University, Hong Kong
Rui Guo,
Jinan University, China
Francesco Baino,
Politecnico di Torino, Italy

****Correspondence:***
Yi-Bin Fan
frankgets@sina.com
Xiao-Zhou Mou
mouxz@zju.edu.cn

[†] These authors have contributed equally to this work

Specialty section:
This article was submitted to Biomaterials, a section of the journal Frontiers in Bioengineering and Biotechnology

Received: *25 June 2020*
Accepted: *17 August 2020*
Published: *17 September 2020*

Citation:
Fu L-Q, Chen X-Y, Cai M-H, Tao X-H, Fan Y-B and Mou X-Z (2020) Surface Engineered Metal-Organic Frameworks (MOFs) Based Novel Hybrid Systems for Effective Wound Healing: A Review of Recent Developments. Front. Bioeng. Biotechnol. 8:576348. doi: 10.3389/fbioe.2020.576348

INTRODUCTION

Skin is the largest organ of the human body that protects the body against external threats, such as injury and microbial attack (Xu et al., 2015). However, skin damage is one of the most common everyday emergencies and could severely affect the health and lives of people, especially when the defect is severe (Admassie et al., 2018). Wounds are usually considered painful injuries of the skin tissue, when dermal layers are cut, punctured, or broken due to external stimulus or damage.

In everyday life, wounds are a complex and challenging clinical problem linked to numerous complications that lead to frequent mortality and morbidity (Natarajan et al., 2000). Wounds are typically categorized into two categories as per their time frame of healing. Wounds that get cured in a predictable period followed by anatomical and functional restoration of tissue are called acute wounds (Harding et al., 2002). Such wounds are usually caused by severe tissue damage or surgery. On the other side, wounds that do not cure in a consistent period contributing to further problems, such as inflammation and healing issues are classified as chronic wounds. Chronic wounds include vascular ulcers, pressure ulcers, and diabetic ulcers (Nethi et al., 2019).

Cutaneous injuries are a global part of medical care, with around 300 million severe patients around the world and 100 million traumatic wound patients. Wounds have an enormous financial burden on healthcare systems globally, representing more than $25 billion annually in the US alone (Sen et al., 2009; Das and Baker, 2016). The wound care products market has expanded massively to over US$ 15 billion, including US$ 12 billion to deal with wound scars (Nethi et al., 2019). Unexpectedly, healthcare providers and patients in the US are charged a cost of around US$ 9 billion annually to perform lower limb amputations resulting from diabetic foot ulcers (Falanga, 2005). The aging population is at heightened risk of the socio-economic and medical pressures induced by complications of wounds (Nethi et al., 2019). Such high health and socio-economic pressures reinforce the need for intensive work to create new therapies in this area.

The process of repairing and regenerating wound tissue is among the most complicated biological mechanism in humans, involving angiogenesis, tissue remodeling, cell proliferation, and others (George Broughton et al., 2006; Qiu et al., 2020). Numerous treatments have also been tested with positive findings to preserve safe skin and prolong the wound healing cycle. Wounds may be handled with conventional as well as new therapies. Fascinating alternatives are conventional therapies that employ larvae, plant extracts, maggots, honey, and propolis. Such conventional medicines are commonly used globally, in particular in Latin America, Asia, and Africa (Pereira and Bartolo, 2016). Besides conventional therapies, there are numerous new approaches. Hyperbaric oxygen therapy is one of the latest wound healing approaches that use oxygen flows to the site of injury and finally retards amputation (Santema et al., 2018). Negative pressure wound therapy is used for various types of both chronic and acute wounds. It helps to improve angiogenesis by discarding interstitial fluids and bacterial infections at the site of the wound and clearing lymph nodes (Armstrong et al., 2002; Schurtz et al., 2018). Currently, bioengineered cell construct has become of paramount importance in the management of venous leg ulcers, which are a form of a life-threatening chronic wound with a high degree of morbidity (Stone et al., 2017). Dressing of polymer-containing materials that imitate the physical and biological properties of the surrounding tissues ultimately helps the process of healing (Pereira and Bartolo, 2016). Surgery is still very a popular treatment for untreated wounds that are not healed (Thakral et al., 2015).

Conventional wound treatment methods have been associated with some drawbacks, such as the occurrence of allergic reactions, uncertain mechanisms of action, possible contamination, fast drying of the wound region, and variability in batch to batch (Walgrave et al., 2005; Jurczak et al., 2007). Medications utilized for wound treatment have certain limitations including contribution to paranoia, peptic ulceration, hyperglycemia, and slow healing of bones. Other limitations include inhibition of the healing process by decreasing cell mobility to injury sites, the effect on collagen operation, hampering fibroblasts formation, minimizing oxygen flow to the wound site, and reducing immunity which delays the healing of wounds (Ovais et al., 2018). Various other factors, such as malnutrition, obesity, diabetes, medication, and lifestyle deregulate the process of wound healing by extending or stopping incidents in any phase of wound healing (Anderson and Hamm, 2012). Also, bacterial infection and the slow separation of fibroblasts may hinder the healing process, contributing to swelling, local pains, and even thus threatening complications (Lai and Rogach, 2017; Ren et al., 2019). Thus, there is a critical need to build alternative solutions to address unmet health challenges involved in wound care management (Nethi et al., 2019). Nanotechnology is an increasingly growing scientific area and has been used to solve various biological issues, both therapeutic and diagnostic. Numerous nanotechnologies have appeared over the last few decades, creating enormous possibilities because of their unique properties and perfect applications. These technologies can address the complexity of the wounds and their specificity. Such nanotechnologies include the use of numerous metal-dependent nanoparticles and metal-organic frameworks (MOFs) (Hamdan et al., 2017; Ren et al., 2019).

Metal-organic frameworks (MOFs) are among nanotechnology's most exciting and high-profile areas that have appeared in the last decade (Hinks et al., 2010). MOFs are a group of crystalline coordinating materials made up of metal ions or clusters widened of organic polydentate ligands (Yu et al., 2018). The term MOFs was coined in 1995, and the filed gained momentum in 1999 after the work of Chui et al. (1999). MOFs have been thoroughly researched for applications in various areas including chemistry, climate, energy, and biomedicine, due to their unique properties such ultra-high surface area, tuned but consistent pore sizes, strong thermal stability, large internal spaces, biocompatibility, and easy synthesis (Yu et al., 2017, 2018). In recent years, MOFs have gained more interest in the field of biomedical applications, such as drug carriers, biological imaging, sensing, and theranostic nanovectors due to their unique benefits of large pores, biodegradation, biocompatibility, increased drug loading, and flexible size (Yu et al., 2017). Currently, MOFs are getting wider attention for wound healing owing to their increased drug loading, surface modulation for targeted delivery and controlled released of the wound healing agents, lesser toxicities, intrinsic angiogenic and antibacterial properties as compared to other nanomaterials (Xiao et al., 2017; Chen et al., 2019). As compare to other nanomaterials, MOFs have metals ions, for instance, copper, as their central structural blocks. Thus, these central blocks of MOFs are intrinsically involved in various wound healing processes, such

as angiogenesis, promotion of vascular endothelial growth, and stabilization and expression of various extracellular skin proteins including collagen and keratin (Xiao et al., 2017, 2018; Kargozar et al., 2019b). Furthermore, certain elements used as structural blocks of MOFs, for instance, zinc and copper, help in wound healing of infectious wounds of *S. aureus* and *E. coli* due to their natural bactericidal properties, thus leading to effective and rapid wound healing. Similarly, MOF-based wound dressing accelerates wound healing due to its bactericidal and anti-inflammatory properties through encouraging cell proliferation, angiogenesis, and collagen deposition (Hinks et al., 2010; Rubin et al., 2018; Hou and Tang, 2019; Kargozar et al., 2019a; Yao et al., 2020). Interestingly, MOFs have free functional groups decorated on their surfaces, thus they provide opportunities for their surface functionalization. Surface engineered MOFs render unique properties, such as targeted delivery, stability, controlled release of their loaded contents, and additional biological properties (Ghaffar et al., 2019). Recently surface engineered MOFs have attracted a greater scientific interest for wound healing due to their intrinsic biological properties and delivery and controlled release of therapeutic agents (Zhang M. et al., 2020; Zhang S. et al., 2020). Moreover, the concept of surface engineered MOFs systems with or without therapeutic agents is gaining increasing popularity for quick and cost-effective wound healing (Yu et al., 2018; Ren et al., 2019; Zhang M. et al., 2020).

To the best of our knowledge, no review has been published on applications of surface engineered MOFs for effective wound healing. This review has been undertaken to highlight the applications of surface engineered MOFs for effective and early wound healing. The process of wound healing will be discussed followed by a detailed literature review for summarizing applications of surface engineered MOFs for wound healing. MOFs wound healing will be discussed in terms of their use as antibacterial agents, therapeutic delivery vehicles, and dressing systems in wound healing. This review will be an excellent addition to the body of scientific knowledge for understanding applications of MOFs for early and effective wound healing.

PROCESS OF WOUND HEALING

Wound healing is a natural physiological process that takes place in reaction to any damage or injury to the tissue. The process includes complex interactions between different types of cells, factors of coagulation, connective tissue, growth factors, cytokines, and the vascular system. Four steps in the wound healing cycle are illustrated in **Figure 1**. The hemostasis is the very first stage in wound healing. After the initial wounding, the bleeding occurs and hemostasis is needed. During hemostasis, bleeding is terminated by the process of platelet aggregation, vasoconstriction, and blood coagulation. The next stage in the healing process is inflammation that is triggered by the inflammatory mediators (prostaglandins and histamine), which increases the nearby vessel's permeation and vasodilation. Inflammation lasts for 4 days, and during this process, immune cells are recruited to reduce infection and stimulate capillary growth. After Inflammation, the next stage is the proliferative phase, in which the wound area is created with fresh collagen- and extracellular matrix (ECM) connective tissue. Myofibroblasts assemble across the wound margin and draw the edges via contracting, which facilitates the healing process rapidly (Brown et al., 1988; Naseri et al., 2017). The last stage of the proliferation process is re-epithelialization, wherein epithelial cells expand and migrate through the wound. A moist wound atmosphere speeds this cycle up. This stage of wound healing may last for several months and is characterized by the continuous low rate of collagen degradation, synthesis, and reorganization. In compromised patients, various factors lead to poor or slow healing, thus this in turn results in the development of chronic wounds. Examples of such wounds are ulcers in diabetic patients (Junker et al., 2013).

Surface Engineered MOFs in Wound Healing

In the current decade, substantial progress has been made in the widespread usage of MOFs in the field of pharmaceutical therapy, owing to their well-defined porous aperture, fast drug loading, increased medication bioavailability, and long operation duration (Li et al., 2017; Wu and Yang, 2017; Abánades Lázaro et al., 2018). The high structural designability and flexible functionality of the MOFs in specific create synergistic effects with the drugs, helping to make them potential candidates for healing multiple kinds of wounds (Liu et al., 2019; Zhang et al., 2019b). MOFs are widely used for wound healing owing to their increased drug loading, surface modulation for targeted delivery and controlled released of the wound healing agents, lesser toxicities, intrinsic angiogenic and antibacterial properties as compared to other nanomaterials (Xiao et al., 2017; Chen et al., 2019). The wound healing properties of MOFs can be further improved through their surface engineering. Interestingly, MOFs have free functional groups decorated on their surfaces, thus they provide opportunities for their surface functionalization or engineering. Surface engineered MOFs render unique properties, such as targeted delivery, stability, controlled release of their loaded contents, and additional biological properties (Ghaffar et al., 2019; Zhang S. et al., 2020). Many functional biological molecules can be chemically or physically conjugated or adsorbed on the surfaces of MOFs via surface engineering, thus leading to synergistic properties. Furthermore, surface engineered MOFs render improved sustain release properties, therefore, they efficiently maintain the therapeutic concentration of their loaded drugs for a longer time (Meng et al., 2020). Applications of surface engineered for wound healing can be discussed under the following sub-headings.

Bactericidal Surface Engineered MOFs in Wounds Healing

Among the complexities, the bacterial infection has become a major issue that has a major impact on normal skin healing (Zhang et al., 2019a). Metallic antibacterial agents, such as zinc, silver, copper-based oxides, or ions have been employed for the last few decades to kill or inhibit the growth of bacteria across the wounds (Chen et al., 2018). Nevertheless, the usage of metallic

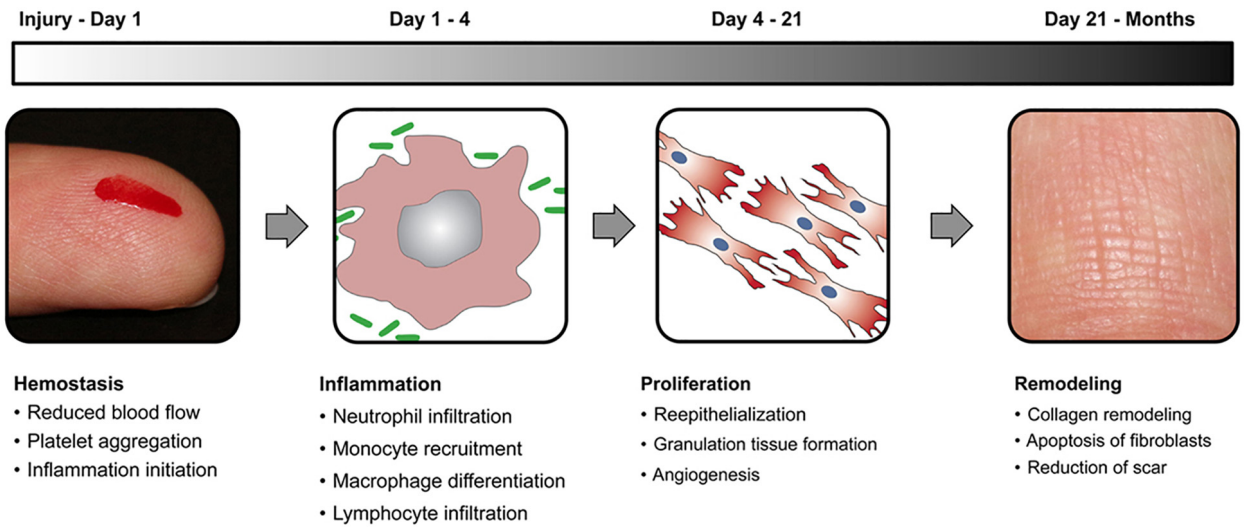

FIGURE 1 | A schematic representation of wound healing stages with a time scale for each stage. Reproduced from Das and Baker (2016).

antibacterial agents is also dangerous because of their possible toxicity caused by the sudden release of metal ions (Dreifke et al., 2015). Hence there is a considerable therapeutic need to alleviate the toxic effects of metallic antibacterial agents by delaying the discharge of metal ions. Some scientists have previously shown the antibacterial ability of MOFs that lead to their slow release of metal ions (Zhuang et al., 2011; Lu et al., 2014). Because of its adjustable chemical and physical properties, the release of metal ions from MOFs becomes suitable for fine-tuning, making MOFs suitable for wound dressing (Zhang et al., 2014; Mason et al., 2015).

In a recent study, Luo and colleagues developed versatile surface engineered MOFs systems with properties of both photodynamic therapy (PDT) and photothermal therapy (PTT). The novel system was highly efficient in achieving antibacterial activity against bacterial species in wound infections. UIO-66 MOFs were synthesized and were surface engineered in a way that they contained Prussian blue (used for PTT) in core and porphyrins (used for PDT) as a shell. This core-shell PB@MOF not just to acquires Prussian blue's photothermal influence (**Figure 2**) but also attaches porphyrin's photodynamic value, thereby demonstrating an outstanding synergistic activity toward bacterial infection. Those versatile MOFs demonstrated good activity toward *S. Aurores* and *E. Coli*, the bacterial genus most widespread in infections, under optimization situations of PTT and PDT. They further researched the synthesized MOFs for their extracorporeal wound healing infection of rat form *S. aureus*. After 14 days of therapy, full wound healing was observed without injury in the key rat organs, demonstrating the health of dual surface-engineered MOFs (Hou and Tang, 2019).

A recent study reported the fabrication of a powerful surface-adaptive, on-demand antimicrobial nanoplatform using surface engineered MOFs for effective healing of the infectious wound. Photo-sensitive MOFs were surface-functionalized with hyaluronic acid (HA) followed by their loading on Ag ions. The novel multi-functional MOFs showed good biocompatibility with non-targeted cells, as negatively charged HA prevented the release of Ag ions. While in the presence of targeted bacteria, the secreted hyaluronidase degraded HA on and produced positively charged nanoparticles. This in turn increased the MOFs affinity toward bacteria and resulted in a synergistic antibacterial effect due to the released Ag ions and generation of reactive oxygen species under visible light irradiation. When further studied *in vivo*, the novel multi-functional MOFs showed significant impacts on the treatment of multidrug-resistant wounded bacteria in mice models (Zhang et al., 2019b). In a similar study, silver nanoparticles of ultra-small size were synthesized using γ-cyclodextrin MOFs. These MOFs embedded with silver nanoparticles exhibited increased bacterial inhibition. GRGDS peptide, which promotes hemostatic plug formation through binding to integrin GPIIb-IIIa receptor on activated platelets was used for further surface functionalization of these MOFs. These surface-functionalized MOFs showed elevated wound healing through hemostatic effects in synergy with the antibacterial effect of silver nanoparticles embedded in MOFs (Shakya et al., 2019).

In another recent study, surface engineered niacin MOFs were fabricated with alginate shell and copper-/zinc-niacin framework cores and used for wound healing. The niacin MOFs were having outstanding properties of angiogenesis, antioxidant, and antibacterial. The alginate shells of the smart MOFs were bacteria responsively degradable. The niacin MOFs were capable of releasing copper, zinc, and calcium ions in an intelligent, controllable, and programmable manner in response to the degree of infections. The released ion destroyed infectious microbes through their membrane destruction and induced the outflow of nutrient substances. They also activated copper/zinc superoxide dismutase (Cu/Zn-SOD) to eliminate oxygen free radicals and rescuing the cells from an oxidative stress injury. Furthermore, the simultaneously released niacin promoted hemangiectasis and the absorption of functional metal

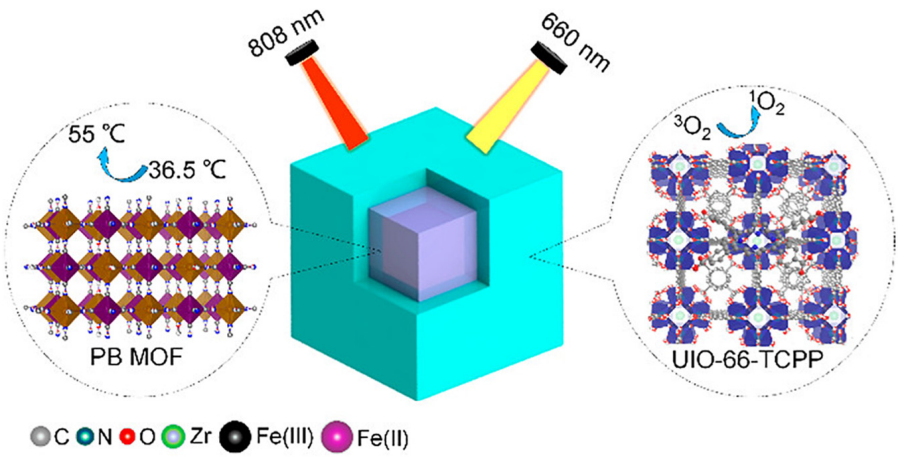

FIGURE 2 | Schematic presentation of the core-shell structure of UIO-66 MOFs. The surface engineered MOFs contain Prussian blue as a core and porphyrin as a shell for simultaneous PDT and PTT therapies against bacteria in wound healing. Used with permission from Hou and Tang (2019). Note to readers: Further permissions related to the material excerpted should be directed to the ACS).

ions. Additionally, the continuously generated niacin facilitated hemangiectasis and uptake of functional metal ions. These MOFs further improved the healing process of the wound of the injured full-thickness skin defect model (Chen et al., 2019).

Surface Engineered MOFs in Multi-Functional Dressings for Effective Wound Healing

During the healing process, the tissue must be protected from infectious diseases and other environmental external damage (Sen et al., 2009). Wound dressings are preferred for protecting wounds from bacterial colonization and other environmental hazards. Distinct wound dressings were required to fight bacteria by embedding bactericidal ingredients like polymeric substances and metal ions (Yao et al., 2020). The dressings are also made from inherent hydrophilic fabrics, like cotton, polymers, and hydrogels, to promote the infiltration of released active ingredients into wounds (Dhivya et al., 2015). Nevertheless, many other hydrophilic dressings have tiny evident contact angle (CA); elevated biofluids could be strongly stuck to the rough matrix of the dressing after they have been wet (Shi et al., 2019). Unabsorbed biofluids can overhydrate the wound that can cause vulnerability to microbial invasion, tissue edge maceration, and extracellular matrix damage, bacterial colonization, and tissue damage (Okan et al., 2007; Wild et al., 2010). Therefore, the development of new and multifunctional protective wound dressings is urgently needed. Highly porous MOFs surface modified with functional bactericidal materials is currently getting increasing interest for the fabrication of effective and safe wound dressing materials. Being intrinsically bactericidal, further surface modification of MOFs can synergistically improve their wound healing activity. Furthermore, they can also be loaded with therapeutic substances and release them in a programmable manner, thus leading to effective wound healing with higher safety (Xiao et al., 2017; Yao et al., 2020).

Most recently, Yao et al. reported the fabrication of omniphobic MOFs based hydrogel porous wound dressing for inhibition of bacteria invasion and acceleration of wound healing. The novel MOFs based hydrogel showed a controlled release of the non-toxic zinc ions anti-inflammatory and bactericidal. Besides, the wound dressing relying on MOFs has speeded up the wound healing in an infected full-thickness skin defect model due to angiogenesis, synergistic antibacterial effects, reduced inflammation, the proliferation of fibroblasts and collagen deposition (Yao et al., 2020). In another most recent study, Han et al. (2020) synthesized photosensitive wound dressing hydrogels using MOFs modified with double-bond modified chitosan, Prussian blue, and quaternary ammonium. The synthetic hydrogels showed excellent photothermal characteristics under near-infrared light irradiation of 808 nm. MOFs based novel hydrogel was capable of capturing bacteria tightly through electrostatic interactions due to the presence of chitosan. The presence of bactericidal chitosan and photothermal Prussian blue in the MOFs based hydrogel synergistically increased its antibacterial effects. When used as a wound dressing for wound cuts in rates, the MOFs based hydrogel demonstrated increased wound healing without causing injuries in other organs (Han et al., 2020).

The application of copper ions has already shown potential likely by encouraging angiogenesis in wound healing applications. Copper is a well-known antimicrobial agent and can significantly enhance healing by lowering the risk of wound infection. Even so, identifying treatment options using copper ions involves additional copper salts or oxides to be applied to the wound site, subjecting the patient to highly harmful levels of copper ions and leading in inconsistent effects (Mandinov et al., 2003; Guo et al., 2013; Amna et al., 2014). The toxicity can be mitigated, though, when copper ions are gradually emitted from a repository at the wound. Xiao et al. developed a highly safe cooperative cooper MOFs that were surface engineered through their embedding into an antioxidant

thermoresponsive citrate-based hydrogel for accelerated wound healing in diabetic mice. These smart surface engineered cooper MOFs hydrogel showed significantly accelerated wound healing with higher safety owing to their controlled release capability of copper ion (Xiao et al., 2017). A recent study by Yu et al. (2018) reported the fabrication of copper- or zinc-MOF-laden hydrogels containing vitamin for effective wound healing. The novel MOF-laden hydrogel microfibers of alginate shells and copper- or zinc-vitamin frame cores use a microfluidic coaxial capillary spinning method (**Figure 3**). Due to the antioxidation and antibiosis features of their controllably released vitamin ligands, zinc ions, and copper ions, the novel MOFs system demonstrated the practical value in tissue wound healing (Yu et al., 2018). A similar approach for fabrication of effective wound dressing was adopted by Ren et al. They synthesized copper-based MOFs loaded with chitosan-based multi-functional films (HKUST-1/CS) for effective antibacterial and wound healing purposes. Due to the slow release of copper ion and the presence of high contents of chitosan in these MOFs, an improved antibacterial activity against *S. aureus* and *E. coli* was achieved. Furthermore, novel MOFs based these multi-functional films effectively prevented *S. aureus* bacteria-derived wound infection (**Figure 4**) and enhanced the cutaneous wound repair without recurrence by stimulating the formation of blood vessels, epidermis and dermis (Ren et al., 2019).

In another similar recent study, Wang et al. copper-based MOFs surface modified with chitosan/polyvinyl alcohol fibers as a wound dressing for enhanced antibacterial and wound properties. The MOFs based novel dressing materials showed increased antibacterial against *S. aureus* and *E. coli*, the most common bacterial species in wound infections. In animal studies, contrasted with commercial dressings of chitosan and chitosan/PVA fibers, these MOFs surface modified with fibers were more potent to heal the wound with minimum inflammation (Wang et al., 2020). In another recent study, Yang et al. synthesized surface engineered MOF derived photo-responsive nanocarbon for safe, rapid, and synergistic chemophotothermal bacterial disinfection of wounds. The novel surface engineered MOFs demonstrated nearly 100% bactericidal activity at a very low dose. They also particularly efficient and healthy disinfection of skin wounds that were comparable with vancomycin (Yang et al., 2019).

Surface Engineered MOFs in Therapeutics Delivery for Wound Healing

Owing to their porous nature and large surface area, MOFs are used as depot systems for loading and delivering therapeutic agents for wound healing. Studies have recently identified that NO plays a key role in the wound repair process, demonstrating that growing endogenous NO synthesis or exogenous NO can inhibit inflammation, promote angiogenesis and enhance collagen deposition throughout the healing process (Zhou et al., 2017; Champeau et al., 2018). To obtain an effective NO-based therapy for diabetic wound healing, however, regulating the NO-release activity and preserving its optimal concentration is essential. Owing to their unique properties including, porosity and extreme-high specific surface area, adjustable particle size, easy to be functionalized, and low skeleton density, MOFs have emerged versatile carriers for NO delivery for effective wound healing. Also, due to their more active sites that can sustainably incorporate with more gas molecules, MOFs show admirable superiority in delivery and gas storage (Furukawa et al., 2013;

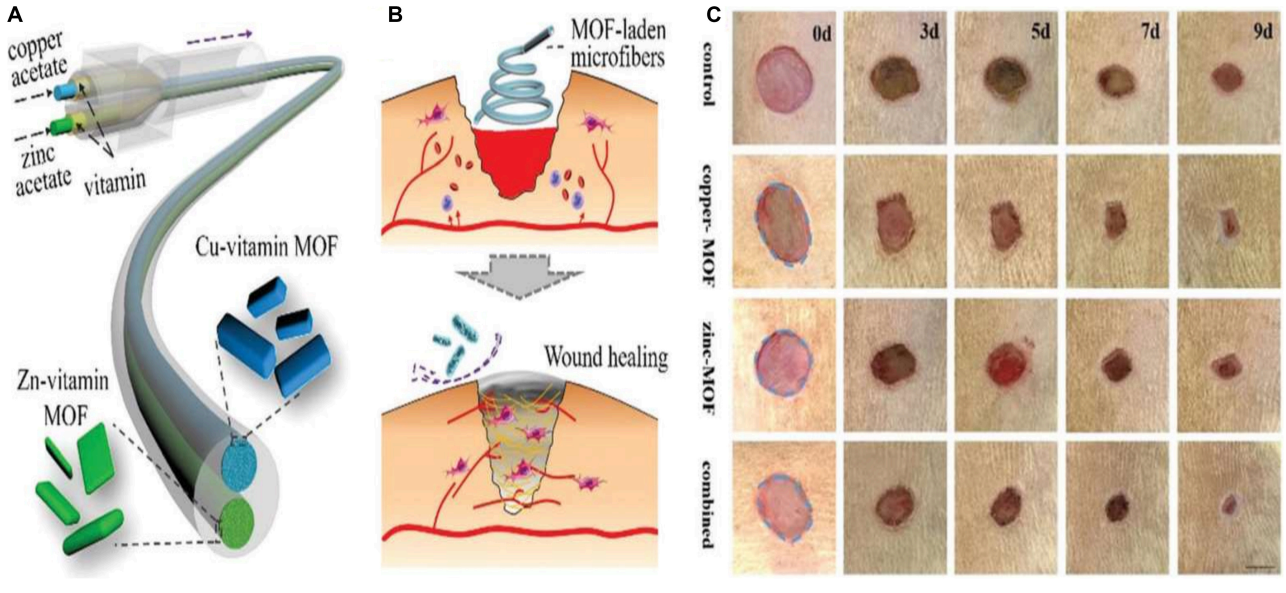

FIGURE 3 | (A) Schematic presentation for vitamin MOF-laden hydrogel microfibers fabrication, **(B)** Schematic presentation for wound healing applications of the fabricated vitamin MOF-laden the application of the microfibers in the wound healing process, and **(C)** Representative photos of the skin wounds treated with fabricated MOFs systems. Reproduced from reference Yu et al. (2018) permission conveyed through Copyright Clearance Center, Inc.

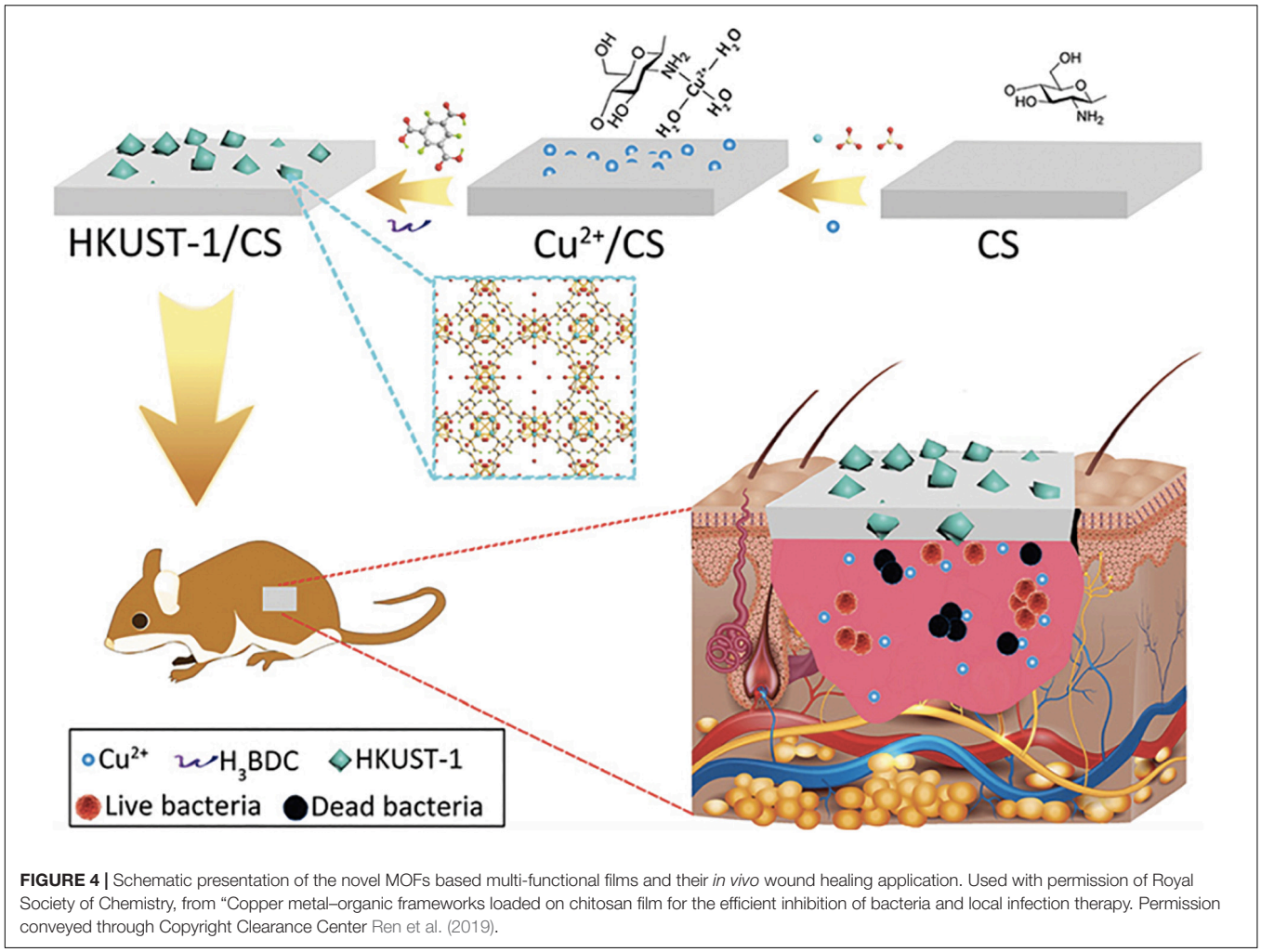

FIGURE 4 | Schematic presentation of the novel MOFs based multi-functional films and their *in vivo* wound healing application. Used with permission of Royal Society of Chemistry, from "Copper metal–organic frameworks loaded on chitosan film for the efficient inhibition of bacteria and local infection therapy. Permission conveyed through Copyright Clearance Center Ren et al. (2019).

Li et al., 2016). Within the MOFs, in particular, there are many coordinately unsaturated metal sites (CUS) that can establish close relationships with NO. This ability makes the MOF a successful vehicle for NO storage applications for permanent and long shelf life (Hinks et al., 2010).

Diabetic wounds are serious complications associated with diabetes. Their healing process is extremely slow or they even do not heal. Researchers have found that high sugar contents prevent the production of endogenous NO, thus inhibit the healing of diabetic wounds (Schäffer et al., 1997; Luo et al., 2004). Thus, externally applied NO has become an effective therapeutic strategy for quick and effective healing of diabetic wounds. In a most recent study, copper-based core-shell MOFs surface engineered with 4-(Methylamino) pyridine and prepared through the electrospinning method was reported as a NO-loading and sustained release system for enhanced diabetic wound healing (Zhang P. et al., 2020). The surface engineered MOFs system revealed long release and half-life storage stability, higher biodegradability, and biocompatibility. Furthermore, copper ions and NO synergistically stimulated angiogenesis, promoted collagen deposition and inhibited inflammation in the wound area, thus resulting in complete healing of the diabetic wound in 2 weeks in mice.

In another recent study, Li et al. designed and developed cobalt-based nano MOFs (ZIF-67) as carriers for loading and delivering a pro-angiogenic drug dimethyloxalylglycine for long-term therapy of diabetic wound. The drug-loaded MOFs were further surface engineered into a dual cooperative controllable release system through their incorporation into micro-patterned PLLA/Gelatin nanofibrous scaffolds. The novel system was capable of releasing the loaded drug as well as copper ions continuously for more than 15 days. *In vitro* study has demonstrated that the released copper ions and drug from the novel surface engineered MOFs system could therapeutically enhance the migration, proliferation, and tube formation of the human umbilical vein endothelial cells by upregulating the expression of angiogenesis-related genes and triggering a hypoxia response. Besides, the *in vivo* findings showed that the latest surface built MOFs system could substantially enhance angiogenesis, collagen deposition, and reduce inflammation in diabetes wounds (Li et al., 2020). In another study, copper-based MOFs nanoparticles were synthesized and were further modified with folic acid. Surface modification of MOFs with

folic acid not only reduced the copper-related toxicity but also significantly accelerated the wound healing process in diabetic mice (Xiao et al., 2018).

CONCLUSION AND FUTURE PERSPECTIVES

Wounds not only present severe medical complications but also lead to an enormous financial burden on healthcare systems globally. Currently used conventional wound healing strategies have become less effective due to various issues associated with them. Researchers are exploring alternative that is highly safe, effective, and result in early wound healing. MOFs are highly tunable hybrid materials and have recently attracted greater scientific attention for effective wound healing due to their prominent properties. Surface engineering of MOFs with unique functional materials can overcome issues associated with conventional wound healing methods, thus resulting in early and effective wound healing with higher safety. Our survey of the literature shows that, during the last 3 years, surface engineered MOFs have been reported for effective wound healing. They have been reported as antibacterial agents, therapeutic delivery vehicles, and dressing systems in wound healing. Such surface-modified MOFs accelerated wound healing through their inherent bactericidal properties, releasing their contents in a controllable manner and aiding to physiological processes of wound healing. Being a new area of research, all the studies have been carried out *in vitro* or *in vivo* in animal wound models. Yet no surface-modified MOFs system has been entered clinical studies. Having versatile structures and being capable of functionalization with multiple active molecules, they are expected to be promising candidates for wound healing shortly. However, this will require the researchers to explore them in more advanced levels.

AUTHOR CONTRIBUTIONS

LQF and XYC wrote and collected the data. MHC and XHT arranged the data and designed the figures. YBF and XZM revised the manuscript and designed and supervised the whole study. All authors contributed to the article and approved the submitted version.

FUNDING

This study was supported by the Zhejiang Provincial Science and Technology Projects (No. LGF20H180007 to LQF), the National Natural Science Foundation of China (No. 81672430 to XZM), the Zhejiang Provincial Natural Science Foundation of China (LY20H110002 to YBF), the General Project Funds from the Health Department of Zhejiang Province (2020KY446 to YBF), the Outstanding Young People Fund in Zhejiang Provincial People's Hospital (ZRY2018C004 to YBF), and the Hangzhou Medical and Health Science and Technology Project (No. OO20190807 to LQF).

REFERENCES

Abánades Lázaro, I., Haddad, S., Rodrigo-Munþoz, J. M., Marshall, R. J., Sastre, B., del Pozo, V., et al. (2018). Surface-functionalization of Zr-fumarate MOF for selective cytotoxicity and immune system compatibility in nanoscale drug delivery. *ACS Appl. Mater. Interf.* 10, 31146–31157. doi: 10.1021/acsami.8b11652

Admassie, M., Tsige, E., and Chanie, M. (2018). Isolation, identification and antibiotic susceptibility pattern of bacteria isolated from wounds of patients attending at arsho advanced medical laboratory. *Science* 7, 20–24. doi: 10.11648/j.sjcm.20180702.12

Amna, T., Hassan, M. S., Yang, J., Khil, M.-S., Song, K.-D., Oh, J.-D., et al. (2014). Virgin olive oil blended polyurethane micro/nanofibers ornamented with copper oxide nanocrystals for biomedical applications. *Intern. J. Nanomed.* 9:891. doi: 10.2147/ijn.s54113

Anderson, K., and Hamm, R. L. (2012). Factors that impair wound healing. *J. Am. Coll. Clin. Wound Spec.* 4, 84–91. doi: 10.1016/j.jccw.2014.03.001

Armstrong, D. G., Lavery, L. A., Abu-Rumman, P., Espensen, E. H., Vazquez, J. R., Nixon, B. P., et al. (2002). Outcomes of subatmospheric pressure dressing therapy on wounds of the diabetic foot. *Ostomy/Wound Manag.* 48, 64–68.

Brown, G. L., Curtsinger, L. J., White, M., Mitchell, R. O., Pietsch, J., Nordquist, R., et al. (1988). Acceleration of tensile strength of incisions treated with EGF and TGF-beta. *Ann. Surg.* 208:788. doi: 10.1097/00000658-198812000-00019

Champeau, M., Póvoa, V., Militão, L., Cabrini, F. M., Picheth, G. F., Meneau, F., et al. (2018). Supramolecular poly (acrylic acid)/F127 hydrogel with hydration-controlled nitric oxide release for enhancing wound healing. *Acta Biomater.* 74, 312–325. doi: 10.1016/j.actbio.2018.05.025

Chen, G., Yu, Y., Wu, X., Wang, G., Gu, G., Wang, F., et al. (2019). Microfluidic electrospray niacin metal-organic frameworks encapsulated microcapsules for wound healing. *Research* 2019:6175398. doi: 10.34133/2019/6175398

Chen, G., Yu, Y., Wu, X., Wang, G., Ren, J., and Zhao, Y. (2018). Bioinspired multifunctional hybrid hydrogel promotes wound healing. *Adv. Funct. Mater.* 28:1801386. doi: 10.1002/adfm.201801386

Chui, S. S. Y., Lo, S. M. F., Charmant, J. P. H., Orpen, A. G., and Williams, I. D. A. (1999). Chemically functionalizable nanoporous material [Cu3(TMA)2(H2O)3]n. *Science* 283, 1148–1150. doi: 10.1126/science.283.5405.1148

Das, S., and Baker, A. B. (2016). Biomaterials and nanotherapeutics for enhancing skin wound healing. *Front. Bioeng. Biotechnol.* 4:82. doi: 10.3389/fbioe.2016.00082

Dhivya, S., Padma, V. V., and Santhini, E. (2015). Wound dressings–a review. *Biomedicine* 5:22.

Dreifke, M. B., Jayasuriya, A. A., and Jayasuriya, A. C. (2015). Current wound healing procedures and potential care. *Mater. Sci. Eng. C* 48, 651–662. doi: 10.1016/j.msec.2014.12.068

Falanga, V. (2005). Wound healing and its impairment in the diabetic foot. *Lancet* 366, 1736–1743. doi: 10.1016/s0140-6736(05)67700-8

Furukawa, H., Cordova, K. E., O'Keeffe, M., and Yaghi, O. M. (2013). The chemistry and applications of metal-organic frameworks. *Science* 341:1230444.

George Broughton, I., Janis, J. E., and Attinger, C. E. (2006). The basic science of wound healing. *Plast. Reconstruct. Surg.* 117, 12S–34S.

Ghaffar, I., Imran, M., Perveen, S., Kanwal, T., Saifullah, S., Bertino, M. F., et al. (2019). Synthesis of chitosan coated metal organic frameworks (MOFs) for increasing vancomycin bactericidal potentials against resistant S. aureus strain. *Mater. Sci. Eng. C* 105:110111. doi: 10.1016/j.msec.2019.110111

Guo, L., Panderi, I., Yan, D., Szulak, K., Li, Y., Chen, Y., et al. (2013). A comparative study of hollow copper sulfide nanoparticles and hollow gold nanospheres on degradability and toxicity. *ACS Nano* 7, 8780–8793. doi: 10.1021/nn403202w

Hamdan, S., Pastar, I., Drakulich, S., Dikici, E., Tomic-Canic, M., Deo, S., et al. (2017). Nanotechnology-driven therapeutic interventions in wound healing:

potential uses and applications. *ACS Cent. Sci.* 3, 163–175. doi: 10.1021/acscentsci.6b00371

Han, D., Li, Y., Liu, X., Li, B., Han, Y., Zheng, Y., et al. (2020). Rapid bacteria trapping and killing of metal-organic frameworks strengthened photo-responsive hydrogel for rapid tissue repair of bacterial infected wounds. *Chem. Eng. J.* 396:125194. doi: 10.1016/j.cej.2020.125194

Harding, K., Morris, H., and Patel, G. (2002). Clinical review Healing chronic wounds. *Br. Med. J.* 324, 160–163.

Hinks, N. J., McKinlay, A. C., Xiao, B., Wheatley, P. S., and Morris, R. E. (2010). Metal organic frameworks as NO delivery materials for biological applications. *Micropor. Mesopor. Mater.* 129, 330–334. doi: 10.1016/j.micromeso.2009.04.031

Hou, K., and Tang, Z. (2019). Powerful dual metal-organic framework heterointerface for wound healing. *ACS Cent. Sci.* 5, 1488–1489. doi: 10.1021/acscentsci.9b00837

Junker, J. P., Kamel, R. A., Caterson, E., and Eriksson, E. (2013). Clinical impact upon wound healing and inflammation in moist, wet, and dry environments. *Adv. Wound Care* 2, 348–356. doi: 10.1089/wound.2012.0412

Jurczak, F., Dugré, T., Johnstone, A., Offori, T., Vujovic, Z., Hollander, D., et al. (2007). Randomised clinical trial of Hydrofiber dressing with silver versus povidone–iodine gauze in the management of open surgical and traumatic wounds. *Intern. Wound J.* 4, 66–76. doi: 10.1111/j.1742-481x.2006.00276.x

Kargozar, S., Hamzehlou, S., and Baino, F. (2019a). Can bioactive glasses be useful to accelerate the healing of epithelial tissues? *Mater. Sci. Eng. C* 97, 1009–1020. doi: 10.1016/j.msec.2019.01.028

Kargozar, S., Mozafari, M., Hamzehlou, S., and Baino, F. (2019b). Using bioactive glasses in the management of burns. *Front. Bioeng. Biotechnol.* 7:62. doi: 10.3389/fbioe.2019.00062

Lai, W.-F., and Rogach, A. L. (2017). Hydrogel-based materials for delivery of herbal medicines. *ACS Appl. Mater. Interf.* 9, 11309–11320. doi: 10.1021/acsami.6b16120

Li, B., Wen, H. M., Cui, Y., Zhou, W., Qian, G., and Chen, B. (2016). Emerging multifunctional metal–organic framework materials. *Adv. Mater.* 28, 8819–8860. doi: 10.1002/adma.201601133

Li, H., Lv, N., Li, X., Liu, B., Feng, J., Ren, X., et al. (2017). Composite CD-MOF nanocrystals-containing microspheres for sustained drug delivery. *Nanoscale* 9, 7454–7463. doi: 10.1039/c6nr07593b

Li, J., Lv, F., Li, J., Li, Y., Gao, J., Luo, J., et al. (2020). Cobalt-based metal–organic framework as a dual cooperative controllable release system for accelerating diabetic wound healing. *Nano Res.* 13, 2268–2279. doi: 10.1007/s12274-020-2846-1

Liu, X., Yan, Z., Zhang, Y., Liu, Z., Sun, Y., Ren, J., et al. (2019). Two-Dimensional metal–organic framework/enzyme hybrid nanocatalyst as a benign and self-activated cascade reagent for in vivo wound healing. *ACS Nano* 13, 5222–5230. doi: 10.1021/acsnano.8b09501

Lu, W., Wei, Z., Gu, Z.-Y., Liu, T.-F., Park, J., Park, J., et al. (2014). Tuning the structure and function of metal–organic frameworks via linker design. *Chem. Soc. Rev.* 43, 5561–5593. doi: 10.1039/c4cs00003j

Luo, J.-D., Wang, Y.-Y., Fu, W.-L., Wu, J., and Chen, A. F. (2004). Gene therapy of endothelial nitric oxide synthase and manganese superoxide dismutase restores delayed wound healing in type 1 diabetic mice. *Circulation* 110, 2484–2493. doi: 10.1161/01.cir.0000137969.87365.05

Mandinov, L., Mandinova, A., Kyurkchiev, S., Kyurkchiev, D., Kehayov, I., Kolev, V., et al. (2003). Copper chelation represses the vascular response to injury. *Proc. Natl. Acad. Sci. U.S.A.* 100, 6700–6705. doi: 10.1073/pnas.1231994100

Mason, J. A., Oktawiec, J., Taylor, M. K., Hudson, M. R., Rodriguez, J., Bachman, J. E., et al. (2015). Methane storage in flexible metal–organic frameworks with intrinsic thermal management. *Nature* 527, 357–361. doi: 10.1038/nature15732

Meng, J., Liu, X., Niu, C., Pang, Q., Li, J., Liu, F., et al. (2020). Advances in metal–organic framework coatings: versatile synthesis and broad applications. *Chem. Soc. Rev.* 49, 3142–3186. doi: 10.1039/C9CS00806C

Naseri, S., Lepry, W. C., and Nazhat, S. N. (2017). Bioactive glasses in wound healing: hope or hype? *J. Mater. Chem. B* 5, 6167–6174. doi: 10.1039/C7TB01221G

Natarajan, S., Williamson, D., Stiltz, A. J., and Harding, K. (2000). Advances in wound care and healing technology. *Am. J. Clin. Dermatol.* 1, 269–275.

Nethi, S. K., Das, S., Patra, C. R., and Mukherjee, S. (2019). Recent advances in inorganic nanomaterials for wound-healing applications. *Biomater. Sci.* 7, 2652–2674. doi: 10.1039/c9bm00423h

Okan, D., Woo, K., Ayello, E. A., and Sibbald, G. (2007). The role of moisture balance in wound healing. *Adv. Skin Wound Care* 20, 39–53. doi: 10.1097/00129334-200701000-00013

Ovais, M., Ahmad, I., Khalil, A. T., Mukherjee, S., Javed, R., Ayaz, M., et al. (2018). Wound healing applications of biogenic colloidal silver and gold nanoparticles: recent trends and future prospects. *Appl. Microbiol. Biotechnol.* 102, 4305–4318. doi: 10.1007/s00253-018-8939-z

Pereira, R. F., and Bartolo, P. J. (2016). Traditional therapies for skin wound healing. *Adv. Wound Care* 5, 208–229. doi: 10.1089/wound.2013.0506

Qiu, H., Pu, F., Liu, Z., Liu, X., Dong, K., Liu, C., et al. (2020). Hydrogel-based artificial enzyme for combating bacteria and accelerating wound healing. *Nano Res.* 13, 496–502. doi: 10.1007/s12274-020-2636-9

Ren, X., Yang, C., Zhang, L., Li, S., Shi, S., Wang, R., et al. (2019). Copper metal–organic frameworks loaded on chitosan film for the efficient inhibition of bacteria and local infection therapy. *Nanoscale* 11, 11830–11838. doi: 10.1039/c9nr03612a

Rubin, H. N., Neufeld, B. H., and Reynolds, M. M. (2018). Surface-anchored metal-organic framework-cotton material for tunable antibacterial copper delivery. *ACS Appl. Mater. Interf.* 10, 15189–15199. doi: 10.1021/acsami.7b19455

Santema, K. T., Stoekenbroek, R. M., Koelemay, M. J., Reekers, J. A., Van Dortmont, L. M., Oomen, A., et al. (2018). Hyperbaric oxygen therapy in the treatment of ischemic lower-extremity ulcers in patients with diabetes: results of the DAMO2CLES multicenter randomized clinical trial. *Diabetes Care* 41, 112–119.

Schäffer, M. R., Tantry, U., Efron, P. A., Ahrendt, G. M., Thornton, F. J., and Barbul, A. (1997). Diabetes-impaired healing and reduced wound nitric oxide synthesis: a possible pathophysiologic correlation. *Surgery* 121, 513–519. doi: 10.1016/s0039-6060(97)90105-7

Schurtz, E., Differding, J., Jacobson, E., Maki, C., and Ahmeti, M. (2018). Evaluation of negative pressure wound therapy to closed laparotomy incisions in acute care surgery. *Am. J. Surg.* 215, 113–115. doi: 10.1016/j.amjsurg.2017.08.009

Sen, C. K., Gordillo, G. M., Roy, S., Kirsner, R., Lambert, L., Hunt, T. K., et al. (2009). Human skin wounds: a major and snowballing threat to public health and the economy. *Wound Repair Regen.* 17, 763–771. doi: 10.1111/j.1524-475x.2009.00543.x

Shakya, S., He, Y., Ren, X., Guo, T., Maharjan, A., Luo, T., et al. (2019). Ultrafine silver nanoparticles embedded in cyclodextrin metal-organic frameworks with GRGDS functionalization to promote antibacterial and wound healing application. *Small* 15:1901065. doi: 10.1002/smll.201901065

Shi, L., Liu, X., Wang, W., Jiang, L., and Wang, S. A. (2019). Self-pumping dressing for draining excessive biofluid around wounds. *Adv. Mater.* 31:1804187. doi: 10.1002/adma.201804187

Stone, R. C., Stojadinovic, O., Rosa, A. M., Ramirez, H. A., Badiavas, E., Blumenberg, M., et al. (2017). A bioengineered living cell construct activates an acute wound healing response in venous leg ulcers. *Sci. Transl. Med.* 9:eaaf8611. doi: 10.1126/scitranslmed.aaf8611

Thakral, G., La Fontaine, J., Kim, P., Najafi, B., Nichols, A., and Lavery, L. A. (2015). Treatment options for venous leg ulcers: effectiveness of vascular surgery, bioengineered tissue, and electrical stimulation. *Adv. Skin Wound Care* 28, 164–172. doi: 10.1097/01.asw.0000462328.60670.c3

Walgrave, S. E., Warshaw, E. M., and Glesne, L. A. (2005). Allergic contact dermatitis from propolis. *Dermatitis* 16, 209–215. doi: 10.1097/01206501-200512000-00004

Wang, S., Yan, F., Ren, P., Li, Y., Wu, Q., Fang, X., et al. (2020). Incorporation of metal-organic frameworks into electrospun chitosan/poly (vinyl alcohol) nanofibrous membrane with enhanced antibacterial activity for wound dressing application. *Intern. J. Biol. Macromol.* 158, 9–17. doi: 10.1016/j.ijbiomac.2020.04.116

Wild, T., Rahbarnia, A., Kellner, M., Sobotka, L., and Eberlein, T. (2010). Basics in nutrition and wound healing. *Nutrition* 26, 862–866. doi: 10.1016/j.nut.2010.05.008

Wu, M. X., and Yang, Y. W. (2017). Metal–organic framework (MOF)-based drug/cargo delivery and cancer therapy. *Adv. Mater.* 29:1606134. doi: 10.1002/adma.201606134

Xiao, J., Chen, S., Yi, J., Zhang, H. F., and Ameer, G. A. (2017). A cooperative copper metal–organic framework-hydrogel system improves wound healing in diabetes. *Adv. Funct. Mater.* 27:1604872. doi: 10.1002/adfm.201604872

Xiao, J., Zhu, Y., Huddleston, S., Li, P., Xiao, B., Farha, O. K., et al. (2018). Copper metal-organic framework nanoparticles stabilized with folic acid improve wound healing in diabetes. *ACS Nano* 12, 1023–1032. doi: 10.1021/acsnano.7b01850

Xu, R., Luo, G., Xia, H., He, W., Zhao, J., Liu, B., et al. (2015). Novel bilayer wound dressing composed of silicone rubber with particular micropores enhanced wound re-epithelialization and contraction. *Biomaterials* 40, 1–11. doi: 10.1016/j.biomaterials.2014.10.077

Yang, Y., Deng, Y., Huang, J., Fan, X., Cheng, C., Nie, C., et al. (2019). Size-transformable metal–organic framework–derived nanocarbons for localized chemo-photothermal bacterial ablation and wound disinfection. *Adv. Funct. Mater.* 29:1900143. doi: 10.1002/adfm.201900143

Yao, X., Zhu, G., Zhu, P., Ma, J., Chen, W., Liu, Z., et al. (2020). Omniphobic ZIF-8@hydrogel membrane by microfluidic-emulsion-templating method for wound healing. *Adv. Funct. Mater.* 30:1909389. doi: 10.1002/adfm.201909389

Yu, J., Mu, C., Yan, B., Qin, X., Shen, C., Xue, H., et al. (2017). Nanoparticle/MOF composites: preparations and applications. *Mater. Horiz.* 4, 557–569. doi: 10.1039/c6mh00586a

Yu, Y., Chen, G., Guo, J., Liu, Y., Ren, J., Kong, T., et al. (2018). Vitamin metal–organic framework-laden microfibers from microfluidics for wound healing. *Mater. Horiz.* 5, 1137–1142. doi: 10.1039/c8mh00647d

Zhang, M., Qiao, R., and Hu, J. (2020). Engineering metal–organic frameworks (MOFs) for controlled delivery of physiological gaseous transmitters. *Nanomaterials* 10:1134. doi: 10.3390/nano10061134

Zhang, S., Ye, J., Sun, Y., Kang, J., Liu, J., Wang, Y., et al. (2020). Electrospun fibrous mat based on silver (I) metal-organic frameworks-polylactic acid for bacterial killing and antibiotic-free wound dressing. *Chem. Eng. J.* 2020:124523. doi: 10.1016/j.cej.2020.124523

Zhang, P., Li, Y., Tang, Y., Shen, H., Li, J., Yi, Z., et al. (2020). Copper-based metal–organic framework as a controllable nitric oxide-releasing vehicle for enhanced diabetic wound healing. *ACS Appl. Mater. Interf.* 12, 18319–18331. doi: 10.1021/acsami.0c01792

Zhang, W., Lu, G., Cui, C., Liu, Y., Li, S., Yan, W., et al. (2014). A family of metal-organic frameworks exhibiting size-selective catalysis with encapsulated noble-metal nanoparticles. *Adv. Mater.* 26, 4056–4060. doi: 10.1002/adma.201400620

Zhang, Y., Chang, M., Bao, F., Xing, M., Wang, E., Xu, Q., et al. (2019a). Multifunctional Zn doped hollow mesoporous silica/polycaprolactone electrospun membranes with enhanced hair follicle regeneration and antibacterial activity for wound healing. *Nanoscale* 11, 6315–6333. doi: 10.1039/c8nr09818b

Zhang, Y., Sun, P., Zhang, L., Wang, Z., Wang, F., Dong, K., et al. (2019b). Silver-Infused porphyrinic metal–organic framework: surface-adaptive, on-demand nanoplatform for synergistic bacteria killing and wound disinfection. *Adv. Funct. Mater.* 29:1808594. doi: 10.1002/adfm.201808594

Zhou, X., Wang, H., Zhang, J., Li, X., Wu, Y., Wei, Y., et al. (2017). Functional poly (ε-caprolactone)/chitosan dressings with nitric oxide-releasing property improve wound healing. *Acta Biomater.* 54, 128–137. doi: 10.1016/j.actbio.2017.03.011

Zhuang, J. L., Ceglarek, D., Pethuraj, S., and Terfort, A. (2011). Rapid room-temperature synthesis of metal–organic framework HKUST-1 crystals in bulk and as oriented and patterned thin films. *Adv. Funct. Mater.* 21, 1442–1447. doi: 10.1002/adfm.201002529

Conflict of Interest: The authors declare that the research was conducted in the absence of any commercial or financial relationships that could be construed as a potential conflict of interest.

frontiers in Bioengineering and Biotechnology

ORIGINAL RESEARCH
published: 18 December 2020
doi: 10.3389/fbioe.2020.592833

Insulin-Containing Wound Dressing Promotes Diabetic Wound Healing Through Stabilizing HIF-1α

Peilang Yang[1†], Di Wang[2†], Yan Shi[1†], Mingzhong Li[3], Min Gao[1], Tianyi Yu[1], Dan Liu[1], Jie Zhang[1], Jizhuang Wang[1], Xiong Zhang[1] and Yan Liu[1]**

[1] Department of Burn and Plastic Surgery Ruijin Hospital Affiliated to Shanghai Jiao Tong University School of Medicine, Shanghai, China, [2] Department of Anesthesiology, Shanghai Jiao Tong University Affiliated Sixth People's Hospital, Shanghai, China, [3] National Engineering Laboratory for Modern Silk, College of Textile and Clothing Engineering, Soochow University, Suzhou, China

OPEN ACCESS

Edited by:
Kai Zheng,
University of Erlangen-Nuremberg, Germany

Reviewed by:
Qingqing Yao,
Wenzhou Medical University, China
Jun Wu,
Shenzhen Second People's Hospital, China

***Correspondence:**
Xiong Zhang
xiong@medmail.com.cn
Yan Liu
rjliuyan@126.com

[†] These authors have contributed equally to this work

Specialty section:
This article was submitted to Tissue Engineering and Regenerative Medicine, a section of the journal Frontiers in Bioengineering and Biotechnology

Received: 08 August 2020
Accepted: 23 November 2020
Published: 18 December 2020

Citation:
Yang P, Wang D, Shi Y, Li M, Gao M, Yu T, Liu D, Zhang J, Wang J, Zhang X and Liu Y (2020) Insulin-Containing Wound Dressing Promotes Diabetic Wound Healing Through Stabilizing HIF-1α. Front. Bioeng. Biotechnol. 8:592833. doi: 10.3389/fbioe.2020.592833

HIF-1α is seen as a major regulator during wound healing and controls many wound healing processes, such as angiogenesis, extracellular deposition, and reepithelialization. A diabetic state plays a vicious effect on wound healing, and the destabilization of HIF-1α is a non-negligible factor. Insulin-loaded silk fibroin microparticles were prepared to release insulin by covering the wounds, and this material was proven to promote wound healing in both *in vitro* and *in vivo* studies. In this work, we found that this insulin-containing wound dressing could accelerate diabetic wound healing by promoting reepithelialization, angiogenesis, and extracellular matrix, especially collagen deposition. Meanwhile, HIF-1α was stable and accumulated in insulin-containing dressing to group wound cells, which was significantly unstable in the control group. In further studies, we showed that methylglyoxal (MGO), the main form of advanced glycation end products (AGEs), accumulated significantly and caused the destabilization of HIF-1α in the diabetic state. Insulin could alleviate the MGO-induced HIF-1α unstable state and promote HIF-1α target gene expression and its downstream biological effect such as angiogenesis and wound extracellular matrix deposition.

Keywords: diabetes, wound healing, insulin, HIF-1α, angiogenesis

INTRODUCTION

Diabetic non-healing wound is one of the most common late complication of diabetic patients. The morbidity rate of diabetic non-healing wound ranges from 5 to 20% among all diabetic patients. Diabetic wound puts a huge pressure on the social health economic system for its retarded healing characteristic (Falanga, 2005; Davis et al., 2018). Histologically, diabetic wound shows the characteristics of impaired angiogenesis, reepithelialization, and extracellular matrix deposition (Demidova-Rice et al., 2012). All these characteristics are related to an unstable HIF-1α in the diabetic environment. HIF-1α is considered as the central regulator of wound healing, and it dominates wound healing processes, such as inflammation reaction, angiogenesis, reepithelialization, and extracellular matrix deposition (Hong et al., 2014).

In a diabetic wound environment, the stabilization of HIF-1α would be severely impaired in the hypoxia state, and the instability of HIF-1α is regarded as the major factor of diabetic non-healing wound. In the diabetic state, the instability of HIF-1α is often caused by the accumulation

of advanced glycation end products (AGEs). Recently, methylglyoxal (MGO), the major form of AGEs, has been reported to induce HIF-1α instability in many ways (Ramasamy et al., 2006; Catrina, 2014). Therefore, many researches aim at stabilizing HIF-1α to improve wound healing (Mace et al., 2007; Botusan et al., 2008). Our previous research results show that insulin can act as a growth-like factor to promote wound healing by promoting angiogenesis, reepithelialization, and extracellular matrix deposition (Liu et al., 2009a,b). Based on these results, in this work, we develop a wound dressing by loading insulin into silk fibroin (SF) microparticles (Li et al., 2017). As many functions of insulin on wound healing overlapped with the functions of HIF-1α, we in this research intend to check the effects of insulin-containing dressing material on diabetic wound healing and whether insulin takes effect through regulating HIF-1α stabilization.

MATERIALS AND METHODS

Reagents

Streptozocin (STZ), insulin for cell culture, and MGO were from Sigma-Aldrich (St. Louis, MO, United States). ProLong gold antifade mounting reagent with DAPI was purchased from Thermo Fisher Scientific (Carlsbad, CA, United States). RPMI 1640, DMEM, and phosphate buffer solution (PBS) were obtained from GIBCO (Carlsbad, CA, United States). Chemiluminescence reagent was from Millipore (Billerica, MA, United States). Insulin was from Roche chemical (Houston, TX, United States). OxiSelect MGO Competitive ELISA Kit was purchased from Cell Biolabs (San Diego, CA, United States). Matrigel was from BD Biosciences (Waltham, MA, United States).

The following antibodies were obtained from various suppliers: PECAM-1, collagen I, and collagen III were from Abcam (Cambridge Science Park, Cambridge); CBP, GLUT-1, VEGF-A, HIF-1α, and HRP-labeled secondary antibody were from Cell Signaling Technology (Danvers, MA, United States); and donkey anti-rabbit Alexa Fluor 488 was purchased from Thermo Fisher Scientific (Carlsbad, CA, United States).

Animals

Forty male Sprague-Dawley rats, 6 weeks old and weighing 120–140 g, were purchased from Shanghai Laboratory Animal Center in the Chinese Academy of Sciences and housed at the Animal Science Center of Shanghai Jiao Tong University, School of Medicine (SJTUSM). The animals were maintained under a 12-h light/dark cycle at 22°C. Thirty rats were used to develop diabetes by a reported method. In brief, the rats were fasted for 16 h followed by a single dose of STZ (60 mg/kg BW dissolved in 0.1 mM citrate buffer) intraperitoneally (Junod et al., 1969). Rats were left to develop diabetes for 8 weeks. Random plasma glucose was measured, and a glucose level >300 mg/L was considered diabetic. The rest of the rats were set as normal control (Norm). The animal procedures were performed in accordance with the rules of the Animal Care Committee of SJTUSM, and all experiment protocols were approved by the SJTUSM Institutional Animal Care and Use Committee.

Preparation of SF Microparticles

The preparation of SF microparticles with or without insulin was described in a previous study as follows (Li et al., 2017).

(1) Preparation of SF solution: Briefly, *Bombyx mori* silk fibers (Huzhou, China) were degummed three times in 0.05% Na_2CO_3 solution at 98–100°C for 30 min and dried at 60°C after thorough rinsing. The fibroin extract was dissolved in a ternary solvent of $CaCl_2$:CH_3CH_2OH:H_2O (1:2:8 molar ratio) at 72 ± 2°C for 1 h. The solution was then dialyzed in cellulose tubes (MWCO 9–14 kDa) in deionized water for 4 days.

(2) Preparation of SF microparticles: 100 mg insulin (27.5 IU/mg; from porcine, Wanbang Biochemical Pharmaceutical Co., Ltd., Xuzhou, China) was dissolved in 10 ml of 0.01 N HCl; then the pH of the solution was adjusted to 7.0 ± 0.1 using 0.1 N NaOH. The SF solution was diluted to 2.0 wt.% and mixed with glycerol at 30 wt.% of SF weight. The resulting insulin solution and SF solution were used as core and shell for coaxial electrostatic differentiation, respectively.

(3) Preparation of microparticle-loaded SF sponge dressing: The SF solution was diluted to 2.0 wt.%, and then 2-morpholinoethanesulfonic acid/*N*-hydroxysuccinimide/1-ethyl-3-(3-dimethylaminopropyl)carbodiimide hydrochloride (MES/NHS/EDC) was added to the SF solution at 20/10/20 wt.% of SF weight, respectively. Nine hundred microliters of the above mixed solution was added into a round aluminum box (D = 40 mm, H = 15 mm, V = 10 ml) and frozen at −80°C for 30 min. Then 10-mg SF microparticles were evenly laid on a frozen SF solution layer and frozen at −80°C for 15 min. On top of it, 700 μl of the above mixed solution was added to cover the microparticles and frozen at −80°C for 15 min, followed by 10-mg SF microparticles and 900 μl SF solution at a similar process. Then the SF mixture composite with two layers of microparticles was frozen at −80°C for 4 h and further freeze-dried to obtain microparticle-loaded SF sponge dressing. The dressings were sterilized with γ-ray irradiation and stored at 4°C.

Scanning Electron Microscopy

The morphology of samples was observed by a scanning electron microscope (SEM, S-4800, Hitachi, Japan) described as before (Li et al., 2017). The size of microparticles was analyzed on the basis of SEM images with the Nano Measurer analysis software (Department of Chemistry, Fudan University, China. 2008 Jie Xu).

In vitro Insulin Release

The *in vitro* insulin release was determined as described before (Zhao et al., 2012; Li et al., 2017). Insulin was labeled with fluorescein isothiocyanate (FITC) (Sigma-Aldrich). Three hundred microliters of FITC solution (10 mg/ml in dimethyl sulfoxide) was added to 10 ml of insulin solution (15 mg/ml in bicarbonate buffer, pH = 8.5, 0.1 M) and stirred at room temperature for 60 min. Next, 200 μl of 1 M hydroxylammonium chloride solution was added and stirred for 10 min at room temperature. The insulin was then purified using a 10 mm × 300 mm column with Sephadex G-50

equilibrated in 0.1 M sodium bicarbonate buffer (pH = 8.5) to remove any unreacted FITC. The fluorescent images were captured using an inverted fluorescence microscope (Olympus IX71, Japan). Physically absorbed microparticles were used as a control group. Ten milligrams of pure SF microparticles was directly immersed into 2 ml of FITC–insulin solution to adsorb insulin by permeation and physical absorption, which were named insulin-adsorbed microparticles. The remaining amount of insulin in solution was quantified to calculate the adsorption amount using a fluorescence spectrophotometer (FM4P TCSPC, Horiba Jobin Yvon), and the loading ratio in the insulin-adsorbed microparticles was about 5.5%. The insulin release profiles were determined by immersing 10 mg of microparticles and a sponge dressing containing 10 mg of microparticles in 10 ml of PBS (10 mM, pH 7.4). The samples were incubated in a water bath at 37°C with a 100-rpm shaking. One milliliter of medium was collected and replaced with an equal volume of fresh PBS after centrifugation at predetermined time points. The amount of released insulin was quantified using a fluorescence spectrophotometer.

Wounding Procedure

One day before wounding, rats were anesthetized with a single intraperitoneal injection of thiopental sodium (40 mg/kg BW); the hairs on the back were shaved and thoroughly removed using the Nair hair remover lotion. On the day of wounding, the rats were anesthetized with thiopental sodium and a dose of tramadol. The animals' backs were incised to produce a 1.5 cm × 1.5 cm wound.

In the first part, the rats were separated into two groups: the normal non-diabetic group (Norm) and the diabetic group (DM). In the second part, the rats were also separated into two groups: the group in which the diabetic wound was dressed with SF microparticles without insulin (Ctrl) and the group in which the diabetic wound was dressed with SF microparticles containing insulin (INS).

Measurement of Wound Closure

Rats were anesthetized with thiopental sodium at the 5th and 11th days after wounding. The wounds were photographed and drawn on transparent tracing papers, and the papers were scanned. The wound sizes were analyzed using ImageJ software. The unhealed rate was calculated by comparing the unhealed wound area to the original wound area.

Histological Observation

The wounds, including 5 mm of adjacent normal skin, along with the subcutaneous fat tissue were harvested at the 5th and 11th days after wounding. The tissue was fixed in 4% paraformaldehyde and embedded in paraffin. Sections with 6–7 μm thickness were stained with hematoxylin and eosin (H&E) for histological and morphometric observation and evaluation. Masson trichrome staining was used for collagen deposition evaluation.

Immunohistochemistry

The wounds were harvested and fixed as mentioned above, and sections were then deparaffinized, rehydrated, and washed in distilled water. The sections were placed in 95∼98°C antigen retrieval citrate buffer in a container for 10–15 min. Endogenous peroxidase activity was blocked by placing the sections in 3% hydrogen peroxide in methanol for 10 min. Non-specific staining was blocked with normal goat serum, and the sections were incubated with anti-rat PECAM-1, VEGF-A, or HIF-1α overnight at 4°C. After washing, HRP-labeled secondary antibody was applied for 1 h at room temperature and then with diaminobenzidine and counterstained with hematoxylin.

Immunofluorescence

Cells were washed with PBS three times and fixed with 4% paraformaldehyde in PBS at a pH of 7.4 for 5 min. The cells were incubated for 10 min with PBS containing 0.25% Triton X-100. Non-specific staining was blocked with normal goat serum, and the sections were incubated with anti-human HIF-1α overnight at 4°C. After washing, Alexa Fluor 488-labeled secondary antibody was applied for 1 h at room temperature. Coverslips were mounted with a drop of ProLong gold antifade mounting reagent with DAPI and sealed with nail polish to prevent drying and movement under the microscope.

Western Blot

The tissues were homogenized by pulverization in liquid nitrogen and transferred to tissue lysis buffer with a protease inhibitor cocktail following centrifugation at 12,000 rpm for 15 min. The supernatants were removed and stored at −80°C. An equal amount of protein per lane (50 μg) was separated by 5–12% SDS-PAGE and transferred to a polyvinylidene difluoride membrane. The membranes were blocked by 5% non-fat powdered milk in Tris–buffered saline with Tween-20 (TBST) and then incubated with anti-PECAM-1, collagen I, collagen III, VEGF-A, CBP, GLUT-1, and HIF-1α primary antibody in 5% non-fat milk in TBST overnight at 4°C. The membrane was then washed extensively with TBST and then incubated with the secondary antibody for 1 h at room temperature. Bands were visualized with enhanced chemiluminescence. Relative quantities of protein were determined using a densitometer and presented in comparison with β-actin expression.

Cell Culture

HUVECs and fibroblasts were purchased from ATCC and cultured as recommended.

HUVEC Tube Formation Assay

The tube formation assays were operated according to the manufacturer's instruction. Briefly, the Matrigel was thawed overnight on ice at 4°C, and the vial was swirled to ensure that the material is evenly dispersed when the Matrigel thawed. Chilled Matrigel (10 mg/ml) was added at 0.3 ml per well with pre-cooled tips, and the entire growth surface of 24-well culture plates were covered completely and evenly. Plates were incubated at 37°C for 45 min. The remaining liquid was carefully removed

from the culture well without disturbing the layer of Matrigel just before use. Passage 4 HUVECs were detached, and the cells were resuspended in culture medium with 5 serum at 1×10^6 cells/ml with or without 800 μM MGO or with 800 μM MGO and 10^{-6} M insulin. Into each well was added 300 μl of the cell suspension, and the angiogenesis assay plate was incubated for 12 h at 37°C, at 5% CO_2 atmosphere. Cells were monitored and photographed using an inverted microscope.

Statistical Analysis

Data analysis was performed using GraphPad Prism software (GraphPad Software Inc). *T*-tests were used to determine the significance of pairwise differences between means, unpaired *T*-tests was used for comparison between two groups, and one-way ANOVA (Dunnett's *post hoc* test) was used to determine significance between means of several groups. Data satisfying the assumptions of ANOVA were verified before performing the tests. A *p*-value less than 0.05 was considered significant statistically, and a *p*-value less than 0.01 was considered statistically highly significant. Data are shown as mean ± standard deviation (SD).

RESULTS

Diabetic Wounds Showed Significantly Retarded Healing Characteristics

Compared with normal wounds, diabetic wounds showed an obviously delayed wound healing feature. As shown in **Figure 1A**, the reepithelialization of diabetic wounds was significantly slower than that of normal wounds. On the 11th day, when normal wounds show an almost completed reepithelialization, there still existed a large area of un-epithelialization in the diabetic wound. Meanwhile, the angiogenesis of diabetic wounds was also significantly disrupted in the diabetic state, and it was characterized as aberrant, with a leaky neovascular network and lower density compared with the normal wound on the fifth day (**Figure 1B**). The collagen deposition was examined by Masson trichrome staining, which showed lower collagen deposition in diabetic wounds (**Figures 1C,D**). The granular tissue representing the healing quality and extracellular matrix deposition also proved that the diabetic wound healing process was significantly impaired. The thickness of the granular tissue in the diabetic wound healing group was much lower than that of the normal group as shown in **Figures 1E,F**. As the main regulator of wound healing, HIF-1α was significantly unstable in diabetic wounds, which resulted in the non-healing feature of diabetic wounds. In the wounds of our diabetic model, we confirmed that HIF-1α was extremely unstable. As shown in **Figures 1G,H**, we found that the HIF-1α expression in the diabetic wound was significantly lower than that in normal wound.

Insulin-Containing Wound Dressing Promotes Diabetic Wound Healing

Based on our previous research results, topical insulin application could accelerate wound healing, but it had some shortcomings such as the inconvenience of insulin daily application and disruption of glucose level. Based on these reasons, we composed insulin-loaded SF microparticles. The SEM characteristics of this

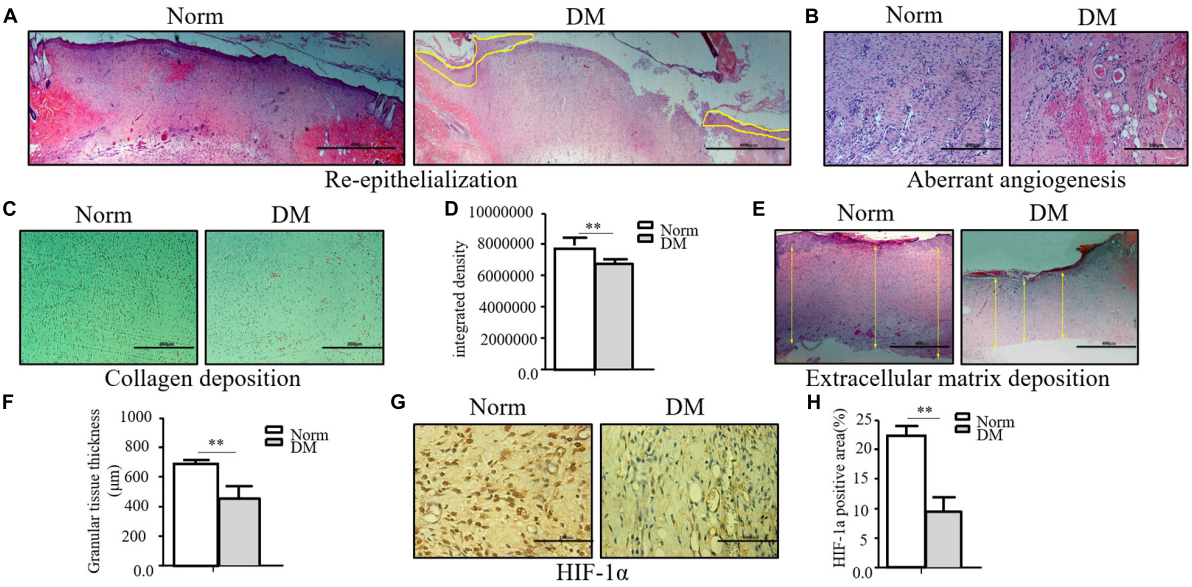

FIGURE 1 | The wound healing process was significantly impaired in the diabetic state. **(A–F)** The diabetic wound manifests characteristics of impaired re-epithelialization **(A)**, aberrant angiogenesis **(B)**, and impaired collagen deposition **(C,D)** examined by Masson trichrome staining. Decreased extracellular matrix deposition **(E,F)** shown by H&E observation. **(G,H)** HIF-1α significantly decreased in diabetic wound. HIF-1α of normal and diabetic wounds was examined through immunohistochemistry. The collagen deposition density, extracellular matrix thickness, and HIF-1α positive area were calculated by ImageJ. Data are shown as mean ± SD. $^{**}p < 0.01$, $n = 3$.

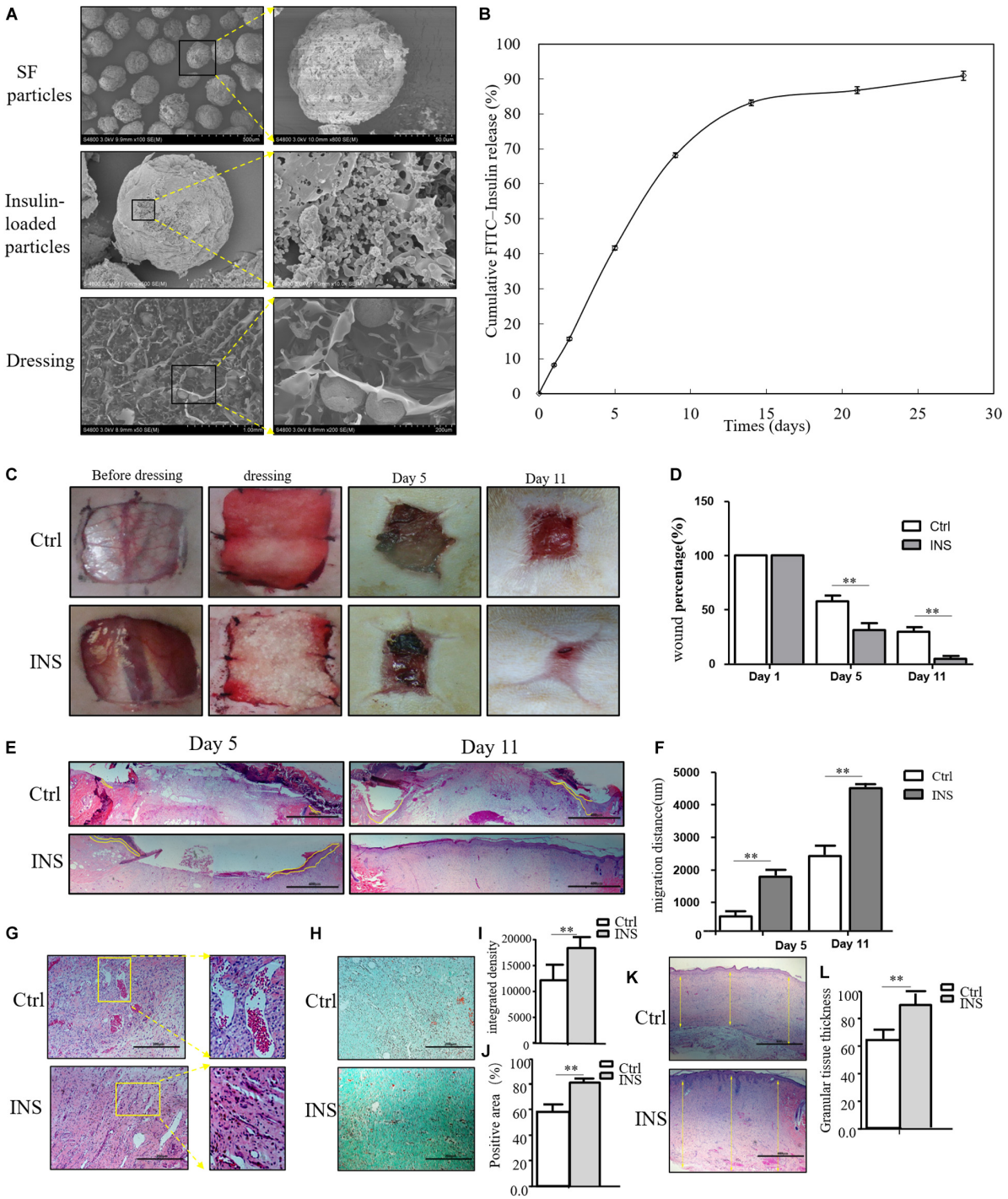

FIGURE 2 | Insulin-containing SF microparticles promote diabetic wound healing. **(A)** The SEM and cross-sectional views of SF microparticles, insulin-encapsulated SF microparticles, and microparticle-loaded SF. **(B)** Cumulative FITC–insulin release from microparticle-loaded SF dressings. **(C,D)** Insulin promoted healing of diabetic wound. After the wounding procedure, the wounds in the control group (Ctrl) were dressed with SF microparticles without insulin; wounds were dressed with the insulin-containing SF microparticles in the insulin group (INS). Wound sizes were recorded on the 1st, 5th, and 11th days after wounding using transparent tracing papers. The unhealed rate of wounds was calculated by Image Pro Plus. Data are shown as mean ± SD. $^{**}p < 0.01$, $n = 5$. **(E,F)** Insulin-containing dressing enhances reepithelialization of diabetic wounds. Reepithelialization was analyzed on the 5th and 11th day of wounding. The migration length of the tongue was calculated by Image Pro Plus. Data are shown as mean ± SD. $^{**}p < 0.01$, $n = 5$. **(G)** Insulin-containing dressing alleviates aberrant angiogenesis of diabetic wounds. Angiogenesis quality of the 5th-day wounds was evaluated by H&E observation. **(H–J)** Insulin-containing dressing promotes collagen deposition of diabetic wounds. Masson trichrome staining was used to check collagen deposition in the wound. The integrated density and positive area of collagen deposition were calculated, and data are shown as mean ± SD. $^{**}p < 0.01$, $n = 5$. **(K,L)** The thickness of the granular tissue was used as a marker of ECM deposition. Data are shown as mean ± SD. $^{**}p < 0.01$, $n = 5$.

material were shown in **Figure 2A**, and this material could continuously release insulin for more than 20 days (**Figure 2B**). In this work, it was investigated whether the material promoted diabetic wound healing. As shown in **Figures 2C,D**, the wound almost healed in the group using insulin-containing dressing (INS) on the 11th day, whereas the control SF microparticles group (Ctrl) still had a large area of non-healing wound. The migration tongues of wounds on the 5th and 11th days also proved that the reepithelialization in the INS group was significantly faster than that in the Ctrl group in **Figures 2E,F**. Furthermore, the aberrant angiogenesis process in diabetic wounds was also improved in the INS group. Compared with the Ctrl group with the abnormally large and leaky neovascular network, the INS group had normal lumen and healthy vascular network as shown in **Figure 2G**. The impaired collagen deposition and extracellular matrix deposition were also ameliorated by insulin application as shown in **Figures 2H–L**.

MGO Accumulated in the Diabetic State and Played a Toxic Effect on Wound Healing-Related Cells

Insulin-containing dressing could promote diabetic wound healing, and its mechanism might relate to an improved HIF-1α signal pathway. However, whether insulin affected the HIF-1α signal pathway to improve the diabetic state is still unknown. In the diabetic state, many factors influenced the stabilization of HIF-1α, and the accumulation of AGEs was regarded as an indispensable one. MGO was the major form of AGEs and accumulated in the serum and tissue homogenate. As shown in **Figure 3A**, the MGO level was significantly higher in both serum and dermis in DM than in Norm. We also analyzed the MGO level in high-glucose cultured HUVECs and fibroblasts, which suggested that a higher glucose culture resulted in a higher MGO accumulation in both kinds of cells shown in **Figure 3B**. Based on the serum MGO level with different concentrations, it is found that MGO inhibited HUVEC and fibroblast proliferation in a concentration-dependent manner. In detail, 800 μM of MGO was sufficient to induce the vicious effects on HUVECs and fibroblasts as shown in **Figure 3C**. Therefore, 800 μM of MGO, as optimal concentration, could significantly destabilize HIF-1α under the hypoxia state in both HUVECs and fibroblasts as shown in **Figures 3D–F**. Meanwhile, 800 μM of MGO also exhibited the effect of inhibiting HUVEC tube formation as shown **Figure 3G**.

Insulin-Containing Dressing Promotes Diabetic Wound Healing by Stabilizing HIF-1α

We next investigate whether insulin application could revise these impairments caused by MGO. The results showed that

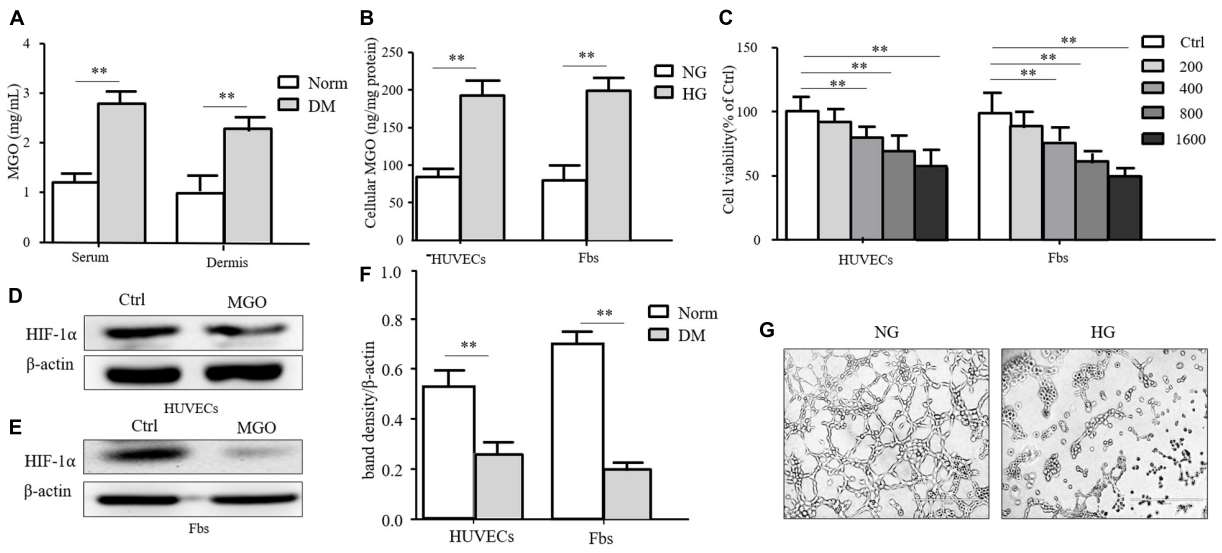

FIGURE 3 | MGO accumulated in the diabetic state and induced an HIF-1α unstable state. **(A)** MGO accumulated in the diabetic state. Eight weeks after diabetic induction, the blood and dorsal dermis of diabetic (DM) and normal (Norm) rats were collected. The serum and dermis homogenate were subjected to MGO analysis. Data are shown as mean ± SD. $^{**}p < 0.01$, $n = 3$. **(B)** High glucose incubation leads to MGO accumulation in HUVECs and fibroblasts. Five days after normal glucose (5.5 mM, NG), HUVECs and fibroblasts treated with high glucose (25 mM, HG) were harvested and lysed. The lysis was subjected to MGO analysis. Data are shown as mean ± SD. $^{**}p < 0.01$, $n = 3$. **(C)** MGO impaired HUVEC and fibroblast viability in a concentration-dependent manner. HUVECs and fibroblasts were separately treated with 0 (control group), 200, 400, 800, and 1,600 μM MGO, and after 24 h of incubation, cells were harvested and subjected to CCK-8 analysis. The viability of each group was compared with that of the control group and presented as the percentage of the control group. Data are shown as mean ± SD. $^{**}p < 0.01$, $n = 3$. **(D–F)** MGO induced unstable HIF-1α in the hypoxia state. After treatment with/without 800 μM MGO, HUVECs and fibroblasts were subjected to hypoxia (1% oxygen concentration) treatment. Twenty-four hours after treatment, cells were harvested and lysed. The lysis was subjected to western blot analysis for the HIF-1α level. Photoshop was used in the quantification of immunoblots. Data are shown as mean ± SD. $^{**}p < 0.01$, $n = 3$. **(G)** MGO impaired angiogenesis. HUVECs were seeded into a Matrigel with/without 800 μM MGO for tube formation analysis. Twelve hours later, the tube formation status in both groups was photographed.

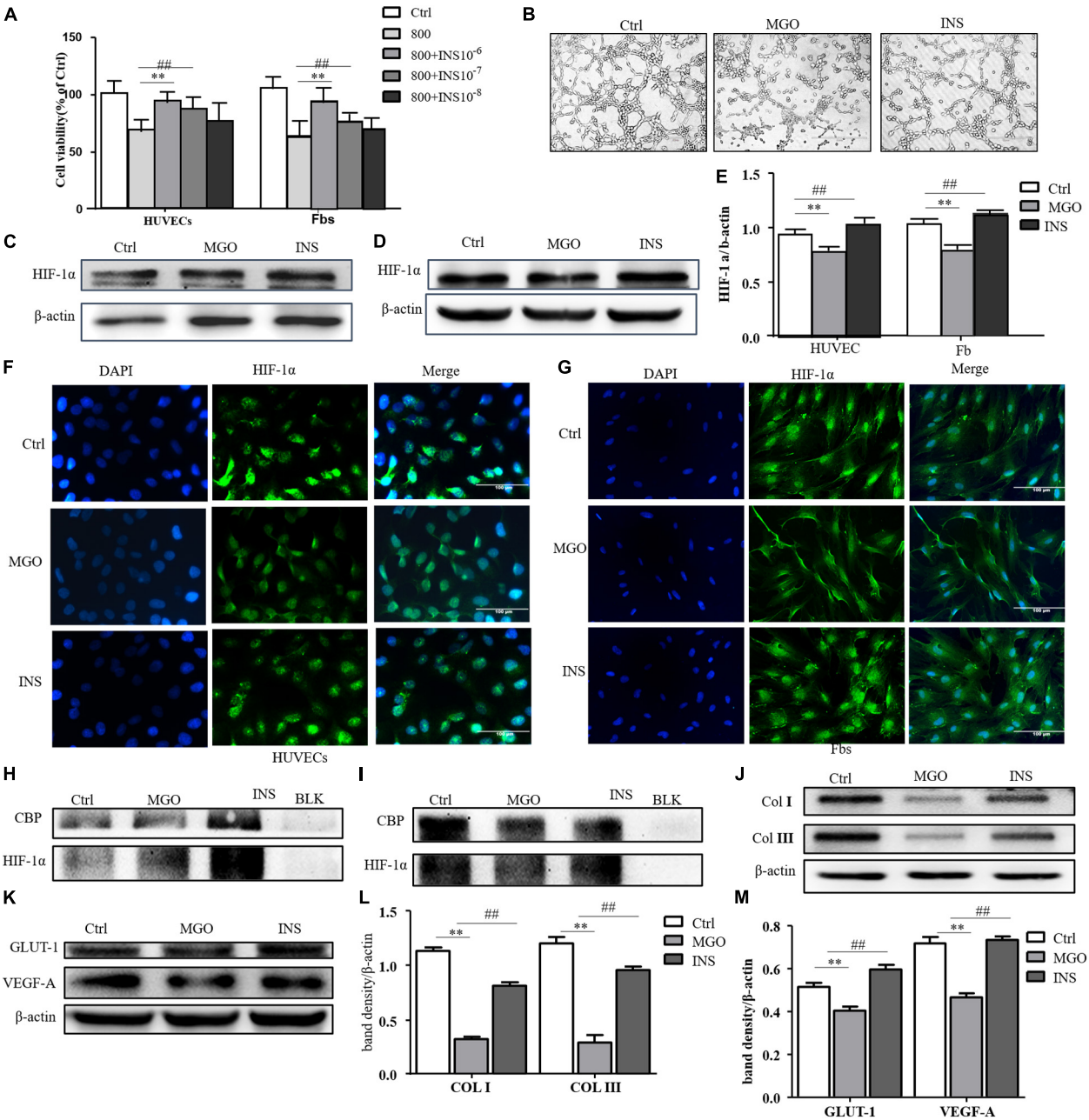

FIGURE 4 | Insulin relieved MGO-induced HIF-1α impairment in wound healing cells. **(A)** Insulin promoted MGO-induced cell viability impairment in a concentration-dependent manner. HUVECs and fibroblasts were pretreated with 0 (control group) and 800 μM MGO for 30 min. Thirty minutes after MGO treatment, 0, 10^{-6}, 10^{-7}, and 10^{-8} M insulin were added to the culture medium. After 24 h of incubation, cells were subjected to CCK-8 analysis. The viability of each group was compared with that of the control group and presented as the percentage of the control group. Data are shown as mean ± SD. **/##$p < 0.01$, $n = 3$. **(B)** Insulin promoted MGO-induced HUVEC angiogenesis impairment. HUVECs were set into three groups: control group (Ctrl) treated without MGO and insulin; MGO group (MGO) treated with 800 μM MGO; insulin group (INS) treated with 800 μM MGO and 10^{-6} M insulin. The treatment was described previously. Twelve hours later, the tube formation status in both groups was photographed. **(C–E)** Insulin alleviated MGO-induced HIF-1α accumulation impairment of HUVECs and fibroblasts. HUVECs and fibroblasts were set as Ctrl, MGO, and INS groups and treated as described above. Twenty-four hours under the hypoxia state (1% oxygen concentration), cells were harvested, and HIF-1α levels were analyzed. Photoshop was used in the quantification of immunoblots. Data are shown as mean ± SD. **/##$p < 0.01$, $n = 3$. *Means Ctrl vs. MGO; #means MGO vs. INS. **(F,G)**. Insulin promoted HIF-1α translocation into HUVECs and fibroblasts. In Ctrl, MGO, and INS groups and after 24 h under the hypoxia state, cells were harvested and fixed with 4% paraformaldehyde. The cells were then subjected to immunofluorescence examination to analyze the HIF-1α accumulation and translocation to the nucleus. **(H,I)** Insulin promoted translation complex formation of HIF-1α and CBP in HUVECs and fibroblasts. Cell lysis of Ctrl, MGO, and INS was subjected to co-IP examination to analyze the HIF-1α and CBP complex formation. **(J–M)** Insulin improved MGO-induced HIF-1α pathway impairment in HUVECs and fibroblasts. Cell lysis of Ctrl, MGO, and INS was subjected to western blot to examine the expression of HIF-1α target genes VEGF-A and GLUT-1 (HUVECs) and collagen I and collagen III (fibroblasts). Photoshop was used in the quantification of immunoblots. Data are shown as mean ± SD. **/##$p < 0.01$, $n = 5$. *Means Ctrl vs. MGO; #means MGO vs. INS.

insulin could revise inhibitions of HUVEC and fibroblast proliferation in a concentration-dependent manner as shown in **Figure 4A**. Meanwhile, 10^{-6} mM of insulin, as optimal concentration, could significantly alleviate MGO-induced HUVEC tube formation impairment as shown in **Figure 4B**. Furthermore, the instability of HIF-1α was also significantly revised in the insulin application group through immunofluorescence. In detail, co-IP of HIF-1α and CBP, the signature of HIF-1α, exerted their transcription functions (**Figures 4C–I**), and protein expression of HIF-1α target genes was significantly enhanced as shown in **Figures 4J–M**. The results showed that insulin promoted HIF-1α stabilization by the translocating into the nucleus.

Insulin-Containing Material Promotes Wound Healing Through HIF-1α and Its Downstream Effector

We confirmed in this work that insulin application could reverse MGO-induced HIF-1α instability and promote its signal effect,

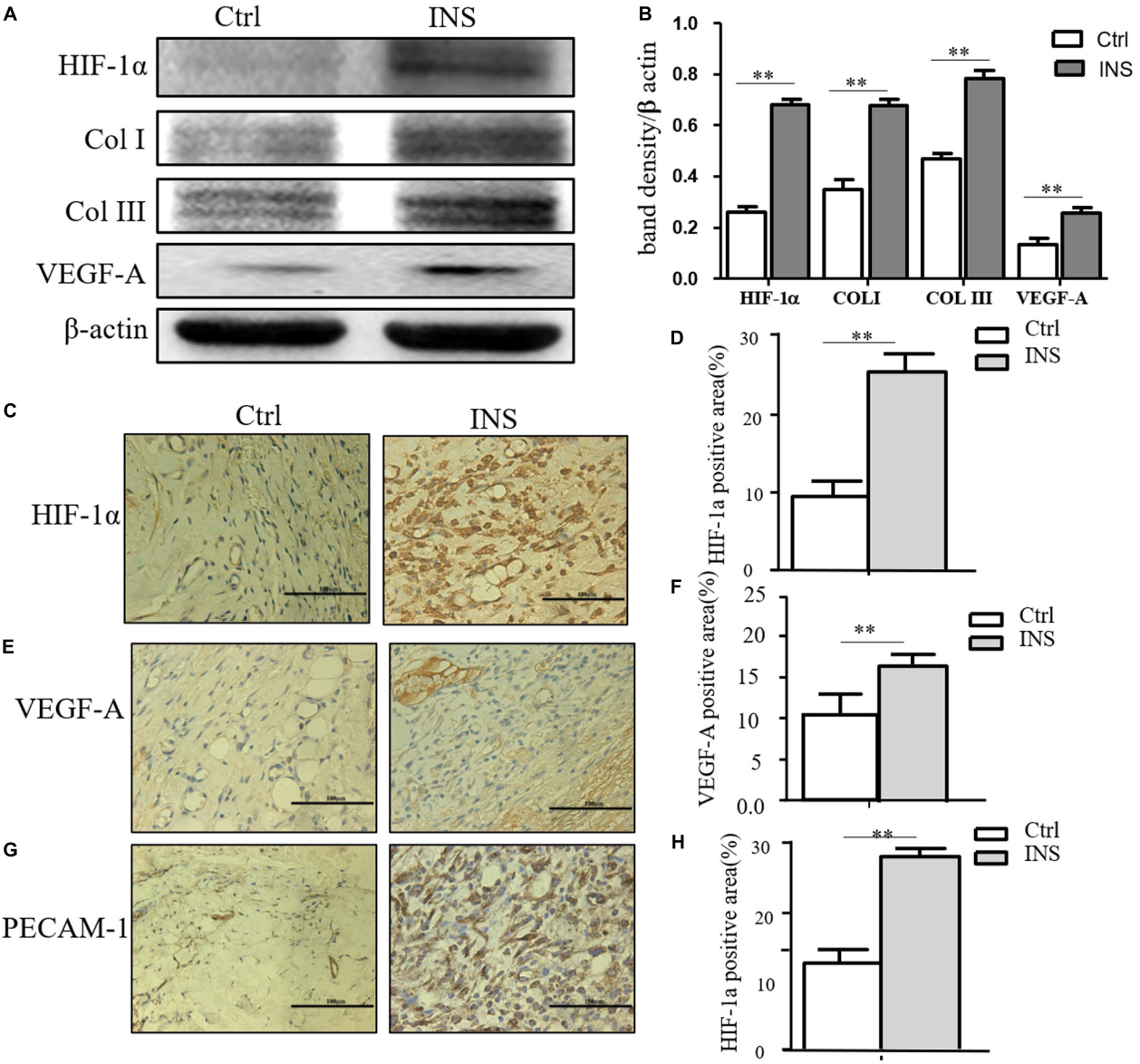

FIGURE 5 | Insulin-containing SF microparticles promoted diabetic wound healing through HIF-1α stabilization. **(A,B)** Insulin-containing dressing promoted HIF-1α stabilization and its downstream protein expression. The expressions of HIF-1α and downstream protein Col I, Col III, and VEGF-A in wounds on the fifth day were analyzed using western blot, and Photoshop was used in the quantification of immunoblots. Data are shown as mean ± SD. $^{**}p < 0.01$, $n = 5$. **(C–F)** Immunohistochemistry examination of HIF-1α and VEGF-A expressions and the positive area of the stain were calculated by ImageJ. Data are shown as mean ± SD. $^{**}p < 0.01$, $n = 5$. **(G,H)** Immunohistochemistry examination of angiogenesis in both groups. PECAM-1 was used as the marker of endothelial cells in rat vessels, and the positive area of the stain was calculated by ImageJ. Data are shown as mean ± SD. $^{**}p < 0.01$, $n = 5$.

an effect of insulin-containing material treating wounds. HIF-1α and its downstream effector including VEGF-A, GLUT-1, Col I, and Col III were significantly higher in insulin-containing dressing wounds as shown in **Figures 5A,B**. The immunochemistry examination of VEGF-A, vessel density, and collagen deposition further proved this assumption (**Figures 5C,D**).

DISCUSSION

Once a wound formed, the healing process initiates. Due to the destruction of blood supply and the high proliferation potential of wound cells, the wound is in an absolute or relative hypoxia state during a considerable part of the time. The process of wound healing in other words is the recovery of tissue structure and oxygen supply. HIF-1α plays a very important role in this process and is constitutively expressed in most cells. However, it is very sensitive to oxygen and would be degraded by the ubiquitin-proteasome immediately under a normoxia state. Under the hypoxia state in the wound healing environment, HIF-1α-degrading pathways are inhibited, and HIF-1α accumulates in the cytoplasm due to the inhibited HIF-1α-degrading pathways, and then it translocates into the nucleus to exert its translation factor function. When forming a transcription complex with HIF-1β, the co-activator CBP initiates a number of gene expression targets to inflammation reaction, angiogenesis, reepithelialization, and extracellular matrix deposition (Zhao et al., 2012). Under the diabetic state, high glucose and its side-products can inhibit the stability of HIF-1α in the hypoxia environment in many ways. MGO is a by-product of cell glucose metabolism in the condition of diabetes mellitus and has a significantly increased concentration in both rats and high-glucose cultured cells. Results showed that MGO can inhibit HIF-1α signal pathways in many ways such as downregulating the stability of HIF-1α through enhancing the chaperone-dependent ubiquitin degradation of HIF-1α (Bento et al., 2010), promoting the activity of PHD activation, and influencing the combination of HIF-1α and HIF-1β or HIF-1α and CBP (Bento and Pereira, 2011). Our results show that MGO affects the stability of HIF-1α and decreases the binding of HIF-1α and CBP. The significantly decreased protein levels of HIF-1α and its downstream target genes after MGO treatment further proved the vicious role that MGO plays in the HIF-1α-mediated wound healing process. The impairment of the HIF-1α pathway was considered as a pivotal mechanism of diabetic non-healing wounds. Promoting the stability of HIF-1α is an important research direction targeting at promotion of diabetic wound healing (Catrina and Zheng, 2016). Our previous researches confirm that insulin can promote wound healing by promoting epidermal migration, angiogenesis, extracellular matrix deposition, etc., which are exactly the downstream effects of HIF-1α. These results focus on HIF-1α and its downstream pathway. The application of insulin can promote the accumulation of HIF-1α in the cytoplasm and nucleus, and then HIF-1α will combine with CBP to activate its downstream transcription. In summary, this study confirmed that the increase of MGO content in diabetes can lead to the instability of HIF-1α, which results in the delay of wound healing due to the damage of the HIF-1α signal pathway and its downstream effects. Wound dressing containing insulin can stabilize HIF-1α, promote the downstream effects related to HIF-1α, and enhance the healing of diabetic wound.

DATA AVAILABILITY STATEMENT

The raw data supporting the conclusions of this article will be made available by the authors, without undue reservation.

ETHICS STATEMENT

The animal study was reviewed and approved by Animal Care Committee of SJTUSM.

AUTHOR CONTRIBUTIONS

All authors listed have made a substantial, direct and intellectual contribution to the work, and approved it for publication.

FUNDING

This study was supported by the project National Natural Science Foundation of China (81170761, 81270909, and 81871564), Shanghai Hospital Development Center (SHDC12014117), Shanghai Municipal Key Clinical Specialty (shslczdzk02302), Shanghai Chinese and Western Medicine Clinical Cooperation Pilot Cultivation Project [ZY(2018–2020)-FWTX-1106], Ruijin Youth NSFC Cultivation Fund (2019QNPY01003), and Shanghai Jiao Tong University Medical Engineering Cross Research Funds (YG2019QNA35).

REFERENCES

Bento, C. F., Fernandes, R., Ramalho, J., Marques, C., Shang, F., Taylor, A., et al. (2010). The chaperone-dependent ubiquitin ligase CHIP targets HIF-1alpha for degradation in the presence of methylglyoxal. *PLoS One* 5:e15062. doi: 10.1371/journal.pone.0015062

Bento, C. F., and Pereira, P. (2011). Regulation of hypoxia-inducible factor 1 and the loss of the cellular response to hypoxia in diabetes. *Diabetologia* 54, 1946–1956. doi: 10.1007/s00125-011-2191-8

Botusan, I. R., Sunkari, V. G., Savu, O., Catrina, A. I., Grunler, J., Lindberg, S., et al. (2008). Stabilization of HIF-1alpha is critical to improve wound healing in diabetic mice. *Proc. Natl. Acad. Sci. U.S.A.* 105, 19426–19431. doi: 10.1073/pnas.0805230105

Catrina, S. B. (2014). Impaired hypoxia-inducible factor (HIF) regulation by hyperglycemia. *J. Mol. Med.* 92, 1025–1034. doi: 10.1007/s00109-014-1166-x

Catrina, S. B., and Zheng, X. (2016). Disturbed hypoxic responses as a pathogenic mechanism of diabetic foot ulcers. *Diabetes Metab. Res. Rev.* 32(Suppl. 1), 179–185. doi: 10.1002/dmrr.2742

Davis, F. M., Kimball, A., Boniakowski, A., and Gallagher, K. (2018). Dysfunctional wound healing in diabetic foot ulcers: new crossroads. *Curr. Diab. Rep.* 8:2.

Demidova-Rice, T. N., Hamblin, M. R., and Herman, I. M. (2012). Acute and impaired wound healing: pathophysiology and current methods for drug delivery, part 1: normal and chronic wounds: biology, causes, and approaches to care. *Adv. Skin Wound Care* 25, 304–314. doi: 10.1097/01.asw.0000416006.55218.d0

Falanga, V. (2005). Wound healing and its impairment in the diabetic foot. *Lancet* 366, 1736–1743. doi: 10.1016/s0140-6736(05)67700-8

Hong, W. X., Hu, M. S., Esquivel, M., Liang, G. Y., Rennert, R. C., McArdle, A., et al. (2014). The role of hypoxia-inducible factor in wound healing. *Adv. Wound Care* 3, 390–399. doi: 10.1089/wound.2013.0520

Junod, A., Lambert, A. E., Stauffacher, W., and Renold, A. E. (1969). Diabetogenic action of streptozotocin: relationship of dose to metabolic response. *J. Clin. Invest.* 48, 2129–2139. doi: 10.1172/jci106180

Li, X., Liu, Y., Zhang, J., You, R., Qu, J., and Li, M. (2017). Functionalized silk fibroin dressing with topical bioactive insulin release for accelerated chronic wound healing. *Mater Sci. Eng. C Mater Biol. Appl.* 72, 394–404. doi: 10.1016/j.msec.2016.11.085

Liu, Y., Petreaca, M., and Martins-Green, M. (2009a). Cell and molecular mechanisms of insulin-induced angiogenesis. *J Cell Mol Med.* 13, 4492–4504. doi: 10.1111/j.1582-4934.2008.00555.x

Liu, Y., Petreaca, M., Yao, M., and Martins-Green, M. (2009b). Cell and molecular mechanisms of keratinocyte function stimulated by insulin during wound healing. *BMC Cell Biol.* 10:1. doi: 10.1186/1471-2121-10-1

Mace, K. A., Yu, D. H., Paydar, K. Z., Boudreau, N., and Young, D. M. (2007). Sustained expression of Hif-1alpha in the diabetic environment promotes angiogenesis and cutaneous wound repair. *Wound Repair Regen.* 15, 636–645. doi: 10.1111/j.1524-475x.2007.00278.x

Ramasamy, R., Yan, S. F., and Schmidt, A. M. (2006). Methylglyoxal comes of AGE. *Cell* 124, 258–260. doi: 10.1016/j.cell.2006.01.002

Zhao, Y. Z., Li, X., Lu, C. T., Xu, Y. Y., Lv, H. F., Dai, D. D., et al. (2012). Experiment on the feasibility of using modified gelatin nanoparticles as insulin pulmonary administration system for diabetes therapy. *Acta Diabetol.* 49, 315–325. doi: 10.1007/s00592-011-0356-z

Conflict of Interest: The authors declare that the research was conducted in the absence of any commercial or financial relationships that could be construed as a potential conflict of interest.

frontiers in Bioengineering and Biotechnology

ORIGINAL RESEARCH
published: 28 January 2021
doi: 10.3389/fbioe.2021.631191

Gold Nanoparticles Combined Human β-Defensin 3 Gene-Modified Human Periodontal Ligament Cells Alleviate Periodontal Destruction *via* the p38 MAPK Pathway

Lingjun Li[1†], Yangheng Zhang[1†], Min Wang[1], Jing Zhou[2], Qian Zhang[1], Wenrong Yang[3], Yanfen Li[1]* and Fuhua Yan[1]**

[1] Nanjing Stomatological Hospital, Medical School of Nanjing University, Nanjing, China, [2] Key Laboratory of Oral Biomedical Research of Zhejiang Province, The Affiliated Stomatological Hospital, Zhejiang University School of Medicine, Zhejiang University School of Stomatology, Hangzhou, China, [3] School of Life and Environmental Science, Centre for Chemistry and Biotechnology, Deakin University, Geelong, VIC, Australia

Periodontitis is a chronic inflammatory disease with plaques as the initiating factor, which will induce the destruction of periodontal tissues. Numerous studies focused on how to obtain periodontal tissue regeneration in inflammatory environments. Previous studies have reported adenovirus-mediated human β-defensin 3 (hBD3) gene transfer could potentially enhance the osteogenic differentiation of human periodontal ligament cells (hPDLCs) and bone repair in periodontitis. Gold nanoparticles (AuNPs), the ideal inorganic nanomaterials in biomedicine applications, were proved to have synergetic effects with gene transfection. To further observe the potential promoting effects, AuNPs were added to the transfected cells. The results showed the positive effects of osteogenic differentiation while applying AuNPs into hPDLCs transfected by adenovirus encoding hBD3 gene. *In vivo*, after rat periodontal ligament cell (rPDLC) transplantation into SD rats with periodontitis, AuNPs combined hBD3 gene modification could also promote periodontal regeneration. The p38 mitogen-activated protein kinase (MAPK) pathway was demonstrated to potentially regulate both the *in vitro* and *in vivo* processes. In conclusion, AuNPs can promote the osteogenic differentiation of hBD3 gene-modified hPDLCs and periodontal regeneration *via* the p38 MAPK pathway.

Keywords: gold nanoparticles, human β-defensin 3 gene, osteogenic differentiation, p38 MAPK pathway, periodontal ligament cells

OPEN ACCESS

Edited by:
Kai Zheng,
University of Erlangen Nuremberg, Germany

Reviewed by:
Francesca Diomede,
University of Studies G. d'Annunzio Chieti and Pescara, Italy
Zeqian Xu,
Tübingen University Hospital, Germany
Thanaphum Osathanon,
Chulalongkorn University, Thailand

****Correspondence:***
Fuhua Yan
yanfh@nju.edu.cn
Yanfen Li
liyanfen2003@126.com
Wenrong Yang
wenrong.yang@deakin.edu.au

† These authors have contributed equally to this work

Specialty section:
This article was submitted to Biomaterials, a section of the journal Frontiers in Bioengineering and Biotechnology

Received: *19 November 2020*
Accepted: *11 January 2021*
Published: *28 January 2021*

Citation:
Li L, Zhang Y, Wang M, Zhou J, Zhang Q, Yang W, Li Y and Yan F (2021) Gold Nanoparticles Combined Human β-Defensin 3 Gene-Modified Human Periodontal Ligament Cells Alleviate Periodontal Destruction via the p38 MAPK Pathway. Front. Bioeng. Biotechnol. 9:631191. doi: 10.3389/fbioe.2021.631191

INTRODUCTION

Inflammatory responses and bone loss occurring in periodontitis have become the most critical and challenging problem to be solved to achieve healthy periodontal tissues (Taut et al., 2013; Bassir et al., 2016). Human β-defensin 3 (hBD3), a small molecule cationic antimicrobial peptide consisting of 45 amino acids, is perceived to be the most promising antimicrobial peptide (Harder et al., 2001; Dhople et al., 2006). Former studies have demonstrated that hBD3 is perceived to be the most promising antimicrobial peptide and can potentially promote the osteogenic

differentiation of human periodontal ligament cells (hPDLCs) in inflammatory microenvironments (Zhou et al., 2018). However, recombinant hBD3 is extremely expensive and difficult to store. Therefore, our team previously synthesized adenovirus vectors containing the hBD3 gene and successfully transfected them into hPDLCs. The enhancement effects of osteogenic differentiation and bone regeneration have also been observed after hBD3 gene transfection (Li et al., 2020).

Gold nanoparticles (AuNPs) are recognized as ideal inorganic nanomaterials concerning biomedicine applications, including drug delivery, diagnostic imaging, and targeting therapy, due to their excellent biocompatibility and versatility in surface modification (Dreaden et al., 2012; Hu et al., 2020). For decades, nanotechnology, such as nanofabrication, nanofiltration, and synergistic therapy, has revealed an inextricable relationship with viral biology. A study in 2003 showed that AuNPs can be spectroscopic enhancers by covering viruses with 2.5–4.5 nm AuNPs (Dragnea et al., 2003). Guo et al. (2010) demonstrated the feasibility of using charge-reversal functional AuNPs as a means of improving the nucleic acid delivery efficiency. Another study proved that gold-based nanoparticles complexed with exogenous pDNA improved transfection efficiency in human mesenchymal stem cells (Yi et al., 2019). Hence, we supposed that AuNPs could also promote hBD3 gene transfection in PDLCs thereby promoting osteogenesis and bone regeneration.

The process of osteogenic differentiation involves the activation of multiple signaling pathways (Long et al., 2019; Ohashi et al., 2019). Among these, the p38 MAPK pathway is one of the critical pathways; it has been reported to regulate the osteogenesis process in various cells, including hPDLCs (Yi et al., 2010; Ren et al., 2013; Li et al., 2020). There are few reports about hBD3 and osteogenesis, yet other cationic antimicrobial peptides like LL37 were demonstrated to affect the proliferation and differentiation of MC3T3-E1 cells (Shen et al., 2019) and could enhance bone regeneration in a rat calvarial bone defect through p38 MAPK pathways (Kittaka et al., 2013).

Hence, we aim to evaluate the role of AuNPs in the osteogenic differentiation process of hBD3 gene transfected hPDLCs in inflammatory microenvironments. Further experiments were conducted to explore the potential mechanism underlying these phenomena. SD rat periodontal ligament cells (rPDLCs) transfected with the hBD3 gene and AuNPs were transplanted into rats with periodontitis to observe the effects of AuNPs *in vivo*.

MATERIALS AND METHODS

We declared that all experiments adhered to standard biosecurity and institutional safety procedures. For *in vitro* experiments, at least four replicate wells per group were set up, and an average of six SD rats per group were used for animal experiments.

Gold Nanoparticle Characterization

Gold nanoparticles with diameters of 45 nm were synthesized at the School of Life and Environmental Science, Centre for Chemistry and Biotechnology, Deakin University. The concentration of the gold colloid solution was approximately 0.25 mM. The next step was adding 100 μL of 0.1 mM L-cysteine (Sigma-Aldrich, St. Louis, MO, United States) solution into every 5 mL of AuNPs with stirring for 2 h. The AuNPs were rinsed by centrifugation to remove unbound L-cysteine and dispersed in deionized water (Kalmodia et al., 2013; Weng et al., 2013; Zhang et al., 2017). Our team has previously demonstrated that L-cysteine-modified AuNPs of 45 nm and 10 μM are appropriate and biocompatible when applied to hPDLCs (Zhang et al., 2017).

Cell Culture and Gene Transfection

Human periodontal ligament cells from healthy donors were obtained from ScienCell (ScienCell Research Laboratories, San Diego, CA, United States). The cells were cultured in Dulbecco's modified Eagle's medium (DMEM, Gibco, Grand Island, NY, United States) with 1% penicillin/streptomycin (Gibco, Grand Island, NY, United States) and 10% fetal bovine serum (FBS, ScienCell Research Laboratories, San Diego, CA, United States) at 37°C in 5% CO_2. Every other day, the medium was refreshed, and cells between passages 2 and 6 were used. Osteogenic differentiation medium (growth medium supplemented with 50 μg/mL ascorbic acid (Sigma-Aldrich, St. Louis, MO, United States), 10 mM β-glycerophosphate (Sigma-Aldrich, St. Louis, MO, United States), and 100 nM dexamethasone (Sigma-Aldrich, St. Louis, MO, United States) was used to replace the original growth medium every 2 days.

The recombinant adenovirus carried the human beta defensin-3 gene (Ad-hBD3) was purchased from the GenePharma company (GenePharma, Shanghai, China). The hPDLCs were transfected with Ad-hBD3 according to our former study (Li et al., 2020).

Quantitative Real-Time PCR

The mRNA levels of hBD3 and osteogenesis-related genes were determined by Quantitative Real-Time PCR (qRT-PCR). Six-well plates with growth medium were chosen to seed hPDLCs (1×10^5 cells/well). The transfections of Ad-hBD3 were conducted when the cell fusion rate reached 80%. On day 3, after hBD3 expression was identified, the medium with AuNPs (45 nm, 10 μM) was replaced for the next experiment. *Escherichia coli*-LPS (1 μg/mL) was added into the medium 2 h later, ensuring that the AuNPs were already taken in by the cells (Alkilany and Murphy, 2010). TRNzol reagent (Tiangen, Beijing, China) was adopted to extract total RNA from the cells. The reverse transcription of total RNA to cDNA was performed by using the PrimeScript RT Reagent Kit (Takara, Otsu, Japan). The sequences of the primers for qRT-PCR are shown in **Table 1**. Each gene cycle threshold (ct) was normalized based on the ct of GAPDH examined simultaneously on the same plate and then calculated by the comparative $2^{-\Delta\Delta Ct}$ method. All of the samples were run in triplicate.

Western Blot

The expression levels of hBD3, osteogenesis-related, p38, and p-p38 proteins were measured by WB assay. Cells were lysed in RIPA buffer (Beyotime, Shanghai, China). The total proteins were denatured by boiling for 5 min, resolved by 10% gradient

TABLE 1 | Primer sequences.

Primer name	Forward primer sequence (5′–3′)	Reverse primer sequence (5′–3′)
GAPDH	GGCGTGATGGCTTATTTGTT	GGCGTGATGGCTTATTTGTT
Runx2	AACCCACGAATGCACTATCCA	CGGACATACCGAGGGACATG
COL1	CTGCAAGAACAGCATTGCAT	GGCGTGATGGCTTATTTGTT
ALP	CCGTGGCAACTCTATCTTTGG	GCCATACAGGATGGCAGTGA
hBD3	AAGCCTAGCAGCTATGAGGATCC	TGTGTTTATGATTCCTCCATGACC

sodium dodecyl sulfate-polyacrylamide gel electrophoresis and then transferred onto polyvinylidene difluoride membranes (Millipore, Bedford, MA, United States). Five percent skim milk powder was used for blocking; 2 h later, the membranes were incubated overnight with primary antibodies, anti-hBD3 (ab19270), anti- ALP (ab83259), anti-Runx2 (ab23981), anti-COL1 (ab96723) (Abcam, Cambridge, United Kingdom), anti-p38 (#8690 S), and anti-p-p38 (#4511 S) (CST, MA, United States), with anti-β-actin (BS6008M) (Bioworld, MN, United States) as the housekeeping gene, at 4°C, and then antirabbit or anti-mouse secondary antibody was added and incubated for 1 h. A Tanon 5200 chemiluminescent imaging system (Tanon, Shanghai, China) was utilized to visualize the proteins. Image J software was used to quantify images of western blot bands. After converting the image western blot bands into a grayscale picture, we eliminated background influence and then set quantitative parameters and units to quantify. The results were exported from Image J and analyzed by graphpad prism 6.

Transmission Electron Microscopy

Transmission electron microscopy (TEM) was used to examine the uptake of the AuNPs. hPDLCs (1×10^5 cells/well) were seeded into six-well plates and cultured in a growth medium overnight. Then, the osteogenic differentiation medium containing modified AuNPs (45 nm, 10 μM) was prepared to replace the former medium. After culturing for 7 days, the cells were fixed with 2.5% glutaraldehyde, and subsequently, in 1% osmium tetroxide, dehydrated in a graded series of ethanol and ultimately embedded in epoxy resin. Ultrathin sections were examined with TEM (HT7700, Hitachi Company, Tokyo, Japan) at an accelerating voltage of 120 kV.

Alkaline Phosphatase Activity and Staining Assay

The alkaline phosphatase (ALP) assay kit (Abcam, MA, United States) was used to assess the ALP activity. After transfection, hPDLCs (3.0×10^4 cells/well) were seeded into 24-well plates. The medium was changed into an osteogenic differentiation medium with AuNPs (45 nm, 10 μM) after culturing overnight. After culturing for 7 days, the cells were rinsed twice with PBS. After a series of steps following the manufacturer's instructions, the final solution was added to the plates. The absorbance was assessed at 405 nm by a SpectraMax M3 microplate reader (Molecular Devices, Sunnyvale, CA, United States). The ALP activity level was defined relative to the control group as a percentage after measuring a standard curve. The measurement of ALP staining was conducted on the same day according to the manufacturer's instructions (BCIP/NBT ALP staining kit, Beyotime Institute of Biotechnology, Shanghai, China).

ARS Staining

After cultured for 3 weeks, the cells were rinsed twice with PBS and fixed in 4% paraformaldehyde for 30 min. The cells were washed with distilled water (DW), treated with 2% alizarin red S solution (Sigma-Aldrich, United States) for 5 min, and then washed 3–5 times with DW to remove the unbound alizarin red S (ARS). For the quantification of alizarin red S staining, cells were desorbed with 10% (w/v) cetylpyridinium chloride (Sigma-Aldrich, St. Louis, MO, United States); then, the absorbance was measured at 562 nm by a SpectraMax M3 microplate reader. The stained plates were air-dried and examined under a light microscope (Olympus IMT-2, Tokyo, Japan) and photographed with a digital camera (Canon EOS 550D, Tokyo, Japan).

Culture and Identification of rPDLCs

Female Sprague–Dawley Rats (5 weeks old) were sacrificed and then their six molars were extracted and placed into 0.1% collagenase I solution for shaking for 2 h at 37°C. After centrifugation, cells were resuspended in growth medium at 37°C in 5% CO_2 for 3–5 days when cell adherence was observed. Afterward, the refresh frequency of the culture medium was every 2 days. After 1–2 passages, cells were fixed by 4% paraformaldehyde for the subsequent immunofluorescence staining of anti-cytokeratin and anti-vimentin (CST, MA, United States), which were used to identify the cell origin. Cells were seeded into 96-well plates (5.0×10^3 cells/well), cultured for 10 days while adding 10 μL/well reagents of the cell counting kit-8 (CCK8) each day, and then incubated at 37°C in 5% CO_2 for 4 h. The absorbance was measured with a SpectraMax M3 microplate reader (Molecular Devices, Sunnyvale, CA, United States) at a wavelength of 450 nm. Cell viability was expressed as the relative absorbance after excluding the background absorbance.

Experimental Periodontitis and rPDLCs Transplantation

Female Sprague–Dawley Rats (5 weeks old) were randomly allocated into different groups ($N = 6$ experimental rats per group): a blank group (without ligature and cell transplantation), control group (with ligature alone), Ad-hBD3 group (with ligature and cell transplantation treated with Ad-hBD3), and Ad-hBD3 + AuNPs group (with ligature and cell transplantation treated with Ad-hBD3 and AuNPs). Silk threads soaked in a bacterium solution of *Porphyromonas gingivalis* ahead for 2 h were used to ligature the bilateral maxillary second molars of the SD rats. rPDLCs with different treatments were dissociated into cell suspension with 0.9% NaCl (1×10^4 cells/μL) and then injected by a 100-μL microsyringe (Hamilton, Bonaduz, Switzerland) at the mesial, middle, and distal sites of palatal gingival tissues around the ligatured molars. After 2 and 24 h,

relevant gingival tissues were gathered to make frozen sections to confirm the rPDLC transplantation. rPDLC transplantations were performed once per week, and 2 weeks later, all rats were sacrificed and sampled.

Micro-CT Analysis

The maxillary bone samples of the SD rats were trimmed and placed into 4% paraformaldehyde fixative solution for 24 h. On the next day, the samples were collected and prepared for micro-CT scanning with a Skyscan 1176 (Bruker, Karlsruhe, Germany). The scanning parameters were as follows: a rotation angle of 360°, a tube voltage of 70 kV, a tube current of 353 μA, an X-ray exposure time of 404 ms, and a scanning layer thickness of 18 μm. The data were reconstructed with NRecon software and then imported into CTVox and CTAn software to obtain three-dimensional (3D) images and relative data. We selected the alveolar bone area around the root of the second molar form alveolar bone crest to apical as the ROI. There were almost 100 slides in different groups.

Histological Analysis

Two weeks later, the SD rats were sacrificed by euthanasia. The right maxillas were collected to be fixed in 4% paraformaldehyde for 48 h and then placed into 10% EDTA decalcifying solution for 1 month. Afterward, the specimens were dehydrated with a gradient series of 40, 50, 60, 70, 80, 90, and 95% ethanol for 12 h each, and they were finally soaked in a 95% ethanol and xylene solution mixture (1:1) for 12 h to make them transparent. After sectioning the samples to a thickness of 5 μm, they were stained with a p-p38 antibody, and the mean density of p-p38 was measured in three different samples.

Statistical Analysis

All statistical calculations were performed with SPSS23 statistical software (SPSS, Chicago, IL, United States). Quantitative data were expressed as the mean ± standard deviation (SD). Significant differences were determined using Student's t-test (for normally distributed samples where the total sample content is small (e.g., $n < 30$), the overall standard deviation σ is unknown) or one-way ANOVA (comparison of population means corresponding to three or more groups of samples) followed by the Bonferroni test. Statistical significance was determined by different tests depending on the situation and was considered statistically significant at p-values of less than 0.05.

RESULTS

Cellular Uptake and Localization of AuNPs

After AuNPs (45 nm, 10 μM) treatment and cultured for 7 days, the ingestion and positioning of AuNPs in hPDLCs were detected by TEM. **Figure 1** shown that AuNPs taken up by cells were generally found in intracellular vesicles. We could also observe one or two AuNPs clustered together in some cells. For the most part, AuNPS were detected in cellular organelles including lysosome and autophagosome.

Osteogenic Enhancement of AuNPs on Transfected hPDLCs

The results of ALP and ARS staining revealed that the ALP staining color was darker in the Ad-hBD3 + AuNPs groups than that in the Ad-hBD3 groups. The number of mineral nodules was also higher in the Ad-hBD3 + AuNPs groups (**Figures 2A,B**). qRT-PCR and western blot assay were conducted on day 7. The results showed that ALP, Runx2, and COL1 expressions were significantly higher in AuNP-treated groups than in AuNP-free groups at both the mRNA and protein levels (**Figures 2C,D**).

Activation of p38 MAPK Pathway *in vitro*

To investigate the potential mechanism of the osteogenesis-promoting effects of AuNP on hBD3 gene transfected hPDLCs in inflammatory microenvironments, the following experiments were conducted. On day 7, the expression of p-p38 as the specific protein in the p38 MAPK pathway was extremely high in Ad-hBD3 + AuNPs groups (**Figure 3C**), which demonstrated that the p38 MAPK pathway was activated. Besides, after adding the p38 MAPK pathway inhibitor, SB203580, into the hPDLCs, ALP, Runx2, and COL1 expression decreased significantly both at the mRNA and protein level, which proved that the expression of osteogenesis-related genes and proteins could be regulated by the p38 MAPK pathway (**Figure 3D**). ALP on day 7 and ARS stainings on day 21 showed a similar trend, which means that the p38 MAPK pathway might still regulate the subsequent osteogenic differentiation process (**Figures 3A,B**).

Primary Culture and Transplantation of rPDLC

Figure 4A presents the cells isolated from the periodontal ligament tissues of SD rats. Immunofluorescence results showed that the cultured cells could express vimentin (red) but not cytokeratin, which indicates that they were mesoderm-derived. The three cell growth phases, lag, log (exponential), and plateau, were observed from the cell growth curve measured by CCK8. Our team has already proved that rPDLCs transfected with Ad-hBD3 could successfully express hBD3 (Li et al., 2020). Fluorescence images showed rPDLCs transfected with Ad-hBD3 after cultured for 3 days (**Figure 4B**). **Figure 4C** showed immunofluorescence images at 2 and 24 h after cell injection. The transplanted cells were diffusely distributed within the tissue at 2 h and after 24 h were more clustered around blood vessels.

Promotion of Periodontal Regeneration After Transplantation of Ad-hBD3 Transfected rPDLC Treated With AuNPs

The SD rats were sacrificed after 2 weeks, and the bilateral maxillary bone was sampled for micro-CT scanning. The following 3D images show that the alveolar bone loss around the ligatured molars of the control group was much more obvious than that of other groups, which means that we created experimental periodontitis successfully. Also, Ad-hBD3, and Ad-hBD3 + AuNP groups presented less bone resorption and a higher bone mineral density and bone volume ratio (**Figure 5**). The results indicated that AuNPs can reduce

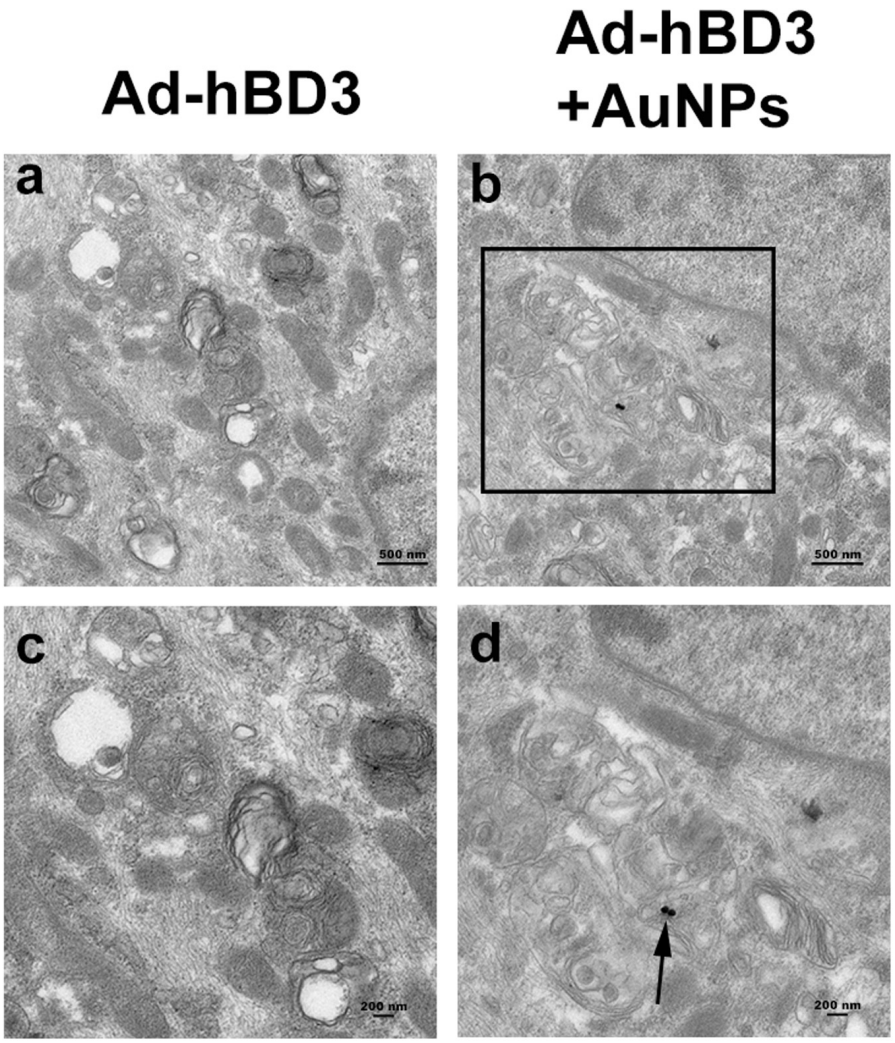

FIGURE 1 | Cellular uptake of AuNPs in hPDLCs. hPDLCs were transfected by Ad-hBD3 and treated with AuNPs (45 nm, 10 μM) depending on the grouping. **(A)** TEM images of groups on day 7 without AuNPs. **(B)** TEM images of groups on day 7 with AuNPs. Panels **(C,D)** were high power views of the indicated portion in panels **(A,B)** separately. Arrows indicate internalized AuNPs.

bone destruction and potentially promote bone regeneration in SD rats with periodontitis after transplantation of Ad-hBD3 transfected rPDLC.

H&E and Masson's trichrome staining results showed that in the control group, the alveolar bone around the second molar was resorbed obviously, the hyperplasia of gingival epithelial spikes and thickened stratum spinosum could be observed, as was the inflammatory cells infiltration and collagen fibers destruction. In Ad-hBD3 + AuNPs group where hBD3-rPDLCs were treated with AuNPs, we observed less inflammatory cells along with lighter epithelial spikes hyperplasia in the gingival epithelium, and the collagen fibers arranged more orderly in Ad-hBD3 + AuNPs group than the control group. Furthermore, altered and broken collagen fibers could be repaired in those groups (**Figure 6A**). Besides, the inflammatory cytokines of IL6, TNF-α, and IFN-γ in serum were also detected by ELISA assay (**Figure 6B**).

Activation of p38 MAPK Pathway *in vivo*

Immunohistochemistry experiments of p-p38 were conducted to evaluate whether the p38 MAPK pathway was involved while applied *in vivo*. The results showed that the p-p38 expression level in Ad-hBD3 + AuNPs groups was higher than that in Ad-hBD3 groups and the expression levels of p-p38 in the Ad-hBD3 + AuNPs groups were higher than that in the Ad-hBD3 group (**Figure 7**).

DISCUSSION

In periodontitis, the inflammatory microenvironments around the periodontal tissues could cause the absorption and destruction of alveolar bone (Preshaw and Bissett, 2019). How to reduce bone destruction and obtain bone regeneration in the inflammatory microenvironments has drawn much

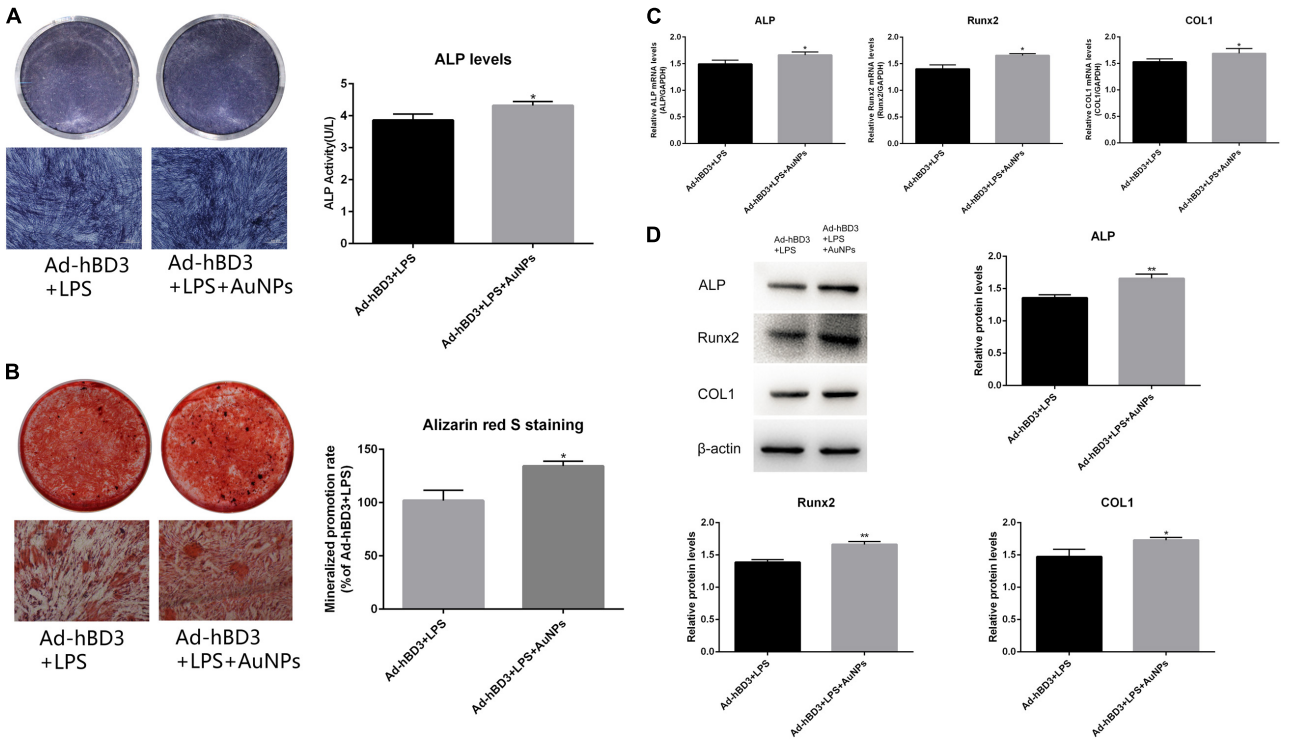

FIGURE 2 | ALP and ARS staining assays of hPDLCs. **(A)** ALP staining and activity on day 7, **(B)** Alizarin red S staining of mineralized nodules on day 21. Osteogenesis-related gene and protein expression. hPDLCs were transfected by Ad-hBD3 and treated with AuNPs. *E. coli*-LPS was added in all groups to create inflammatory microenvironments. **(C)** qRT-PCR and **(D)** western blot analysis of ALP, Runx2, and COL1 gene and protein expressions on day 7 (*$p < 0.05$ and **$p < 0.01$).

attention (Kong et al., 2013; Zhou et al., 2018). In our study, 1 μg/mL *E. coli*-LPS was chosen to create the inflammatory microenvironment according to a former study (Bindal et al., 2018). As a vital component of the periodontium, hPDLCs not only produce collagen but also produce mineralized tissue and have high levels of ALP activity. Some studies have found that hPDLCs can express bone-associated proteins, such as osteonectin, to form mineralized nodules, which means that they might potentially be osteogenic cells (Jonsson et al., 2011).

Antimicrobial peptides have been noted to play an essential role in maintaining the health status against disease in a fluctuant oral microenvironment (Pizzolato-Cezar et al., 2019; Vila et al., 2019). Human β-defensin 3 was shown to have broad-spectrum antimicrobial activity and also enhance the proliferation and osteogenic differentiation of hPDLCs (Wang et al., 2011; Zhou et al., 2018). However, synthetic recombinant hBD3 is too expensive to widely apply to disease treatment. In our former study, hPDLCs transfected by adenovirus containing the hBD3 gene were observed to express the hBD3 protein for at least 7 days. After transfection, Ad-hBD3-hPDLCs showed higher expression of osteogenic-related genes and proteins than normal hPDLCs in inflammatory microenvironments (Li et al., 2020).

Considering the potential synergistic therapeutic effects of modified AuNPs and adenovirus (Saini et al., 2006), Ad-hBD3-hPDLCs were then treated with AuNPs. TEM images display the cellular uptake of AuNPs (45 nm, 10 μM) in hPDLCs and their localization, mostly in autophagosomes and lysosomes. Another study explained the specific mechanism of AuNP uptake and the process through the endocytotic pathways (endosomes/lysosomes), revealing the intracellular diffusion coefficients as well as the characteristic transport velocities of endocytotic vesicles of AuNPs (Huefner et al., 2014). Viruses, as inherently structured nanoparticles, have many similar properties as nanomaterials, for example, nanoscale size and cellular uptake (Sirotkin et al., 2014). As a result, they can reveal many meaningful interdisciplinary applications. Viruses can form crystals, which are useful in generating long-range 3D ordered solids of nanostructured materials and can be used in X-ray systems (Falkner et al., 2005). Wang et al. (2003) found that AuNPs of 8–15 nm coupled to oligonucleotide detection probes could be used to detect hepatitis B and hepatitis C viruses in serum samples, which can be used to achieve the faster diagnosis of patients. In the field of gene therapy, a study showed that targeted delivery of AuNPs to the tumor tissue could be realized by a virus that expresses the receptor protein (Zharov et al., 2005). There are also some studies concerning the osteogenic induction effects of AuNP on various cells (Li et al., 2016; Xiang et al., 2018). In our study, Ad-hBD3 + AuNP treated hPDLCs showed the enhancement of osteogenic differentiation in inflammatory microenvironments, upregulated ALP activity, and promoted the mineralization of hPDLCs. This synergistic effect might be due to the enhancement effects of AuNPs in gene transfection.

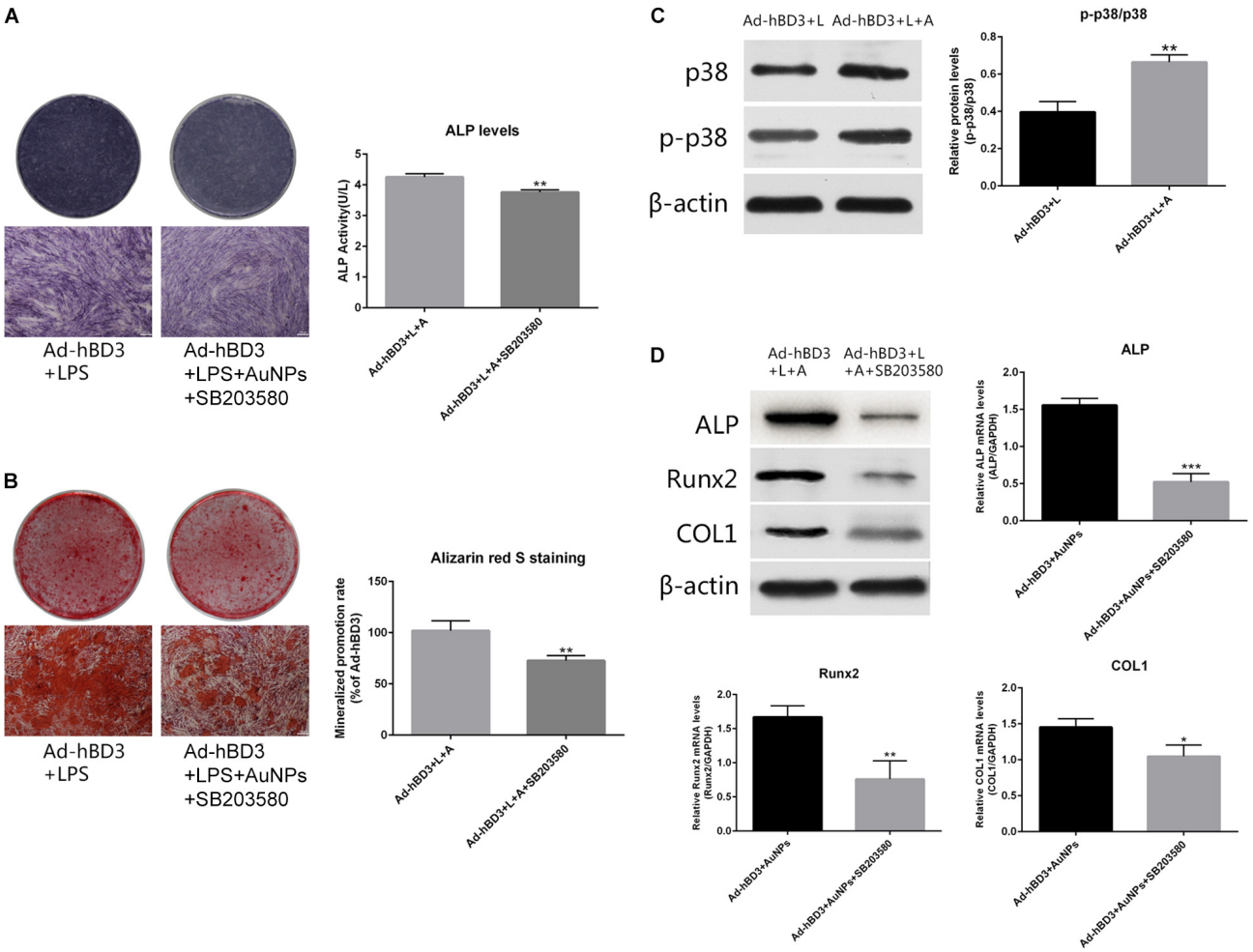

FIGURE 3 | Effects of AuNPs on p38 MAPK pathway activation in hBD3 gene transfected hPDLCs. **(A)** ALP staining and ALP activity on day 7 after adding SB203580; **(B)** Alizarin red S staining of mineralized nodules on day 21 after adding SB203580; **(C)** High expression of p-p38 was observed in Ad-hBD3 + AuNPs groups; **(D)** Bone-related gene and protein expressions after adding SB203580. Groups treated with the inhibitor showed low expression of ALP, Runx2, and COL1 (*$p < 0.05$, **$p < 0.01$, and ***$p < 0.001$).

Rajesh et al. found that the gold nanoparticle-based targeted gene delivery system could target ovarian cancers caused by mutated p53 (Kotcherlakota et al., 2019).

The p38 mitogen-activated protein kinases (MAPKs) in mammals participate in various cellular activities involving proliferation, differentiation, and innate immunity. Yi et al., found that the p38 MAPK pathway can regulate the osteogenic differentiation of mesenchymal stem cells treated by AuNPs (Xiang et al., 2018). Wu et al. (2013) also indicated that p38 MAPK signaling plays a special role in the osteogenic differentiation of human periodontal ligament stem cells, which agrees with our results.

Furthermore, the results of *in vivo* experiments revealed the potential regeneration effects of AuNPs after Ad-hBD3 transfected rPDLCs. Former studies showed that the local transplantation of stem cells could promote tissue regeneration (Cooney et al., 2016; Li et al., 2018). In our study, after hBD3 gene transfection and AuNP treatment, rPDLCs showed some characteristics of stem cells, such as osteogenesis promotion effects, exactly as they did *in vitro*. Besides, the Ad-hBD3 + AuNPs group exhibited more powerful inhibiting effects of alveolar bone absorption than the Ad-hBD3 group, which indicates that modified AuNPs also worked *in vivo*. The immunohistochemical assay of p-p38 indicated that the p38 MAPK pathway might also be activated *in vivo* after adding AuNP into Ad-hBD3 transfected cells.

In conclusion, AuNPs combined hBD3 gene-modified hPDLCs could promote cell osteogenesis *in vitro* and reduce periodontal damage *in vivo*, and the p38 MAPK pathway might potentially regulate the process. Further studies are still needed to track transplanted cells *in vivo* to ensure that enough rhPDLCs was loaded. It is more rigorous if we used nude rats instead of normal rats to excluded the difference of immune response between individuals. We will continue to explore the more specific cellular mechanism of the relationship with AuNPs and gene transfection.

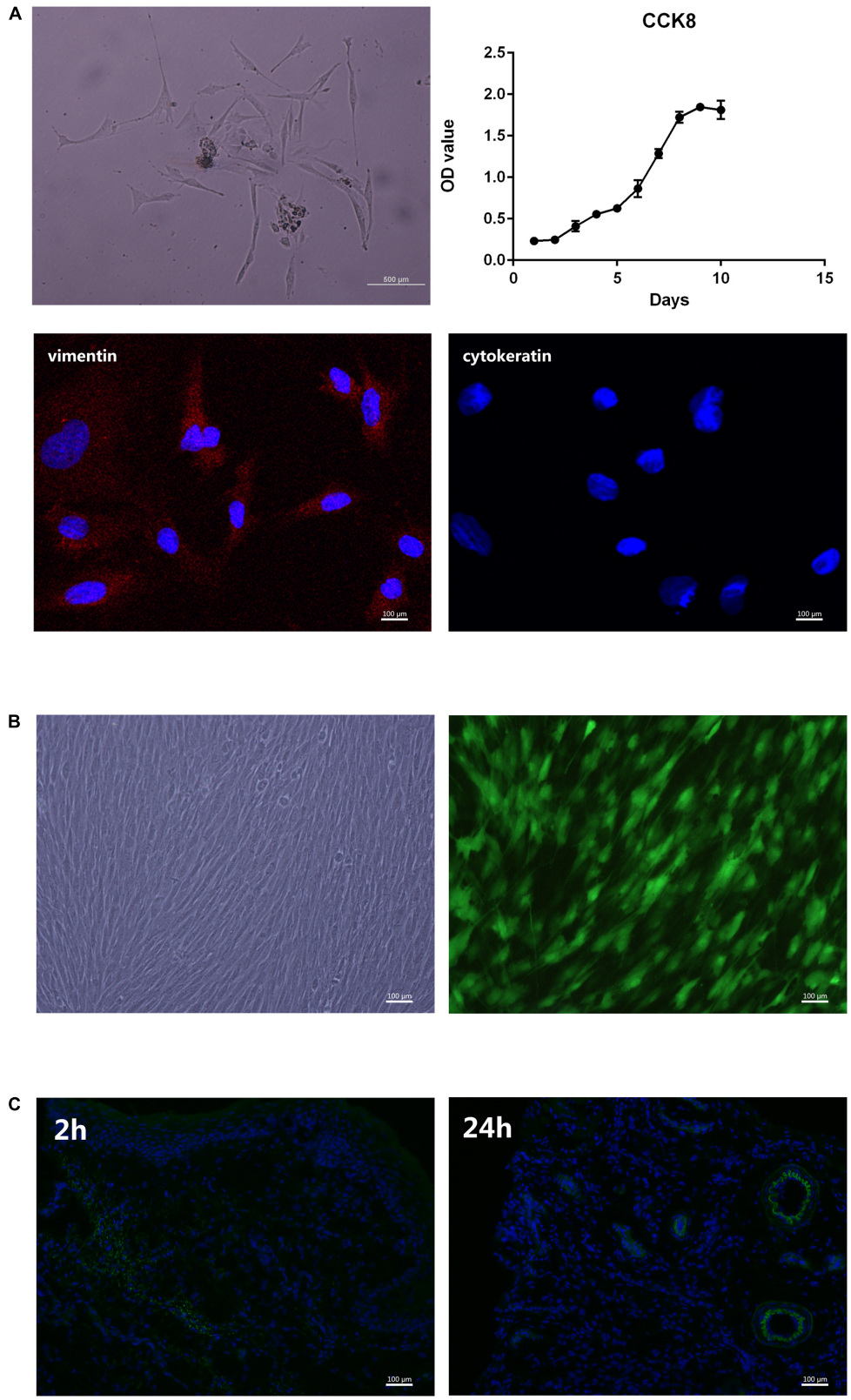

FIGURE 4 | Primary culture and transplantation of rPDLC. **(A)** Characterization of rPDLCs: Cells isolated from periodontal ligament tissues of SD rats; growth curve of cultured cells; positive expression of vimentin (red); and negative expression of cytokeratin; **(B)** Fluorescence images of rPDLCs after transfection; **(C)** immunofluorescence images at 2 and 24 h after cell injection.

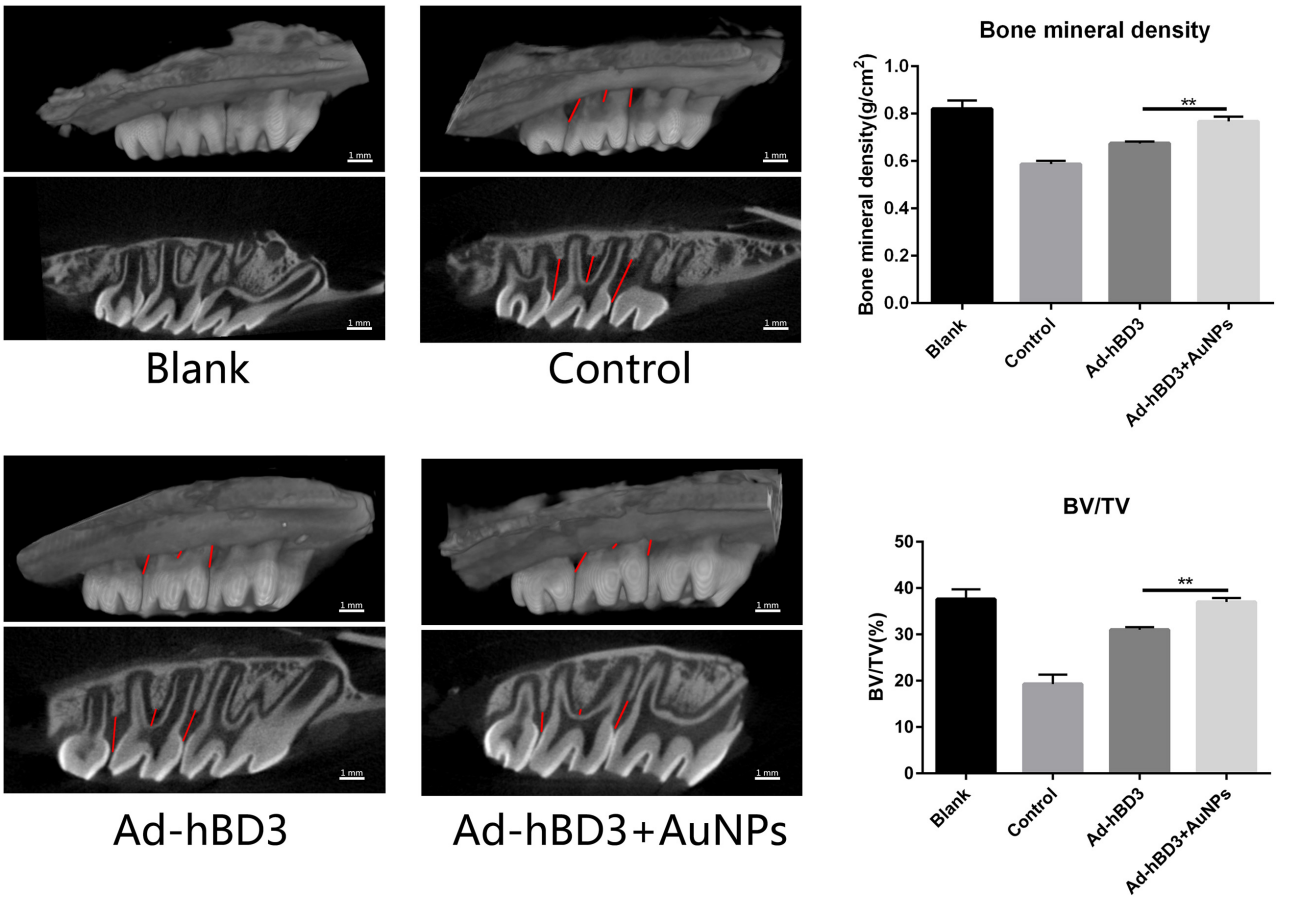

FIGURE 5 | Three-dimensional reconstruction images, bone mineral density (BMD), and the ratio of bone volume to tissue volume (BT/TV). Ad-hBD3 + AuNPs groups showed less bone loss and higher BMD and BV/TV than Ad-hBD3 groups (**$p < 0.01$).

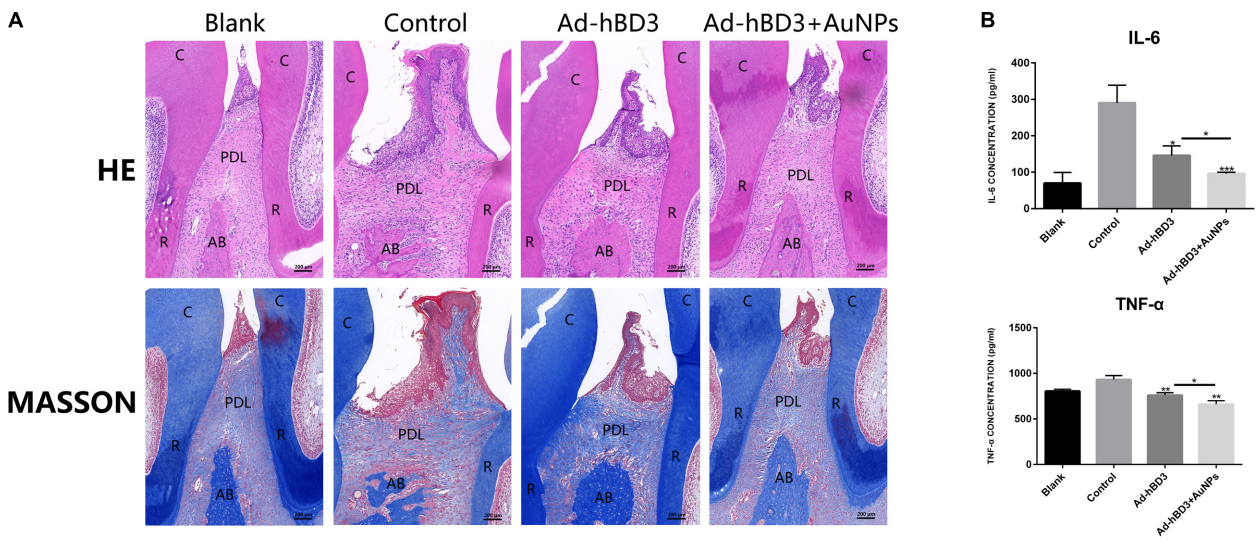

FIGURE 6 | H&E, Masson's trichrome stainings of ligatured areas and expression of inflammatory cytokine in serum. **(A)** Ad-hBD3 + AuNPs groups showed alleviative gingival inflammation and bone loss than Ad-hBD3 groups. **(B)** Ad-hBD3 + AuNPs groups showed less expression of IL-6 and TNF-α. (original magnification: ×50; scale bar 200 μm; C, crown; R, root; AB, alveolar bone; PDL, periodontal ligament; (*$p < 0.05$, **$p < 0.01$, and ***$p < 0.001$).

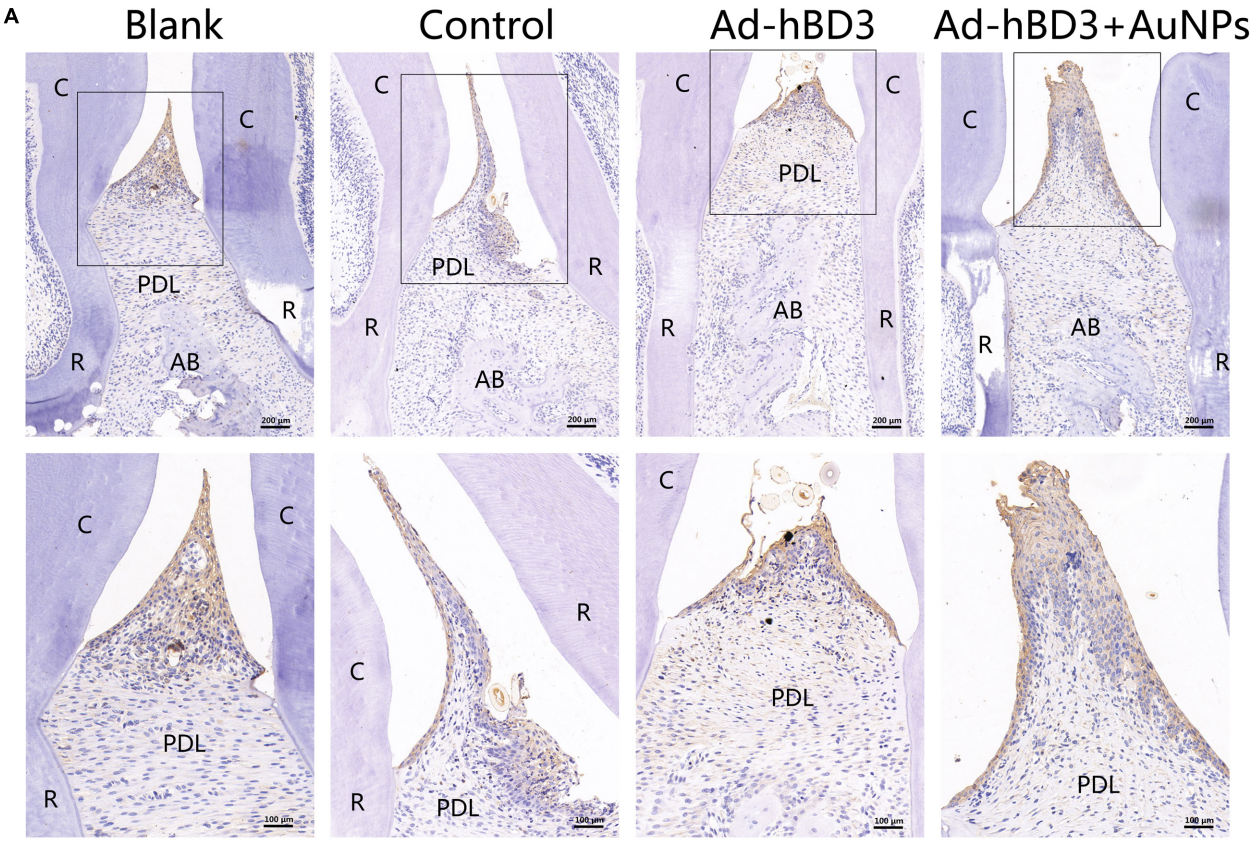

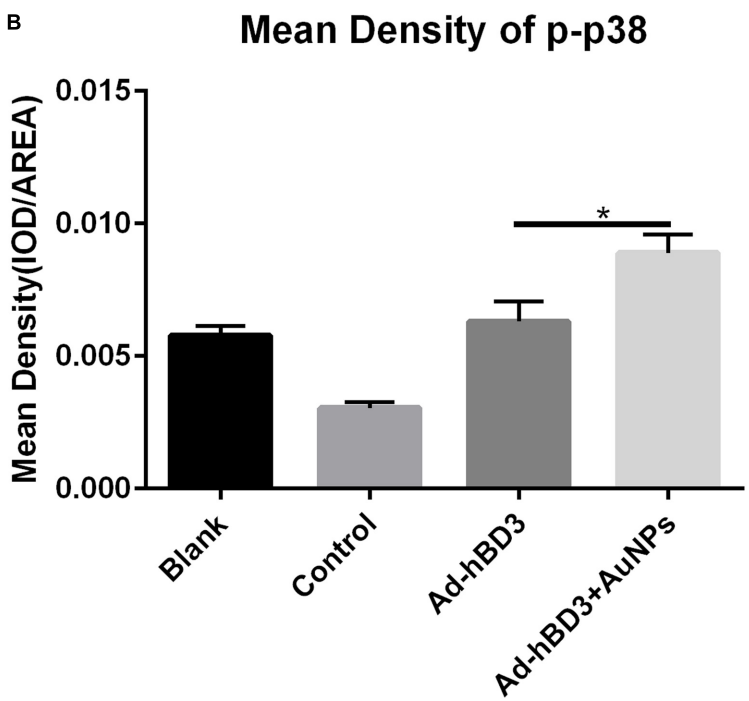

FIGURE 7 | p-p38 staining and mean density (*$p < 0.05$). **(A)** Positive expression of p-p38 in the different groups; **(B)** mean density of p-p38 expression in the different groups (original magnification of a: ×100 and ×200; scale bar 100 μm and 50 μm; R, root; AB, alveolar bone; PDL, periodontal ligament).

CONCLUSION

Our study demonstrated the enhanced effect of osteogenic differentiation while applying AuNPs into Ad-hBD3-hPDLCs and uncovered its potential mechanism *via* the p38 MAPK pathway. The *in vivo* experiments illustrated the further effects of AuNPs on tissue engineering and periodontal regeneration after transplantation of Ad-hBD3-rPDLCs. These findings suggest that AuNPs might be promising nominees in genetic engineering technology with adenoviral vectors to achieve better therapeutic effects in different diseases.

DATA AVAILABILITY STATEMENT

The datasets presented in this study can be found in online repositories. The names of the repository/repositories and accession number(s) can be found below: GenBank, accession number BankIt2403139 B3180_hBD3(EE).seqMW305475.

ETHICS STATEMENT

All animal experiments were approved by the Ethics Committee of Nanjing Stomatological Hospital, Medical School of Nanjing University. The animal experiments were conducted at the Nanjing Mergene Biotechnology Development Co., Ltd., (accreditation number: SYXK 2017-0066) according to the policies and guidelines for institutional animal care of Nanjing University, Nanjing, China.

AUTHOR CONTRIBUTIONS

LL and YZ wrote the manuscript. LL and JZ conducted the experiments. QZ and MW provided the valuable suggestions. WY, YL, and FY advised the work and modified the manuscript. All authors have approved the final version of the manuscript.

FUNDING

This work was supported by the National Natural Science Foundation Project (Nos. 81771078 and 81570982), Jiangsu Provincial Medical Innovation Team (No. CXTDB2017014), and the Nanjing Clinical Research Center for Oral Diseases (No. 2019060009).

ACKNOWLEDGMENTS

We thank the staff at the Central Laboratory of Stomatology, Nanjing Stomatological Hospital, Medical School of Nanjing University for their kind help.

REFERENCES

Alkilany, A. M., and Murphy, C. J. (2010). Toxicity and cellular uptake of gold nanoparticles: what we have learned so far? *J. Nanopart. Res.* 12, 2313–2333. doi: 10.1007/s11051-010-9911-8

Bassir, S. H., Wisitrasameewong, W., Raanan, J., Ghaffarigarakani, S., Chung, J., Freire, M., et al. (2016). Potential for stem cell-based periodontal therapy. *J. Cel Physiol.* 231, 50–61. doi: 10.1002/jcp.25067

Bindal, P., Ramasamy, T. S., Kasim, N. H. A., Gnanasegaran, N., and Chai, W. L. (2018). Immune responses of human dental pulp stem cells in lipopolysaccharide-induced microenvironment. *Cell. Biol. Inter.* 42, 832–840. doi: 10.1002/cbin.10938

Cooney, D. S., Wimmers, E. G., Ibrahim, Z., Grahammer, J., Christensen, J. M., Brat, G. A., et al. (2016). Mesenchymal stem cells enhance nerve regeneration in a rat sciatic nerve repair and hindlimb transplant model. *Sci. Rep.* 6:31306. doi: 10.1038/srep31306

Dhople, V., Krukemeyer, A., and Ramamoorthy, A. (2006). The human beta-defensin-3, an antibacterial peptide with multiple biological functions. *Biol. Biophsacta Biomech.* 1758, 1499–1512. doi: 10.1016/j.bbamem.2006.07.007

Dragnea, B., Chen, C., Kwak, E.-S., Stein, B., and Kao, C. C. (2003). Gold nanoparticles as spectroscopic enhancers for in vitro studies on single viruses. *J. Am. Chem. Soc.* 125, 6374–6375. doi: 10.1021/ja0343609

Dreaden, E. C., Alkilany, A. M., Huang, X., Murphy, C. J., and El-Sayed, M. A. (2012). The golden age: gold nanoparticles for biomedicine. *Chem. Soc. Rev.* 41, 2740–2779. doi: 10.1039/c1cs15237h

Falkner, J. C., Turner, M. E., Bosworth, J. K., Trentler, T. J., Johnson, J. E., Lin, T., et al. (2005). Virus crystals as nanocomposite scaffolds. *J. Am. Chem. Soc.* 127, 5274–5275. doi: 10.1021/ja044496m

Guo, S., Huang, Y., Jiang, Q., Sun, Y., Deng, L., Liang, Z., et al. (2010). Enhanced gene delivery and siRNA silencing by gold nanoparticles coated with charge-reversal polyelectrolyte. *ACS Nano* 4, 5505–5511. doi: 10.1021/nn101638u

Harder, J., Bartels, J., Christophers, E., and Schroder, J. M. (2001). Isolation and characterization of human beta -defensin-3, a novel human inducible peptide antibiotic. *J. Biol. Chem.* 276, 5707–5713. doi: 10.1074/jbc.m008557200

Hu, X., Zhang, Y., Ding, T., Liu, J., and Zhao, H. (2020). Multifunctional gold nanoparticles: a novel nanomaterial for various medical applications and biological activities. *Front. Bioeng. Biotech.* 8:990. doi: 10.3389/fbioe.2020.00990

Huefner, A., Septiadi, D., Wilts, B. D., Patel, I. I., Kuan, W. L., Fragniere, A., et al. (2014). Gold nanoparticles explore cells: cellular uptake and their use as intracellular probes. *Methods* 68, 354–363. doi: 10.1016/j.ymeth.2014.02.006

Jonsson, D., Nebel, D., Bratthall, G., and Nilsson, B. O. (2011). The human periodontal ligament cell: a fibroblast-like cell acting as an immune cell. *J. Periodontal. Res.* 46, 153–157. doi: 10.1111/j.1600-0765.2010.01331.x

Kalmodia, S., Harjwani, J., Rajeswari, R., Yang, W., Barrow, C. J., Ramaprabhu, S., et al. (2013). Synthesis and characterization of surface-enhanced Raman-scattered gold nanoparticles. *Int. J. Nanomed.* 8, 4327–4338. doi: 10.2147/IJN.S49447

Kittaka, M., Shiba, H., Kajiya, M., Fujita, T., Iwata, T., Rathvisal, K., et al. (2013). The antimicrobial peptide LL37 promotes bone regeneration in a rat calvarial bone defect. *Peptides* 46, 136–142. doi: 10.1016/j.peptides.2013.06.001

Kong, X., Liu, Y., Ye, R., Zhu, B., Zhu, Y., Liu, X., et al. (2013). GSK3beta is a checkpoint for TNF-alpha-mediated impaired osteogenic differentiation of mesenchymal stem cells in inflammatory microenvironments. *Biochim. Biophys. Acta* 1830, 5119–5129. doi: 10.1016/j.bbagen.2013.07.027

Kotcherlakota, R., Vydiam, K., Jeyalakshmi Srinivasan, D., Mukherjee, S., Roy, A., Kuncha, M., et al. (2019). Restoration of p53 function in ovarian cancer mediated by gold nanoparticle-based EGFR targeted gene delivery system. *ACS Biomater. Sci. Eng.* 5, 3631–3644. doi: 10.1021/acsbiomaterials.9b00006

Li, G., Han, N., Zhang, X., Yang, H., Cao, Y., Wang, S., et al. (2018). Local injection of Allogeneic stem cells from apical papilla enhanced periodontal tissue regeneration in Minipig model of Periodontitis. *Biomed. Res. Int.* 2018:3960798. doi: 10.1155/2018/3960798

Li, J., Zhang, J., Wang, X., Kawazoe, N., and Chen, G. (2016). Gold nanoparticle size and shape influence on osteogenesis of mesenchymal stem cells. *Nanoscale* 8, 7992–8007. doi: 10.1039/c5nr08808a

Li, L., Jiang, H., Chen, R., Zhou, J., Xiao, Y., Zhang, Y., et al. (2020). Human β-defensin 3 gene modification promotes the osteogenic differentiation of human

periodontal ligament cells and bone repair in periodontitis. *Int. J. Oral Sci.* 12:13. doi: 10.1038/s41368-020-0078-6

Long, H., Zhu, Y., Lin, Z., Wan, J., Cheng, L., Zeng, M., et al. (2019). miR-381 modulates human bone mesenchymal stromal cells (BMSCs) osteogenesis via suppressing Wnt signaling pathway during atrophic nonunion development. *Cell Death Dis.* 10:470. doi: 10.1038/s41419-019-1693-z

Ohashi, E., Kohno, K., Arai, N., Harashima, A., Ariyasu, T., and Ushio, S. (2019). Adenosine N1-oxide exerts anti-inflammatory effects through the PI3K/Akt/GSK-3β signaling pathway and promotes osteogenic and adipocyte differentiation. *Biol. Pharm. Bull.* 42, 968–976. doi: 10.1248/bpb.b18-00988

Pizzolato-Cezar, L. R., Okuda-Shinagawa, N. M., and Machini, M. T. (2019). Combinatory therapy antimicrobial peptide-antibiotic to minimize the ongoing rise of resistance. *Front. Microbiol.* 10:1703. doi: 10.3389/fmicb.2019.01703

Preshaw, P. M., and Bissett, S. M. (2019). Periodontitis and diabetes. *Br. Dent. J.* 227, 577–584. doi: 10.1038/s41415-019-0794-5

Ren, L., Yang, Z., Song, J., Wang, Z., Deng, F., and Li, W. (2013). Involvement of p38 MAPK pathway in low intensity pulsed ultrasound induced osteogenic differentiation of human periodontal ligament cells. *Ultrasonics* 53, 686–690. doi: 10.1016/j.ultras.2012.10.008

Saini, V., Zharov, V. P., Brazel, C. S., Nikles, D. E., Johnson, D. T., and Everts, M. (2006). Combination of viral biology and nanotechnology: new applications in nanomedicine. *Nanomedicine* 2, 200–206. doi: 10.1016/j.nano.2006.07.002

Shen, X., Al-Baadani, M. A., He, H., Cai, L., Wu, Z., Yao, L., et al. (2019). Antibacterial and osteogenesis performances of LL37-loaded titania nanopores in vitro and in vivo. *Int. J. Nanomed.* 14, 3043–3054. doi: 10.2147/ijn.s198583

Sirotkin, S., Mermet, A., Bergoin, M., Ward, V., and Etten, J. L. V. (2014). Viruses as nanoparticles: structure versus collective dynamics. *Phys. Rev. E Statis. Nonlinear Soft Math. Phys.* 90:022718.

Taut, A. D., Jin, Q., Chung, J. H., Galindo-Moreno, P., Yi, E. S., Sugai, J. V., et al. (2013). Sclerostin antibody stimulates bone regeneration after experimental periodontitis. *J. Bone Miner. Res.* 28, 2347–2356. doi: 10.1002/jbmr.1984

Vila, T., Rizk, A. M., Sultan, A. S., and Jabra-Rizk, M. A. (2019). The power of saliva: antimicrobial and beyond. *PLoS Pathol.* 15:e1008058. doi: 10.1371/journal.ppat.1008058

Wang, H., Watanabe, H., Ogita, M., Ichinose, S., and Izumi, Y. (2011). Effect of human beta-defensin-3 on the proliferation of fibroblasts on periodontally involved root surfaces. *Peptides* 32, 888–894. doi: 10.1016/j.peptides.2011.02.002

Wang, Y. F., Pang, D. W., Zhang, Z. L., Zheng, H. Z., Cao, J. P., and Shen, J. T. (2003). Visual gene diagnosis of HBV and HCV based on nanoparticle probe amplification and silver staining enhancement. *J. Med. Virol.* 70, 205–211. doi: 10.1002/jmv.10379

Weng, Z., Wang, H., Vongsvivut, J., Li, R., Glushenkov, A. M., He, J., et al. (2013). Self-assembly of core-satellite gold nanoparticles for colorimetric detection of copper ions. *Anal. Chim. Acta* 803, 128–134. doi: 10.1016/j.aca.2013.09.036

Wu, Y., Yang, Y., Yang, P., Gu, Y., Zhao, Z., Tan, L., et al. (2013). The osteogenic differentiation of PDLSCs is mediated through MEK/ERK and p38 MAPK signalling under hypoxia. *Arch. Oral Biol.* 58, 1357–1368. doi: 10.1016/j.archoralbio.2013.03.011

Xiang, Z., Wang, K., Zhang, W., Teh, S. W., Peli, A., Mok, P. L., et al. (2018). Gold nanoparticles inducing osteogenic differentiation of stem cells: a review. *J. Clust. Sci.* 29, 1–7. doi: 10.1007/s10876-017-1311-0

Yi, C., Liu, D., Fong, C.-C., Zhang, J., and Yang, M. (2010). Gold nanoparticles promote osteogenic differentiation of mesenchymal stem cells through p38 MAPK pathway. *ACS Nano* 4, 6439–6448. doi: 10.1021/nn101373r

Yi, S. W., Park, J. S., Kim, H. J., Lee, J. S., Woo, D. G., and Park, K.-H. (2019). Multiply clustered gold-based nanoparticles complexed with exogenous pDNA achieve prolonged gene expression in stem cells. *Theranostics* 9, 5009–5019. doi: 10.7150/thno.34487

Zhang, Y., Kong, N., Zhang, Y., Yang, W., and Yan, F. (2017). Size-dependent effects of gold nanoparticles on osteogenic differentiation of human periodontal ligament progenitor cells. *Theranostics* 7, 1214–1224. doi: 10.7150/thno.17252

Zharov, V. P., Kim, J. W., Curiel, D. T., and Everts, M. (2005). Self-assembling nanoclusters in living systems: application for integrated photothermal nanodiagnostics and nanotherapy. *Nanomedicine* 1, 326–345. doi: 10.1016/j.nano.2005.10.006

Zhou, J., Zhang, Y., Li, L., Fu, H., Yang, W., and Yan, F. (2018). Human & beta;-defensin 3-combined gold nanoparticles for enhancement of osteogenic differentiation of human periodontal ligament cells in inflammatory microenvironments. *Int. J. Nanomed.* 13, 555–567. doi: 10.2147/ijn.s150897

Conflict of Interest: The authors declare that the research was conducted in the absence of any commercial or financial relationships that could be construed as a potential conflict of interest.

frontiers in Bioengineering and Biotechnology

ORIGINAL RESEARCH
published: 17 February 2021
doi: 10.3389/fbioe.2021.632029

Enhanced Cells Anchoring to Electrospun Hybrid Scaffolds With PHBV and HA Particles for Bone Tissue Regeneration

Joanna E. Karbowniczek, Łukasz Kaniuk, Krzysztof Berniak, Adam Gruszczyński and Urszula Stachewicz**

Faculty of Metals Engineering and Industrial Computer Science, AGH University of Science and Technology, Kraków, Poland

Hybrid materials combining organic and inorganic compounds used as scaffolds are highly beneficial in bone regeneration. In this study, we successfully produced by blend electrospinning poly(3-hydroxybutyric acid-co-3-hydrovaleric acid) (PHBV) scaffolds enriched with hydroxyapatite (HA) particles to biomimic bone tissue for improved and faster regeneration processes. The morphology, fiber diameters, and composition of the scaffolds were investigated by scanning electron microscopy (SEM) techniques followed by focused ion beam (FIB) sectioning to verify HA particles integration with PHBV fibers. *In vitro* cell culture was performed for 7 days and followed with the cell proliferation test (CellTiter-Blue® Assay). Additionally, cell integration with the scaffold was visualized by confocal and SEM imaging. We developed a simple way of obtaining hybrid scaffolds by electrospinning PHBV solution with HA particles without any post-processing. The PHBV + HA scaffold enhanced cell proliferation and filopodia formation responsible for cell anchoring within the created 3D environment. The obtained results show the great potential in the development of hybrid scaffolds stimulating bone tissue regeneration.

Keywords: electrospinning, fibers, PHBV, hydroxyapatite (HA), tissue scaffold, bone regeneration, confocal microscopy, FIB-SEM

OPEN ACCESS

Edited by:
Kai Zheng,
University of Erlangen-Nuremberg, Germany

Reviewed by:
Yaping Ding,
University of Helsinki, Finland
Liliana Liverani,
University of Erlangen-Nuremberg, Germany

****Correspondence:***
Joanna E. Karbowniczek
jkarbow@agh.edu.pl
Urszula Stachewicz
ustachew@agh.edu.pl

Specialty section:
This article was submitted to Biomaterials, a section of the journal Frontiers in Bioengineering and Biotechnology

Received: *21 November 2020*
Accepted: *21 January 2021*
Published: *17 February 2021*

Citation:
Karbowniczek JE, Kaniuk Ł, Berniak K, Gruszczyński A and Stachewicz U (2021) Enhanced Cells Anchoring to Electrospun Hybrid Scaffolds With PHBV and HA Particles for Bone Tissue Regeneration. Front. Bioeng. Biotechnol. 9:632029. doi: 10.3389/fbioe.2021.632029

INTRODUCTION

The tissue regeneration process is strongly dependent on cell interaction with the materials used as a scaffold to enhance their growth and development. A widely exploited approach of tissue engineering aims to create functional structures in laboratory conditions that after implantation will replace, restore, or improve the functions of damaged or diseased organs. For this purpose, it combines cells, scaffolds, and signals in the form of growth factors or structural, mechanical, and electrical stimuli (Cassidy and Cartmell, 2013; Salinas et al., 2018). Designing the proper scaffold for each tissue type is crucial as it creates the whole microenvironment where cellular development takes place (Stevens and George, 2005). Bone tissue is a complex structure with a hierarchical arrangement of extracellular matrix (ECM) built of collagen type I and hydroxyapatite (HA) crystals. The presence of inorganic compounds ensures high strength, hardness, and rigidity essential for bones, whereas organic compounds provide flexibility and the reduction of brittleness (Alford et al., 2015). Altogether the structure and composition of ECM support the dynamic processes of bone formation and resorption during growth, remodeling, and healing

(Filippi et al., 2020). To mimic the bone structure often hybrids or composite scaffolds, combining organic and inorganic components are prepared. This biomimetic approach in producing hybrid scaffolds has gained much attention over the last few years (Xing et al., 2019; Lyons et al., 2020). Therefore, various types of natural and synthetic polymers are studied in combination with bioactive ceramics to create osteoconductive scaffolds (Filippi et al., 2020; Lyons et al., 2020).

Highly porous composite scaffolds were prepared by different methods, e.g., solvent casting-particulate leaching (Baek et al., 2012; Wu et al., 2017), 3D printing (Huang et al., 2018), sponge replication followed by dip coating (Thomas and Bera, 2020), phase inversion technique (Podporska-Carroll et al., 2014), electrospinning (Suslu et al., 2014), and a combination of electrospinning and electrospraying (Ramier et al., 2014). Among these listed techniques electrospinning is especially interesting as it allows for the production in single-step hybrid meshes from a mixed polymer solution and ceramic particles. Therefore, in a simple, fast, and cost-effective way, it is possible to obtain suitable scaffolds for cardiac tissue engineering (Mani et al., 2019), neural guidance (Farzamfar et al., 2019), diabetic wound healing (Augustine et al., 2020), and bone regeneration (Bai et al., 2015; Sadat-Shojai, 2016; Kouhi et al., 2018).

The goal of producing hybrid scaffolds mimicking the ECM of bone is to obtain a supportive structure with tailored mechanical and surface properties. By using exposed bioactive compounds in the scaffolds we are able to promote cell anchoring and adhesion for further tissue development. Another aspect is related to material selection such as a piezoelectric polymer that can better biomimic bone tissue properties. The most studied piezoelectric polymers are poly(vinylidene fluoride) (PVDF) (Szewczyk et al., 2019a,b), poly(L-lactide) (PLLA), and poly(3-hydroxybutyric acid-co-3-hydrovaleric acid) (PHBV) (Lyons et al., 2020). Adding HA particles to bone tissue scaffolds (Fernandez-Yague et al., 2015; Yi et al., 2016) is often combined with piezoelectric and biodegradable polymers (Sultana and Wang, 2008). Apart from the most wildly studied bone scaffold material, polycaprolactone (PCL), another highly biocompatible material with desirable degradation time frames is PHBV (Chen and Wu, 2005). Previously, hybrid scaffolds based on PHBV electrospun fibers were immersed in simulated body fluids (SBF) for HA deposition (Ito et al., 2005), or directly prepared by electrospinning the suspension containing both the polymer and ceramic particles (Tong et al., 2010; Paşcu et al., 2013; Kouhi et al., 2015; Brunetti et al., 2020). Various properties of such scaffolds were studied, including: degradation (Ito et al., 2005), bioactivity and mechanical properties (Paşcu et al., 2013; Kouhi et al., 2015) as well as *in vitro* biocompatibility (Tong et al., 2010). These studies showed a high potential of hybrid scaffolds based on electrospun PHBV fibers with HA particles for tissue engineering.

Our unique studies take a single-step approach by electrospinning PHBV mixed with HA particles including the direct characterization of particle distribution within fibers and scaffolds by using advanced microscopy techniques. Therefore, in this study, we aimed to prove that hybrid scaffolds based on electrospun PHBV fibers enriched with HA particles enhance bone regeneration processes better in comparison to solely PHBV scaffolds. Morphology, fiber diameters, and composition of the scaffolds were investigated by scanning electron microscopy (SEM) techniques followed by focused ion beam (FIB) sectioning to expose fiber interiors, providing an excellent approach to show the incorporation of HA particles inside the PHBV fibers and their presence on the fibers' surface. *In vitro* osteoblasts culture was incubated for 7 days to verify their proliferation with a CellTiter-Blue® Assay. Additionally, cell integration with the scaffold was visualized by confocal and SEM imaging. We confirmed the beneficial effect of hybrid scaffolds on osteoblasts adhesion, spreading, proliferation, and filopodia formation through a combination of fibers' topography and composition.

MATERIALS AND METHODS

Materials and Scaffolds Preparation

Poly(3-hydroxybutyric acid-co-3-hydrovaleric acid) (PHV content 2 wt%, M_w = 450,000 g·mol^{-1}, Helian Polymers, Netherlands) was dried before solution preparation for 4 h at 40°C. Two types of solutions were prepared: 8% PHBV and a blend of 8% PHBV with 1% of HA (particles size <200 nm, Sigma-Aldrich, United Kingdom). For the PHBV solution, 8 wt% of the polymer was dissolved in a chloroform and dimethylformamide (DMF) mixture (9:1, v/v, both solvents Sigma-Aldrich, United Kingdom). For the solution PHBV+HA, 0.1 g of HA particles were dispersed in the chloroform:DMF (9:1 v/v) mixture in an ultrasonic bath (Bandelin, Germany) for 10 min, and subsequently, 0.8 g of PHBV was added. Both solutions were stirred on a heated magnetic stirrer (IKA, Germany) for 4 h at 45°C until complete dissolution of the polymer. The solution containing nanoparticles was again ultrasonicated for 10 min prior to electrospinning. Both solutions were electrospun using an EC-DIG device with a climate control system (IME Technologies, Netherlands) at 25°C and RH = 40%. A voltage of 17 kV was applied to the stainless needle with an inner diameter of 0.8 mm, keeping a 20 cm distance to the grounded collector, the flow rate was 0.1 ml·min^{-1} for both solutions. Two types of scaffolds were produced: solely polymer - named PHBV, and the hybrid, which combines polymer and ceramic – named PHBV + HA.

Scaffolds Characterization

To study the morphology of the PHBV and PHBV + HA scaffolds, samples were imaged by scanning electron microscopy (SEM, Merlin Gemini II, Zeiss, Germany) at 2 kV, 100 pA, and a working distance (WD) in the range of 5–8 mm, using a secondary electrons (SE) detector. Prior to SEM observations, all samples were coated with a 5-nm Au layer using a rotary pump sputter coater (Q150RS, Quorum Technologies, United Kingdom). The average fiber diameters (D_f) were measured from 100 fibers from SEM images using the ImageJ software (v. 1.51j8, United States), see histograms presented in **Figure 1**. Additionally, we used SEM images to estimate the spacings between fibers in scaffolds based on 10 measurements. The incorporation of HA particles into the PHBV fibers was

confirmed by energy dispersive X-ray spectroscopy (EDS) using an detector (Brucker, Germany). EDS imaging and maps were done at 7 kV, 500 pA, WD = 8 mm, and a collecting time of 30 min. The merged images of the SE signal with a distribution of carbon (C), calcium (Ca), and phosphorous (P) can be seen in **Figure 2**. Additionally, individual fibers of the PHBV + HA sample were sliced by a focused ion beam (FIB) at 30 kV and 50 pA using a NEON CrossBeam 40EsB (Zeiss, Germany). The exposed fiber cross-section was imaged by a energy selective backscattered (EsB) detector, at 3 kV, 50 pA, and WD = 5 nm.

Cell Culture

The *in vitro* studies were performed on both types of samples (PHBV and PHBV + HA) using human osteoblast-like cell line MG-63 (Sigma-Aldrich, United Kingdom). Samples were cut into 15-mm diameter circles, placed in 24-well plates, and sterilized for 30 min in UV light. Cells were seeded in the scaffolds at a concentration of 2×10^4 cells per 1 ml in culture media containing Dulbecco's Modified Eagle Medium supplemented with 10% fetal bovine serum (FBS), 2% antibiotics (penicillin/streptomycin), 1% amino acids, and 1% L-glutamine (all reagents Sigma-Aldrich, United Kingdom). Samples with cells were incubated in 37°C, 90% humidity, and 5% CO_2 atmosphere for up to 7 days. The medium was replaced every 2 days.

Cell Viability

Cell proliferation was evaluated using the CellTiter-Blue® Assay (Promega, United States) after 1, 4, and 7 days of incubation, tissue culture polystyrene (TCPS) was used as control. At each time point media was replaced with 1 ml of media containing 10% of CellTiter-Blue® reagent and incubated for 4 h at 37°C. From each well, 100 μm of reagent was transferred to a 96-well plate in triplicates and fluorescence was read at 560/590 nm using the microplate reader GloMax® Discover System (Promega, United States).

Cell Imaging: Confocal and SEM

After 1, 4, and 7 days of cell growth, one sample of the PHBV and PHBV + HA scaffolds were fixed with 4% paraformaldehyde (Sigma-Aldrich, United Kingdom) for 30 min. The samples were washed three times with phosphate-buffered saline (PBS, Biomed Lublin, Poland) before and after application of a fixative. Subsequently, samples were incubated in 0.1% Triton X-100 for 5 min, followed by washing in PBS and next incubated in 3% bovine serum albumin (BSA, Sigma-Aldrich, United Kingdom) for 30 min. After washing in PBS, the samples were incubated for 1 h in Alexa Fluor™ 488 Phalloidin (1:400, Thermo Fisher Scientific, United States), then washed three times in PBS and finally stained with DAPI (Sigma-Aldrich, United Kingdom) for 5 min (1:1000) and again washed three times with PBS. The images were acquired using a Zeiss LSM 900 confocal microscope (Zeiss, Germany). In all the experiments, the Plan-Apochromat 63x/1.4 Oil DIC M27 objective was used. Imaging was performed using the 405 nm or 488 nm or 633 nm laser lines for exciting DAPI, Alexa Fluor™ 488, and PHBV fibers, respectively. The z-stacks were recorded with the 0.4 μm step.

Cells on PHBV and composite PHBV + HA scaffolds were fixed after 1, 4, and 7 days of growth with 2.5% glutaraldehyde (Sigma Aldrich, United Kingdom) for 1 h at 4°C. Afterward, they were washed three times with PBS and dehydrated in series of ethanol (Avantor, Poland) solutions, with increasing amounts of alcohol (50, 70, 90, and 100%). Each sample was incubated in each ethanol solution for 5 min and twice in the 100% solution, followed by incubation in HMDS (Sigma-Aldrich, United Kingdom) under a fume hood until the complete evaporation of the solvent. The samples were mounted in Al holders by carbon tape and gold-sputtered with a 5 nm layer. Samples were imaged by SEM, with the settings previously described for scaffolds characterization.

Statistics

Statistical analysis of cell proliferation was done using one-way Analysis of variance (ANOVA) followed by Tukey's *post hoc* test in Origin Pro (ver. 2020b, United States). Differences were considered statistically significant when $p < 0.05$.

RESULTS

Scaffold Characterization

From electrospinning, we obtained randomly oriented fibers with an average diameter of 2.92 ± 0.28 μm for PHBV and 3.76 ± 0.37 μm for PHBV + HA, see **Figure 1**. The electrospun PHBV fibers were characterized by smooth morphology, with few porous fibers in the network (**Figures 1A,B**). Whereas, the addition of HA particles caused a 30% increase in fiber diameter, and fibers' morphology was more porous and rougher (**Figures 1D,E**). The large diameter of fibers created large spacing between individual fibers, in many cases exceeding 40 μm (see **Figure 1D**), allowing us to obtain a 3D scaffold with a highly porous structure.

The presence of HA particles was confirmed by the EDS mapping as well as imaging with the EsB detector at the fiber cross-section. HA particles were uniformly distributed within the scaffold structure, both on the surface of fibers (**Figures 1E**, **2**) and inside fibers (**Figure 3**). They tended to form local aggregates as can be seen in the high magnification image in **Figure 2A**. Via EDS mapping (**Figure 2**), we confirmed that particles visible in the SEM images were composed of Ca and P (main elements of HA), whereas the main component of the fibers was carbon. Imaging with the EsB detector provided compositional contras where variation in grayscale within the sample structure allowed for the identification of different compounds. Therefore, bright spots visible inside the fiber (**Figure 3B**) can be identified as HA particles, since Ca and P are heavier elements than C which is found in the PHBV fibers. Particles near to the fiber border change the morphology from mostly smooth, this was observed for PHBV fibers, to highly irregular and porous fibers observed for the PHBV + HA scaffold, see **Figures 1B,E**. Multiple small, surface pores with a diameter below 100 nm were present along the hybrid fibers. Additionally, we noticed larger pores inside the PHBV + HA fibers with sizes up to 500 nm (**Figure 3B**).

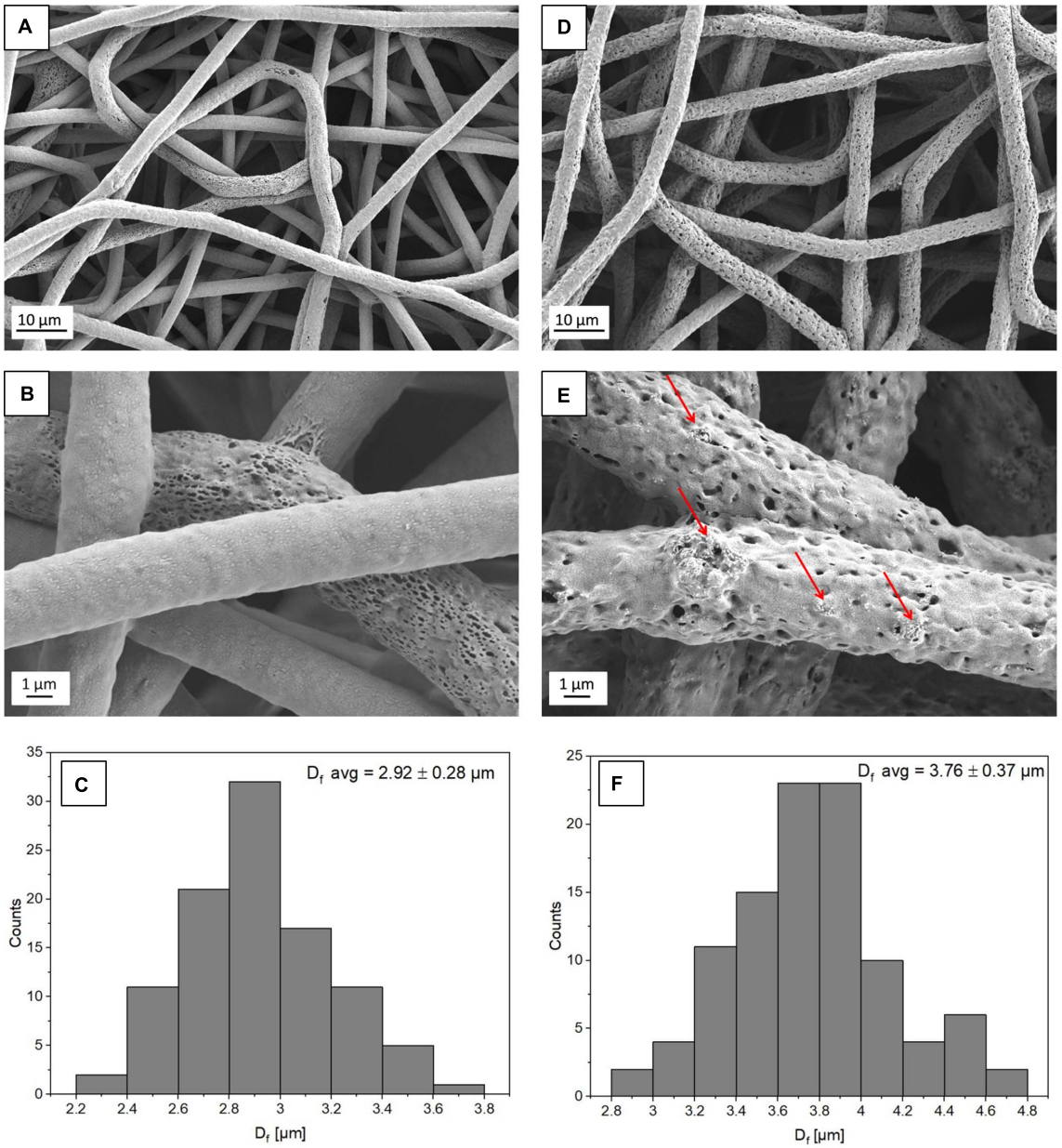

FIGURE 1 | SEM micrographs showing the morphology of **(A,B)** PHBV fibers and **(D,E)** PHBV + HA hybrids. The red arrows indicate HA particles; **(C,F)** histograms indicate the fiber diameter distribution for PHBV fibers and PHBV with HA fibers, respectively.

Cell Culture

Using a CellTiter-Blue® assay we could monitor cells proliferation over 7 days of incubation on PHBV and PHBV + HA scaffolds and control surface of TCPS, see **Figure 4**. This assay contains high purity dark blue resazurin, which is reduced by viable cells to pink resorufin. The fluorescent signal is proportional to the number of viable cells. After 1 day of cell incubation, the number of cells was at the same level with no statistically significant difference, for PHBV and PHBV + HA scaffolds. However, a significantly higher number was found in the TCPS control. Notably, cells required more time to attach and multiply in the 3D structure of both scaffolds while the flat surface of modified PS was specially prepared to favor cell growth. After 4 days of incubation, we observed a high proliferation of cells on TCPS and only moderate proliferation on both scaffolds. After 7 days, a higher number of cells on the PHBV + HA scaffold compared to the PHBV scaffold and control was detected. In the control sample after this time, cells occupied all available surfaces, so their multiplication was slowed down; while the 3D structure of the PHBV + HA scaffolds provided much more space for cells to grow and spread.

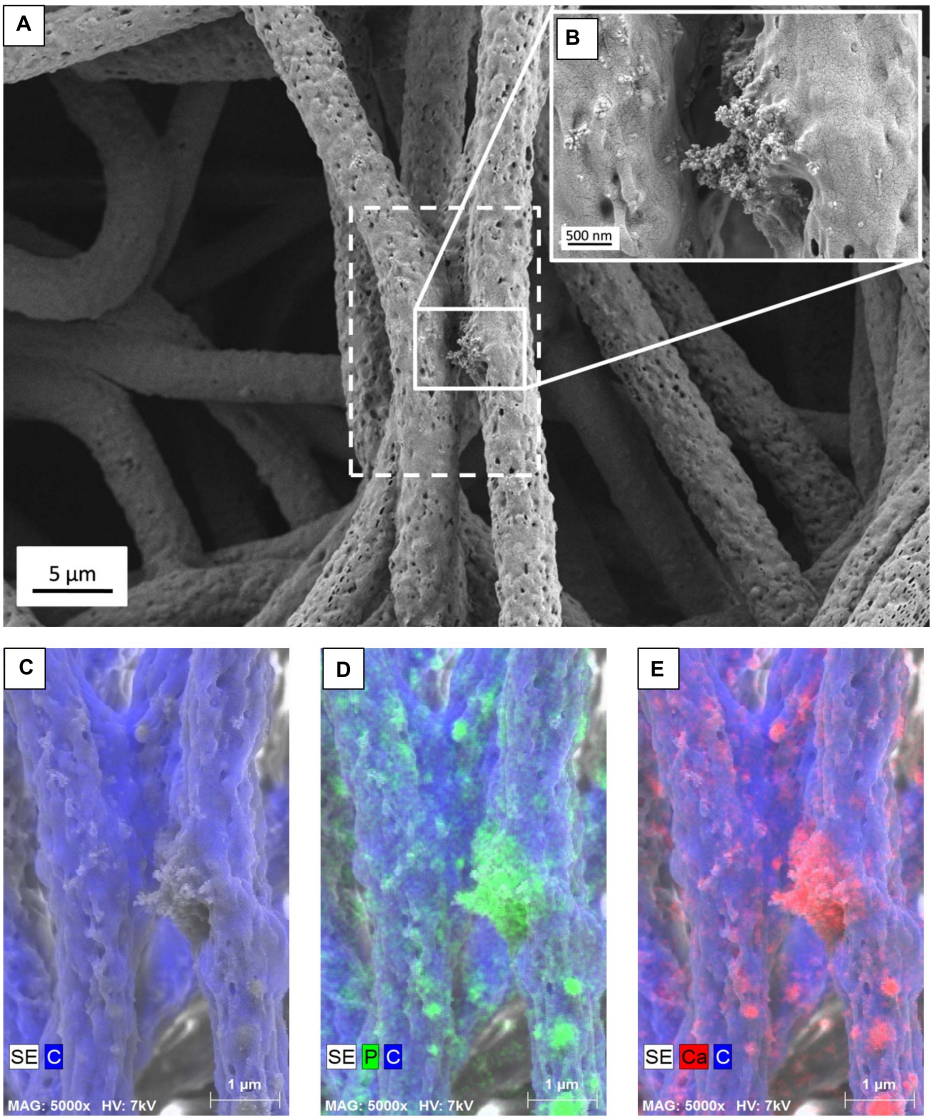

FIGURE 2 | (A) SEM micrograph of PHBV + HA fibers with the area of EDS mapping marked with a dashed line, **(B)** Inset image showing magnified area of HA particles, **(C)** SE image with C distribution, **(D)** SE image with C and P distribution, **(E)** SE image with C and Ca distribution.

Our confocal microscopy observations confirmed the results of the proliferation test, showing constant multiplication of cells (an increase of their number) on both tested materials over the incubation period, see **Figure 5**. Additionally, a higher cell number was observed on the PHBV + HA scaffolds at each time point (**Figures 5D–F**). In **Figure 5**, we show only the actin fiber staining corresponding to cell spreading and relative quantity over a large imaging area. In the Supporting Information file, we provide a similar figure including the autofluorescence from PHBV fibers, see **Supplementary Figure 1**.

Figure 6 presents the morphology of cells growing on PHBV and PHBV + HA scaffolds. Using the laser with a wavelength of 633 nm, we observed the autofluorescence of PHBV fibers. Therefore, while performing confocal imaging we could also include fibers in the images, allowing us to observe the arrangements of the cells in the context of the 3D scaffold structure. After 1 day of incubation, the cells were mainly round in shape, but starting to form some filopodia to reach adjacent fibers, especially in the PHBV + HA scaffold. After 4 days, the cell shape become elongated, osteoblasts were reaching distant fibers, and in many cases, overlapping them. The increased number of filopodia allowed cells to explore the 3D scaffolds' structure and create cell-to-cell interactions. After 7 days, many more cells were visible within the imaging area (see **Figure 6F**). They tended to be stretched along fibers; however, they were also forming multiple connections and filopodia in all directions. In the case of the PHBV + HA scaffold, we could observe cells forming long structures above 40 µm in length to communicate with each other.

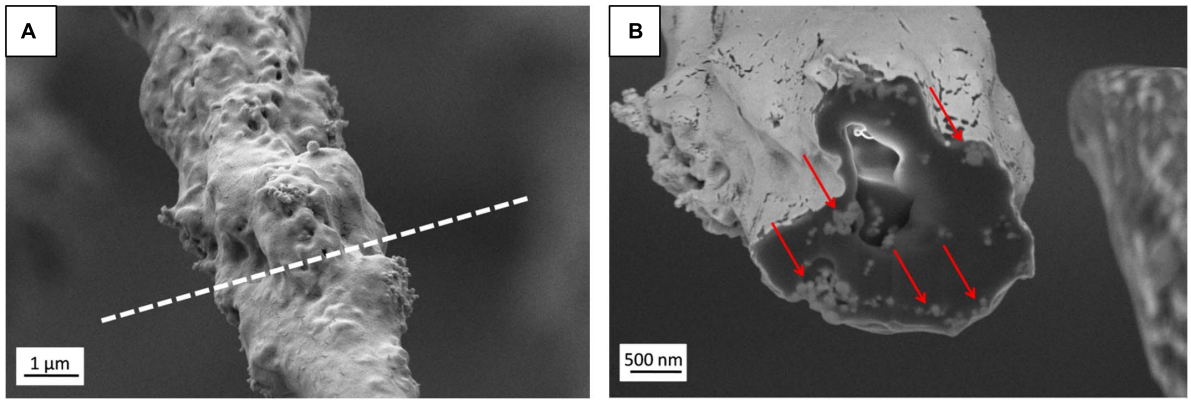

FIGURE 3 | (A) SEM micrograph (SE detector) of individual PHBV + HA fiber with the region of FIB cutting marked by a dashed line, **(B)** Image of fiber cross-section (EsB detector) with HA particles indicated by red arrows.

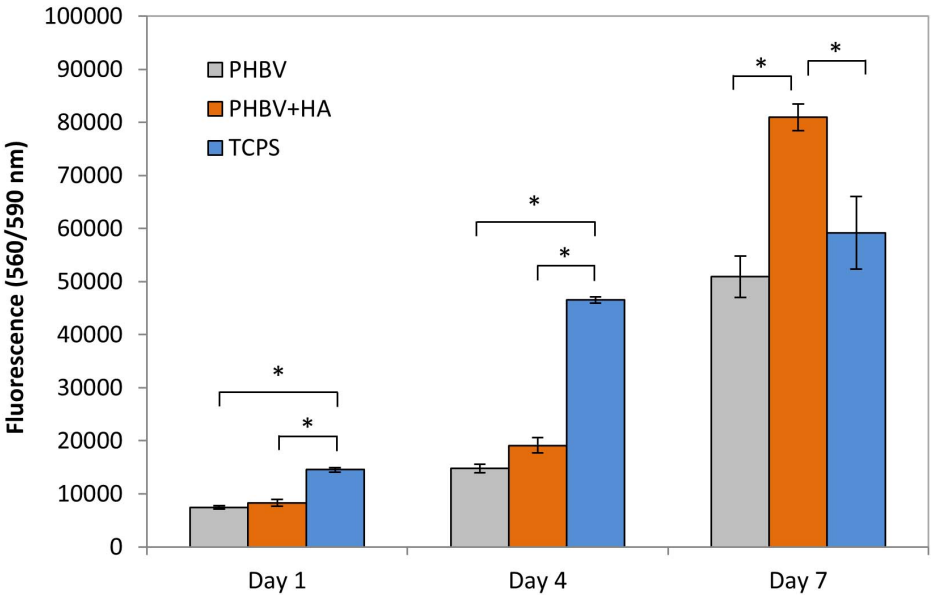

FIGURE 4 | Cell proliferation based on a CellTiter-Blue® assay. *statistical significance calculated with ANOVA followed by Tukey's post hock tests, $p < 0.05$.

Figure 7 shows the representative z-stacks showing cell integration with PHBV + HA scaffolds after 4 and 7 days of incubation. Z-stacks in confocal microscopy enable the collection of a series of consecutive images to study the whole cell structure with all protrusions, also reaching deep into the scaffold structure. In the case of cells growing on flat surfaces, like glass slides or TCPS, they create focal adhesion points and explore the environment in one horizontal plane. Whereas, cells growing on 3D scaffolds make connections in all possible directions, especially if the porosity allows them to migrate inside the material. In the case of the example osteoblasts growing on the PHBV + HA scaffold for 4 days (**Figure 7A**), the main cell body was located between three neighboring, intersecting fibers and the cell formed multiple filopodia to attach and sense them. Imaging deeper into the scaffold structure, we could observe that the cell was additionally forming an approximate 30-µm long attachment to another fiber. Therefore, the osteoblast was reaching 19.2 µm into the depth of the PHBV + HA scaffold. After 7 days of incubation, cell proliferation on the PHBV + HA scaffold was very high, therefore, multiple daughter cells close to each other were detected, see **Figure 7B**. Osteoblasts were mostly growing along the hybrid fibers, however, they created multiple adhesions to other nearby fibers. The whole structure shows that cells were intertwined between the fibers attaching to them from all directions. As we moved deeper into the PHBV + HA scaffold more osteoblasts were visible in the center and left bottom of the imaged area, see **Figure 7B**. This z-stack covers the thickness of 13.6 µm, but more cells were present below and above the imaged volume.

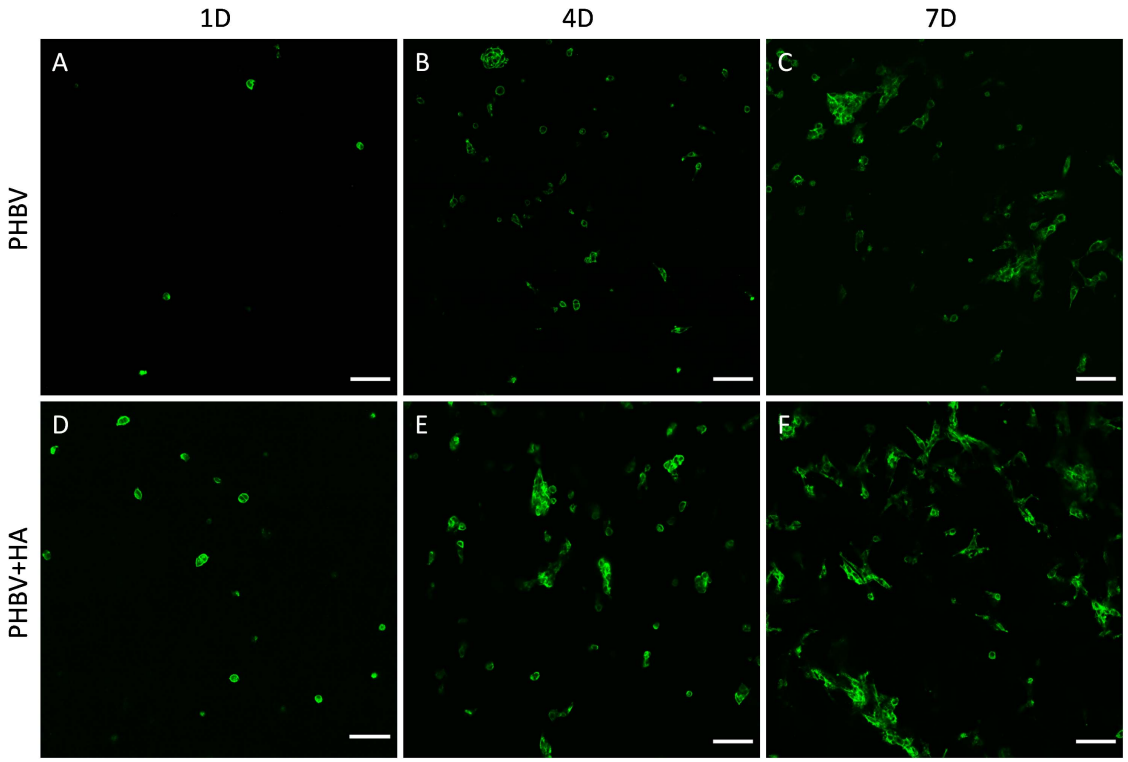

FIGURE 5 | Confocal images of cell spreading on **(A–C)** the PHBV and **(D–F)** PHBV + HA scaffolds after 1, 4, and 7 days (1D, 4D, and 7D) of incubation, actin fibers stained with Alexa Fluor™ 488 Phalloidin (green), scale bar 100 μm.

Additionally, SEM imaging was performed to reveal in great detail the cell integration with electrospun scaffolds, and to verify cell adaptation to variation in the surface morphology of fibers. The interactions at the interfaces between fibers and osteoblasts growing for 7 days in the PHBV and PHBV + HA scaffolds are shown in **Figure 8**. Cells that grew on smooth PHBV fibers were spreading between and adhering to many surrounding fibers (**Figure 8A**). Often cells were overlapping PHBV fibers with filopodia, see **Figure 8B**. From the microscopy observation, we noticed that cells on the PHBV + HA fibers were elongated reaching more distant fibers than those on PHBV fibers, as well as perfectly occupying small spaces in between fibers, see **Figure 8C**. Importantly, the rough and porous surface of PHBV + HA fibers with exposed ceramic particles provided multiple anchoring points for cells and encouraged the formation of sensing filopodia which are visible in **Figure 8E**. Moreover, we observed much more deposits and fibrils on the surface of cells growing on the PHBV + HA scaffold (**Figures 8C,D**) compared to solely polymer fibers (**Figures 8A,B**). These collagen fibrils are typical for an early stage of ECM formation (Metwally et al., 2019). In this study, both types of PHBV electrospun scaffolds were highly porous with large spacing between fibers. Therefore, while seeding cells only a few of them attached to the topmost fibers, whereas the majority fell deeper and attached, spread, and proliferated throughout. This has been proven by deep confocal imaging inside the scaffolds' structures as presented in **Figure 7**. Additionally, with FIB-SEM, by slicing the samples we could visualize the cross-section of cell integration in between the PHBV + HA fibers, see **Figure 9**. The imaged cell was perfectly stretched along the fibers as shown in **Figure 9A**, but it formed an additional anchoring point using the small gap between fibers' crossing as indicated by the higher magnification SEM micrograph in **Figure 9B**.

DISCUSSION

Scaffold Characterization

We successfully produced two types of scaffolds with two distinct morphologies affecting the cell spreading, adhesion, and proliferation. The obtained diameter of PHBV fibers was close to the value of 2.79 ± 0.2 μm, as previously reported (Kaniuk et al., 2020). The morphology and size of fibers prepared via electrospinning were affected by the polymer solution, environmental conditions, and applied electric field (Krysiak et al., 2020; Szewczyk et al., 2020). It was followed by mechanical (Ura et al., 2020) and surface properties (Metwally et al., 2020). Therefore, PHBV-based scaffolds described in Suslu et al. (2014) had significantly smaller diameters of 571 ± 160 nm compared to our study, however, similarly, they obtained increased fiber diameter with the addition of HA particles. The addition of an inorganic filler can cause either an increase or decrease in electrospun fiber diameter depending on particle size as well as the viscosity and conductivity of

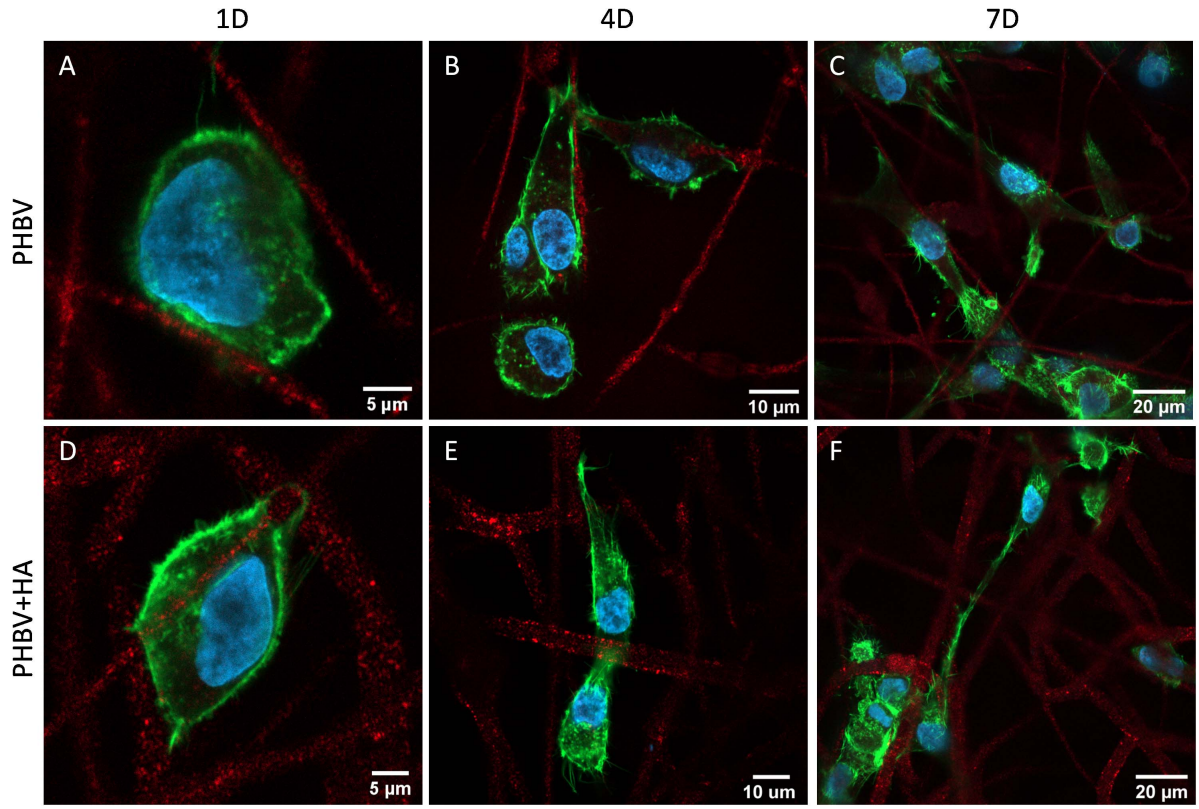

FIGURE 6 | Confocal images showing cell morphology on **(A–C)** the PHBV and **(D–F)** PHBV + HA scaffolds after 1, 4, and 7 days (1D, 4D, and 7D) of incubation; nucleus stained with DAPI (blue); actin fibers stained with Alexa Fluor™ 488 Phalloidin (green); autofluorescence of PHBV fibers (red).

suspension. Augustine et al. (2020) observed a slight decrease of fiber diameter compared to solely polymer fibers for fibers containing PHBV and CeO_2 nanoparticles (diameter below 10 nm). However, the described results were flawed by a large error as the standard deviations were near or higher than average values. Whereas, Kouhi et al. (2015, 2018) reported a slight increase in fiber diameter for electrospun composites of PHBV-bredigite as well as PHBV + HA compared to PHBV scaffolds (bredigite particle size was 25 nm and HA 23 nm). Different findings were described by Paşcu et al. (2013) for PHBV fibers with HA nanoparticles. Fibers electrospun from 15% PHBV solution had diameters over 9 µm, whereas after adding 5% of HA to the polymer solution the resulting fiber diameter was three times higher and reached over 18 µm. Porous fibers are most often obtained by the careful selection of solvents as well as high humidity during electrospinning due to phase separation (Metwally et al., 2020; Szewczyk and Stachewicz, 2020). A different approach was described by Lyu et al. (2016) for blended PHB with polyethylene oxide (PEO) fibers followed by immersion in SBF for 4 weeks causing PEO leaching and pore formation on fibers. In the case of our electrospun PHBV fibers, the porosity was caused by the vapor-induced phase separation (VIPS) (Huang and Thomas, 2020; Szewczyk and Stachewicz, 2020), which was enhanced by the addition of hygroscopic HA particles, which was also observed and described for electrospun PHBV with the addition of PLLA (Wagner et al., 2014).

Often when blend electrospinning from a suspension containing organic and inorganic compounds, the applied particles are entirely embedded inside the polymer fibers (Bai et al., 2015; Sadat-Shojai, 2016; Kouhi et al., 2018). Whereas, using the post-processing of electrospun scaffolds for fiber decoration with ceramic particles by spraying or precipitation after soaking in simulated body fluid (SBF) solution results in particles only covering fibers (Gupta et al., 2009; Ramier et al., 2014). The imaging of particle distribution within electrospun fibers is challenging. SEM provides excellent information about the morphology of electrospun materials, therefore particles occurring on the surface of the fiber can be easily imaged (Ramier et al., 2014; Suslu et al., 2014), while embedded particles can be identified by thickened fiber areas, similar to beads (Sadat-Shojai, 2016; Kouhi et al., 2018). Transmission electron microscopy (TEM) is often used to investigate a few hundred-nanometer fibers, resulting in 2D images, which in some cases can give inconclusive information on whether particles are outside or inside fibers (Ramier et al., 2014). Various microscopy techniques complement each other thus applying several of them is necessary to obtain complete structural information about hybrid materials. Additional insights into material structure and particle distribution can be acquired from FIB-SEM cross-sections,

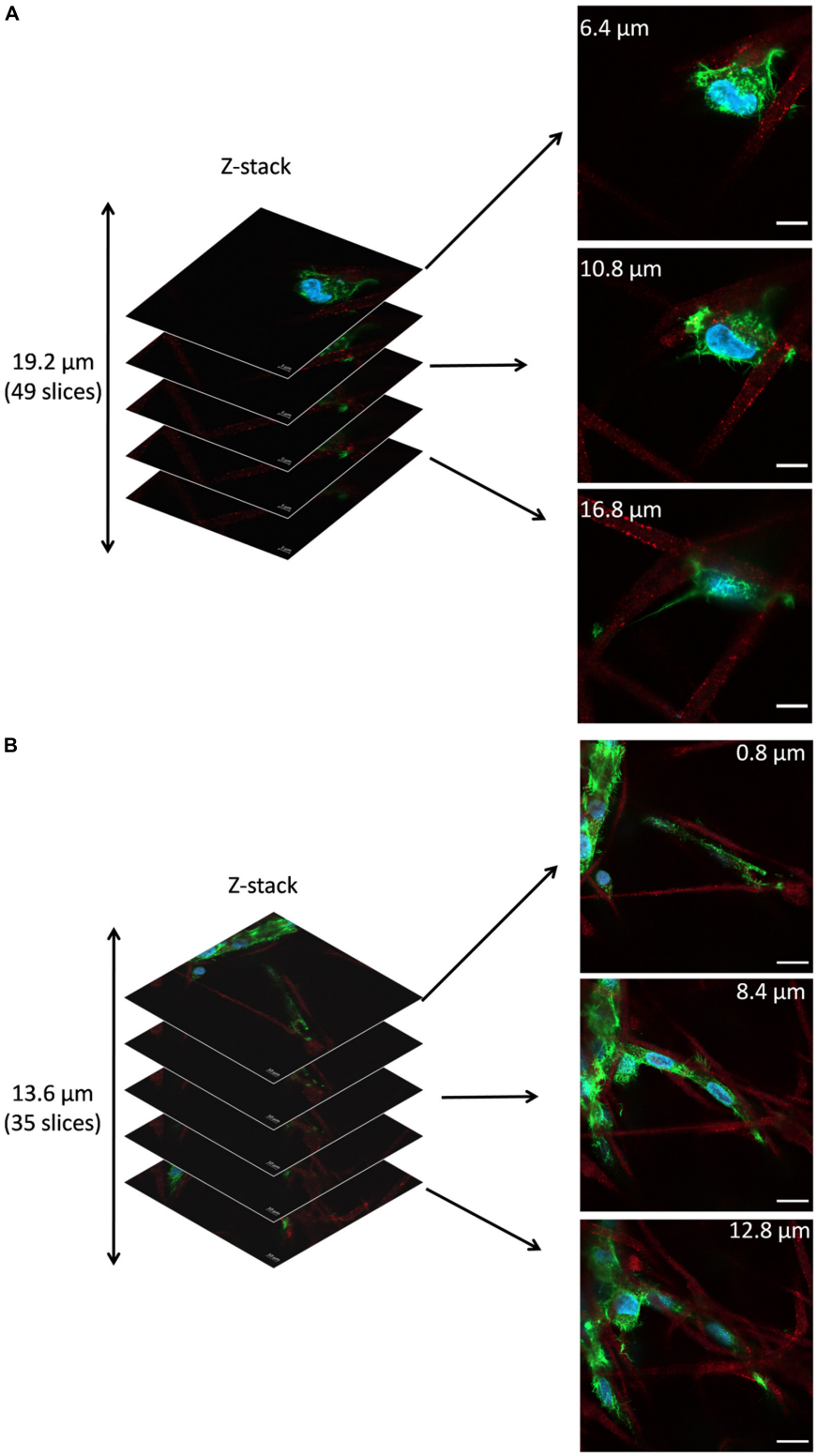

FIGURE 7 | Z-stacks of confocal images: **(A)** Cell in PHBV + HA scaffold after 4 days of incubation, scale bar 10 µm, **(B)** Cells in PHBV + HA scaffold after 7 days of incubation, scale bar 20 µm.

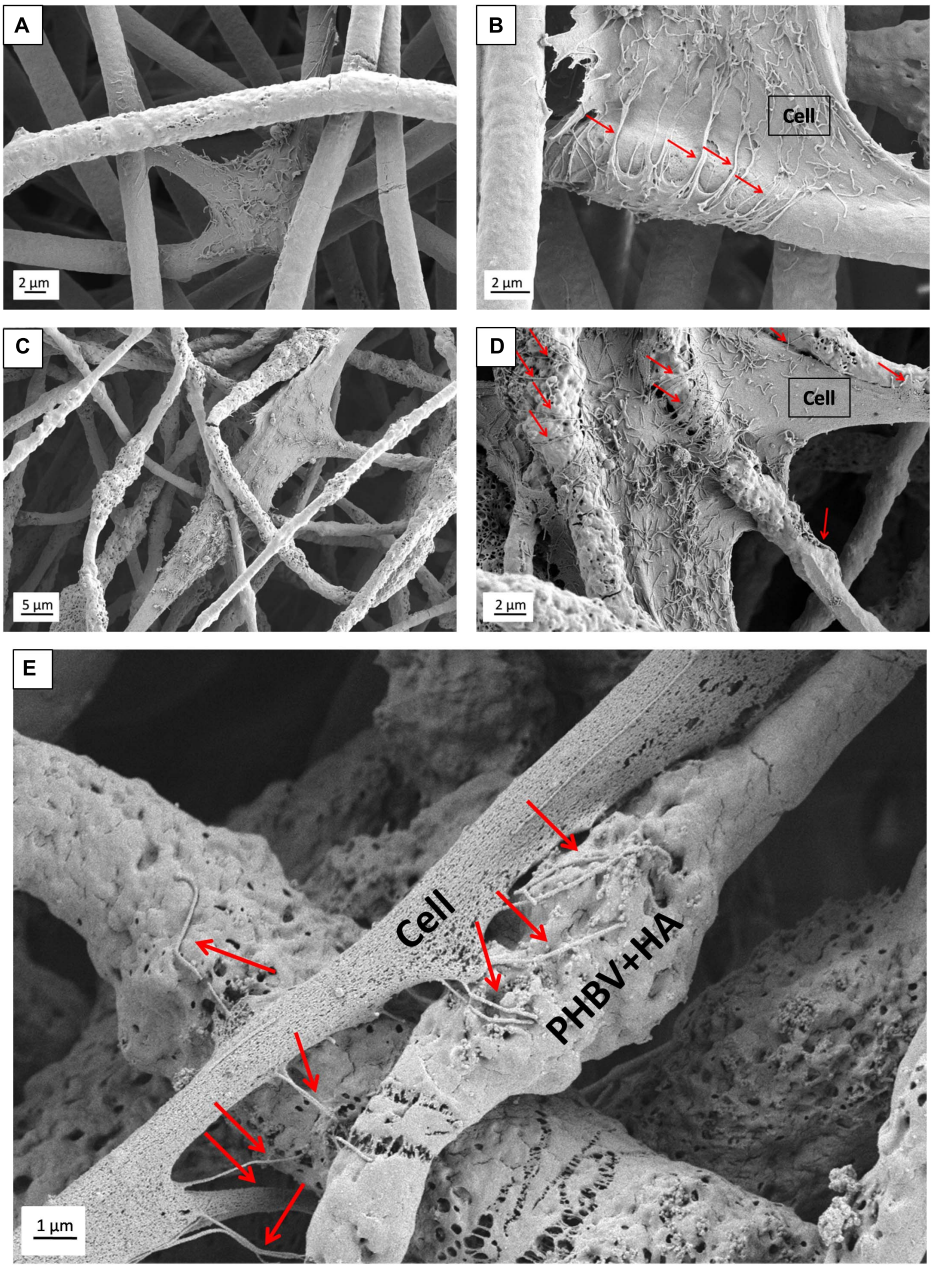

FIGURE 8 | SEM micrograph SE detector showing cell morphology after 7 days of incubation on: **(A,B)** PHBV fibers, **(C,D)** PHBV + HA fibers; **(E)** higher magnification micrograph showing in detail the filopodia attachment to the rough and porous surface of PHBV fibers with HA particles exposed on their surfaces. Red arrows indicate filopodia interacting with fibers.

as shown in **Figure 3**. Furthermore, based on the collection of consecutive SEM images registered after FIB cutting and subsequent reconstruction of the investigated area, it is possible to obtain 3D information regarding particle shape and position inside electrospun fibers (Cherpinski et al., 2019). Particles included inside the fibers affect their mechanical properties by increasing elastic modulus and tensile strength, changing their stiffness, and creating a more rigid scaffold (Ramier et al., 2014; Kouhi et al., 2018; Ivanoska-Dacikj et al., 2020), but the availability of the bioactive compound is limited since they are inside and dependent on polymer degradation. A too high concentration of ceramic filler in blend electrospinning (Kouhi et al., 2018; Ivanoska-Dacikj et al., 2020) can deteriorate mechanical properties, even below values for solely polymer fibers. A similar effect of decreased mechanical performance was observed for fibers covered with an excess of particles, like in the case of applying electrospraying (Ramier et al., 2014). Therefore, careful optimization of the amount as well as the distribution

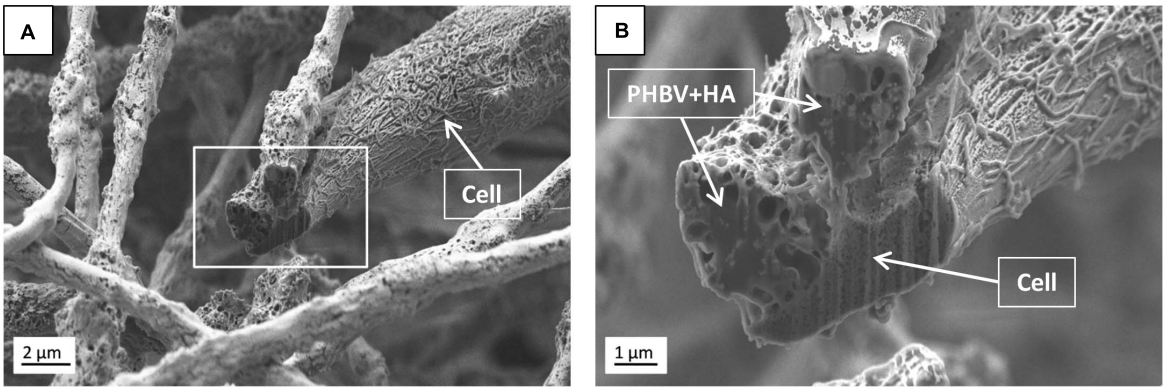

FIGURE 9 | SEM micrographs (SE detector) of **(A)** the cross-section performed using FIB to visualize the cell ingrowth between PHBV + HA fibers after 7 days of incubation, **(B)** higher magnification, enlarging the square from **(A)**.

of particles within hybrid fibers is needed to prepare desired scaffold-supporting bone tissue regeneration. An advantage of our composite organic-inorganic system is the presence of HA particles both outside and inside the electrospun fibers obtained within a single-step method.

Cell Culture

Scaffolds' architecture, surface properties as well as composition are crucial to guide bone cell attachment, proliferation, and maturation toward tissue regeneration (Zhu et al., 2020). It was proven that the moderate surface roughness of electrospun fibers created by beads on the fibers (Luo et al., 2012) or fibers porosity (Metwally et al., 2020) can promote initial bone cell adhesion and spreading followed by proliferation and differentiation. Additional improvement can be achieved by adding ceramic particles into the polymer network, therefore, reinforcing the scaffold with bioactive compounds which better match the mechanical and biological properties of bone tissue (Li and Chang, 2004; Bai et al., 2015; Wu et al., 2017). In our work, increased cell proliferation on the hybrid PHBV + HA scaffold is attributed to irregular fibers with surface porosity and the availability of HA particles. All together they contribute to structural signaling for cells with nano- and micro-roughness as well as biological signaling with the release of Ca and P ions. Cells in contact with the complex 3D structure of electrospun scaffolds need more time to form strong adhesion points and spread, only after they are settled, can the boost in proliferation occur. After the initial moderate cell proliferation, we observed a significant increase between the 4th and 7th day of cell culture on both PHBV-based scaffolds. Similar observations were previously reported for mouse pre-osteoblasts (MC3TC-E1) growing on PHB/HA hybrids (Sadat-Shojai, 2016). Even more time was needed for SaOS-2 cells growing on HA/PHBV scaffolds, where increased cell proliferation was noted between the 7th and 10th days of incubation (Suslu et al., 2014). For successful bone tissue regeneration, scaffolds with the right mechanical performance must also provide sufficient porosity for inside cell infiltration as well as nutrient and metabolite flow (Zhu et al., 2020). Electrospun membranes with a fiber diameter below 1 µm result in a scaffold with small pore sizes, even though the porosity of the whole structure is very high. In such a case, the scaffold serves as a 2D structure limiting cell ingrowth so they only form a surface layer (Luo et al., 2012; Ura et al., 2019). In this study, fiber diameters in both the PHBV-based scaffolds exceeded 2.5 µm with large pores, resulting in cell attachment and proliferation deep inside the structure, as we show on the z-stack confocal images in **Figure 7**. Also, the large spacing between fibers promoted cell elongation, stretching, and long cellular protrusion formation to bridge the gap between neighboring fibers and establish cell-to-cell communication. For cells, topography sensing is how they interact with the environment, which is done through filopodia formation (Albuschies and Vogel, 2013). The structure of electrospun PHBV-based scaffolds with micrometer-sized fibers provided cells with micro-features that they overlapped while establishing cell-material connections, as can be seen in **Figures 8B,D**. Whereas, the presence of HA particles and irregular fibers in the PHBV + HA scaffold additionally created nano-roughness that enhanced sensing filopodia formation to explore the material structure by cells, thus cell anchoring occurred as illustrated in **Figure 8E**.

Scaffolds in tissue engineering are designed to play a temporary supportive role, enabling cell attachment and guiding tissue development. After fulfilling its task, scaffolds should degrade to the biocompatible products and at the same time cells should secrete their own ECM. The collagen fibrils formation on the surface of osteoblasts followed by early mineralization is a typical sign of cell development toward bone tissue regeneration. These events can be enhanced by various signals: biological growth factors (Borsani et al., 2018), the addition of bioactive mineral particles (Kouhi et al., 2018), or scaffolds' properties like surface charge (Szewczyk et al., 2019a). In our study fibers' roughness, porosity, and HA presence in electrospun hybrid PHBV + HA scaffolds enhanced early collagen and mineral deposit formation on osteoblasts after 7 days of incubation, compared to PHBV scaffolds, as we can see in **Figure 8**.

Conclusion

This study represents a simple way of obtaining hybrid scaffolds by blend electrospinning a PHBV solution with HA particles without any post-processing. We successfully electrospun PHBV + HA and obtained a rough morphology of the fibers that eventually increased cell anchorage and proliferation. HA nanoparticles were well-adhered to the surface but were also present inside fibers, which is crucial for longer cell culture studies. We have proven this with EDS and FIB-SEM analysis. The combination of organic-inorganic components in a scaffold affects not only cell development and mobility but also ECM formation in the form of collagen fibrils and mineral deposits on their surface. This is one of the most desired processes that researchers want to obtain in bone tissue regeneration within such short-term studies. Importantly, the high porosity and distance between fibers (pore sizes in our scaffolds) allowed for the cell deep integration with fibers which has been shown via z-stack confocal imaging. We successfully created a suitable 3D environment for bone regeneration processes which is proven by cell integration and enhanced anchoring within the whole scaffold structure. These results show the great potential in the development of hybrid scaffolds which stimulate and intensify filopodia formation thus promoting desired specific cell activities in tissue regeneration processes.

DATA AVAILABILITY STATEMENT

The original contributions presented in the study are included in the article/**Supplementary Material**, further inquiries can be directed to the corresponding authors.

AUTHOR CONTRIBUTIONS

JEK and US contributed to the conception and design of the study. ŁK and JEK performed the electrospinning. JEK performed the cell culture, SEM imaging, statistical analysis, and wrote the first draft of the manuscript. KB completed the confocal microscopy imaging. AG performed the FIB-SEM microscopy. KB and US wrote the sections of the manuscript. All authors contributed to the manuscript revision, read, and approved the submitted version.

FUNDING

This study was financially supported by the grant PRELUDIUM 15, No. 2018/29/N/ST8/02032, financed by the National Science Center in Poland. The confocal microscopy study was performed within the "Nanofiber-based sponges for atopic skin treatment" project carried out within the First TEAM program of the Foundation for Polish Science co-financed by the European Union under the European Regional Development Fund, project no POIR.04.04.00-00-4571/17-00 and supported by the infrastructure at the International Center of Electron Microscopy for Materials Science (IC-EM) at the AGH University of Science and Technology.

SUPPLEMENTARY MATERIAL

The Supplementary Material for this article can be found online at: https://www.frontiersin.org/articles/10.3389/fbioe.2021.632029/full#supplementary-material

REFERENCES

Albuschies, J., and Vogel, V. (2013). The role of filopodia in the recognition of nanotopographies. *Sci. Rep.* 3, 1–9. doi: 10.1038/srep01658

Alford, A. I., Kozloff, K. M., and Hankenson, K. D. (2015). Extracellular matrix networks in bone remodeling. *Int. J. Biochem. Cell Biol.* 65, 20–31. doi: 10.1016/j.biocel.2015.05.008

Augustine, R., Hasan, A., Patan, N. K., Dalvi, Y. B., Varghese, R., and Antony, A. (2020). Cerium oxide nanoparticle incorporated electrospun poly(3-hydroxybutyrate-co-3-hydroxyvalerate) membranes for diabetic wound healing applications. *ACS Biomater. Sci. Eng.* 6, 58–70. doi: 10.1021/acsbiomaterials.8b01352

Baek, J. Y., Xing, Z. C., Kwak, G., Yoon, K. B., Park, S. Y., and Park, L. S. (2012). Fabrication and characterization of collagen-immobilized porous PHBV/HA nanocomposite scaffolds for bone tissue engineering. *J. Nanomater.* 2012, 1–11. doi: 10.1155/2012/171804

Bai, J., Dai, J., and Li, G. (2015). Electrospun composites of PHBV/pearl powder for bone repairing. *Prog. Nat. Sci. Mater. Int.* 25, 327–333. doi: 10.1016/j.pnsc.2015.07.004

Borsani, E., Bonazza, V., Buffoli, B., Nocini, P. F., Albanese, M., Zotti, F., et al. (2018). Beneficial effects of concentrated growth factors and resveratrol on human osteoblasts in vitro treated with bisphosphonates. *Biomed. Res. Int.* 2018, 1–13. doi: 10.1155/2018/4597321

Brunetti, L., Degli Esposti, M., Morselli, D., Boccaccini, A. R., Fabbri, P., and Liverani, L. (2020). Poly(hydroxyalkanoate)s meet benign solvents for electrospinning. *Mater. Lett.* 278:128389. doi: 10.1016/j.matlet.2020.128389

Cassidy, N. J., and Cartmell, S. H. (2013). Electrical stimulation: a novel tool for tissue engineering. *Tissue Eng. Part B Rev.* 19, 48–57. doi: 10.1089/ten.TEB.2012.0183

Chen, G., and Wu, Q. (2005). The application of polyhydroxyalkanoates as tissue engineering materials. *Biomaterials* 26, 6565–6578. doi: 10.1016/j.biomaterials.2005.04.036

Cherpinski, A., Szewczyk, P. K., Gruszczyński, A., Stachewicz, U., and Lagaron, J. M. (2019). Oxygen-scavenging multilayered biopapers containing palladium nanoparticles obtained by the electrospinning coating technique. *Nanomaterials* 9, 1–19. doi: 10.3390/nano9020262

Farzamfar, S., Salehi, M., Mohammad, S., Javad, T., Korosh, V., and Arman, M. (2019). A novel polycaprolactone/carbon nanofiber composite as a conductive neural guidance channel : an in vitro and in vivo study. *Prog. Biomater.* 8, 239–248. doi: 10.1007/s40204-019-00121-3

Fernandez-Yague, M. A., Akogwu, S., McNamara, L., Zeugolis, D. I., Pandit, A., and Biggs, M. J. (2015). Biomimetic approaches in bone tissue engineering : integrating biological and physicomechanical strategies. *Adv. Drug Deliv. Rev.* 84, 1–29. doi: 10.1016/j.addr.2014.09.005

Filippi, M., Born, G., Chaaban, M., and Scherberich, A. (2020). Natural polymeric scaffolds in bone regeneration. *Front. Bioeng. Biotechnol.* 8:474. doi: 10.3389/fbioe.2020.00474

Gupta, D., Venugopal, J., Mitra, S., Giri Dev, V. R., and Ramakrishna, S. (2009). Nanostructured biocomposite substrates by electrospinning and electrospraying for the mineralization of osteoblasts. *Biomaterials* 30, 2085–2094. doi: 10.1016/j.biomaterials.2008.12.079

Huang, B., Caetano, G., Vyas, C., Blaker, J. J., Diver, C., and Bártolo, P. (2018). Polymer-ceramic composite scaffolds: the effect of hydroxyapatite and β-tri-calcium phosphate. *Materials* 11:129. doi: 10.3390/ma11010129

Huang, C., and Thomas, N. L. (2020). Fabrication of porous fibers via electrospinning: strategies and applications. *Polym. Rev.* 60, 595–647. doi: 10.1080/15583724.2019.1688830

Ito, Y., Hasuda, H., Kamitakahara, M., Ohtsuki, C., Tanihara, M., and Kang, I. K. (2005). A composite of hydroxyapatite with electrospun biodegradable nanofibers as a tissue engineering material. *J. Biosci. Bioeng.* 100, 43–49. doi: 10.1263/jbb.100.43

Ivanoska-Dacikj, A., Bogoeva-Gaceva, G., Krumme, A., Tarasova, E., Scalera, C., and Stojkovski, V. (2020). Biodegradable polyurethane/graphene oxide scaffolds for soft tissue engineering : in vivo behavior assessment. *Int. J. Polym. Mater. Polym. Biomater.* 69, 1–11. doi: 10.1080/00914037.2019.1655754

Kaniuk, Ł, Krysiak, Z. J., Metwally, S., and Stachewicz, U. (2020). Osteoblasts and fibroblasts attachment to poly(3-hydroxybutyric acid-co-3-hydrovaleric acid) (PHBV) film and electrospun scaffolds. *Mater. Sci. Eng. C* 110, 1–8. doi: 10.1016/j.msec.2020.110668

Kouhi, M., Fathi, M., Prabhakaran, M. P., Shamanian, M., and Ramakrishna, S. (2018). Enhanced proliferation and mineralization of human fetal osteoblast cells on PHBV-bredigite nanofibrous scaffolds. *Mater. Today Proc.* 5, 15702–15709. doi: 10.1016/j.matpr.2018.04.181

Kouhi, M., Prabhakaran, M. P., Shamanian, M., Fathi, M., Morshed, M., and Ramakrishna, S. (2015). Electrospun PHBV nanofibers containing HA and bredigite nanoparticles: fabrication, characterization and evaluation of mechanical properties and bioactivity. *Compos. Sci. Technol.* 121, 115–122. doi: 10.1016/j.compscitech.2015.11.006

Krysiak, Z. J., Kaniuk, Ł, Metwally, S., Szewczyk, P. K., Sroczyk, E. A., and Peer, P. (2020). Nano- and microfiber PVB patches as natural oil carriers for atopic skin treatment. *ACS Appl. Bio Mater.* 3, 7666–7676. doi: 10.1021/acsabm.0c00854

Li, H., and Chang, J. (2004). Fabrication and characterization of bioactive wollastonite/PHBV composite scaffolds. *Biomaterials* 25, 5473–5480. doi: 10.1016/j.biomaterials.2003.12.052

Luo, C., Li, L., Li, J., Yang, G., Ding, S., and Zhi, W. (2012). Modulating cellular behaviors through surface nanoroughness. *J. Mater. Chem.* 22, 15654–15664. doi: 10.1039/c2jm32007j

Lyons, J. G., Plantz, M. A., Hsu, W. K., Hsu, E. L., and Minardi, S. (2020). Nanostructured biomaterials for bone regeneration. *Front. Bioeng. Biotechnol.* 8:922. doi: 10.3389/fbioe.2020.00922

Lyu, L. X., Huang, N. P., and Yang, Y. (2016). Accelerating and increasing nano-scaled pore formation on electrospun poly(3-hydroxybutyrate-co-3-hydroxyvalerate) fibers. *J. Biomater. Sci. Polym. Ed.* 27, 1155–1169. doi: 10.1080/09205063.2016.1184122

Mani, M. P., Jaganathan, S. K., Faudzi, A. A., and Sunar, M. S. (2019). Engineered electrospun polyurethane composite patch combined with bi-functional components rendering high strength for cardiac tissue engineering. *Polymers* 11, 1–16.

Metwally, S., Ferraris, S., Spriano, S., Krysiak, Z. J., Kaniuk, Ł, and Marzec, M. M. (2020). Surface potential and roughness controlled cell adhesion and collagen formation in electrospun PCL fibers for bone regeneration. *Mater. Des.* 194, 1–11. doi: 10.1016/j.matdes.2020.108915

Metwally, S., Karbowniczek, J. E., Szewczyk, P. K., Marzec, M. M., Gruszczyński, A., Bernasik, A., et al. (2019). Single-step approach to tailor surface chemistry and potential on electrospun PCL fibers for tissue engineering application. *Adv. Mat. Interfac.* 6:1801211. doi: 10.1002/admi.201801211

Paşcu, E. I., Stokes, J., and McGuinness, G. B. (2013). Electrospun composites of PHBV, silk fibroin and nano-hydroxyapatite for bone tissue engineering. *Mater. Sci. Eng. C* 33, 4905–4916. doi: 10.1016/j.msec.2013.08.012

Podporska-Carroll, J., Ip, J. W. Y., and Gogolewski, S. (2014). Biodegradable poly(ester urethane) urea scaffolds for tissue engineering: interaction with osteoblast-like MG-63 cells. *Acta Biomater.* 10, 2781–2791. doi: 10.1016/j.actbio.2014.02.016

Ramier, J., Bouderlique, T., Stoilova, O., Manolova, N., Rashkov, I., and Langlois, V. (2014). Biocomposite scaffolds based on electrospun poly (3-hydroxybutyrate) nanofi bers and electrosprayed hydroxyapatite nanoparticles for bone tissue engineering applications. *Mater. Sci. Eng. C* 38, 161–169. doi: 10.1016/j.msec.2014.01.046

Sadat-Shojai, M. (2016). Electrospun polyhydroxybutyrate/hydroxyapatite nanohybrids: microstructure and bone cell response. *J. Mater. Sci. Technol.* 32, 1013–1020. doi: 10.1016/j.jmst.2016.07.007

Salinas, E., Hu, J., and Athanasiou, K. (2018). A guide for using mechanical stimulation to enhance. *Tissue Eng. Part B Rev.* 24, 345–358. doi: 10.1089/ten.teb.2018.0006

Stevens, M. M., and George, J. H. (2005). Exploring and engineering the cell surface interface. *Science* 310, 1135–1138. doi: 10.1126/science.1106587

Sultana, N., and Wang, M. (2008). PHBV/PLLA-based composite scaffolds containing nano-sized hydroxyapatite particles for bone tissue engineering. *J. Exp. Nanosci.* 3, 121–132. doi: 10.1080/17458080701867429

Suslu, A., Albayrak, A. Z., Urkmez, A. S., Bayir, E., and Cocen, U. (2014). Effect of surfactant types on the biocompatibility of electrospun HAp/PHBV composite nanofibers. *J. Mater. Sci. Mater. Med.* 25, 2677–2689. doi: 10.1007/s10856-014-5286-1

Szewczyk, P. K., Metwally, S., Karbowniczek, J. E., Marzec, M. M., Stodolak-Zych, E., and Gruszczyński, A. (2019a). Surface-potential-controlled cell proliferation and collagen mineralization on electrospun polyvinylidene fluoride (PVDF) fiber scaffolds for bone regeneration. *ACS Biomater. Sci. Eng.* 5, 582–593. doi: 10.1021/acsbiomaterials.8b01108

Szewczyk, P. K., Metwally, S., Krysiak, Z. J., Kaniuk, Ł, Karbowniczek, J. E., and Stachewicz, U. (2019b). Enhanced osteoblasts adhesion and collagen formation on biomimetic polyvinylidene fluoride (PVDF) films for bone regeneration Enhanced osteoblasts adhesion and collagen formation on biomimetic polyvinylidene fl uoride (PVDF) films for bone regeneration. *Biomed. Mater.* 14, 1–8. doi: 10.1088/1748-605X/ab3c20

Szewczyk, P. K., and Stachewicz, U. (2020). The impact of relative humidity on electrospun polymer fibers: from structural changes to fiber morphology. *Adv. Colloid Interf. Sci.* 286:102315. doi: 10.1016/j.cis.2020.102315

Szewczyk, P. K., Ura, D. P., and Stachewicz, U. (2020). Humidity controlled mechanical properties of electrospun polyvinylidene fluoride (PVDF) fibers. *Fibers* 8, 1–9. doi: 10.3390/fib8100065

Thomas, A., and Bera, J. (2020). Fabrication and characterization of polymer-infiltrated glass ceramic-titania scaffold for bone substitution. *Mater. Technol.* 35, 168–178. doi: 10.1080/10667857.2019.1661142

Tong, H. W., Wang, M., Li, Z. Y., and Lu, W. W. (2010). Electrospinning, characterization and in vitro biological evaluation of nanocomposite fibers containing carbonated hydroxyapatite nanoparticles. *Biomed. Mater.* 5:054111. doi: 10.1088/1748-6041/5/5/054111

Ura, D. P., Karbowniczek, J. E., Szewczyk, P. K., and Metwally, S. (2019). Cell integration with electrospun PMMA nanofibers, microfibers, ribbons, and films : a microscopy study. *Bioengineering* 6, 1–12.

Ura, D. P., Rosell-Llompart, J., Zaszczyńska, A., Vasilyev, G., Gradys, A., and Szewczyk, P. K. (2020). The role of electrical polarity in electrospinning and on the mechanical and structural properties of as-spun fibers. *Materials* 13, 1–18. doi: 10.3390/ma13184169

Wagner, A., Poursorkhabi, V., Mohanty, A. K., and Misra, M. (2014). Analysis of porous electrospun fibers from poly(l-lactic acid)/poly(3-hydroxybutyrate-co-3-hydroxyvalerate) blends. *ACS Sustain. Chem. Eng.* 2, 1976–1982. doi: 10.1021/sc5000495

Wu, J., Wu, Z., Xue, Z., Li, H., and Liu, J. (2017). PHBV/bioglass composite scaffolds with co-cultures of endothelial cells and bone marrow stromal cells improve vascularization and osteogenesis for bone tissue engineering. *RSC Adv.* 7, 22197–22207. doi: 10.1039/c7ra02767b

Xing, F., Li, L., Zhou, C., Long, C., Wu, L., and Lei, H. (2019). Regulation and directing stem cell fate by tissue engineering functional microenvironments: scaffold physical and chemical cues. *Stem Cells Int.* 2019, 1–16. doi: 10.1155/2019/2180925

Yi, H., Rehman, F. U., Zhao, C., Liu, B., and He, N. (2016). Recent advances in nano scaffolds for bone repair. *Bone Res.* 4, 1–11. doi: 10.1038/boneres.2016.50

Zhu, L., Luo, D., and Liu, Y. (2020). Effect of the nano/microscale structure of biomaterial scaffolds on bone regeneration. *Int. J. Oral Sci.* 12, 1–15. doi: 10.1038/s41368-020-0073-y

Conflict of Interest: The authors declare that the research was conducted in the absence of any commercial or financial relationships that could be construed as a potential conflict of interest.

frontiers in Bioengineering and Biotechnology

ORIGINAL RESEARCH
published: 31 March 2021
doi: 10.3389/fbioe.2021.630745

Preparation and Properties of Antibacterial Polydopamine and Nano-Hydroxyapatite Modified Polyethylene Terephthalate Artificial Ligament

Yang Wu[1], Yuhan Zhang[1], Ren Zhang[2] and Shiyi Chen[1]**

[1] Department oft of Orthopaedic Sports Medicine, Huashan Hospital Affiliated to Fudan University, Shanghai, China, [2] Center for Analysis and Measurement, Fudan University, Shanghai, China

OPEN ACCESS

Edited by:
Antonio Jesus Salinas, Complutense University of Madrid, Spain

Reviewed by:
Chunyi Wen, Hong Kong Polytechnic University, Hong Kong
Nenad Filipovic, University of Kragujevac, Serbia

***Correspondence:**
Ren Zhang
zhangren@fudan.edu.cn
Shiyi Chen
cshiyi@163.com

Specialty section:
This article was submitted to Biomaterials, a section of the journal Frontiers in Bioengineering and Biotechnology

Received: 18 November 2020
Accepted: 24 February 2021
Published: 31 March 2021

Citation:
Wu Y, Zhang YH, Zhang R and Chen S (2021) Preparation and Properties of Antibacterial Polydopamine and Nano-Hydroxyapatite Modified Polyethylene Terephthalate Artificial Ligament. Front. Bioeng. Biotechnol. 9:630745. doi: 10.3389/fbioe.2021.630745

Due to its great biomechanical property, the polyethylene terephthalate (PET) artificial ligament has become one of the most promising allografts for anterior cruciate ligament (ACL) reconstruction. However, because of its chemical and biological inertness, PET is not a favored scaffold material for osteoblast growth, which promotes the ligament-bone healing. Meanwhile, in consideration of prevention of potential infection, the prophylactic injection of antibiotic was used as a post-operative standard procedure but also has the increasing risk of bacterial resistance. To face these two contradictions, in this article we coated a polydopamine (PDA) nano-layer on the PET ligament and used the coating as the adhesion interlayer to introduce nano-hydroxyapatite (nHA) and silver atoms to the surface of PET ligament. Because of the mild self-polymerization reaction of dopamine, the thermogravity analysis (TGA), Raman spectrum, and tensile test results show that the modification procedure have no negative effects on the chemical stability and mechanical properties of the PET. The results of NIH3T3 cell culture show that the PDA and nHA could effectively improve the biocompatibility of PET artificial ligament for fibroblast growth, and staphylococcus aureus antibacterial test results show that the Ag atom provided an antibacterial effect for PET ligament. As shown in this paper, the nano-PDA coating modification procedure could not only preserve the advantages of PET but also introduce new performance characteristics to PET, which opens the door for further functionalization of PET artificial ligament for its advanced development and application.

Keywords: polydopamine, nano-hydroxyapatite, PET, anterior cruciate ligament, antibacterial, artificial ligament

INTRODUCTION

The rupture of the anterior cruciate ligament (ACL) is a serious surgical injury, especially with the increasing participation of extreme exercise and high-intensity exercise in recent years (Monk et al., 2016). The rupture of anterior cruciate ligament makes the patient unable to control the knee joint and seriously affect the quality of life. In order to treat this injury, artificial ligaments are usually used to replace broken ligaments in surgery to reconstruct the patient's control of the knee joint (Lai et al., 2018). At present, an artificial polymer artificial ligament based on a

polyethylene terephthalate (PET) bundle, with high mechanical strength, high chemical inertness, and no biological toxicity is commonly used as an artificial ligament in anterior cruciate ligament reconstruction (ACLR). However, PET artificial ligament cannot effectively promote bone healing and patient recovery, which might lead to tunnel enlargement and delay recovery of patients because of its chemical inertia (Gao et al., 2010). To overcome this defect, many research groups have developed different protocols, such as chemical coating (Ding et al., 2019), mechanical mixing, and so on. For the chemical inertness of PET, the preceding methods may lead to ineffectively attachment of modified layer and even fall off. Therefore, it is necessary to find a modified method with good biocompatibility, strong adhesion, and easy operation.

On the other hand, intraoperative infection during ACLR has serious consequences and might induce infectious osteomyelitis (Ridley et al., 2018). As a routine, intravenous injection of broad-spectrum antibiotics for patients is wildly recommended to avoid infection, which however brings the risk of antibiotic abuse. If the precise antibacterial in the surgical site can be achieved, it can not only effectively avoid infection but also avoid the abuse of antibiotics. Therefore, we hope to achieve this goal through certain antibacterial modification of PET ligament.

Dopamine (DA) has a similar structure with dihydroxyphenylalanine (DOPA) contained in the mucin secreted by mussels, such as catechol functional groups and lysine end amino groups, which have been proved to have high adhesion properties. DA can be oxidized and self-polymerized in alkaline environment, forming a strong sticky polydopamine (PDA) layer on the surface of the material, thus achieving the coating on the surface of various materials (Zhang et al., 2016). As the self-polymerization of DA has the advantages, such as convenient preparation, environment-friendship reaction, and high-efficiency process, PDA have attracted more and more researchers to participate in the its application (Ryu et al., 2010; Shi et al., 2014). The research results show that the modification of the PDA-modified method can significantly improve the biological and pharmaceutical properties of the materials, and the good application prospect of the modified PDA method.

Hydroxyapatite is the main component of vertebrate bones and teeth, which has good bioactivity and biocompatibility. Hydroxyapatite not only has strong corrosion resistance but also strong osteoinduction (Bose and Tarafder, 2012). At present, the research on hydroxyapatite in bone substitute materials mainly focuses on hydroxyapatite coating and human bone biomimetic regeneration materials (Szczes et al., 2017). Meanwhile, nano-hydroxyapatite (nHA) has larger specific surface area and better biological properties than hydroxyapatite because of its nano effect; therefore, there have been reports on osteoinduction of nHA in recent decades (Zhou and Lee, 2011). In this study, nHA was coated on the surface of the PET artificial ligament for the purpose of promoting its biocompatibility and improving osseointegration after ACLR.

Silver has been used as a broad antibacterial material for thousands of years. Silver ions could bond with protein through the sulfur/nitrogen/oxygen atom on the amino acid side chain, which causes the destruction of cell membrane function and leads to the inhibition of bacterial growth (Lemire et al., 2013). In recent years, the silver antibacterial medical products, such as silver ion dressing, have been certified by FDA and used in surgery (Chernousova and Epple, 2013), and silver nano-particles were used in antibacterial modification of PET artificial ligament (Wang K. et al., 2020). Antibacterial ability of silver has following characteristics, such as broad-spectrum and sustained release, which make silver good candidate for antibacterial materials of artificial ligament.

In this paper, we modified nHA and silver atoms on the surface of PET artificial ligament through the PDA layer without damaging the mechanical properties of PET. There are three steps as shown in **Figure 1**. First step: A layer of DA was modified on the surface of PET artificial ligament by self-polymerization of DA hydrochloride in alkaline and weak oxidation environment, which is expected to improve the surface properties of the PET artificial ligaments, such as biocompatibility and modifiable. Second step: in order to verify the modification of the PET artificial ligaments in the PDA layer, this article will also use the adhesion properties of PDA to modify the nHA on the surface of the PET artificial ligament, which may improve the cell proliferation of the PET artificial ligament. Third step: the silver nitrate reacts with PDA and nHA on the PET surface to generate silver compounds and provide PET ligament the antibacterial ability.

EXPERIMENT

Materials

DA hydrochloride, Tris(hydroxymethyl)aminomethane (Tris), hydrochloric acid (HCl), copper sulfate ($CuSO_4$), and 30% hydrogen peroxide (H_2O_2) were purchased from Sigma-Aldrich, United States. The nHA was purchased from Aladdin reagent, China. The other reagents were purchased from Sinopharm Chemical Reagent limited corporation, China. The clinical PET artificial ligament was purchased from Shanghai Kinetic Co., Ltd. (KMC).

Characterization

The scanning electron microscope image was scanned by Phenom Prox (Phenom, Holland) after Conductive Coating with gold on samples. Raman spectrum was recorded by XploRA Raman spectrometer (Horiba Jobin Yvon, France) with an 80mW 785nm wavelength excitation laser. The thermogravimetric analysis (TGA) was recorder by Pyris 1 TGA (Perkinelmer, United States). Tensile testing was tested by Instron 5966 Universal Testing Systems (Instron, United States). Elemental analysis was tested by PerkimElmer Optima 8000DV.

Modification of Polydopamine and nHA

10 cm-length PET artificial ligament was placed in a 15 mL plastic centrifuge tube, then 10 mL 50 mM pH8.8 Tris-HCl buffer solution, 25 uL 1M $CuSO_4$, 100 uL 30% H_2O_2 and DA were added to the tube, respectively. After mixing the reaction solution completely, the tube was placed in 37°C water-bath for 6 h. Finally, the PET ligament was washed by deionized

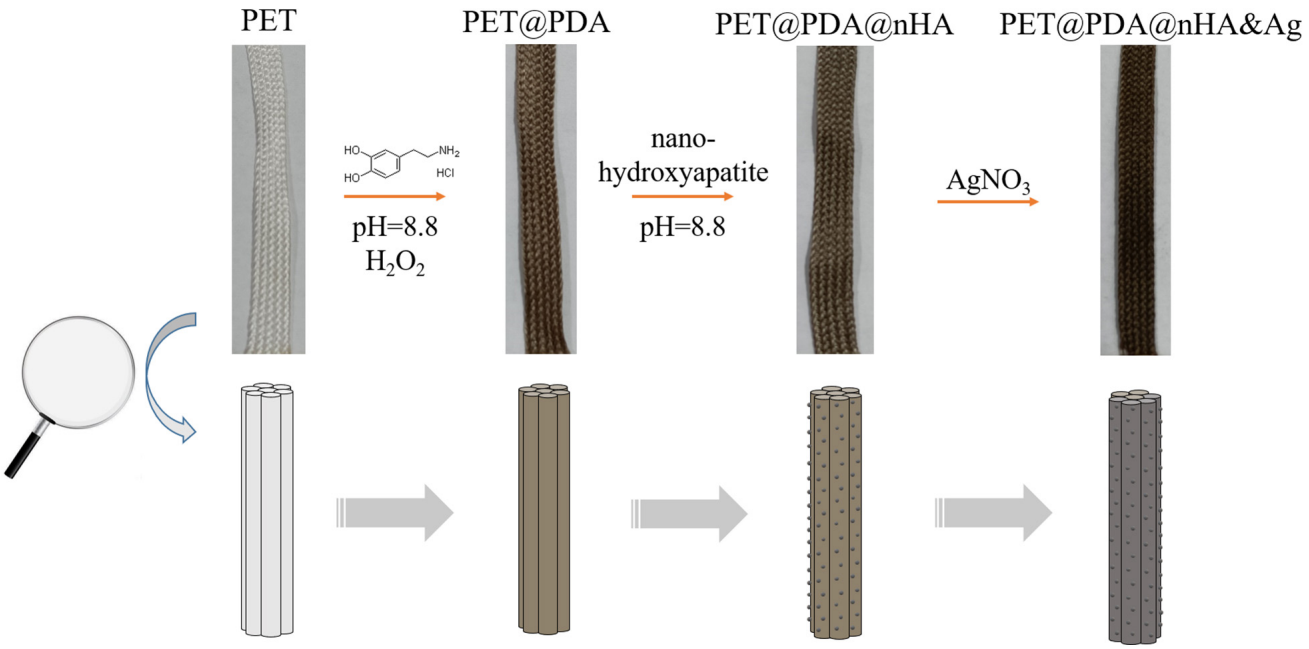

FIGURE 1 | The schematic diagram of the PET ligament modification process. Up line is the photo images of ligaments, and down line is morphology change diagram of ligament fibers.

water for 3 times and dried in 25°C ovens. The prepared PDA-modified PET ligament (PET@PDA ligament) was placed in a 15 mL plastic centrifuge tube, then 10 mL 50 mM pH8.8 Tris-HCl buffer solution, 25 μL 1 M $CuSO_4$, 100 μL 30% H_2O_2, 20 mg DA and 100 mg nHA were added to tube, respectively. The nHA reaction solution was mixed by rotary mixer for 2 h. Then the nHA modified PET@PDA ligament (PET@PDA@nHA ligament) was dried in 25°C ovens.

Modification of Silver Atoms

A 10 cm PET, PDA-modified, PDA- and nHA-modified PET artificial ligament was placed in a 15 mL plastic centrifuge tube, then 15 mL 100 mg silver nitrate contained aqueous solution was added. The solution was placed on rotary blender for 2 h. Then the ligament was washed five times. The abbreviation of the above three Ag modified ligaments was PET@Ag, PET@PDA@Ag and PET@PDA@nHA&Ag, respectively.

The Antibacterial Performance

Staphylococcus aureus (SA, CMCC26003) was cultured in LB medium until the OD600 value was about 0.6, which was corresponding to 108 CFU/mL concentrations. The bacterial solution was diluted to 10^5 CFU/mL at the dilution ratio of 1:1,000. The tested samples were placed in 2 mL bacterial solution at 37°C for 24 h to detect the optical density (OD) value.

Cell Proliferation to NIH3T3 and MG-63 Cells

To evaluate the cytotoxicity and osseointegration of the modified ligaments, the metabolic viability of cells cultured with the ligaments (one 5 mm-long fiber of ligament) was measured using the Cell Counting Kit-8 (CCK-8) assay on mouse embryonic fibroblast cell line (NIH3T3) and human osteosarcoma cell line (MG-63). First, the NIH3T3 and MG-63 cells were seeded in a 96-well tissue culture plate at a seeding density of 10,000 cells/well for 24 h, respectively. After the cell adheres to the wall, the ligaments were clamped into the pore plate. Then, after 72 h of incubation, the solution was removed from the well plates. PBS was used to wash the ligaments for two times, then add 1 mL 10% CCK8 medium and continue culturing for 2 h. Finally, the solution was removed into a 96-pore ELISA plate for testing.

RESULTS AND DISCUSSION

The Modification of PDA

In alkaline and oxidizing atmosphere, the hydroxyl group of DA is oxidized to quinone structure. Then the quinone type DA was polymerized through the carbon atoms on the benzene ring, resulting in the formation of DA (Liu et al., 2014). The polymerization of DA can be observed on the macro level, usually manifested by obvious color changes in the substrate material involved in the polymerization of DA. Similar to the color changes in literature (Zhang et al., 2016), PET artificial ligaments are transformed from white to gray black (**Figure 1**) after being modified by PDA, indicating that the PDA has been modified on the surface of the PET. It is worth noting that, from the color distribution of the PDA-modified PET artificial ligaments, the modification of PDA is uniform, indicating that the modification method of the PDA can be applied to the large batch preparation of the artificial ligaments of the PET@PDA.

To investigate the formation process of PDA layer, a series of different amount of DA-modified PET ligament was processed, and the SEM images was shown in **Figure 2**. As **Figure 2** shows, the surface of pure PET (**Figure 2A**, 0 mg DA) is smooth, and there is no significant foreign body on it. When the amount of DA is up than 5 mg, the significant roughened particles could be observed, which may indicate the growth process of PDA on the substrate surface. When the DA amount is up to 20 mg, the continuous PDA layer is formed as shown in **Figure 2D**, when DA amount continue increasing, the roughness is also increasing (**Figures 2E,F**). The SEM results show that the PDA layer is formed from the distributed particles at the beginning of the PDA layer by the increasing of the DA amount.

Raman spectroscopy is a non-destructive and sensitive surface analysis method, which can identify the structure or composition of the material surface by the vibration spectrum of the material. By analyzing the Raman spectra of PET and PET@PDA artificial ligaments, the adhesion of PDA on PET can be verified structurally. As shown in **Figure 3**, the Raman spectra of PET@PDA have 1192, 1,385 and 1,550 cm^{-1} scattering peaks, which is absent in the PET's spectrum, and the three peaks are were contributed from the PDA signal, which originate from the vibration of aromatic rings and aliphatic C–C and C–O stretching, respectively. Meanwhile, the baseline of PET is flat, but the baseline of PET@PDA has apparent fluctuation, which is contributed from PDA, which is originated from the complexity of PDA's structure (Li et al., 2018).

In order to verify whether the main structure of PET was damaged after DA modification, the thermogravimetric analysis was used. TGA could reflect the thermal stability and composition of materials by studying the mass loss of materials during the heating process. **Figure 4A** is the thermogravimetric curve of PET and PET@PDA. In the chart, the two materials have shown the similar weight-loss curves. Differential thermal gravity (DTG) curves of two materials can be obtained by differential treatment of thermogravimetric curves, as shown in **Figure 4B**. The DTG curves show that the weight-loss rates of the two materials are almost the same, indicating that the thermal stability of PET has not changed after modification with PDA. On the other hand, by analyzing the onset decomposition temperature (**Figures 4C,D**), it is found that the temperatures of both materials are about 410°C. The data of DTG and onset

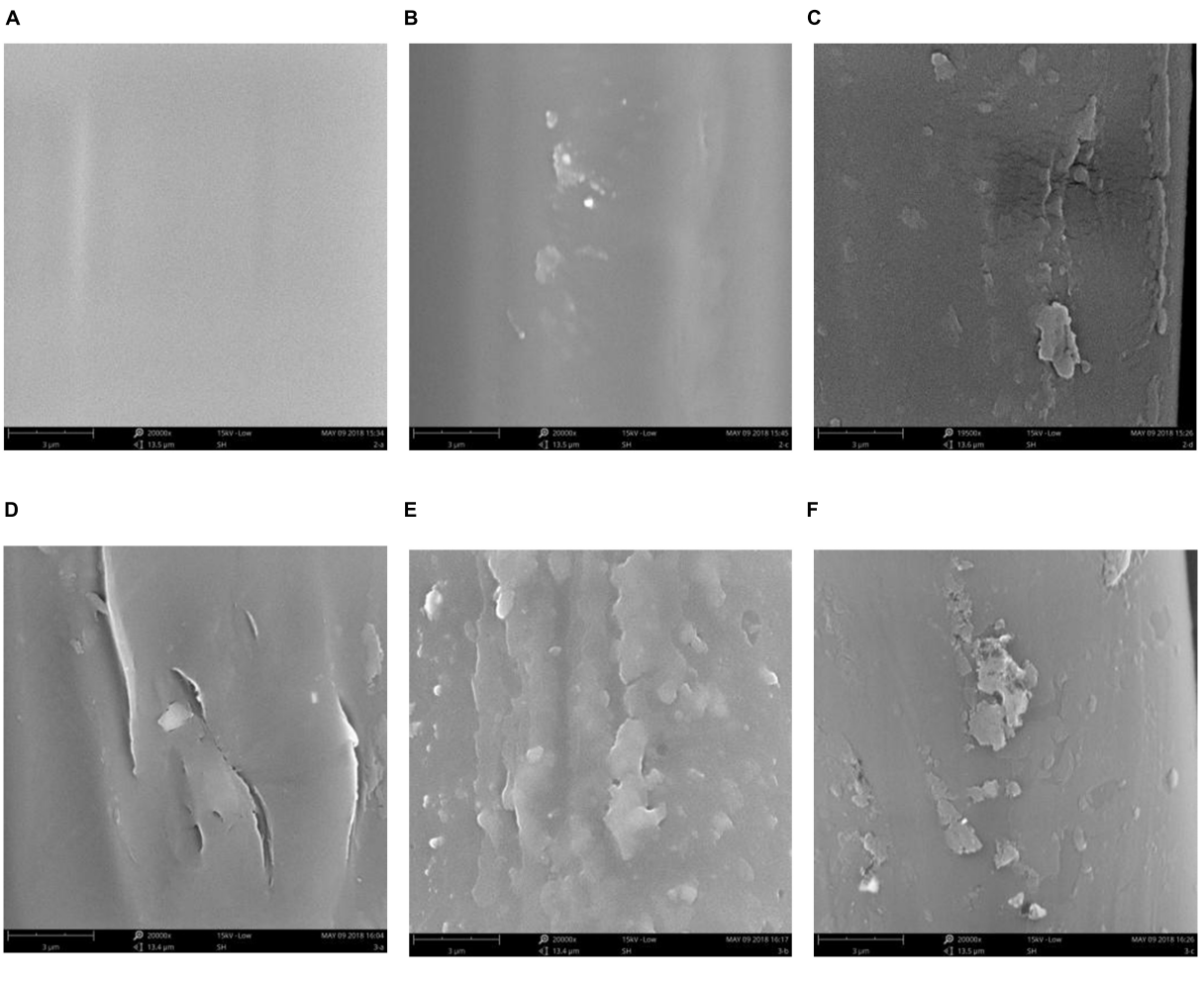

FIGURE 2 | Surface SEM images of different DA-concentration-modified PET ligament. **(A)** 0 mg, **(B)** 5 mg, **(C)** 10 mg, **(D)** 20 mg, **(E)** 50 mg, and **(F)** 100 mg.

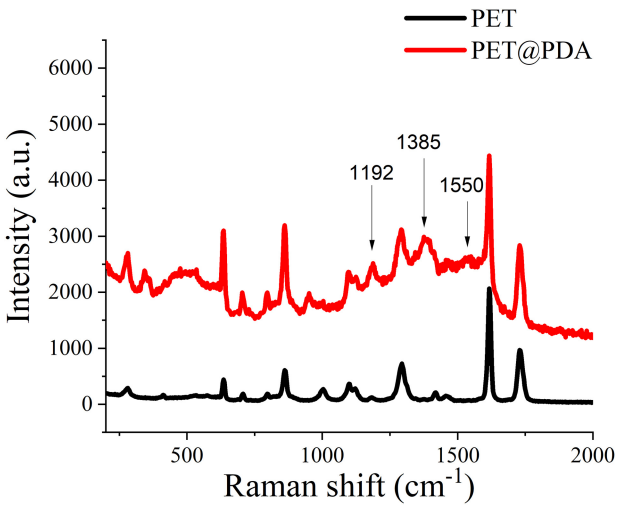

FIGURE 3 | Raman spectrum of PET artificial ligament (black) and PDA-modified PET artificial ligament (red).

decomposition temperature show that the thermal stability of PET has not changed after PDA modification, indicating the modification of PDA has not changed the chemical properties of the material. On the other hand, no signal of PDA was observed in DTG, which may be due to the insufficient content of PDA on the PET surface to form a signal in the DTG curve, which also indicates that the PDA modification method is an accurate and nano-scale surface modification method.

The Modification of nHA

PDA not only can modify the surface of PET but also can be used as an adhesive layer to bond other functional materials to the surface of PET. nHA is widely used in the field of bone growth, bone healing, and so on as a surface component of bone structure (Sadat-Shojai et al., 2013). In order to promote the bone growth and healing of the PET ligament and bone junction, we use the PDA on the PET fiber as the adhesive layer and adhere nHA to the PET ligament, thus preparing the hydroxyapatite-modified PET@PDA ligament (PET@PDA@nHA). There are two methods to prepare PET@PDA@nHA. One is to adhere to the PDA after the preparation of the PET@PDA (two-step), and the other is to add nHA in the DA polymerization process (one-step). **Figure 5** is the SEM image of the two methods followed by nHA, in which the **Figure 5A** is the two-step method, and the **Figure 5B** is the one-step method of PET@PDA@nHA. It can be seen from the diagram that there are obvious differences between the two modified materials, in which the two-step modified PET@PDA@nHA fibers have more nHA on the surface than the one-step method. The results of Raman spectra also show the same results. From **Figure 5C**, it could be seen that the two-step modified fibers can see the more obvious Raman signal of nHA, while the one-step method can hardly see the signal of nHA. The results of SEM and Raman spectra indicated that PDA did play a role in the functional material adhesion layer, and the two-step modification of PET fibers had more efficient modification efficiency.

The Modification of Silver Atoms

Because the surface of PDA is rich in various reductive organic groups, such as amino group, phenolic hydroxyl group and so on, it has been used to reduce metal ions to metal atoms (Wang Z. et al., 2020). When the PET@PDA ligament was placed in a certain concentration of silver nitrate solution, silver ions were first adsorbed on the surface of PDA and then were reduced to silver atoms by PDA. On the other hand, nHA particles bound on the surface of PDA could form insoluble salts with silver ions because of phosphate radicals, which could also adsorb silver ions on nHA. **Figure 6A** is a scanning electron microscope (SEM) image of PET@PDA@nHA and PET@PDA@nHA&Ag, and the results of energy dispersive spectrometer (EDS). It can be seen from the SEM images that the morphology of PET@PDA@nHA does not change significantly after it reacts with $AgNO_3$, and no obvious new nano-structure is produced. However, different results could be seen on the EDS signal. In the figure, no Ag signal is found on PET@PDA@nHA. While there is an obvious Ag peak in the signal of PET@PDA@nHA&Ag, which indicates that although there is no change in morphology, silver atoms had been adsorbed on the surface of PET ligament after reacting with silver nitrate. By comparing the percentage changes of each element (**Figure 6B**), which was analyzed from EDS data, it can be seen that after nHA adheres to PDA, the signal of phosphorus element with content of about 1% appears in EDS signal, and more than 10% silver element appears after reaction with $AgNO_3$. The results of EDS well reflect the adsorption process of nHA and Ag on the surface of PET@PDA artificial ligament in different experimental stages.

At the same time, PDA and nHA may have different reaction abilities with silver ion, which may lead to different Ag^+ adsorption capacity between PET@PDA and PET@PDA@nHA. In order to verify this inference, PET@PDA and PET@PDA@nHA prepared by the reaction of PET with different concentrations of DA react with silver nitrate solution of the same concentration (concentration of 10 mg/mL). After that, inductively coupled plasma-atomic emission spectrometry (ICP-AES) was used to measure the mass of silver adsorbed on PET with certain mass. The results are shown in **Figure 6C**. It can be seen from the figure that when the concentration of DA is less than 20 mg/mL, the mass of silver nitrate adsorbed on the surface of two artificial ligaments is rare. When the concentration of DA is greater than 20 mg/mL, a large number of silver atoms can be adsorbed on the surface of PET ligament. The highest adsorption amount appears at the concentration of 50 mg/mL, and the adsorption amount of Ag decreases at higher concentration. The variation of the adsorption capacity may be due to the following reasons: (1) When the concentration of DA is less than 20 mg/mL, hydrogen peroxide tends to oxidize DA completely due to the low concentration of DA in the solution of DA polymerization reaction. As the concentration of DA is higher than 20 mg/mL, the equivalent concentration of hydrogen peroxide is not enough to completely oxidize DA, thus initiating the self-polymerization of DA leading to the formation of a

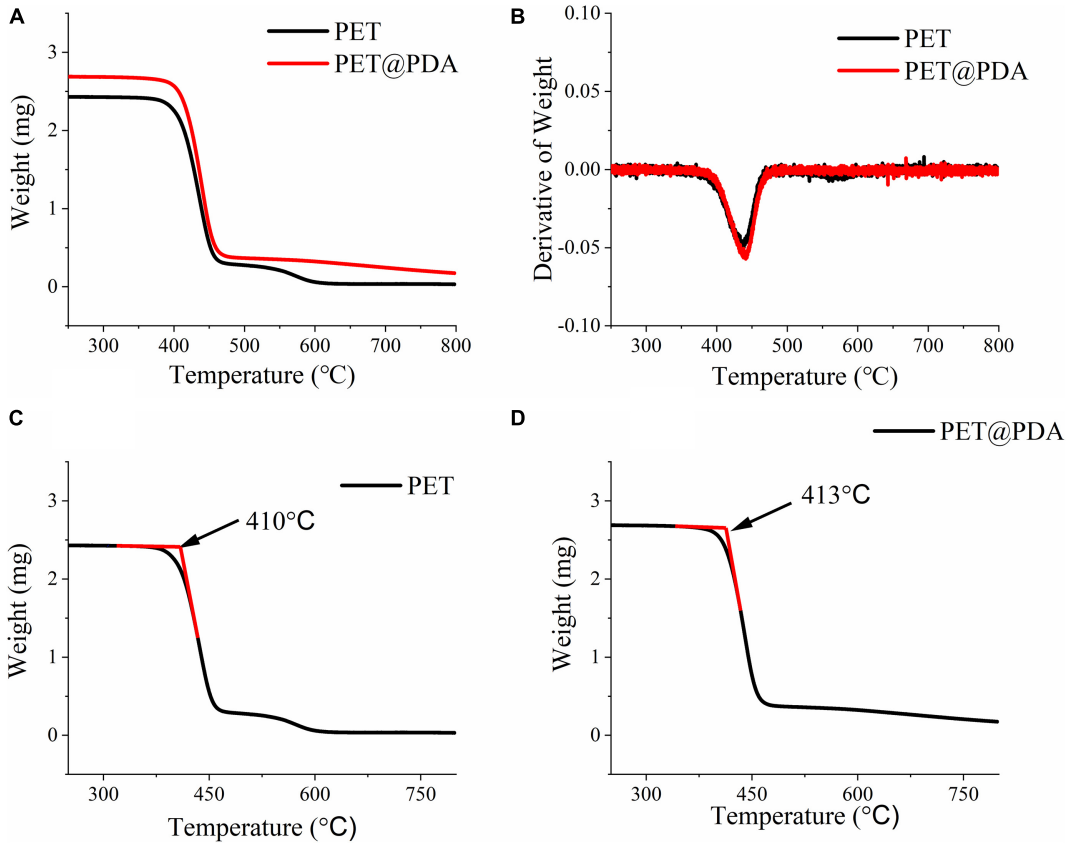

FIGURE 4 | Thermal gravity curve **(A)** and differential thermal gravity curve **(B)** of PET and PET@PDA ligament. Onset decomposition temperature of PET **(C)** and PET@PDA **(D)** ligament.

large number of PDA on the PET surface; and (2) When the concentration of DA is high enough, the PDA on the surface of PET would grow too thick due to the fast reaction speed. When Ag^+ reacts with PDA, part of PDA may fall off from the surface due to oxidation, and the lower layer of PDA without silver atom is exposed, which leads to the relative decrease of Ag content in ICP test. Although the **Figure 6C** show that PET@PDA@nHA adsorb less Ag atoms, which may be due to the fact that the binding ability of nHA to silver is relatively weak than PDA, it also shows that both PDA and nHA can effectively bind Ag atoms, which provides a good basis for the next step of antibacterial using silver ions.

Mechanical Property

One of the reasons that the PET artificial ligament can be used in ACLR are its strong mechanical properties, which can guarantee the patient's joint can bear daily activity and even a certain intensity after the operation. The mechanical performance of the modified ligaments is a key indicator. **Figure 7** enumerates the SEM images and the mechanical properties of the PET, PET@PDA, PET@PDA@nHA (two-step method), and PET@PDA@nHA&Ag artificial ligament. From the figure, we can see that the mechanical properties of the four ligaments have no obvious difference, and the elastic modulus are all maintained at 1,100–1,200 MPa, indicating that the modification process has no negative effect on the main mechanical structure of the fiber.

Release of Silver Ion and Antibacterial Properties

Ag^+ could destroy the combination of polysaccharides on the cell wall of bacteria, thus affecting the physiological function of cell wall. At the same time, after entering the pathogen cell, Ag^+ could combine with the thiol group in the functional protein, which affects the normal proliferation of pathogenic bacteria and leads to the death of pathogenic bacteria. Therefore, the materials that could release silver ions would acquire antibacterial ability. However, the realization of this function requires that silver atoms could be oxidized and dissociated into silver ions to enter the surrounding environment of pathogenic bacteria (Rai et al., 2009). Ag atoms could be oxidized by dissolved oxygen in aqueous solution and further form silver ions dissolved in aqueous solution. At the same time, silver phosphate compounds, as a kind of insoluble salt, could gradually dissociate silver ions in solution, especially under acidic conditions. The synovial fluid in the knee joint can provide a good environment for the

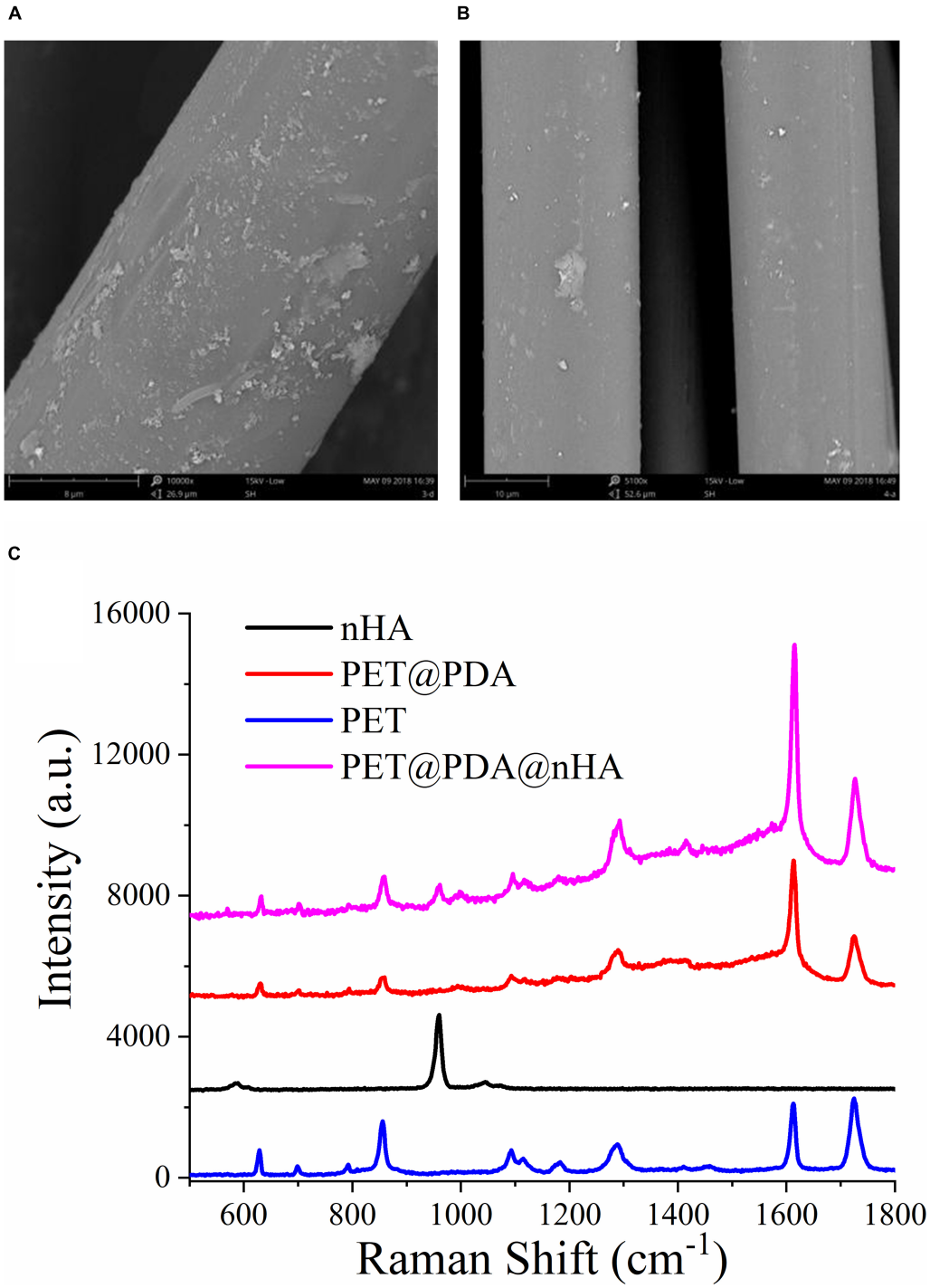

FIGURE 5 | SEM images of PET@PDA@nHA, which were modified by two steps **(A)** and one step **(B)** reaction, and Raman spectra of PET and PET@PDA@nHA **(C)**.

release of silver ions, which may provide the basis for the antibacterial PET ligament.

In order to understand the release of Ag^+ from Ag-modified ligaments, PET soaked in Ag^+ solution (PET@Ag), PET@PDA@Ag, and PET@PDA@nHA&Ag ligaments were placed in normal saline with pH value of 7.4, and the Ag^+ concentrations were detected when ligaments were soaked in normal saline for different time. **Figure 8A** shows the release curve of Ag^+, in which the concentration of DA for PET modified in two ligaments is 50 mg/mL. It can be seen from the figure that the silver ion concentration in the solution of the two ligaments (PET@PDA@Ag and PET@PDA@nHA&Ag) gradually increases

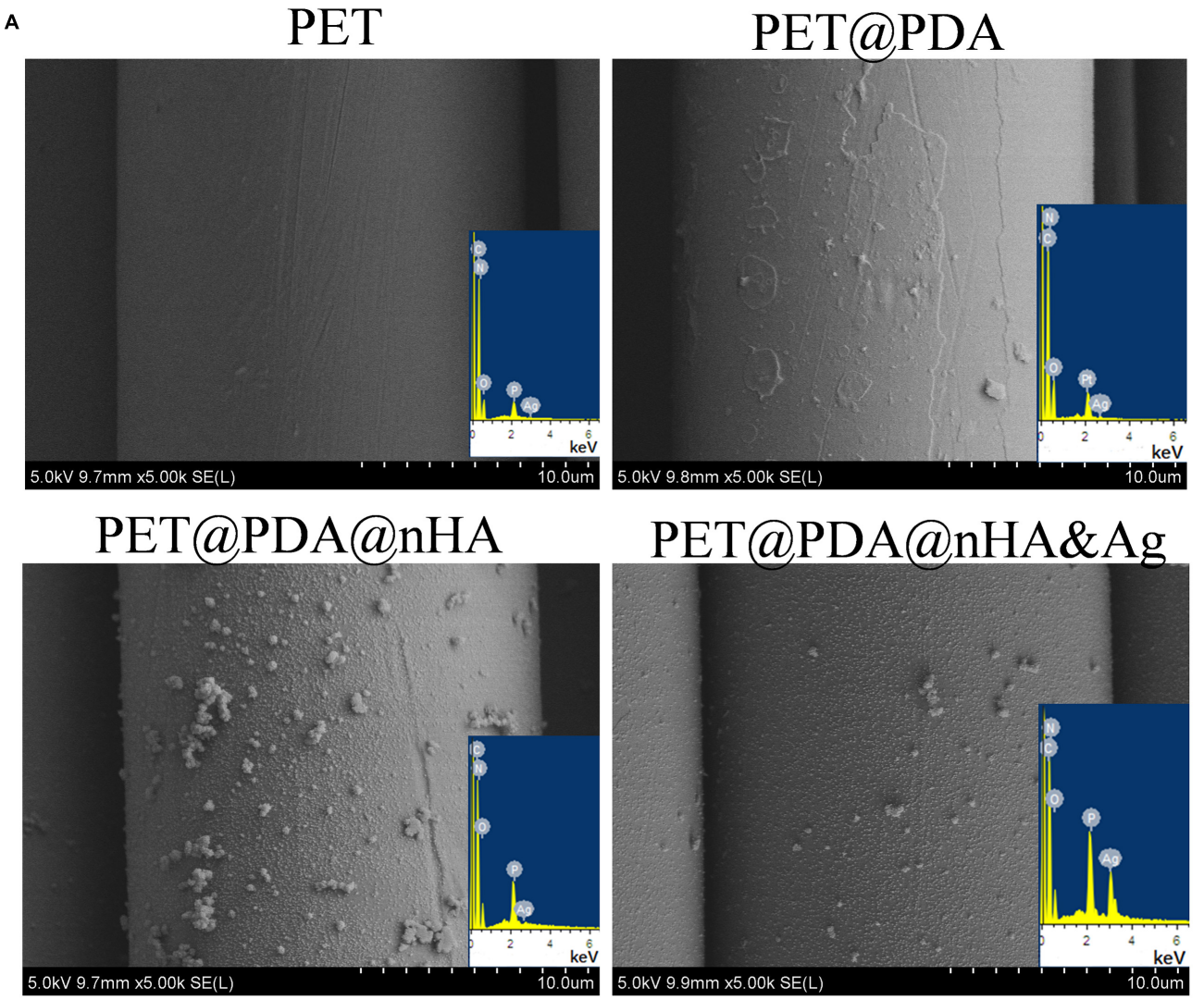

FIGURE 6 | SEM and eds of four PET ligaments **(A)**, weight percentage of five element **(B)** and Ag **(C)** in PET@PDA@Ag and PET@PDA@nHA&Ag ligaments.

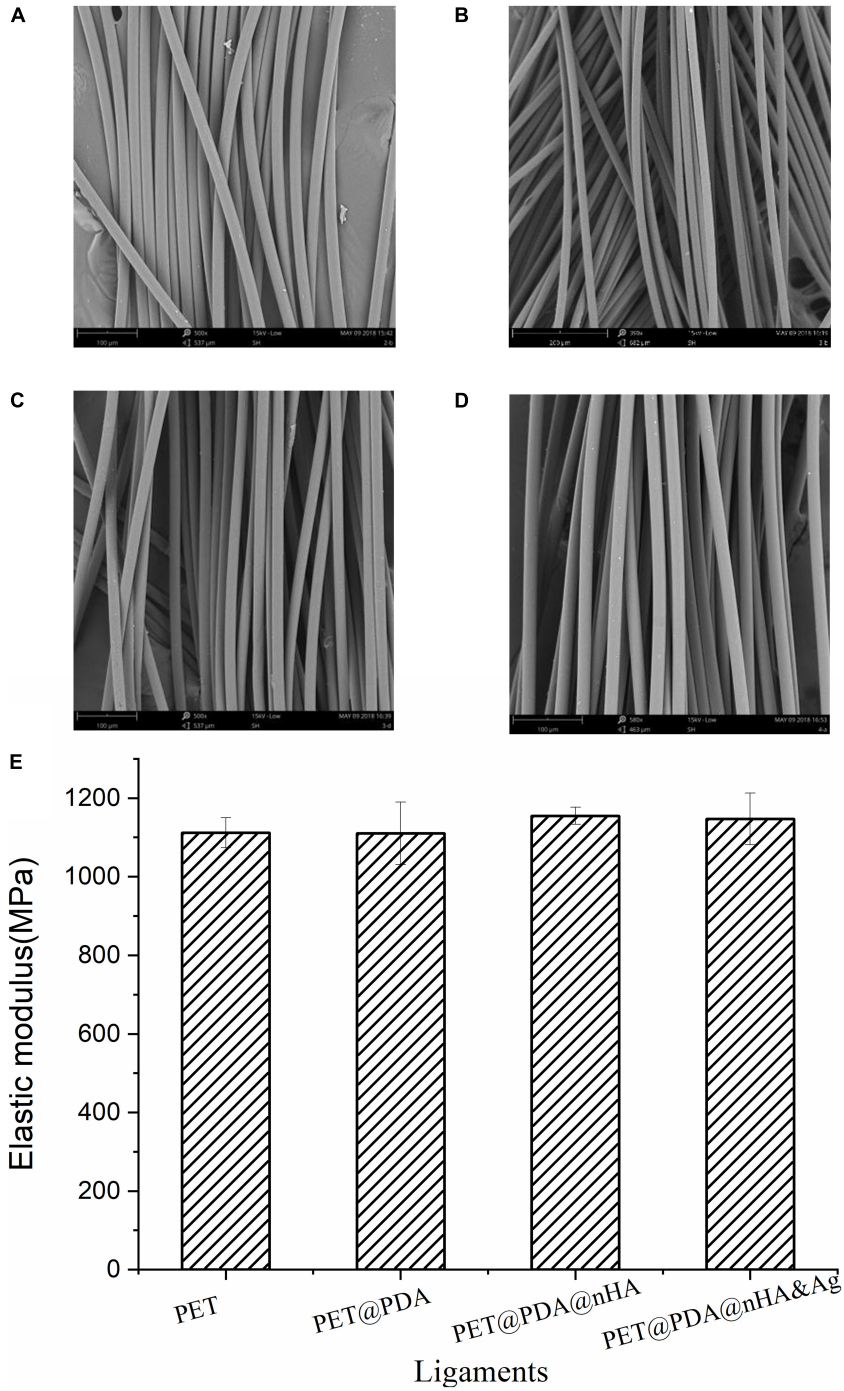

FIGURE 7 | SEM images of PET **(A)**, PET@PDA **(B)**, PET@PDA@nHA **(C)**, and PET@PDA@nHA&Ag **(D)** ligament fibers and **(E)** the elastic modulus of the four ligaments.

with the increase of immersion time in different release time. After soaking for 6 days (144 h), the silver ion concentration in the solution reached 0.22 mg/L. At the same time, it can also be noticed that the artificial ligament modified with nHA has a higher concentration of released Ag^+, which is related to the higher Ag^+ release efficiency of silver phosphate complex, which has weak solubility in an aqueous solution. However, compared with the other two ligaments, the Ag^+ concentration of pure PET was much lower than that of the other two ligaments. The silver ion release curves indicated that both PDA and nHA could form a silver adsorption layer on the PET surface with a sustained release effect.

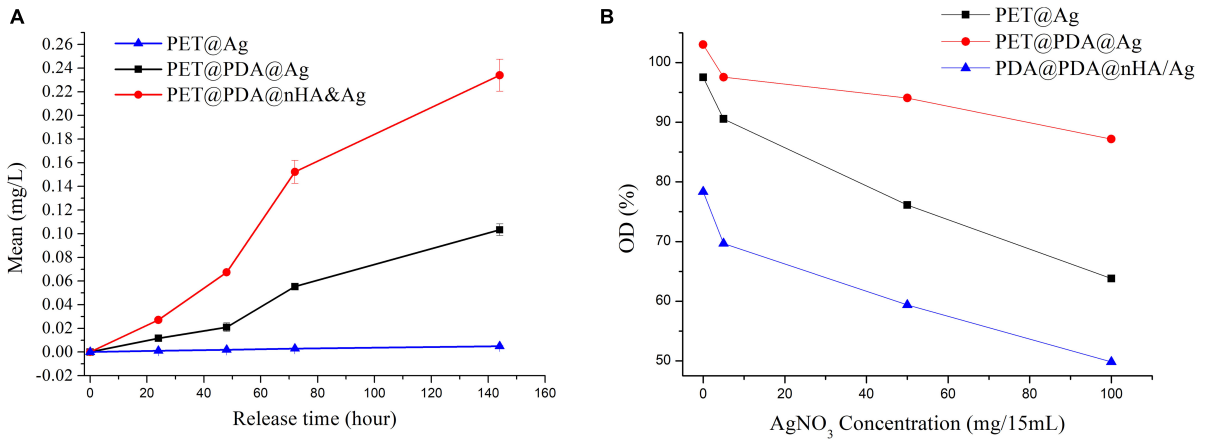

FIGURE 8 | (A) The release curve of silver ion of different ligaments, and **(B)** effect of Ag^{+} reaction concentration on antibacterial ability.

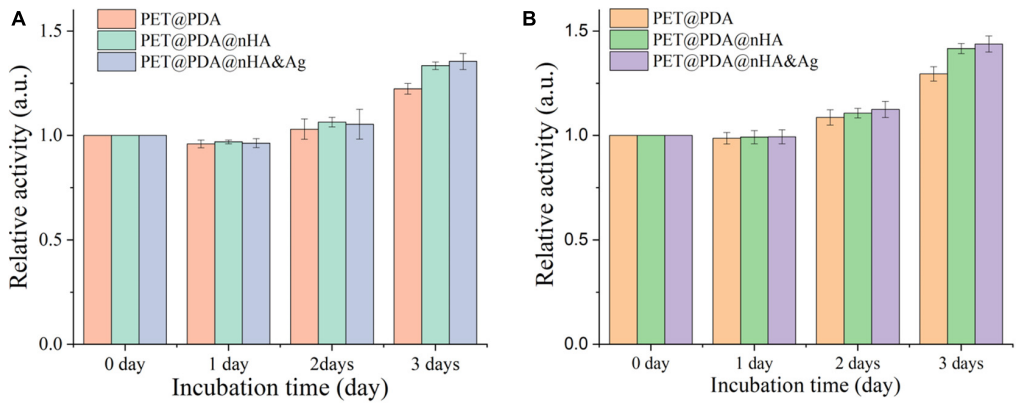

FIGURE 9 | (A) NIH3T3 and **(B)** MG-63 cell proliferation of three kinds of ligaments.

To analyze the antibacterial ability of three ligaments, $AgNO_3$-soaked PET, PET@PDA@Ag, and PET@PDA@nHA&Ag tested against *Staphylococcus aureus*. The results are shown in **Figure 8B**. As shown in the figure, $AgNO_3$-soaked PET, PET@PDA@Ag, and PET@PDA@nHA&Ag artificial ligaments had a certain antibacterial effect after reacting with the $AgNO_3$ solution of a certain concentration, which was similar to previous literature reports (Wang K. et al., 2020), and the antibacterial ability increased with the increase of $AgNO_3$ reaction concentration, which indicated that the increase of silver ion concentration in the reaction solution had an obvious promoting effect on the antibacterial effect of the artificial ligament. On the other hand, it can also be observed that before the interaction with silver ions, the antibacterial ability of three kinds of ligaments also has an obvious difference. Compared with the control group without any material, the OD value (103%) of a pure PET artificial ligament has no decrease, or even a slight increase, which indicates that the pure PET artificial ligament has no antibacterial property. Compared with the control group, the PET@PDA@nHA ligament has an obvious bacteriostatic effect, and its OD value is 78, while the OD value of the PET@PDA ligament was 98, which means its antibacterial effect was not significant. With the increase of the silver nitrate concentration, the antibacterial properties of all three ligaments were significantly improved. When the concentration of $AgNO_3$ in the reaction solution was increased to 6.6 mg/mL, the OD values of PET@Ag, PET@PDA@Ag, and PET@PDA@nHA&Ag were 87, 64, and 50, respectively. The results showed that the antibacterial effect of the materials initiated by silver nitrate could be promoted when the presence of PDA and nHA on the PET surface. The reason for the above phenomenon is that pure PET has a high degree of chemical inertia, which makes it difficult for silver ions to react with PET ligaments. But with the increase of silver ion concentration, its antibacterial effect can be attributed to the effect of electrostatic adsorption and a small amount of silver ions reduced by PET. However, the surface of PET modified by PDA is covered with a reduced layer of DA, which makes the ligaments more capable of reacting with silver ions. For PET@PDA@nHA&Ag, the surface-modified nHA contains a large number of phosphate radicals, and the pKa value of silver phosphate (monohydrate phosphate, dihydrogen phosphate) is relatively high. The formation of these insoluble substances can also promote the sustained release of silver ions in the water.

Cell Proliferation

Due to nHA and PDA having good biocompatibility, here we use the CCK8 assay to verify whether PET surface-modified PDA and nHA promoted cell proliferation and osseointegration, and whether the introduction of Ag atom brought biological toxicity. The results are shown in **Figure 9**. From **Figure 9**, it can be seen that the two cell lines showed similar rules in the process of culture. First, the number of cells in the three modified ligaments on the first day of culture was slightly less than that in pure PET ligaments (relative activity < 1), while the number of cells in the second and third days was significantly higher than that in pure PET ligaments (relative activity > 1). The experimental results show that PDA effectively improves the cell proliferation on the surface of the PET ligament, which may be due to the fact that PDA could effectively change the hydrophobic state of the PET surface (Cai et al., 2018). PDA contains rich amino and hydroxyl groups, which could infiltrate all kinds of nutrients needed for cell proliferation in the water phase on the surface of PET, and amino groups could help the cell to proliferate on the PET surface (Cai et al., 2018). Meanwhile, it also can be seen that nHA-modified ligaments have higher cell activity than PDA-modified ligaments on the second and third day of cell culture. The reason may be that the existence of nHA increases the specific surface area of the PET surface (Lee et al., 2007). nHA, as a major inorganic ceramic material and an essential component of the bone, can further promote the proliferation of osteoblasts on the PET surface. The above factors are the reason why MG-63 osteoblasts in **Figure 9** show higher cell activity when cultured with two kinds of ligaments modified with PDA and nHA, (The cell viability of NIH3T3 and MG-63 cultured with PET@PDA@nHA&Ag on the third day was 1.35 and 1.43, respectively), and this result also indicates that the co-existence of PDA and nHA has an add-on effect on the proliferation of osteoblasts. The above results showed that the existence of PDA and nHA could promote the proliferation of cells, and the adsorption of Ag atoms did not significantly affect the growth of cells.

CONCLUSION

In this paper, we use the self-polymerization of DA derived from the adhesion principle of mussels, in weak oxidizing and weak alkaline aqueous solutions, and the surface of the PET artificial ligament was successfully modified with PDA. Then, nHA was modified on the surface of PET by using PDA as adhesive layer. TGA showed that the mechanical properties and chemical stability of the PET ligament were not affected by the modification procedure. In the third step, we successfully adsorbed silver atoms on the PET surface by using the reducibility of DA and the phosphate contained in nHA. By testing mechanical tensile, it is found the modification of PDA, nHA, and Ag have no negative effect on the mechanical strength. The results of the silver ion release test showed that the modification of PDA and nHA on the PET surface could provide the sustained release of silver ions into an aqueous solution, and the results of the antibacterial test showed that the PET surface modified with silver atom had significant antibacterial properties. The results of the biological activity test showed that both PDA and nHA could significantly enhance the cell proliferation; meanwhile, the presence of Ag atoms did not significantly affect the growth of cells. On the other hand, this study also faces some challenges in the further clinical application, such as how to adapt to the tissue growth transition between the bone tunnel and joint cavity in the process of tendon–bone healing, and so on. In summary, this modification method of nHA and silver atom based on PDA provides a new insight to further improve the biocompatibility and expand the function of the PET artificial ligament.

DATA AVAILABILITY STATEMENT

The raw data supporting the conclusions of this article will be made available by the authors, without undue reservation.

AUTHOR CONTRIBUTIONS

All authors listed have made a substantial, direct and intellectual contribution to the work, and approved it for publication.

FUNDING

This study was supported by the National Science Foundation for Young Scientists of China (Grant No. 81601882).

SUPPLEMENTARY MATERIAL

The Supplementary Material for this article can be found online at: https://www.frontiersin.org/articles/10.3389/fbioe.2021.630745/full#supplementary-material

REFERENCES

Bose, S., and Tarafder, S. (2012). Calcium phosphate ceramic systems in growth factor and drug delivery for bone tissue engineering: a review. *Acta Biomater.* 8, 1401–1421. doi: 10.1016/j.actbio.2011.11.017

Cai, J. Y., Wan, F., Dong, Q. L., Jiang, J., Ai, C. C., Sheng, D. D., et al. (2018). Silk fibroin and hydroxyapatite segmented coating enhances graft ligamentization and osseointegration processes of the polyethylene terephthalate artificial ligament in vitro and in vivo. *J. Mater. Chem. B* 6, 5738–5749. doi: 10.1039/c8tb01310a

Chernousova, S., and Epple, M. (2013). Silver as antibacterial agent: ion, nanoparticle, and metal. *Angew. Chem.* 52, 1636–1653. doi: 10.1002/anie.201205923

Ding, X. Q., Wang, S. H., Jin, W. H., Liu, X. W., Chen, J., and Chen, S. Y. (2019). Encapsulation of a nanoporous simvastatin-chitosan composite to enhance osteointegration of hydroxyapatite-coated polyethylene terephthalate ligaments. *Int. J. Nanomed.* 14, 4881–4893. doi: 10.2147/ijn.S210687

Gao, K., Chen, S. Y., Wang, L. D., Zhang, W. G., Kang, Y. F., Dong, Q. R., et al. (2010). Anterior cruciate ligament reconstruction with LARS artificial ligament: a multicenter study with 3-to 5-year follow-up. *Arthroscopy* 26, 515–523. doi: 10.1016/j.arthro.2010.02.001

Lai, C. C. H., Ardern, C. L., Feller, J. A., and Webster, K. E. (2018). Eighty-three per cent of elite athletes return to preinjury sport after anterior cruciate ligament reconstruction: a systematic review with meta-analysis of return to sport rates, graft rupture rates and performance outcomes. *Br. J. Sports Med.* 52, 128–138. doi: 10.1136/bjsports-2016-096836

Lee, H. J., Kim, S. E., Choi, H. W., Kim, C. W., Kim, K. J., and Lee, S. C. (2007). The effect of surface-modified nano-hydroxyapatite on biocompatibility of poly(epsilon-caprolactone)/hydroxyapatite nanocomposites. *Eur. Polym. J.* 43, 1602–1608. doi: 10.1016/j.eurpolymj.2007.02.030

Lemire, J. A., Harrison, J. J., and Turner, R. J. (2013). Antimicrobial activity of metals: mechanisms, molecular targets and applications. *Nat. Rev. Microbiol.* 11, 371–384. doi: 10.1038/nrmicro3028

Li, T. D., Zhang, R., Chen, H., Huang, Z. P., Ye, X., Wang, H., et al. (2018). An ultrasensitive polydopamine bi-functionalized SERS immunoassay for exosome-based diagnosis and classification of pancreatic cancer. *Chem. Sci.* 9, 5372–5382. doi: 10.1039/c8sc01611a

Liu, Y. L., Ai, K. L., and Lu, L. H. (2014). Polydopamine and its derivative materials: synthesis and promising applications in energy, environmental, and biomedical fields. *Chem. Rev.* 114, 5057–5115. doi: 10.1021/cr400407a

Monk, A. P., Davies, L. J., Hopewell, S., Harris, K., Beard, D. J., and Price, A. J. (2016). Surgical versus conservative interventions for treating anterior cruciate ligament injuries. *Cochrane Database Syst. Rev.* 4:CD011166. doi: 10.1002/14651858.CD011166.pub2

Rai, M., Yadav, A., and Gade, A. (2009). Silver nanoparticles as a new generation of antimicrobials. *Biotechnol. Adv.* 27, 76–83. doi: 10.1016/j.biotechadv.2008.09.002

Ridley, T. J., Rud, C. T., Krych, A. J., and Macalena, J. A. (2018). Bacterial contamination of a marking pen in anterior cruciate ligament reconstruction. *Orthop. J. Sports Med.* 6:2325967118772043. doi: 10.1177/2325967118772043

Ryu, J., Ku, S. H., Lee, H., and Park, C. B. (2010). Mussel-inspired polydopamine coating as a universal route to hydroxyapatite crystallization. *Adv. Funct. Mater.* 20, 2132–2139. doi: 10.1002/adfm.200902347

Sadat-Shojai, M., Khorasani, M. T., Dinpanah-Khoshdargi, E., and Jamshidi, A. (2013). Synthesis methods for nanosized hydroxyapatite with diverse structures. *Acta Biomater.* 9, 7591–7621. doi: 10.1016/j.actbio.2013.04.012

Shi, X. T., Li, L., Ostrovidov, S., Shu, Y. W., Khademhosseini, A., and Wu, H. K. (2014). Stretchable and micropatterned membrane for osteogenic differentation of stem cells. *ACS Appl. Mater. Interfaces* 6, 11915–11923. doi: 10.1021/am5029236

Szczes, A., Holysz, L., and Chibowski, E. (2017). Synthesis of hydroxyapatite for biomedical applications. *Adv. Colloid Interface Sci.* 249, 321–330. doi: 10.1016/j.cis.2017.04.007

Wang, K., Ma, Q., Zhang, Y. M., Wang, S. D., and Han, G. T. (2020). Ag NPs-assisted synthesis of stable Cu NPs on PET fabrics for antibacterial and electromagnetic shielding performance. *Polymers* 12:783. doi: 10.3390/polym12040783

Wang, Z., Zou, Y., Li, Y. W., and Cheng, Y. Y. (2020). Metal-containing polydopamine nanomaterials: catalysis, energy, and theranostics. *Small* 16:1907042. doi: 10.1002/smll.201907042

Zhang, C., Ou, Y., Lei, W. X., Wan, L. S., Ji, J., and Xu, Z. K. (2016). CuSO4/H2O2-induced rapid deposition of polydopamine coatings with high uniformity and enhanced stability. *Angew. Chem.* 55, 3054–3057. doi: 10.1002/anie.201510724

Zhou, H., and Lee, J. (2011). Nanoscale hydroxyapatite particles for bone tissue engineering. *Acta Biomater.* 7, 2769–2781. doi: 10.1016/j.actbio.2011.03.019

Conflict of Interest: The authors declare that the research was conducted in the absence of any commercial or financial relationships that could be construed as a potential conflict of interest.

frontiers in Bioengineering and Biotechnology

ORIGINAL RESEARCH
published: 13 April 2021
doi: 10.3389/fbioe.2021.665305

Graphene-Reinforced Titanium Enhances Soft Tissue Seal

Jianxu Wei†, Shichong Qiao†, Xiaomeng Zhang, Yuan Li, Yi Zhang, Shimin Wei, Junyu Shi and Hongchang Lai**

Department of Oral and Maxillo-facial Implantology, Shanghai Ninth People's Hospital, School of Medicine, Shanghai Jiao Tong University, Shanghai, China

The integrity of soft tissue seal is essential for preventing peri-implant infection, mainly induced by established bacterial biofilms around dental implants. Nowadays, graphene is well-known for its potential in biocompatibility and antisepsis. Herein, a new titanium biomaterial containing graphene (Ti-0.125G) was synthesized using the spark plasma sintering (SPS) technique. After material characteristics detection, the subsequent responses of human gingival fibroblasts (HGFs) and multiple oral pathogens (including *Streptococci mutans*, *Fusobacterium nucleatum*, and *Porphyromonas gingivalis*) to the graphene-reinforced sample were assessed, respectively. Also, the dynamic change of the bacterial multispecies volume in biofilms was evaluated using absolute quantification PCR combined with Illumina high-throughput sequencing. Ti-0.125G, in addition to its particularly pronounced inhibitory effect on *Porphyromonas gingivalis* at 96 h, was broadly effective against multiple pathogens rather than just one strain. The reinforced material's selective responses were also evaluated by a co-culture model involving HGFs and multiple strains. The results disclosed that the graphene-reinforced samples were highly effective in keeping a balance between the favorable fibroblast responses and the suppressive microbial growth, which could account for the optimal soft tissue seal in the oral cavity. Furthermore, the underlying mechanism regarding new material's bactericidal property in the current study has been elucidated as the electron transfer, which disturbed the bacterial respiratory chain and resulted in a decrease of microbial viability. According to the Kyoto Encyclopedia of Genes and Genomes (KEGG) database, the PICRUSt tool was conducted for the prediction of microbial metabolism functions. Consequently, it is inferred that Ti-0.125G has promising potentials for application in implant dentistry, especially in enhancing the integrity of soft tissue and improving its resistance against bacterial infections around oral implants.

Keywords: fibroblasts, bacteria, bioactive materials, peri-implant infections, sequencing

OPEN ACCESS

Edited by:
Kai Zheng,
University of Erlangen Nuremberg, Germany

Reviewed by:
Annabel Braem,
KU Leuven, Belgium
Håvard Jostein Haugen,
University of Oslo, Norway

****Correspondence:***
Hongchang Lai
hongchanglai@126.com
Junyu Shi
sakyamuni_jin@163.com

† These authors have contributed equally to this work

Specialty section:
This article was submitted to Tissue Engineering and Regenerative Medicine, a section of the journal Frontiers in Bioengineering and Biotechnology

Received: *07 February 2021*
Accepted: *24 March 2021*
Published: *13 April 2021*

Citation:
Wei J, Qiao S, Zhang X, Li Y, Zhang Y, Wei S, Shi J and Lai H (2021) Graphene-Reinforced Titanium Enhances Soft Tissue Seal. Front. Bioeng. Biotechnol. 9:665305. doi: 10.3389/fbioe.2021.665305

INTRODUCTION

The integrity of the soft tissue seal is vital for the long-term success of dental implants, which can prevent bacterial invasion and protect the underneath osseointegration. Nowadays, commercial pure titanium (Cp-Ti) has been commonly used as a transmucosal component of the implant for decades due to its superior biocompatibility, corrosion resistance, and excellent mechanical properties (Yue et al., 2014). However, there are some burning questions demanding prompt

solutions, such as Cp-Ti weakly performs in bactericidal effect and soft tissue integration. These limitations make transmucosal applications of implants susceptible to the colonization of oral pathogens, which contribute to the high risks of peri-implant infection and even lead to implant failure (Mellado-Valero et al., 2013).

Graphene (Gr), a two-dimensional carbon material, has not only showed the potential of its excellent biocompatibility to various mammalian cells but also exhibited an ideal bactericidal characteristic to microorganisms (Sanchez et al., 2012; Jia et al., 2016). Currently, Gr is often introduced into titanium by coating techniques such as chemical vapor deposition. However, the benefit of the coating layer is paired with the risk of layer peeling due to the compromised adhesion strength between Gr and titanium surface (Gu et al., 2018). Therefore, in order to tailor Cp-Ti with favorable bactericidal property and fast gingival attachment, a novel Gr-reinforced titanium (Ti-0.125G) was fabricated using the spark plasma sintering (SPS) technique in our study, which made Gr evenly dispersed in titanium with a tight bond.

Various bacterial aggregated and formed as biofilms on the implant surface are often regarded as the prelude of peri-implant infection. Previous investigations mainly used one or two microbes to evaluate the antibacterial activity of biomaterials, which was limited to reflect the reality in nature (Pereira et al., 2015; Schmidt et al., 2016; Sridhar et al., 2016). Here, for evaluating Ti-0.125 G's antimicrobial property more precisely, we mimicked the oral condition and constructed a multispecies biofilm containing typical pathogens of peri-implantitis like *Streptococci mutans* (*S. mutans*), *Fusobacterium nucleatum* (*F. nucleatum*), and *Porphyromonas gingivalis* (*P. gingivalis*). The dynamic changes of the bacterial multispecies biofilm were subsequently determined by absolute quantification PCR and 16S rRNA sequencing. In addition, although HGFs were mostly selected to assess the soft tissue attachment to biomaterials, the biomaterials' selective responses to bacteria and HGFs were often neglected. In this regard, a co-culture model involving the aforementioned pathogens and HGFs was established to evaluate the effect of Ti-0.125G on soft tissue seal. This model served as a better mimicry accounting for a "race-for-the-surface" between the bacterial multispecies and HGFs in the transmucosal region (Zhao et al., 2014).

Herein, a novel Ti-0.125G was fabricated by the SPS technique and aimed to be the emergence profile component for implants. The antibacterial activity of the Ti-0.125G against the above multiple pathogens was assessed by morphological observation, live/dead fluorescent staining, spread plate test, and Illumina high-throughput sequencing. Also, the soft tissue responses to Ti-0.125G were evaluated *in vitro*. The selective response of the Gr-reinforced sample was assessed by the co-culture model containing HGFs and the pathogenic multispecies. Besides, an attempt has been made to explain the underlying mechanism of Ti-0.125 G's bactericidal property. Ti-0.125G has a promising antibacterial potential and it may have a wide range of clinical applications in promoting soft tissue integration (**Supplementary Appendix Scheme**).

MATERIALS AND METHODS

Sample Preparation

Commercially pure titanium (Cp-Ti) powder (average diameter 30 μm, sphere-like, Grade IV) and graphene powder were obtained from the Institute of Solidification Science and Technology, Shanghai Jiao Tong University. For mixing graphene powder with Ti powder uniformly, we firstly added graphene powder into anhydrous ethanol (Sigma-Aldrich, United States) and performed 2–3 h ultrasonic dispersion. After 1,000–1,500 r/min magnetic stirring and 100–200 r/min ball-milling, the Ti/Gr composite powder (particle size of 10–60 μm) was eventually obtained through 240-mesh sieves. Next, spark plasma sintering (SPS) was carried out in the vacuum environment at 900°C and 50 MPa to obtain disk-shaped samples (10 mm diameter, 1 mm thickness). Then the disks were polished with *SiC* paper (150 rpm, 20 N, EcoMet 30, Buehler, Germany), and washed with anhydrous ethanol, acetone (Sigma-Aldrich, United States), and de-ionized (DI) water sequentially (30 min each) in an ultrasonic bath. The control and the test groups were labeled as Cp-Ti and Ti-0.125G, respectively.

Characterization of the Sample

The surface morphology of samples was detected using a scanning electron microscopy (SEM; ZEISS Gemini 300). The surface chemical characteristic was roughly detected by analyzing 10 points dispersed on the materials' surfaces using energy dispersive spectroscopy (EDS; OXFORD Xplore). The points on Cp-Ti were chosen randomly while they were elaborately picked out on Ti-0.125G, including the points inside and outside the graphene-like aggregates (which appeared black under SEM observation), as well as those on the boundary lines (N = 10). The phase transformation of the material was detected using X-ray diffraction (XRD; rigaku Ultima IV, Japan) patterns at a step size of 0.02° in a 2θ range of 20-80° (30 kV, 20 mA). The morphology of graphene was semi-quantitatively determined by Raman spectroscopy (λ = 532 nm, LabRAM HR Evolution, Horiba France SAS). The surface hydrophilicity was examined using a water contact angle measurement (DSA100, Kruss). The nano-hardness and elastic modulus of samples were characterized using a nano-indentation test (Agilent Tech, Nano Indenter G200). The surface roughness values involving Ra and Rq were determined using an atomic force microscopy (AFM; Nanonavi E-Sweep). The current-voltage (I-V) characteristics of specimens were obtained using an electrochemical analyzer (Reference 3,000, Gamry) with suitable voltage (−6–6 V) at the frequency of 100 mV/s. The material's electrochemical characteristics including Mott-Schottky curve were evaluated using an electrochemical system (VersaSTAT 3F, Ametek), and artificial saliva (A7990, Solarbio) was used as the liquid environment for testing.

Bacterial Multispecies Culture

Some typical oral pathogens, including gram-positive *Streptococcus mutans* (*S. mutans*; UA159), gram-negative *Fusobacterium nucleatum* (*F. nucleatum*; ATCC25586), and

Porphyromonas gingivalis (*P. gingivalis*; ATCC33277), were cultured in the brain heart infusion (BHI) broth medium (BD) under standard anaerobic conditions (80%N_2, 10% H_2, and 10% CO_2 at 37°C). Pathogens were harvested during the exponential growth phase for further use.

Bacterial Multispecies Morphology

After incubated with microorganisms for 24 and 48 h, all samples were fixed with 2.5% glutaraldehyde overnight at 4°C. All samples were dehydrated in a series of the ethanol concentration gradient of 30, 50, 75, 90, and 100 v/v% (aq.), and then were freeze-dried, coated with gold, and observed using SEM.

Live/Dead Staining of Bacterial Multispecies

After incubating for 6 and 24 h, the biofilms on specimens were stained with Live/dead® BacLight™ bacterial viability kit solution (Invitrogen). The 1:1 fluorochrome ratio of 10 min reacting time provided the optimum fluorescence effects. Consequently, the intact bacteria were stained fluorescent green, while the non-viable ones with compromised membranes were stained fluorescent red.

Spread Plate Test

The spread plate test demonstrated the antibacterial property during a period (6, 12, 24, and 48 h). In detail, 500 μL mixed bacterial suspension (containing ∼10^6 CFU/mL *S. mutans*, ∼10^7 CFU/mL *F. nucleatum*, and ∼10^7 CFU/mL *P. gingivalis*) was added to the glass disk (the blank). Each sample was placed in a 24-well plate to establish the biofilm. Then the adherent bacterial multispecies were collected in an ultrasonic bath (KQ5200E, 200 W, and 50 Hz) after vortexing. After that, 100 μL solution was evenly spread on the sheep blood agar dish with a sterile cell spreader. After being incubated in the anaerobic condition, colonies of multi-bacteria were counted. The relative colony-forming units [RCFU (%)] and the antibacterial rates [Ra (%)] were analyzed by the following equations:

RCFU (%) = (CFU of Cp-Ti or Ti-0.125G)/CFU of the blank × 100%

Ra (%) = (CFU of the control-CFU of the reinforced sample)/CFU of the control × 100%

Bacterial Biofilm Susceptibility and Viability Assay

Crystal violet (CV) staining and the 3-(4,5-dimethylthiazolyl-2)-2,5-diphenyltetrazolium bromide (MTT) test were used to investigate the bactericidal effect of materials on the formed biofilms. In the beginning, 500 μL BHI medium involving multispecies (∼10^6 CFU/mL *S. mutans*, ∼10^7 CFU/mL *F. nucleatum*, and ∼10^7 CFU/mL *P. gingivalis*) was added on the samples pre-placed in a 24-well plate to develop the biofilms. As for the biofilm susceptibility assay, after incubating for 12, 24, and 48 h, the supernatant was carefully aspirated, and the contaminated samples were rinsed and then fixed with methanol for 15 min at RT. After stained with CV for 10 min, the biofilm-disk complex was washed and dried overnight. The stained biofilm was dissolved with 95% ethanol and its absorbance was recorded at 550 nm wavelength. As for viability assay, after incubating with 0.5 mg/mL MTT for 2 h, the solution was gently decanted before DMSO was added to dissolve the formazan crystals. The absorbance was recorded at 490 nm wavelength.

Absolute Quantification of Bacterial Multispecies

Absolute quantification PCR (AQ-PCR) was conducted to illustrate the biomasses of bacterial multispecies quantitatively in a well-established biofilm After washed with phosphate-buffered saline (PBS; Sigma) to remove the non-adherent colonies. The biofilms were isolated using a 10-min ultrasonic bath at RT. According to the manufacturer's instructions, the total DNA extraction was performed using a DNA isolation kit (Omega). After preparing the mixture solution containing DNA, F-/R-primers, and signaling SYBR Green probe (Vazyme, Q112-02), the samples were reacted sequentially under the initial amplification cycle of 95°C for 5 min, followed by 40 cycles at 95°C for 15 s and 60°C for 30 s. Gene expressions were analyzed by corresponding quantification cycle (Cq) values. The primers used in this assay were listed in **Table 1** and were commercially synthesized (Personalbio Co., Ltd., Shanghai). The final result (the absolute quantity (X0) of each colony) was obtained according to the following correlation: Cq = -KlogX0 + b. The disposal was repeated in triplicate to ensure repeatability.

Illumina 16S rRNA Sequencing of Bacterial Multispecies

Herein, a 10 mm × 1 mm glass disk was regarded as the blank group due to its insulative characteristic compared to the metal disks, excluding the potential electrochemical interferences. The universal reaction of V3-V4 regions of the bacterial 16S rRNA genes was amplified by 338F/806R primers. PCR was conducted according to the previous instructions (Cheng et al., 2019). The unprocessed data was obtained after the first sequencing with an Illumina Miseq sequencing platform (PE300, Personalbio). After the process of quality control, the resulting sequences were clustered into amplicon sequence variants (ASVs) at a 100% similarity using Quantitative Insights Into Microbial Ecology 2 (QIIME2) dada2 clustering. Diagrams were produced with various aspects based on the abundance of ASVs combined with a set of multivariate analyzing tools. A prediction of microbial metabolism functions was provided using PICRUSt (Phylogenetic Investigation of Communities by Reconstruction

TABLE 1 | The prime sequences of bacteria in absolute quantification PCR.

Species	Sequence (5′ to 3′)	Amplicon size (bp)
S. mutans	F: GCCTACAGCTCAGAGATGCTATTC	118
	R: GCCATACACCACTCATGAATTGA	
F. nucleatum	F: CAGCTTGCCATACTGCG	404
	R: ACTGTTAGCAACTACCGATGT	
P. gingivalis	F: GGCCACAAGGGGACTGAGACA	182
	R: TTTAGCCGTCACTTCTTCTGTTGG	

of Unobserved States) tools according to the Kyoto Encyclopedia of Genes and Genomes (KEGG) database.

All 16S sequencing data on gene expressions have been deposited in NCBI's Sequence Read Archive (SRA) and are accessible through accession number PRJNA707007[1].

HGFs Culture

The primary HGFs were obtained from the healthy gingival tissue blocks clinically. All protocols related to humans in this study were approved by the Independent Ethics Committee of Shanghai Ninth People's Hospital affiliated to Shanghai Jiao Tong University School of Medicine (YBKA201906). The gingival tissues were harvested from young adults (18–35 years old, $n = 5$) during oral implant surgeries and cut into fragments with sterile scissors. Then the fragments were covered by glass slices in a 9 cm dish (Corning) and damped with Dulbecco's modified Eagle medium (DMEM; Sigma) containing 10% fetal bovine serum (FBS; Gibco) and 100 U/mL penicillin/streptomycin and 2 mM glutamine at 37°C in a standard humidified incubator. Primary HGFs were isolated 2 weeks later, and passages 2–7 were used in this study.

HGFs Morphology on the Sample

For investigating the morphology of adherent cells, SEM analysis was employed. Briefly speaking, HGFs of 1×10^4 cells per well were seeded on the samples on a 24-well plate. After 1 and 6 h of incubation, the samples were transferred to a new plate and fixed in 2.5% glutaraldehyde overnight at 4°C. The samples were dehydrated sequentially using ethanol solution with concentrations of 30, 50, 75, 90, and 100 v/v% (aq.). Then, the samples were placed in hexamethyldisilazane (HMDS) ethanol solutions and freeze-dried overnight. All samples were sputter-coated with gold before further characterization. Measurements were conducted thrice.

Morphologic details of HGFs were also observed using the confocal laser-scanning microscope (CLSM; Leica). The cells (1×10^4 cells/well) were seeded on the disks in a 24-well plate. At 6 and 24 h, the samples were rinsed twice with PBS, followed by fixed with 4% paraformaldehyde (PFA) and permeabilized with 0.1% Triton X-100. Then, the cellular cytoskeletons and nuclei were sequentially stained with phalloidin and DAPI (Invitrogen), respectively. The disposals followed the protocol provided by the manufacture.

HGFs Adhesion and Proliferation

5×10^4 Fibroblasts per well were cultured with the samples for 1, 4, and 7 days in 24-well plates. After being washed, the specimens were incubated with 500 μL of DMEM plus 50 μL of CCK-8 solution for 1 h at 37°C. The absorbance of the solution was recorded at 490 nm wavelength following the manufacturer's instructions. Besides, cell nuclei fluorescing with DAPI were detected under CLSM detection, and the disposal followed the aforementioned instructions.

[1]https://www.ncbi.nlm.nih.gov/sra/

HGFs Migration

The following experiments detected the migration property of HGFs on different surfaces horizontally and vertically. In wound healing assay, HGFs were grown on the samples overnight with a density of 1×10^6 cells per well until the cells reached confluence. Then, the cell monolayer was wounded carefully with a plastic pipette. After culturing for an additional 0, 6, and 24 h, the cell-disk complex was transferred to another plate and fixed in 4% PFA at each time point. Next, 0.1% Triton X-100 was used to permeate the cell membrane for 10 min. Similarly, DAPI-stained cell nuclei were visualized under CLSM. In fluorescence images, the original wounded region, namely, the area between each border of the monolayer was measured, so as to calculate the number of the migrated cells stained blue in the wounded areas.

In the transwell experiment, 0.4-mm-micropore transwell inserts (Corning Costar, Lowell, MA, United States) were placed upon the samples, which were pre-placed in a 24-well plate. First, HGFs were trypsinized and diluted with serum-free medium. Then, 750 μL DMEM with FBS was added in equal quantity to the lower chamber before 200 μL cell suspension (containing 2×10^5 cells/mL) was pipetted into the inner chamber. The cells were incubated for 12 h and fixed in 4% formaldehyde solution. Before being stained with 0.1 w/v% CV, the cells were permeabilized with 100% methanol at RT. The images of migrated cells were finally recorded under a light microscope (Leica).

qRT-PCR Analysis of HGFs

The total RNA was extracted using the total RNA isolation kit (Omega), then cDNA was generated using the PrimeScript 1st Strand cDNA synthesis kit (TaKaRa). Analyses were performed using the LightCycler 480 II thermocycler (Roche). The primers in this study were synthesized commercially (Shenggong). The corresponding genes and primer sequences were listed in **Table 2**.

Western Blot

HGFs were trypsinized and lysed with a protein extraction reagent. The concentration of protein was recorded sequentially using the Bradford Kit (Beyotime) and the microplate

TABLE 2 | Primer pairs of HGFs in real-time PCR analysis.

Gene	Primers (F = Forward, R = Reverse)
VCL	F: CGAATCCCAACCATAAGCAC
	R: GCCGACTTCCTTCACCATAG
ITGB1	F: TGGAGGAAATGGTGTTTGC
	R: CGTTGCTGGCTTCACAAGTA
FAK	F: CTCCTACTGCCAACCTGGAC
	R: GCCGACTTCCTTCACCATAG
FN1	F: GACCGAAATCACAGCCAGTAG
	R: CATCTCCCTCCTCACTCAGC
COL1A1	F: AAGACATCCCACCAATCACC
	R: CGTCATCGCACAACACCTT
GAPDH	F: TGTGTCCGTCGTGGATCTGA
	R: TTGCTGTTGAAGTCGCAGGAG

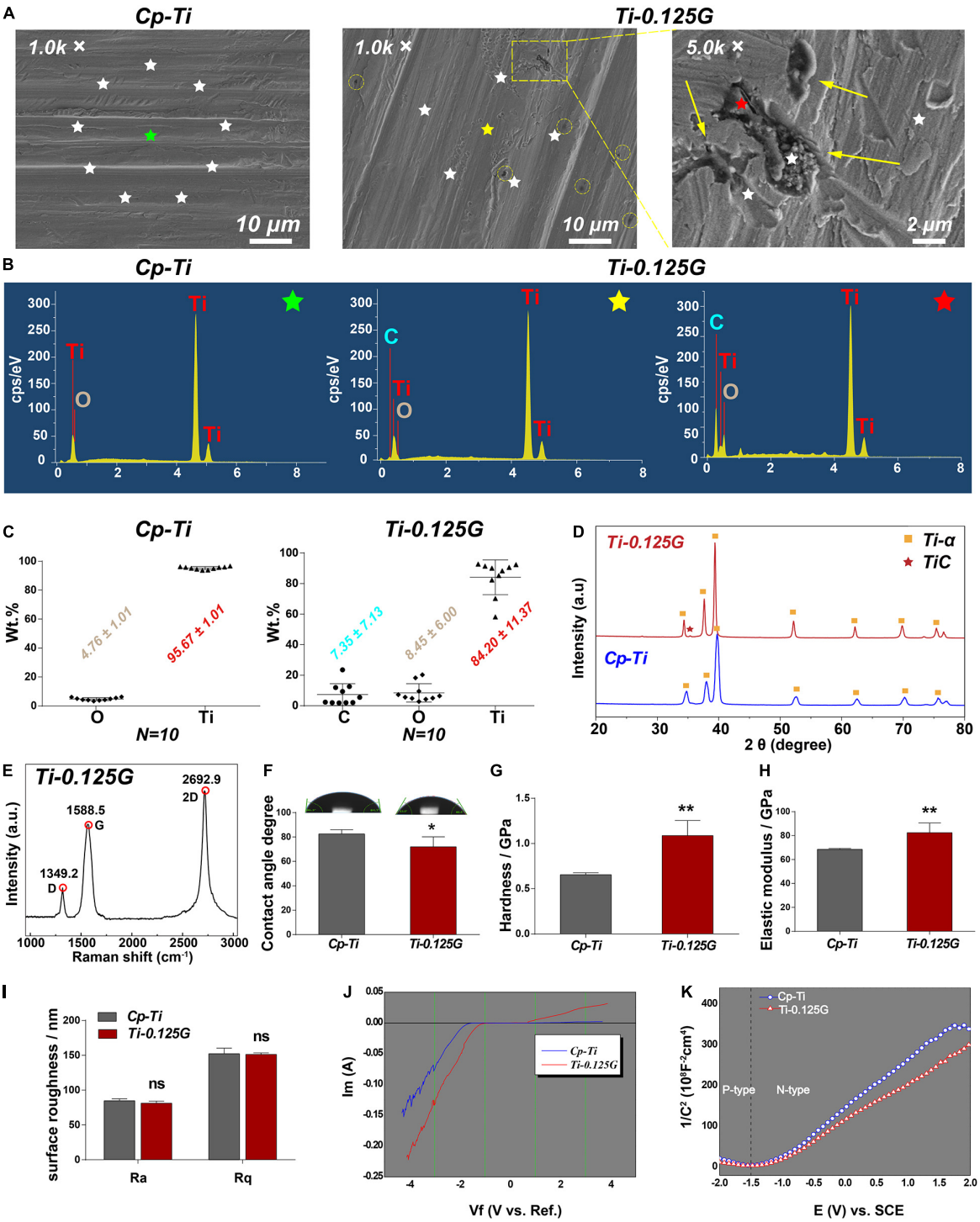

FIGURE 1 | Characterization of the sample. **(A)** SEM micrographs of the samples at different magnification. For the group of Ti-0.125G, the colored circles indicated the distribution of graphene aggregates at 1.0 K × magnification (scale bar = 10 μm), and the arrows marked the agglomerated graphene at 5.0 K × magnification (scale bar = 2 μm). **(B)** The respective EDS points' spectra of Cp-Ti (green-starred) and Ti-0.125G (the point outside the Gr-like aggregate marked as a yellow star and the point inside the Gr-like aggregate marked as a red star). **(C)** The elemental concentrations of C, Ti, and O were measured by EDS semi-quantitative technique (expressed as average ± standard deviation; $N = 10$). **(D)** XRD patterns of Cp-Ti and Ti-0.125G ($2\theta = 20–80°$). **(E)** Raman spectra of Ti-0.125G. **(F)** Wettability analysis (*$p < 0.05$). **(G,H)** Elastic modulus and nano-hardness analyses (**$p < 0.01$). **(I)** Surface roughness. No significant differences in Ra and Rq values. **(J)** The current-voltage (I-V) characteristics. **(K)** The conductivity type was depicted by the Mott-Schottky curves.

spectrophotometer (Bio-Tek, Epoch 2) at 595 nm wavelength. Proteins (20 μg) were loaded and then electro-transferred to a polyvinylidene difluoride (PVDF) membrane, which was incubated subsequently with specific primary antibodies as previously described (Wang X. et al., 2016). Ultimately,the protein bands were quantified using the imaging system (Vilber, Fusion Pulse 6).

The Co-culture Model of Bacterial Multispecies and HGFs

Three species (UA159, ATCC33277, and ATCC25586) and HGFs were sequentially seeded on the samples. 25 μL bacterial suspension [containing $\sim 10^4$ colony-forming units (CFU)/mL *S. mutans*, $\sim 10^5$ CFU/mL *F. nucleatum* and $\sim 10^5$ CFU/mL *P. gingivalis*] was pipetted on the disks in a 24-well plate and cultured anaerobically for 90 min, yielding the volume of 1×10^4 CFU/cm^2 on the specimens (Wang J. et al., 2016). The modified medium (MM) containing $\sim 10^4$ HGFs was distributed into each well and incubated aerobically for 6 and 24 h at 37°C. Specifically, MM was composed of DMEM with 10% FBS and 2% BHI (Foss et al., 2015), both of which were crucial in a balance without benefiting either the cells or the microbes at significant advantages. Bovine serum was added into MM and functionalized as the crevicular fluid surrounding dental implants. At each time point, HGFs were fixed and stained with phalloidin and DAPI, and their morphologies were visualized using CLSM.

Statistics

All data were presented as mean ± standard deviation of at least three independent experiments. The data were statistically analyzed by one-way ANOVA. $P < 0.05$ was regarded as significant.

RESULTS

Characterization of the Sample

We first characterized some key parameters of the Gr-reinforced Ti after the fabrication by the SPS technique. In SEM images, the surface morphology of the two groups seemed to be quite similar except for some black dots existed on Ti-0.125G surface. These dots were like multi-layer graphene aggregates at high magnification (**Figure 1A**). In contrast to the random emission for the Cp-Ti group, the X-rays for the Ti-0.125G group were designedly emitted to the Gr-like aggregates (black), the surrounding areas (gray) and their boundary lines without overlapping ($N = 10$). The EDS spectra (starred in **Figures 1A,B**) noted that C peak was unique in the spectrum of the Ti-0.125G compared to the Cp-Ti. And C peak seemed to exhibit a larger and higher shape since the X-ray emission targeted the graphene-like aggregate rather than the surroundings. Also, depending on the 10-point EDS results, we ultimately indicated that the elemental concentrations of the groups were analyzed as O and Ti accounting for 4.76 ± 1.01 Wt.% and 95.67 ± 1.01 Wt.%, respectively, in Cp-Ti and C, O, and Ti accounting for 7.35 ± 7.13 Wt.%, 8.45 ± 6.00 Wt.%, and 84.20 ± 11.37 Wt.%, respectively, in Ti-0.125G (**Figure 1C**). **Figure 1D** showed the phase and structure of the Cp-Ti and Ti-0.125G. The XRD patterns of the two groups were similar, and the data were well matched with the International Centre for Diffraction Data (ICDD) reference cards. While Ti-0.125G had a narrow Ti peak at 2θ degree of 39.38 (No. 03-065-9622), which was indexed into the C (101) of multi-layer graphene. Furthermore, the peak intensity of Ti-α/Gr at 34.34°and 37.64° was higher than the pure Ti-α peaks due to the presence of Gr. The peak 2θ = 35.34° (Ti-C peak) indicated graphene existed in the reinforced composites after SPS. Furthermore, the Raman spectrum of Ti-0.125G contained three prominent peaks near 1,349.2, 1,588.5, and 2,692.9 cm^{-1}, corresponding to the D, G, and 2D bands of graphene (Fu et al., 2017; **Figure 1E**).

Moreover, the wettability data showed that water droplets spread more widely on Ti-0.125G with smaller contact angles values compared to Cp-Ti (71.95° ± 3.32° < 82.47° ± 1.48°; $p < 0.05$). The values of Ti-0.125G in elastic modulus and the hardness were significantly higher as compared to the control ($p < 0.01$; **Figures 1G,H**). The roughness of the two materials showed no significant differences using AFM detections (**Figure 1I**). In terms of the electrochemical characteristics, when the voltage was -1 volt, the electron flow through both samples ceased (I = 0). As the voltage increased, a thicker oxide membrane such as titanium dioxide was built upon the Cp-Ti to block the electron flow further, which in contrast to the rising current through Ti-0.125G (**Figure 1J**). The Mott-Schottky curves demonstrated that Ti-0.125G was more electrically-conductive as its carriers were denser than those of Cp-Ti (**Figure 1K**).

Bactericidal Ability of the Sample

Bacteria of the exponential growth phase were utilized in the study (**Supplementary Appendix Figure 1**). From a micro-perspective, *S. mutans*, *F. nucleatum*, and *P. gingivalis* exhibited distinct cell shapes on Cp-Ti such as long-chain, long-rod, and short-rod after incubated for 24 and 48 h. Adversely, on the surface of Ti-0.125G, *S. mutans* showed impaired shapes with the flux of intracellular contents, *F. nucleatum* transformed to shorter rod-like structures, and a dozen of *P. gingivalis* remained hardly intact with the collapsed structures (**Figure 2A**). The fluorescent result depicted that Ti-0.125G decreased multispecies quantitatively compared to Cp-Ti (**Figure 2B**). From a macro-perspective, the spread plate test indicated that Ti-0.125G exhibited a stronger anti-multispecies potency by largely decreasing the number of CFU from 12–96 h (**Figure 2D**, $p < 0.01$). Moreover, Ti-0.125G resisted the formation and viability of multispecies biofilm noticeably since it was well-established (**Figures 2G,H**; He et al., 2017).

Quantitative and Proportional Analyses of Bacterial Multispecies

Streptococci mutans, the early colonizer of pathogenic multispecies biofilm, decreased substantially in the blank from 12–96 h. *F. nucleatum*, the later colonizers, increased

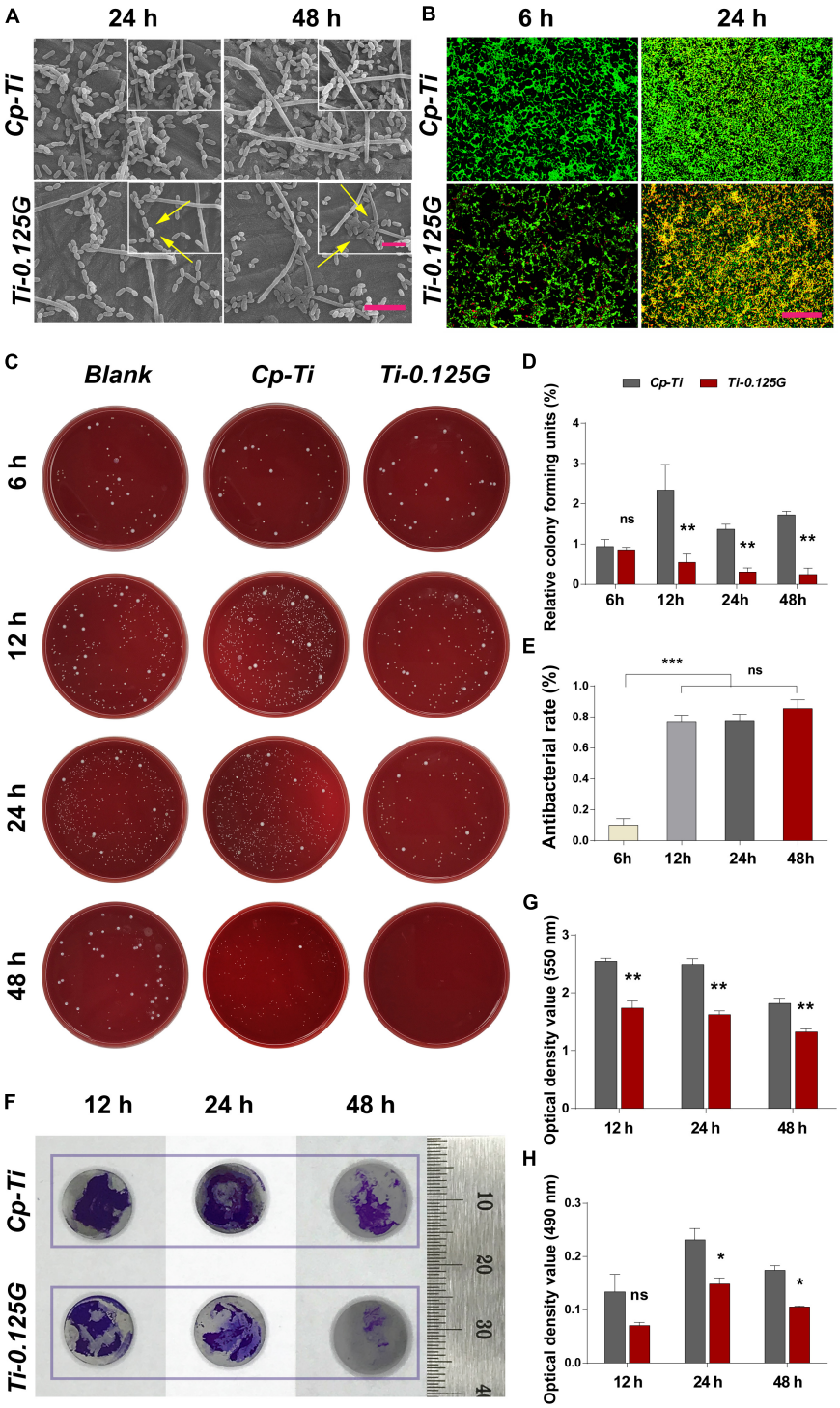

FIGURE 2 | The effects of samples against bacterial multispecies. **(A)** SEM micrographs of multiple bacteria on different samples after 24 and 48 h of incubation. Scale bar = 5 μm. The top right corner insert showed high magnification images (abnormal shapes of microbes were marked by white arrows). Scale bar for inserts = 2 μm. **(B)** CLSM images of bacterial multispecies cultured on different samples for 6 and 24 h. All microbial cells were stained with two well-described probes, interpreting live bacteria (green) and dead ones (red). Scale bar = 50 μm. **(C)** Typical images of re-cultured pathogens (containing *S. mutans, F. nucleatum,* and *P. gingivalis*) colonies on each substrate after 6, 12, 24, and 48 h of incubation. **(D)** and **(E)** Statistical results of relative CFUs and antibacterial rates of all groups. Noted that Ti-0.125G was the most effective in anti-bacteria after 6 h of interaction. $^{**}p < 0.01$, $^{***}p < 0.001$. **(F)** Measurements of biofilm's biomass by CV staining at 12, 24, and 48 h of incubation. Scale bar was supplemented. **(G)** The statistical analysis noted that Ti-0.125G significantly inhibited bacterial multispecies biofilm. $^{**}p < 0.01$. **(H)** Statistical analysis of MTT assay noted that Ti-0.125G reduced the viability of bacterial biofilms after 24 and 48 h of incubation. $^{*}p < 0.05$.

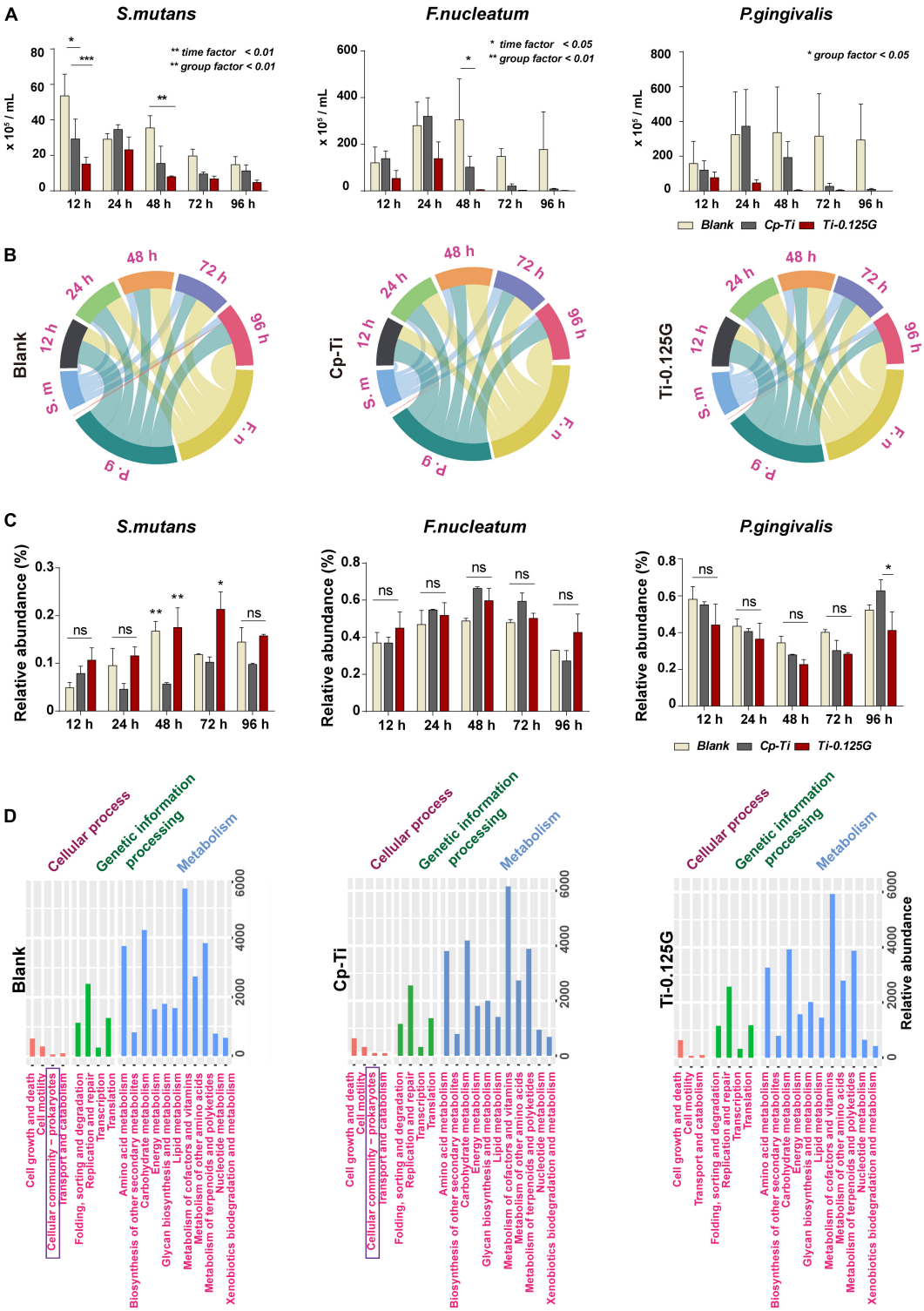

FIGURE 3 | Quantitative and proportional analyses of bacterial multispecies. **(A)** AQ-PCR detected the numbers of pathogens within the multispecies biofilm at 12–96 h of incubation. Dynamic changes in the proportional bacterial biomass in all groups presented in **(B)** a chord diagram and **(C)** a histogram quantitatively. **(D)** PICRUSt2 predictions of microbial functions based on the KEGG database. *$p < 0.05$, **$p < 0.01$.

in all groups from 12–24 h and grew to a maximum at 24 h synchronously, then showed a downward tendency in Cp-Ti and Ti-0.125G from 48–96 h (**Figure 3A**). Reportedly, bacterial multispecies biofilm reached peak viability around implants at 96 h (Bermejo et al., 2019). However, Ti-0.125G highlighted its bactericidal effect with the lowest biomasses of all strains after 96 h of interaction (**Table 3**). According to the proportional analyses, Ti-0.125G showed the most significant resistance against *P. gingivalis*, a principal etiological agent of implant infection (Zhu et al., 2019), with the thinnest arch in chord diagrams at 96 h (**Figure 3B**). Additionally, it was indicated that Ti-0.125G did not specifically target a particular strain except inhibiting *P. gingivalis* at 96 h compared to Cp-Ti (**Figure 3C** and **Supplementary Appendix Figure 2**). In light of Ti-0.125 G's favorable bactericidal effect, the mechanism may be relevant to cellular processes based on the KEGG database.

HGFs Responses to the Sample

A series of cellular responses including morphology, adhesion, proliferation, and migration on the sample were investigated in **Figure 4**. Initially, HGFs exhibited spherical morphologies on Cp-Ti, compared to the varied morphologies with minimal spread on Ti-0.125G. 6 h later, HGFs spread larger with multipolar spindle shapes on Ti-0.125G, resulting in a higher value of Ma/Mo elongation ($p < 0.01$). The similar morphologies were visualized by fluorescent staining on the Gr-reinforced sample (**Supplementary Appendix Figure 3**). Both at 6 and 24 h, HGFs adhered and increased densely on Ti-0.125G as compared to Cp-Ti ($p < 0.05$). In addition, Ti-0.125G exerted more potential to promote HGFs proliferation by extending the incubation time to 4 and 7 days (**Figure 4E**, $p < 0.01$). After interacted for 24 h, the horizontal and vertical migration capabilities of HGFs were triggered significantly by Ti-0.125G (**Figures 4F,H**, $p < 0.01$). Herein, Gr-reinforced sample sparked the HGFs' responses may be due to the increased expressions of adhesion-related genes (VCL, ITGB1, and FAK) and extracellular matrix (ECM) component-related genes (FN1 and COL1A1) at 6 and 24 h ($p < 0.05$). Moreover, the expression of p-FAK was activated with a higher ratio of p-FAK/FAK on the Gr- reinforced sample (**Figure 4K**, $p < 0.05$).

Co-culture Model of Bacterial Multispecies and HGFs

Previous studies focused more on a simple cell-bacteria co-culture model consisting of the mono-factor. Currently, we re-designed the study to more closely resemble natural conditions, as showed in **Figure 5**. In the competition against bacterial multispecies, fewer HGFs covered the Cp-Ti with wizened morphologies, while more robust HGFs grew on the Gr-reinforced sample. In terms of the cell coverage (%), HGFs adhering to the Gr-reinforced surface increased at 24 h ($p < 0.01$), implying that Ti-0.125G had the potential for enhancing soft tissue seal by benefiting the HGFs' viability in the presence of multispecies.

DISCUSSION

The current study fabricated a novel composite (Ti-0.125G) for the transmucosal profile and subsequently explored its dual effects regarding antibacteria and fast gingival attachment. Although better fibroblast adhesion is always in contradiction to less bacterial adhesion, the Gr-reinforced sample was expected to manipulate the "race-for-the-surface" between pathogenic multispecies and HGFs, thus to promote soft tissue integration in a pathogen-rich environment within transmucosal regions.

Reportedly, the SPS technique is more accessible to achieve large-scale productions (Rosa et al., 2012) and contributes to a robust bonding of Ti-0.125G, since titanium atoms acts as electron donors and Gr acts as electron acceptors (Subbiah et al., 2014). Chemical vapor deposition (CVD) is the common technology that deposit single-layer graphene sheets on Ti disk. Reportedly, it may face the grim risk of layer peeling due to compromised adhesion strength between Gr and Ti surface (Gu et al., 2018). In contrast, for our material fabricated by SPS technology, which can largely offset the effect of layer peeling due to the strong bonding between graphene and Ti. As the temperature increases, the bonding strength between Gr and titanium increases (Hu et al., 2017). In our study, the temperature elevated above 900°C, Gr reacted with Ti and eventually became TiC, improving the mechanical properties of the composites. Therefore, the elastic modulus and hardness of Ti-0.125G increased compared to Cp-Ti (**Figures 1G,H**). This advantages Ti-0.125G to be used as transmucosal appliances of the implant as the maximum stress was distributed at implant neck (Alvarez-Arenal et al., 2013), which requires a material with the better mechanical property. Currently, the surface roughness showed no significant variance after mixing with a small dose of

TABLE 3 | Numbers (expressed as the mean and standard error of the mean) of oral pathogens [$\times 10^5$ colony-forming units (CFU)/mL] detected by absolute quantification PCR throughout the whole culturing duration on different samples, using specific primers and probes aimed to the 16S *rRNA* gene.

Bacterial species	Incubation time (hours)	*Blank*	*Cp-Ti*	*Ti-0.125G*
		Mean (SEM) ($\times 10^5$ CFU/mL)		
S. mutans	12 h	53.6 (12.2)	29.3 (11.1)	15.1 (3.7)
	24 h	29.1 (3.2)	34.5 (2.8)	23.2 (7.3)
	48 h	35.4 (6.9)	15.4 (9.7)	8.0 (0.4)
	72 h	19.6 (6.9)	9.5 (1.2)	6.7 (1.6)
	96 h	14.7 (4.5)	11.3 (3.4)	4.7 (1.4)
F. nucleatum	12 h	120.9 (67.3)	138.7 (32.5)	53.4 (33.8)
	24 h	279.7 (101.9)	319.8 (80.0)	138.9 (71.3)
	48 h	304.5 (176)	102.3 (46.0)	4.7 (1.0)
	72 h	147.7 (33.3)	21.3 (9.0)	2.6 (1.0)
	96 h	177.7 (161.5)	8.2 (2.8)	1.6 (0.4)
P. gingivalis	12 h	157.4 (127.3)	121.3 (52.8)	77.13 (32.47)
	24 h	324.3 (246.0)	373.2 (210.4)	46.76 (17.99)
	48 h	336.2 (262.5)	193.1 (91.2)	4.2 (3.2)
	72 h	315.6 (244.3)	27.1 (16.9)	4.2 (2.9)
	96 h	294.0 (206.0)	10.6 (5.0)	0.4 (0.2)

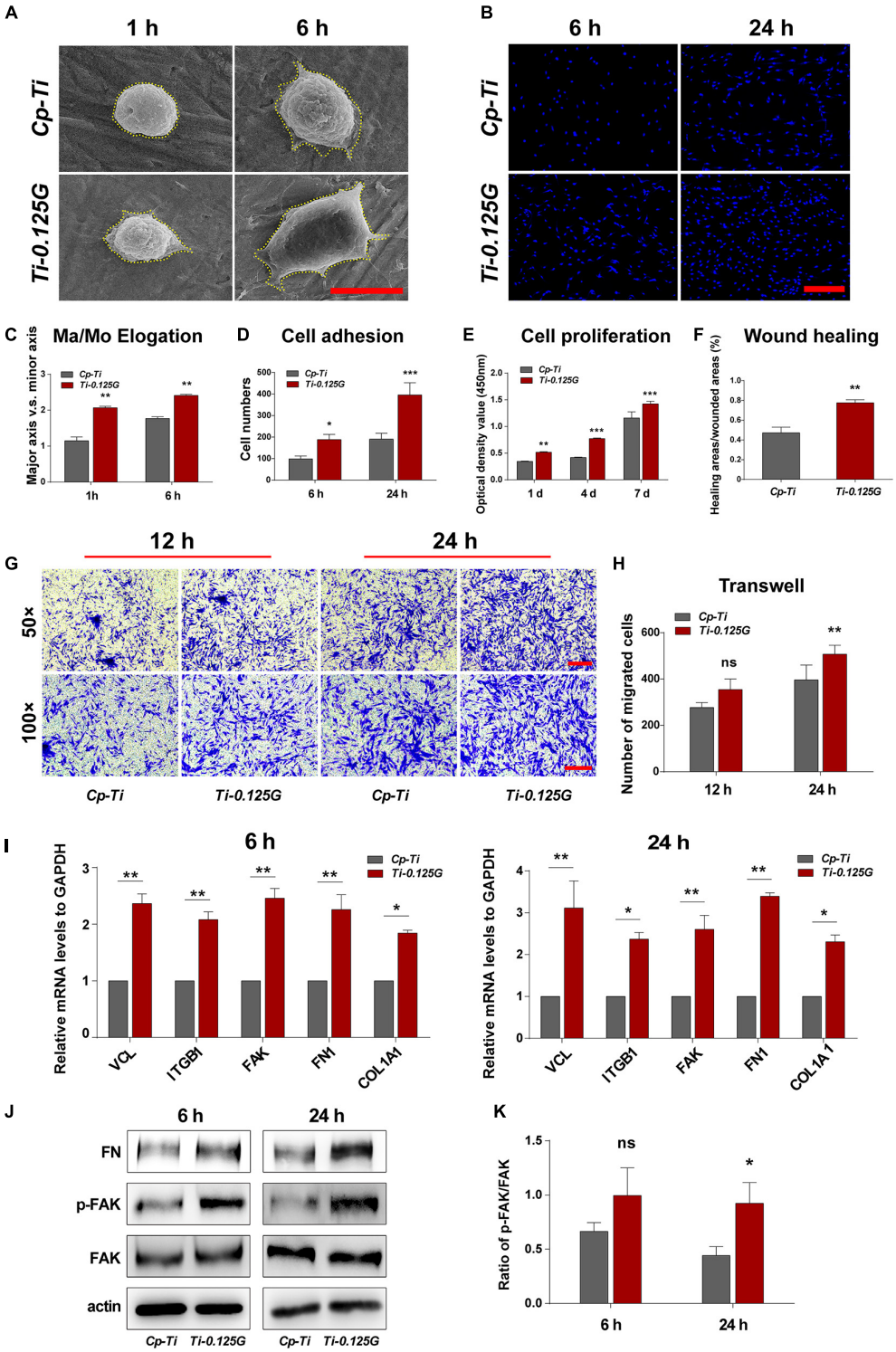

FIGURE 4 | HGFs Responses to the Sample. **(A)** SEM micrographs of HGFs on different samples at 1 and 6 h. Scale bar = 5 μm. **(B)** Initial cell adhesions were observed at 6 and 24 h under CLSM. Scale bar = 250 μm. **(C)** Major axis/Minor axis of HGFs after 1 and 6 h of incubation (**$p < 0.01$). **(D)** Statistical analysis of cell adhesion at the early stage (*$p < 0.05$, ***$p < 0.001$). **(E)** HGFs proliferation properties on different samples were detected *via* CCK-8 for 1, 4, and 7 days (**$p < 0.01$, ***$p < 0.001$). **(F)** Statistical analysis of wound healing assay (**$p < 0.01$) at 24 h. **(G,H)** Transwell assay at 12 and 24 h of incubation, CV-stained HGFs were counted as the migrated cells under the light microscope observation. Scale bar for 50 × /100 × magnification = 200 μm) (**$p < 0.01$). **(I)** Real-time PCR analyses of cell adhesion- and ECM component-related genes expression (*$p < 0.05$, **$p < 0.01$). **(J)** Western blot analyses of signaling proteins, including *FAK*, *p-FAK*, and *FN* **(K)** Increased *FN* adsorption on Ti-0.125G (*$p < 0.05$).

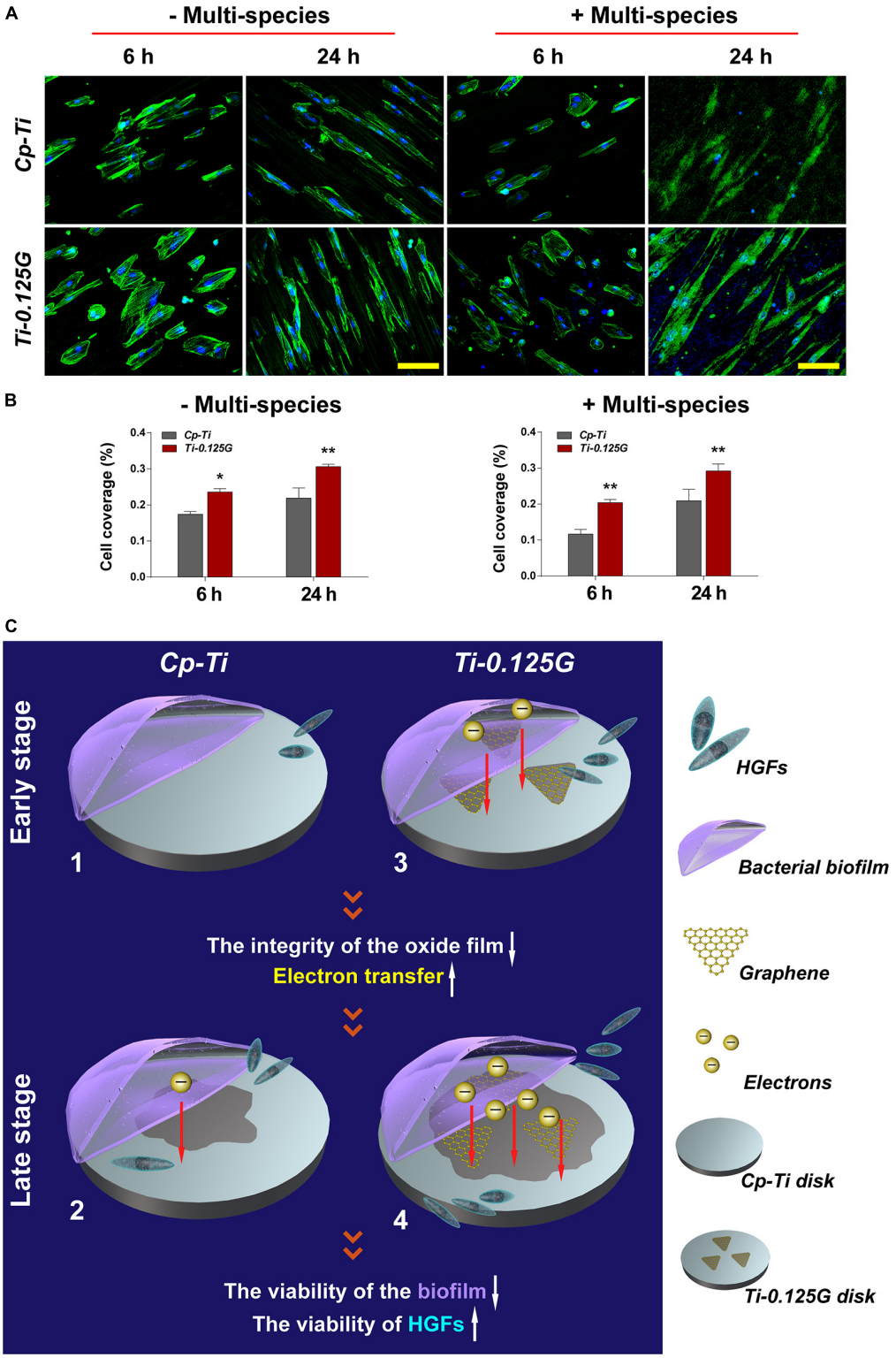

FIGURE 5 | The co-culture model of bacterial multispecies and HGFs. **(A)** CLSM images of HGFs seeded on different samples after 6 and 24 h of contamination by bacterial multispecies biofilms. The green and blue dyes marked the cytoskeleton and nuclei of HGFs, respectively. Scale bar = 100 μm. **(B)** Noted that cell coverage (%) on Ti-0.125G increased as compared to the control (*$p < 0.05$, **$p < 0.01$). **(C)** Schematic circuitry of the proposed mechanism to clarify the bactericidal ability of the Gr-reinforced sample. (1) and (3) The primary stages of a "race-for-the-surface" between bacterial multispecies biofilms and HGFs on Cp-Ti and Ti-0.125G, respectively. (2) and (4) The late stages of a "race-for-the-surface" between bacterial multispecies biofilms and HGFs on Cp-Ti and Ti-0.125G, respectively.

Gr (**Figure 1I**). In terms of the "race-for-the-surface," HGFs gain more advantages than oral pathogens as bacterial adhesion was inclined to reduce due to the surface roughness of Ti-0.125G was regarded as "minimally rough" (Ra < 0.2 μm) (Albrektsson and Wennerberg, 2004; Jin et al., 2019).

Possessing sufficient antimicrobial property is desirable for an implant component in transmucosal regions. Ti-0.125G was found to destroy the intact structures of *S. mutans*, *F. nucleatum*, and *P. gingivalis* extensively, which refined earlier studies mainly focusing on a single gram-positive or negative pathogen (Akhavan et al., 2011; Zhou and Gao, 2014). Multispecies biofilm was reported to be mature after 96 h of adhering (Bermejo et al., 2019), posing a severe challenge since it compromised the integrity of soft tissue around implants. Herein, we gained a deeper understanding of the bactericidal effect of Ti-0.125G on multispecies biofilms in the first 96 h. Given that the blank group inherently reproduced other biofilm models more than a one-off finding (Sánchez et al., 2011), the reliability of the results was ensured in the study. According to the analyses, Ti-0.125G exhibited an effective bactericidal potency against multiple pathogens broadly without suppressing one strain solely, in addition to its particular inhibitory effect on *P. gingivalis* at 96 h. The PICRUSt2 predictions further deduced that its anti-multispecies property might be related to the vanished pathway of "cell community–prokaryotes" in Ti-0.125G compared to the other groups (**Figure 3D**), implying that Ti-0.125G largely attenuated the synergistic effects between oral pathogens in multispecies biofilms (Lamont et al., 2002; Periasamy and Kolenbrander, 2009).

Apart from assessing the bactericidal potency, an ideal implant component was also expected to possess excellent bio-affinity and bio-activity. Previously, the Gr-induced biocompatibility was verified roundly in mesenchymal stem cells and periodontal ligament stem cells (Nayak et al., 2011; Xie et al., 2015). In the present study, Ti-0.125G was detected to motivate the viability, adhesion, and proliferation of HGFs *in vitro*, combined with stimulating HGFs' migration horizontally and vertically (**Figure 4**), which were crucial for protecting soft tissue integrity. ECM and integrins were also found to regulate soft tissue seal by activating FAK to trigger the downstream signals. Moreover, Ti-0.125G was investigated to activate the vinculin (VCL) and phosphorylate FAK, thus FN was deposited to promote HGFs' adhesion and mobility subsequently (Culp, 1978; Grinnell et al., 1980). Therefore, Ti-0.125G was recognized to enhance the histological integration of peri-implant soft tissue *in vitro*. Notably, the co-culture model of bacterial multispecies and HGFs was established to provide a more rigorous mimicry of the peri-implant environment. In the present model with multispecies invasion, Ti-0.125G contributed to the intact and distinct morphologies of HGFs (**Figure 5A**), indicating a stronger antibacterial potency than Cp-Ti. Given the bioactivity aforementioned, Ti-0.125G had the dual effects of serving as a promising transmucosal application by simultaneously benefiting HGFs' responses and suppressing bacterial growth. This paved the way for preserving a competent soft tissue seal around implants.

Ultimately, an attempt had been made to explore the underlying mechanism of bactericidal property, which could be elucidated as a viewpoint of electron transfer from the bacterial biofilm to the sample (**Figure 5C**). To the best of our knowledge, once the extracellular region enhanced the uptake of electrons from bacterial membrane respiratory protein, microbes eventually lost their viability as lacking sufficient ATP to supply the respiratory chain (Hartshorne et al., 2009). In the current model, pathogens exhibited negative potentials in artificial saliva (pH = 5.6–7.6) because their isoelectric points (IP) were generally lower than the surrounding pH, which formed the necessary condition for electron transfer. On the other hand, Gr was an ideal conductor and electron acceptor. TiC composite was also reported to facilitate electron transfer (Shen et al., 2015; Fu et al., 2017). Given the addition of Gr, it would be possible to break the integrity of the oxide film on Cp-Ti surface, activating this poorly conductive surface into a metal-semiconductor surface. In this way, Gr activated the sample to receive more electrons by making it more sensitive to conductivity. Also, the Fermi level of Ti-0.125G surface decreased since Gr possessed a bandgap close to 0 eV (Charlier et al., 2007). Hence, the facile transfer of electrons was achieved from the multispecies biofilm to the sample when the bacterial biofilm aligned its Fermi level with that of the Gr-reinforced substrate, which in turn lead to a decrease in microbial viability. Consequently, Ti-0.125G gained stronger resistance against multiple bacteria and won the "race-for-the-surface" to enhance soft tissue seal.

CONCLUSION

In conclusion, Cp-Ti and Ti-0.125G were synthesized using the spark plasma sintering (SPS) technique. In the current study, the antibacterial and biological properties of the samples were detected roundly. As compared to the control, Ti-0.125G was stronger to suppress the viability of bacterial multispecies biofilms (including *S. mutans*, *F. nucleatum*, and *P. gingivalis*) and activate HGFs bioactivity. The underlying mechanism of the bactericidal property might be summarized as the electron transfer from the bacterial multispecies biofilms to the Gr-reinforced sample. The 16S sequencing and PICRUSt2 functional predictions provided some instructive results.

DATA AVAILABILITY STATEMENT

The data presented in the study are deposited in the Sequence Read Archive, accession number PRJNA70700.

ETHICS STATEMENT

The studies involving human participants were reviewed and approved by the Independent Ethics Committee of Shanghai Ninth People's Hospital affiliated to Shanghai Jiao Tong University School of Medicine No. YBKA201906.

The patients/participants provided their written informed consent to participate in this study.

AUTHOR CONTRIBUTIONS

HL and JS contributed to the conception, design, data acquisition, analysis, and interpretation, and critically revised the manuscript. JW and SQ contributed to design, data acquisition, analysis, and interpretation, drafted, and critically revised the manuscript. XZ and YL contributed to data acquisition and analysis, critically revised the manuscript. YZ and SW contributed to interpretation, and drafted the manuscript. All authors gave final approval and agreed to be accountable for all aspects of the work.

FUNDING

The materials in the current study were provided by Huan She. This study was financially supported by the National Natural Science Foundation of China (81771116 and 81600902), Shanghai Sailing Program (19YF1425900), and Fundamental Research Program Funding of Ninth People's Hospital affiliated to Shanghai Jiao Tong University School of Medicine (JYZZ102).

SUPPLEMENTARY MATERIAL

The Supplementary Material for this article can be found online at: https://www.frontiersin.org/articles/10.3389/fbioe.2021.665305/full#supplementary-material

REFERENCES

Akhavan, O., Ghaderi, E., and Esfandiar, A. (2011). Wrapping bacteria by graphene nanosheets for isolation from environment, reactivation by sonication, and inactivation by near-infrared irradiation. *J. Phys. Chem. B* 115, 6279–6288. doi: 10.1021/jp200686k

Albrektsson, T., and Wennerberg, A. (2004). Oral implant surfaces: part 1–review focusing on topographic and chemical properties of different surfaces and in vivo responses to them. *Int. J. Prosthodont.* 17, 536–543.

Alvarez-Arenal, A., Segura-Mori, L., Gonzalez-Gonzalez, I., and Gago, A. (2013). Stress distribution in the abutment and retention screw of a single implant supporting a prosthesis with platform switching. *Int. J. Oral Maxillofac. Implants* 28, e112–e121. doi: 10.11607/jomi.2813

Bermejo, P., Sanchez, M. C., Llama-Palacios, A., Figuero, E., and Herrera, D. (2019). Topographic characterization of multispecies biofilms growing on dental implant surfaces: an in vitro model. *Clin. Oral Implants Res.* 30, 229–241. doi: 10.1111/clr.13409

Charlier, J.-C., Eklund, P., Zhu, J. and Ferrari, A. (2007). "Electron and phonon properties of graphene: their relationship with carbon nanotubes," in Carbon Nanotubes. Topics in Applied Physics. Vol 111, eds A. Jorio, G. Dresselhaus, and M.S. Dresselhaus (Berlin: Springer). doi: 10.1007/978-3-540-72865-8_21

Cheng, Y. F., Zhang, Q., Li, G. F., Xue, Y., Zheng, X. P., Cai, S., et al. (2019). Long-term effects of copper nanoparticles on granule-based denitrification systems: performance, microbial communities, functional genes and sludge properties. *Bioresour. Technol.* 289:121707. doi: 10.1016/j.biortech.2019.121707

Culp, L. (1978). Biochemical determinants of cell adhesion. *Curr. Top. Membr. Transp.* 11, 327–396. doi: 10.1016/S0070-2161(08)60752-2

Foss, B. L., Ghimire, N., Tang, R., Sun, Y., and Deng, Y. (2015). Bacteria and osteoblast adhesion to chitosan immobilized titanium surface: a race for the surface. *Colloids Surf. B Biointerfaces* 134, 370–376. doi: 10.1016/j.colsurfb.2015.07.014

Fu, C., Li, M., Li, H., Li, C., Qu, C., and Yang, B. (2017). Fabrication of graphene/titanium carbide nanorod arrays for chemical sensor application. *Mater. Sci. Eng. C Mater. Biol. Appl.* 72, 425–432. doi: 10.1016/j.msec.2016.11.089

Grinnell, F., Feld, M., and Minter, D. (1980). Fibroblast adhesion to fibrinogen and fibrin substrata: requirement for cold-insoluble globulin (plasma fibronectin). *Cell* 19, 517–525. doi: 10.1016/0092-8674(80)90526-7

Gu, M., Lv, L., Du, F., Niu, T., Chen, T., Xia, D., et al. (2018). Effects of thermal treatment on the adhesion strength and osteoinductive activity of single-layer graphene sheets on titanium substrates. *Sci. Rep.* 8:8141. doi: 10.1038/s41598-018-26551-w

Hartshorne, R. S., Reardon, C. L., Ross, D., Nuester, J., Clarke, T. A., Gates, A. J., et al. (2009). Characterization of an electron conduit between bacteria and the extracellular environment. *Proc. Natl. Acad. Sci. U. S. A.* 106, 22169–22174. doi: 10.1073/pnas.0900086106

He, J., Zhu, X., Qi, Z., Aldalbahi, A., Shi, J., Song, S., et al. (2017). The inhibition effect of graphene oxide nanosheets on the development of *Streptococcus mutans* biofilms. *Part. Part. Syst. Charact.* 34:1700001. doi: 10.1002/ppsc.201700001

Hu, Z., Chen, F., Xu, J., Ma, Z., Guo, H., Chen, C., et al. (2017). Fabricating graphene-titanium composites by laser sintering PVA bonding graphene titanium coating: microstructure and mechanical properties. *Compos. B Eng.* 134, 133–140. doi: 10.1016/j.compositesb.2017.09.069

Jia, Z., Shi, Y., Xiong, P., Zhou, W., Cheng, Y., Zheng, Y., et al. (2016). From solution to biointerface: graphene self-assemblies of varying lateral sizes and surface properties for biofilm control and osteodifferentiation. *ACS Appl. Mater. Interfaces* 8, 17151–17165. doi: 10.1021/acsami.6b05198

Jin, J., Fei, D., Zhang, Y., and Wang, Q. (2019). Functionalized titanium implant in regulating bacteria and cell response. *Int. J. Nanomedicine* 14, 1433–1450. doi: 10.2147/ijn.s193176

Lamont, R. J., El-Sabaeny, A., Park, Y., Cook, G. S., Costerton, J. W., and Demuth, D. R. (2002). Role of the *Streptococcus gordonii* SspB protein in the development of *Porphyromonas gingivalis* biofilms on streptococcal substrates. *Microbiology* 148(Pt 6), 1627–1636. doi: 10.1099/00221287-148-6-1627

Mellado-Valero, A., Buitrago-Vera, P., Sola-Ruiz, M. F., and Ferrer-Garcia, J. C. (2013). Decontamination of dental implant surface in peri-implantitis treatment: a literature review. *Med. Oral Patol. Oral Cir. Bucal.* 18, e869–e876. doi: 10.4317/medoral.19420

Nayak, T., Andersen, H., Makam, V., Khaw, C., Bae, S., Xu, X., et al. (2011). Graphene for controlled and accelerated osteogenic differentiation of human mesenchymal stem cells. *ACS Nano* 5, 4670–4678. doi: 10.1021/nn200500h

Pereira, J., Tavares, F., Lima, K., Carreiro, A., Henriques, B., Silva, F., et al. (2015). Relation between dental implant joint surfaces and biofilm formation. *Dentistry* 5:296. doi: 10.4172/2161-1122.1000296

Periasamy, S., and Kolenbrander, P. E. (2009). Mutualistic biofilm communities develop with *Porphyromonas gingivalis* and initial, early, and late colonizers of enamel. *J. Bacteriol.* 191, 6804–6811. doi: 10.1128/jb.01006-09

Rosa, V., Della Bona, A., Cavalcanti, B. N., and Nör, J. E. (2012). Tissue engineering: from research to dental clinics. *Dent. Mater.* 28, 341–348. doi: 10.1016/j.dental.2011.11.025

Sánchez, M. C., Llama-Palacios, A., Blanc, V., León, R., Herrera, D., and Sanz, M. (2011). Structure, viability and bacterial kinetics of an in vitro biofilm model using six bacteria from the subgingival microbiota. *J. Periodontal. Res.* 46, 252–260. doi: 10.1111/j.1600-0765.2010.01341.x

Sanchez, V. C., Jachak, A., Hurt, R. H., and Kane, A. B. (2012). Biological interactions of graphene-family nanomaterials: an interdisciplinary review. *Chem. Res. Toxicol.* 25, 15–34. doi: 10.1021/tx200339h

Schmidt, K., Auschill, T., Heumann, C., Frankenberger, R., Eick, S., Sculean, A., et al. (2016). Influence of different instrumentation modalities on the surface characteristics and biofilm formation on dental implant neck, in vitro. *Clin. Oral Implants Res.* 28, 483–490. doi: 10.1111/clr.12823

Shen, T., Zhou, X., Cao, H., Zheng, C., and Liu, Z. (2015). TiO2(B)-CNT-graphene ternary composite anode material for lithium ion batteries. *RSC Adv.* 5, 22449–22454. doi: 10.1039/C5RA01337B

Sridhar, S., Rodrigues, D. C., Abidi, Z., Wilson, T., Valderrama, P., Palmer, K., et al. (2016). In vitro evaluation of the effects of multiple oral factors on dental implants surfaces. *J. Oral Implantol.* 42, 248–257. doi: 10.1563/aaid-joi-D-15-00165

Subbiah, R., Du, P., Van, A., Suhaeri, M., Hwang, M., Lee, K., et al. (2014). Fibronectin-tethered graphene oxide as an artificial matrix for osteogenesis. *Biomed. Mater.* 9:065003. doi: 10.1088/1748-6041/9/6/065003

Wang, J., Li, J., Guo, G., Wang, Q., Tang, J., Zhao, Y., et al. (2016). Silver-nanoparticles-modified biomaterial surface resistant to staphylococcus: new insight into the antimicrobial action of silver. *Sci. Rep.* 6:32699. doi: 10.1038/srep32699

Wang, X., Lu, T., Wen, J., Xu, L., Zeng, D., Wu, Q., et al. (2016). Selective responses of human gingival fibroblasts and bacteria on carbon fiber reinforced polyetheretherketone with multilevel nanostructured TiO2. *Biomaterials* 83, 207–218. doi: 10.1016/j.biomaterials.2016.01.001

Xie, H., Cao, T., Viana Gomes, J., Castro Neto, A., and Rosa, V. (2015). Two and three-dimensional graphene substrates to magnify osteogenic differentiation of periodontal ligament stem cells. *Carbon* 93, 266–275. doi: 10.1016/j.carbon.2015.05.071

Yue, C., Kuijer, R., Kaper, H. J., van der Mei, H. C., and Busscher, H. J. (2014). Simultaneous interaction of bacteria and tissue cells with photocatalytically activated, anodized titanium surfaces. *Biomaterials* 35, 2580–2587. doi: 10.1016/j.biomaterials.2013.12.036

Zhao, B., van der Mei, H. C., Subbiahdoss, G., de Vries, J., Rustema-Abbing, M., Kuijer, R., et al. (2014). Soft tissue integration versus early biofilm formation on different dental implant materials. *Dent. Mater.* 30, 716–727. doi: 10.1016/j.dental.2014.04.001

Zhou, R., and Gao, H. (2014). Cytotoxicity of graphene: recent advances and future perspective. *Wiley Interdiscip. Rev. Nanomed. Nanobiotechnol.* 6, 452–474. doi: 10.1002/wnan.1277

Zhu, B., Meng, H., Huang, B., Chen, Z., and Lu, R. (2019). Detection of T. forsythia and other important bacteria in crestal and subcrestal implants with ligature-induced peri-implant infection in dogs. *J. Periodontol.* 90, 306–313. doi: 10.1002/jper.18-0223

Conflict of Interest: The authors declare that the research was conducted in the absence of any commercial or financial relationships that could be construed as a potential conflict of interest.

frontiers in Bioengineering and Biotechnology

ORIGINAL RESEARCH
published: 01 June 2021
doi: 10.3389/fbioe.2021.661734

Novel Bioactive Glass-Modified Hybrid Composite Resin: Mechanical Properties, Biocompatibility, and Antibacterial and Remineralizing Activity

Xiao Han[1,2†], Yan Chen[3†], Qian Jiang[4], Xin Liu[5*] and Yaming Chen[1,2*]*

[1] Jiangsu Key Laboratory of Oral Diseases, Nanjing Medical University, Nanjing, China, [2] Department of Polyclinics, Affiliated Hospital of Stomatology, Nanjing Medical University, Nanjing, China, [3] Department of Periodontology, Shanghai Key Laboratory of Craniomaxillofacial Development and Diseases, Shanghai Stomatological Hospital, Fudan University, Shanghai, China, [4] Department of Oral Surgery, Shanghai Ninth People's Hospital, Shanghai Jiao Tong University School of Medicine, College of Stomatology, Shanghai Jiao Tong University, National Center for Stomatology, National Clinical Research Center for Oral Diseases, Shanghai Key Laboratory of Stomatology, Shanghai, China, [5] Department of Dental Materials, Shanghai Biomaterials Research & Testing Center, Shanghai Ninth People's Hospital, Shanghai Jiao Tong University School of Medicine, College of Stomatology, Shanghai Jiao Tong University, National Center for Stomatology, National Clinical Research Center for Oral Diseases, Shanghai Key Laboratory of Stomatology, Shanghai, China

Secondary caries seriously limits the lifetime of composite resin. However, integrating all desirable properties (i.e., mechanical, antibacterial, bioactivity, and biocompatibility) into one composite resin is still challenging. Herein, a novel bioactive glass (BAG)-modified hybrid composite resin has been successfully developed to simultaneously achieve excellent mechanical properties, good biocompatibility, and antibacterial and remineralizing capabilities. When the mass fractions of BAG particles were added from 8 to 23 wt %, the original mechanical properties of the composite resin, including flexural strength and compressive strength, were not obviously affected without compromising the degree of conversion. Although the BAG incorporation of mass fractions of 16 wt % to 23 wt % in composite resins reduced cell viability, the viability could be recovered to normal by adjusting the pH value. Moreover, the BAG-modified composite resins that were obtained showed good antibacterial effects against *Streptococcus mutans* and enhanced remineralizing activity on demineralized dentin surfaces with increasing incorporation of BAG particles. The possible mechanisms for antibacterial and remineralizing activity might be closely related to the release of bioactive ions (Ca^{2+}, Si^{4+}), suggesting that its antibacterial and biological properties can be controlled by modulating the amounts of bioactive ions. The capability to balance the mechanical properties, cytotoxicity, antibacterial activity, and bioactivity makes the BAG-modified composite resin a promising prospect for clinical application. Our findings provide insight into better design and intelligent fabrication of bioactive composite resins.

Keywords: composite resin, bioactive glass, antibacterial activity, remineralization, biocompatibility

OPEN ACCESS

Edited by:
Kai Zheng,
University of Erlangen-Nuremberg, Germany

Reviewed by:
Matej Par,
University of Zagreb, Croatia
Saeid Kargozar,
Mashhad University of Medical Sciences, Iran
Jose Bauer,
Federal University of Maranhão, Brazil

***Correspondence:**
Qian Jiang
Jiangqian0720@hotmail.com
Xin Liu
Liuxin0556@163.com
Yaming Chen
yaming_chen@qq.com

†These authors have contributed equally to this work

Specialty section:
This article was submitted to Biomaterials, a section of the journal Frontiers in Bioengineering and Biotechnology

Received: *31 January 2021*
Accepted: *20 April 2021*
Published: *01 June 2021*

Citation:
Han X, Chen Y, Jiang Q, Liu X and Chen Y (2021) Novel Bioactive Glass-Modified Hybrid Composite Resin: Mechanical Properties, Biocompatibility, and Antibacterial and Remineralizing Activity. Front. Bioeng. Biotechnol. 9:661734. doi: 10.3389/fbioe.2021.661734

INTRODUCTION

Dental caries is one of the most prevalent bacterial infectious diseases worldwide and usually leads to defects in dental hard tissue. Over the past decades, due to its unique advantages such as simple operation, minimal invasiveness, and excellent esthetic restorative effects, direct composite resin filling has been the main treatment method to repair dental hard tissue defects. However, a higher annual failure rate has been reported for posterior composite resin restorations than for amalgam restorations, which is attributed primarily to secondary caries (Kopperud et al., 2012; Opdam et al., 2014; Astvaldsdottir et al., 2015). Generally, secondary caries occur on the tooth after composite resin filling because oral biofilm bacteria are more likely to accumulate on the surface of resin restorations, leading to demineralization of dental hard tissues due to acid production, thus destroying the tooth structure and further providing a way for bacterial invasion (Arun et al., 2021). Since secondary caries limit the lifetime of composite resin, it is urgent to endow composite resin with antibacterial properties and remineralizing capability. However, currently, integrating multiple desirable properties (e.g., high strength, antibacterial activity, remineralizing ability, and biocompatibility) into one composite resin is still challenging.

Over the past decade, to combat secondary caries, numerous efforts have been devoted to synthesizing various antibacterial monomers with quaternary ammonium salts or incorporating antibacterial drugs/fillers [e.g., chlorhexidine, fluoride, zinc oxide (ZnO), and silver (Ag)] into the resin matrix to improve the antibacterial properties (Cheng et al., 2012; Zhang et al., 2014; Cocco et al., 2015; Farrugia and Camilleri, 2015; Arun et al., 2021). However, the antibacterial effect of Ag- or ZnO nanoparticle (NP)-based composite resins has been reported not to be long-lasting, and the release of antibacterial agents (e.g., monomer/drug/Ag^{+}) would impair the mechanical properties and increase the risk of damage to human health. Moreover, these antibacterial monomer/drug/metal oxide NPs have no remineralizing ability, largely impeding their development as composite resins (Cocco et al., 2015; Arun et al., 2021). Recently, promising alternatives such as bioactive ceramic particles [e.g., calcium phosphate nanoparticles (NACPs), bioactive glass (BAG), zinc-doped phosphate-based glass] have been exploited as inorganic fillers to construct orthodontic adhesives or composite resins, which have been found to achieve both antibacterial and remineralizing effects (Liu et al., 2018; Par et al., 2019b; Bhadila et al., 2020; Lee et al., 2020). Among bioactive ceramic particles, BAG has attracted increasing interest in dental applications such as toothpaste, dentin desensitizers, orthodontic adhesives, and experimental composite resins (Wang et al., 2010; Yang et al., 2016; Al-Eesa et al., 2019; Aponso et al., 2019; Par et al., 2019a). In particular, BAG-based composites have been reported to inhibit bacterial biofilm penetration into marginal gaps of simulated tooth restorations, showing great potential to eliminate secondary tooth decay after composite resin restorations (Khvostenko et al., 2016). Nevertheless, the incorporation of bioactive materials may reduce the physical properties of composite resin and cause toxic effects (Kurata et al., 2011; Korkut et al., 2016; Cheng et al., 2017). Despite a few studies focused on developing BAG-based bioactive composite resins (Korkut et al., 2016), it is still unclear whether the antibacterial effect is dependent on direct contact with bacteria or the release of substances (e.g., Ca^{2+} or Si^{4+} ions). In addition, the potential risk for the application of BAG to composite resin remains elusive. To date, a systematic understanding of the influence of precise composition control of BAG fillers on their mechanical, antibacterial, remineralizing, and biological effects is still lacking. More importantly, the related antibacterial, remineralizing, and biological mechanisms of BAG-modified composite resins have not been completely elucidated, making it difficult to further improve their mechanical performance and enhance their antibacterial and remineralizing activities.

Herein, in this work, we developed a novel bioactive hybrid composite resin with good mechanical properties, excellent biocompatibility, and antibacterial and remineralizing activity. Subsequently, the regulatory effects of BAG incorporation on the comprehensive properties of the as-prepared composite resins were systematically investigated. Moreover, a possible antibacterial, remineralizing, and cytotoxicity mechanism of bioactive composite resins was proposed based on ion release and pH value. Overall, the BAG-modified composite resins obtained were highly promising composite resin systems for achieving both antibacterial and remineralizing activity with low cytotoxicity, providing insights into better design and intelligent fabrication of bioactive composite resins.

MATERIALS AND METHODS

Preparation of BAG-Modified Hybrid Composite Resin

The experimental BAG-modified composite resins were prepared by mixing the resin matrix and inorganic fillers containing various mass fractions of BAG particles (0, 8, 16, and 23%) by DMG Dental Material Gesellschaft mbH (Hamburg, Germany). As shown in **Table 1**, the as-prepared composite resins had filler/resin ratios similar to the ratios used in commercial composite resin systems (EcuSphere^{TM}; DMG, Hamburg, Germany). The matrix resins were formulated from commercially available monomers and the components

TABLE 1 | The composition of different parameters for BAG-modified composite resin formulations.

Materials	Resin[a] (wt.%)	Total filler (wt.%)		
		Barium glass[b]	Bioactive glass	Fumed silica
BAG0	24%	73%	0%	3%
BAG8	24%	65%	8%	3%
BAG16	24%	57%	16%	3%
BAG23	24%	50%	23%	3%

[a] *EcuspHere resin^{TM} containing photoinitiator and stabilizer provided by the manufacturer.*

[b] *The average particle size of barium glass fillers is ~0.7 μm.*

of the photoinitiator system (EcuSphere^{TM}; DMG, Hamburg, Germany). The surface silanized barium glass filler and the fumed silica were formulated from commercially available inorganic fillers (EcuSphere^{TM}; DMG), and 45S5 BAG particles with an average particle size of 7.26 μm were provided by Beijing Datsing Bio-Tech Co., Ltd. (Beijing Datsing Company, Beijing, China). Briefly, the photoinitiator and organic amine activator were added to the resin monomer mixture and then the viscous resin matrix was obtained. Subsequently, BAG particles were incorporated into inorganic fillers at 0, 8, 16, and 23 wt % by replacing the same amount of silanized barium glass filler with a total filler load maintained at 76 wt %, and then the inorganic fillers were mixed with the resin matrix using a centrifugal mixing device (Speed-Mixer DAC 150 FVZ, Hauschild, Germany). Finally, four kinds of BAG-modified composite resins were prepared, which were designated BAG0 (control), BAG8, BAG16, and BAG23 according to the weight fractions of incorporated BAG particles. Microstructural characterization and element analysis of the as-prepared composite resins were examined using scanning electron microscopy (SEM) with energy-dispersive X-ray spectroscopy (EDS) mapping (Mira3, Tescan, Czechia).

Flexural Strength Testing

According to the requirement of ISO 4049 (Standardization IOF, 2019), bar-shaped test specimens (25 × 2 × 2 mm) were fabricated in stainless-steel split molds and cured by visible light in five overlapping sections on each upper and lower side. After 24-h storage in distilled water at 37°C, five specimens for each composite type were conducted to a three-point bending test using a universal testing machine (Lloyd Instruments Ltd., Fareham Hants, United Kingdom) at a cross-head speed of 0.5 mm/min. Flexural strength was calculated in megapascals (MPa) with the following equation:

$$\sigma_f = \frac{3PL}{2bd2} \quad (1)$$

where σ_f is the flexural strength, P is the load at fracture (N), L is the specimen span (mm), b is the specimen width (mm), and d is the specimen height (mm).

Compressive Strength Testing

Cylindrical-shaped test specimens with 4 mm in diameter and 6 mm in height were prepared in stainless-steel split molds and cured by visible light in five overlapping sections on each upper and lower side and stored in water at 37°C prior to test. After 24 h, five specimens from each composite type were tested using a universal testing machine (Lloyd Instruments Ltd., Fareham Hants, United Kingdom) at a cross-head speed of 1 mm/min. Compressive strength was determined in MPa with the following equation:

$$\sigma_c = \frac{P}{S} = \frac{P}{\pi \times r^2} \quad (2)$$

where σ_c is the compressive strength, P is the maximum load at fracture (N), S is the specimen cross-section area (mm^2), and r is the specimen cross-sectional radius (mm).

Microhardness Testing

Five disk-shaped specimens 6 mm in diameter and 4 mm in thickness were prepared for each composite resin group. The Vickers microhardness of each composite type was measured on the test specimen surface by a microhardness tester (Shanghai Taiming Optical Instrument Co., Ltd., Shanghai, China) with a 50 gf load (0.490 N) for 15 s. The Vickers microhardness was calculated from the expression HV = 0.1891 F/d^2, where HV is the Vickers hardness, F is the test load (N), and d is the mean value of the indentation's diagonal lengths (μm).

Degree of Conversion

The as-prepared composite samples (n = 3/group) were completely cured by visible light for 30 s. The uncured samples were pressed into KBr pellets (d = 1 cm) using spectroscopically pure KBr. The DC was determined by a Fourier transform infrared spectrometer (IR/Nicolet 6700, Thermo Fisher, United States). The spectra of unpolymerized and polymerized composite specimens were recorded at room temperature, corrected by subtracting the background and then converted into the absorbance mode. The DC (%) was calculated using the relative change in the peak height of the spectral band at 1638 cm^{-1} (aliphatic C = C stretching), and the band at 1610 cm^{-1} (aromatic C = C stretching) was used as a reference. DC was calculated according to the following equation:

$$DC\,(\%) = \left(1 - \frac{\left(\frac{1638\ cm^{-1}}{reference}\right)_{peak\ height\ after\ curing}}{\left(\frac{1638\ cm^{-1}}{reference}\right)_{peak\ height\ before\ curing}}\right) \times 100\%$$

Agar Diffusion Test for Cytotoxicity

According to ISO 10993-5 and ISO 7045 (Standardization IOF, 2009, 2011), the agar diffusion test as a cytotoxicity barrier testing method was performed for the non-specific cytotoxicity of the leachable components of the as-prepared composite specimens after diffusion through agar. Disk-shaped specimens 6 mm in diameter and 4 mm in thickness were used for cytotoxicity analysis. In detail, L929 cells (Cell Bank of the Chinese Academy of Sciences, Shanghai, China) were propagated in Eagle's minimum essential medium (MEM) (Gibco, United States) with 10% fetal bovine serum (FBS) (Gibco, United States). Cell suspensions (2.5 × 10^5 cells/ml) were seeded in cell culture dishes (Corning, NY, United States) and incubated at 37°C with 5% CO_2. After 24 h, the medium was replaced with 10 ml of freshly prepared agar medium containing 2 × MEM, and then 10 ml of neutral red solution (0.01% in phosphate-buffered saline, San Aisi Co., Ltd., Shanghai, China) was added to the solidified culture medium in the dark for 20 min. The test specimens were placed on the agar surface along with the positive (polyvinylchloride containing organotin additive sheet) and negative controls (high-density polytetrafluoroethylene sheet) in the same cell culture dish. After 24 h of incubation, as shown in **Tables 2–4**, the decolorization index, lysis index, and cytotoxicity scoring grade were assessed under an optical microscope (Olympus, Japan) according to ISO 7405.

TABLE 2 | The decolorization index.

The decolorization index	Description
0	No decolorization
1	Decolorization only under the specimen
2	Decolorization in a zone not greater than 5 mm from the specimen
3	Decolorization in a zone not greater than 10 mm from the specimen
4	Decolorization in a zone greater than 10 mm from the specimen
5	The total culture is decolorized

TABLE 3 | The cell lysis index.

The cell lysis index	Description
0	No cell lysis detectable
1	Less than 20% cell lysis
2	20–40% cell lysis
3	40–60% cell lysis
4	60–80% cell lysis
5	Greater than 80% cell lysis

TABLE 4 | Cytotoxicity scoring grade.

The scoring grade	Cell response[a]	Description
0	0	Non-cytotoxic
1	1	Slightly cytotoxic
2	2–3	Moderately cytotoxic
3	4–5	Severely cytotoxic

[a]*Cell response scored by the median of the decolorization index and the cell lysis index from each group conducted in quadruplicate.*

MTT Assay for Cytotoxicity

According to ISO 10993.5 and ISO 10993.12 (Standardization IOF, 2009, 2012), disk-shaped specimens 6 mm in diameter and 4 mm in thickness were fabricated. To prepare the extracts of the experimental composite resins, the as-prepared composite specimens were fully immersed in MEM with 10% FBS under sterile conditions at 37°C for 24 h based on a ratio of 3 cm^2/ml [surface area of the sample to volume of extraction vehicle]. The extracts were diluted by twofold serial dilutions in the culture medium and resulted in the following concentrations: 12.5, 25, 50, and 100%. The pH value of the extract of each type of composite resin was measured with an ultrabasic benchtop pH meter (Denver Instrument Co., United States). To clarify the role of pH values on the cytotoxicity, 1 N HCl was added into the extracts slowly, with stirring, to adjust the pH value of the extracts to neutral. Cytotoxicity was assessed by using the MTT assay. Briefly, L929 cells were seeded in 96-well plates for 24 h and then treated with different concentrations of extracts of four kinds of experimental composite resins at 12.5, 25, 50, and 100% for 24 h. Following 24 h of treatment, MTT solution (20 μl, 5 mg/ml) (Amresco, Solon, OH, United States) was added to each well and incubated for an additional 4 h in a 37°C incubator. Subsequently, 150 μl of DMSO was added to dissolve the formazan crystals. The absorbance at 570 nm and 630 nm was measured by a microplate reader (Multiskan GO, Thermo Scientific, Waltham, MA, United States).

Determination of Ion Release and Antibacterial Activity

The antibacterial activity of four experimental composite resins was evaluated using both direct contact and indirect methods of measuring the antibacterial effects of extracts. *Streptococcus mutans* (UA159) was obtained from Shanghai Key Laboratory of Stomatology, Ninth People's Hospital, Shanghai Jiao Tong University School of Medicine (Shanghai, China). Disk-shaped specimens 6 mm in diameter and 4 mm in thickness were used for antibacterial activity measurement. In detail, *S. mutans* (UA159) at a density of 1×10^6 colony-forming units (CFU)/ml in 0.2 ml was seeded on the surface of as-prepared composite specimens in a sterilized 24-well plate containing brain heart infusion (BHI) (1.8 ml/well) (Difco Laboratories, United States) at 37°C under standard anaerobic conditions (80% N_2, 10% H_2, 10% CO_2) for 24 h. After incubation for 24 h, the bacterial suspension was collected from the experimental composite resins. Following dilution with BHI, 0.1 ml of bacterial suspension was placed on a BHI agar plate and further incubated for 24 h; subsequently, the number of bacterial CFU was counted according to previous studies (He et al., 2015; Yu et al., 2017). Furthermore, to determine whether the factors released by the experimental composite resin had antibacterial effects, each type of composite resin specimen was immersed in BHI (2 ml) for 24 h and 72 h. Subsequently, the BHI extracts of composite resins were collected to culture *S. mutans* for 24 h. Then, the bacterial suspension was diluted and placed on agar plates. The bacterial CFU were counted after culturing for 24 h. *S. mutans* was seeded on each type of composite resin at 37°C under standard anaerobic conditions. After being cultured for 24 h, the bacterial samples on the composite resin were fixed with 2% glutaraldehyde, followed by progressive dehydration with anhydrous ethanol, critical-point drying, and gold spraying. The bacterial morphology and adhesion were characterized by SEM (Hitachi S-3400N, Hitachi, Japan). In addition, the concentrations of Si and Ca in the BHI extracts of the as-prepared composite resin specimens after 24 and 72 h were measured by inductively coupled plasma mass spectrometry (ICP-MS) (Agilent Technologies 5100, Agilent Technologies Co., Ltd., United States).

Determination of Dentin Remineralization

Dentin remineralization was studied *in vitro* using simulated body fluid (SBF). SBF with a pH of 7.4 was prepared by dissolving the reagent chemicals NaCl, $NaHCO_3$, KCl, $K_2HPO_4{\cdot}3H_2O$, $MgCl_2{\cdot}6H_2O$, $CaCl_2$, and Na_2SO_4 in deionized water according to a previous study (Mariano et al., 2009). Disk-shaped resin specimens (diameter: 6 mm, height: 4 mm) with different loadings of BAG were prepared. Human teeth were extracted, and the first premolars for orthodontic treatment needs from patients at the Department of Oral Surgery, Ninth People's Hospital, Shanghai Jiao Tong University School of Medicine were collected

and cleaned. The study was approved by the Ethics Committee of Ninth People's Hospital, Shanghai Jiao Tong University School of Medicine. Each tooth was sectioned to obtain 1-mm-thick dentin disks along its horizontal axis below the enamel–dentin junction using a hard tissue slicer (Leica SP1600, Leica, Germany). Prior to use in the experiment, all dentin disk specimens were washed with 0.5% NaClO for 5 min and sterilized with an excess of deionized water and 70% ethanol for 20 min. Subsequently, all dentin disk specimens were completely demineralized in 10% phosphoric acid for 12 h at 25°C (Tezvergil-Mutluay et al., 2017). Each type of cured composite resin specimen was immersed with one demineralized dentin disk specimen in SBF at pH 7.4 and 37°C for 21 days without changing the aqueous medium (Xie et al., 2008). After immersion, all dentin samples were dried at room temperature and cleaned with acetone, and then the dentine surface morphology was observed and analyzed by SEM-EDS (Mira3, Tescan, Czechia).

RESULTS

Characterization of Physicochemical and Mechanical Properties of BAG-Modified Composite Resin

As shown in **Figure 1**, SEM-EDS elemental mapping showed a uniform elemental distribution of Ca, Na, and Si in the BAG-modified composite resins, and the relative content of each element in the experimental composite resins increased with increasing BAG content. After immersion in deionized water for 24 h, the flexural strength and the compression strength in the composite resin were not obviously reduced by the addition of up to 23 wt % BAG particles (**Figures 2A,B**). When the mass ratio of BAG particles incorporated into the composite was 8 wt %, there was no significant difference in the microhardness between the BAG8 group (50.9 ± 1.93) and the control group (48.33 ± 5.18) ($p > 0.05$). When the mass ratio of incorporated BAG particles was increased to 16 and 23 wt %, the microhardness was significantly lower than the microhardness of the control group and the BAG8 group ($p < 0.05$) (**Figure 2C**). Furthermore, after immersion in cell or bacterial culture medium for 24 h, both extracts of composite resin without BAG particles exhibited a pH between 7.2 and 7.4 and increased to 8.8–8.9 for the BAG23 groups, showing a dose-dependent increase in the pH value with increasing BAG incorporation (**Figures 2D,E**). Moreover, the degree of conversion (DC) value was not affected in the experimental resin system by increasing the BAG amounts (**Figure 2F**).

Biocompatibility Assessment of BAG-Modified Composite Resin

According to ISO 10993.5 (Standardization IOF, 2009), an *in vitro* cytotoxicity assay is the first test to evaluate the biocompatibility of biomaterials for medical use. Therefore, two test methods, the agar diffusion test and MTT assay, were used in this study. In the agar diffusion test, the cytotoxic potential of the leachable contents of the test samples was determined after diffusion through an agarose layer by scoring the decolorization area and assessing cell lysis of the cell culture. The decolorization zones in the different groups are presented in **Figure 3**. The cytotoxicity scoring grade based on the decolorization index and the cell lysis index for the different groups are shown in **Table 5**. The negative control showed no cellular decolorization and lysis, while the positive control caused severe cellular decolorization and lysis with a cytotoxicity score of 3. In the various experimental composite resin groups, increasing the amount of BAG fillers from 0 to 23 wt % resulted in a progressive increase in the values of the decolorization index and the lysis index. The BAG8 group showed no cytotoxicity, while the BAG16 group had slight cytotoxicity with a cytotoxicity score of 1, and the BAG23 group had moderate cytotoxicity with a cytotoxicity score of 2 (**Table 5**).

Furthermore, the MTT assay was used to study the effect of the extracts from the BAG-modified composite resins on cell viability. As shown in **Figure 4A**, 12.5–50% extracts of all BAG-modified composite resins did not significantly alter cell viability when compared to the negative control, while 100% extracts of the composite resins with 16 or 23% BAG incorporation significantly reduced cell viability until the addition of a decrease to 8%. However, no concentration-dependent increase in cytotoxicity was observed in the presence of the extracts of all BAG groups. To clarify the role of alkaline pH values in the cytotoxicity of BAG-modified composite resins, the pH value of the extracts of all BAG groups was adjusted to neutral. Interestingly, following exposure to the neutral 100% extracts of BAG16 and BAG23, the cell viability became equal to the cell viability of the control (**Figure 4B**), suggesting that the cytotoxicity of BAG-modified composite resins might be attributed primarily to the increase in extracellular pH values.

Antimicrobial Activity and Ion Release of BAG-Modified Composite Resin

The direct antibacterial effect of various BAG-modified composite resins was determined by counting bacterial colonies. As shown in **Figure 5**, after growing on the surface of BAG-modified composite resin for 24 h, the number of *S. mutans* colonies was significantly lower than the number of *S. mutans* colonies of unmodified composite resin ($p < 0.01$). In addition, a dose-dependent decrease in bacterial colonies was observed in the modified composite resins containing various amounts of BAG microparticles, suggesting that the addition of BAG can effectively improve the antibacterial performance of the composite resin. Moreover, to clarify whether the antibacterial effect depends on indirect action by soluble factors, various composite resin samples were extracted in bacterial culture medium for 24 and 72 h. **Figure 6** indicates that 24 h of extracts from composite resins incorporated with different concentrations of BAG could obviously inhibit the growth of *S. mutans* in a concentration-dependent manner. The difference in the average number of bacterial colonies between composite resins with various amounts of BAG was statistically significant ($p < 0.01$). Similar inhibition was also observed in the groups treated with 72 h of extracts from BAG-modified composite

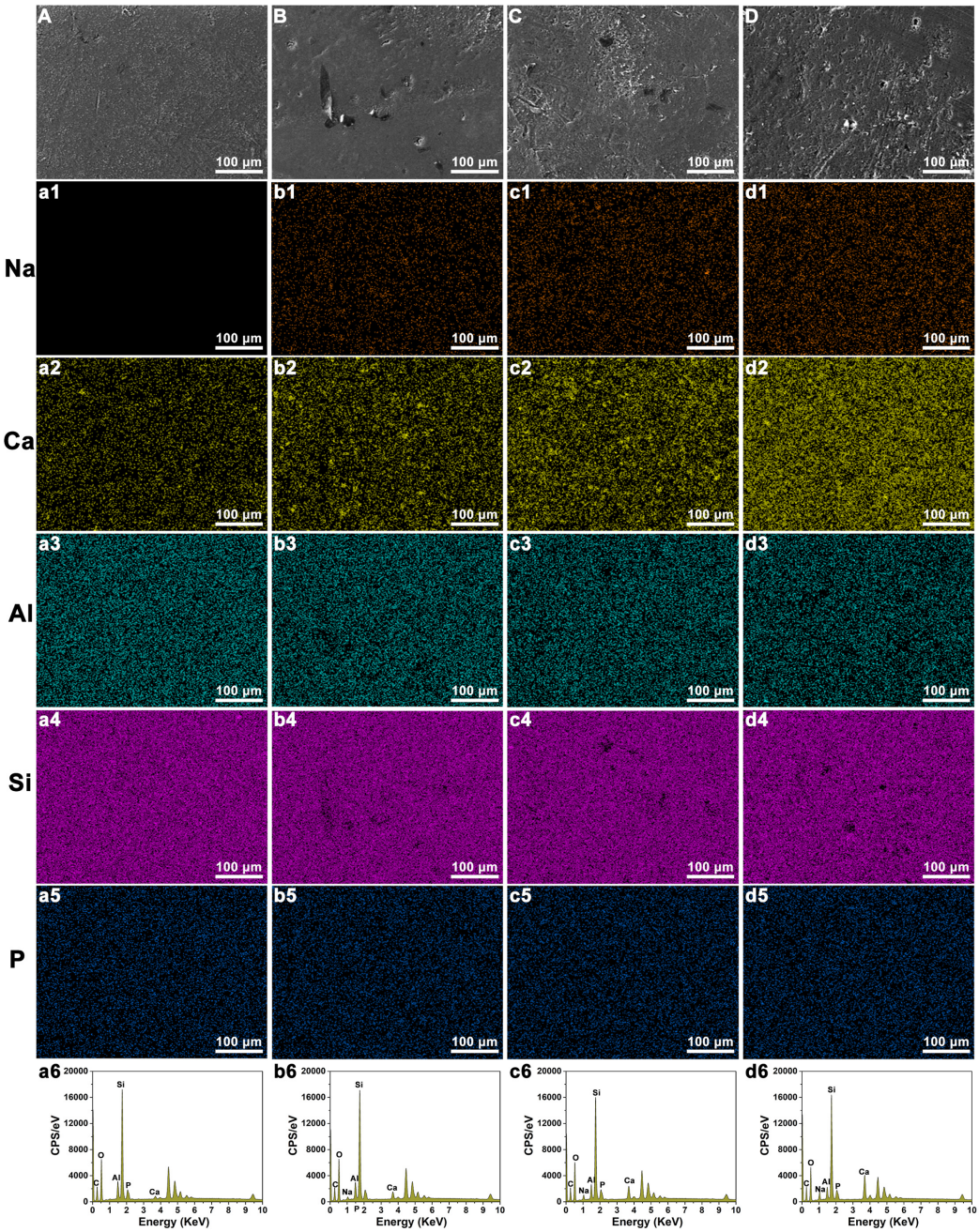

E

	Na (wt.%)	Ca (wt.%)	Al (wt.%)	Si (wt.%)	P (wt.%)	C (wt.%)	O (wt.%)
BAG 0	**0**	**1.15**	**3.51**	**22.55**	**0.34**	**33.04**	**39.39**
BAG 8	**0.85**	**2.93**	**3.40**	**22.29**	**0.45**	**30.27**	**39.82**
BAG 16	**1.66**	**5.30**	**3.02**	**21.06**	**0.66**	**29.29**	**39.01**
BAG 23	**2.63**	**9.02**	**2.35**	**20.16**	**0.74**	**29.49**	**35.60**

FIGURE 1 | Scanning electron microscopy (SEM) with energy-dispersive X-ray spectroscopy (EDS) mapping analysis of bioactive glass (BAG)-modified composite resins. **(A–D)** SEM images; EDS mapping analysis of Na element **(a1–d1)**; Ca element **(a2–d2)**; Al element **(a3–d3)**; Si element **(a4–d4)**; P element **(a5–d5)**. **(A, a1–a6)** BAG0 group; **(B, b1–b6)** BAG8 group; **(C, c1–c6)** BAG16 group; **(D, d1–d6)** BAG23 group; **(E)** Quantitative analysis of various elements in BAG-modified composite resins. BAG0 indicates composite resin without BAG; BAG8 indicates composite resin with 8 wt% BAG; BAG16 indicates composite resin with 16 wt% BAG; BAG23 indicates composite resin with 23 wt% BAG.

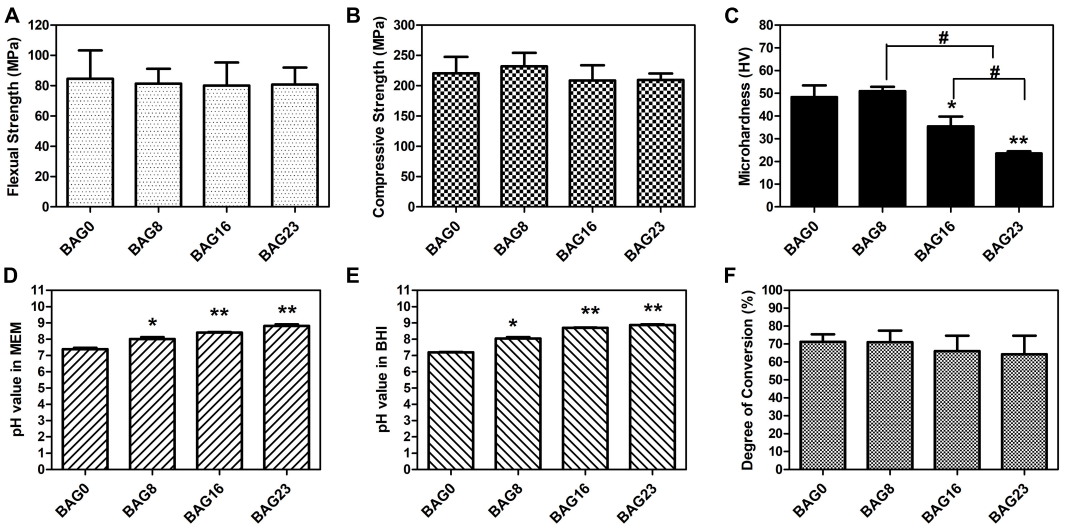

FIGURE 2 | Physicochemical and mechanical properties of bioactive glass (BAG)-modified composite resins. **(A)** Flexural strength. **(B)** Compressive strength. **(C)** Microhardness. The changes in pH values in the extracts of various BAG-modified composite for 24 h in MEM **(D)** and in BHI **(E)**. **(F)** Degree of conversion. MEM: the extracts of various BAG-modified composite resin in MEM with 10% FBS; BHI: the extracts of various BAG-modified composite resin in brain heart infusion (BHI). All the data represent the mean ± SD (n = 5); *$p < 0.05$, **$p < 0.01$ vs. the BAG0 group; #$p < 0.05$ significant difference as compared groups.

resins, and the antibacterial effect in the 72-h extract group was significantly stronger than the antibacterial effect of the 24-h extract group ($p < 0.05$).

The amounts of Ca and Si ions in the BHI extracts of each type of composite resin were determined and are presented in **Figure 7**. Si^{4+} release from the 24-h BHI extracts of experimental composite resins increased from 3.03 ± 0.12 μg/ml to 39.93 ± 1.45 μg/ml with the addition of BAG from 0 to 23 wt %, and Ca^{2+} release from the 24-h extracts increased from 10.37 ± 2.50 μg/ml to 35.97 ± 6.03 μg/ml with BAG incorporation from 0 to 23 wt %. In addition, there were significant differences in Si ion content between the 24-h extracts from BAG-modified composite resins and the 72-h extract group ($p < 0.05$), while no obvious difference was observed in Ca^{2+} release between the 24-h extract group and the 72-h extract group ($p > 0.05$).

The bacterial adhesion and morphology of *S. mutans* on the surface of various composite resins was determined by SEM. **Figure 8** reveals that *S. mutans* adhered well to the surface of unmodified composite resin, and the bacterial morphology was not changed, showing a typical and well-ordered chain-like arrangement. By contrast, the bacterial morphology and structure of *S. mutans* adhered to the surface of the BAG-modified composite resins obviously changed with increasing mass ratio of BAG incorporated into composite resins.

Remineralizing Capability of BAG-Modified Composite Resin

After immersing various BAG-modified composite resins with demineralized dentin disks in SBF for 21 days, the surface microstructure and elemental analysis of the dentin were observed by SEM-EDS. The uniform and smooth morphology of dentin was observed immediately after demineralized treatment or immersion in the blank SBF for 21 days (**Figures 9A,B**). Additionally, dentin tubules were clearly visible on the surface of demineralized dentin in the unmodified composite resin group (**Figure 9C**). By contrast, after immersion with various BAG-incorporated composite resins in SBF for 21 days, with increasing BAG amounts, an increasing number of dentin tubules were occluded by the mineralized layer (**Figures 9D–F**). According to the EDX analysis, a completely demineralized dentin surface immersed in SBF for 21 days showed that calcium was rarely observed. However, with the increase in the content of BAG incorporation, the amounts of calcium and phosphate gradually increased on the dentin surface, indicating that occluding deposits observed in each experimental group were calcium-rich mineralized layers and showing that BAG-modified composite resins have good remineralizing properties.

DISCUSSION

The present study successfully developed a novel bioactive hybrid composite resin with antibacterial and remineralizing activity by incorporating different weight fractions of BAG particles. SEM-EDS mapping indicated that BAG particles were homogeneously distributed in the resin matrix (**Figure 1**). Mechanical properties such as compressive strength, flexural strength, and microhardness are important for load-bearing applications of composite resin; thus, incorporation of BAG particles into the composite resin to achieve antibacterial and remineralizing functions should not sacrifice the mechanical properties of the composite resin. In this study, the flexural strength of the experimental composite resin containing 0 to 23 wt % BAG particles fulfilled the requirement of ISO

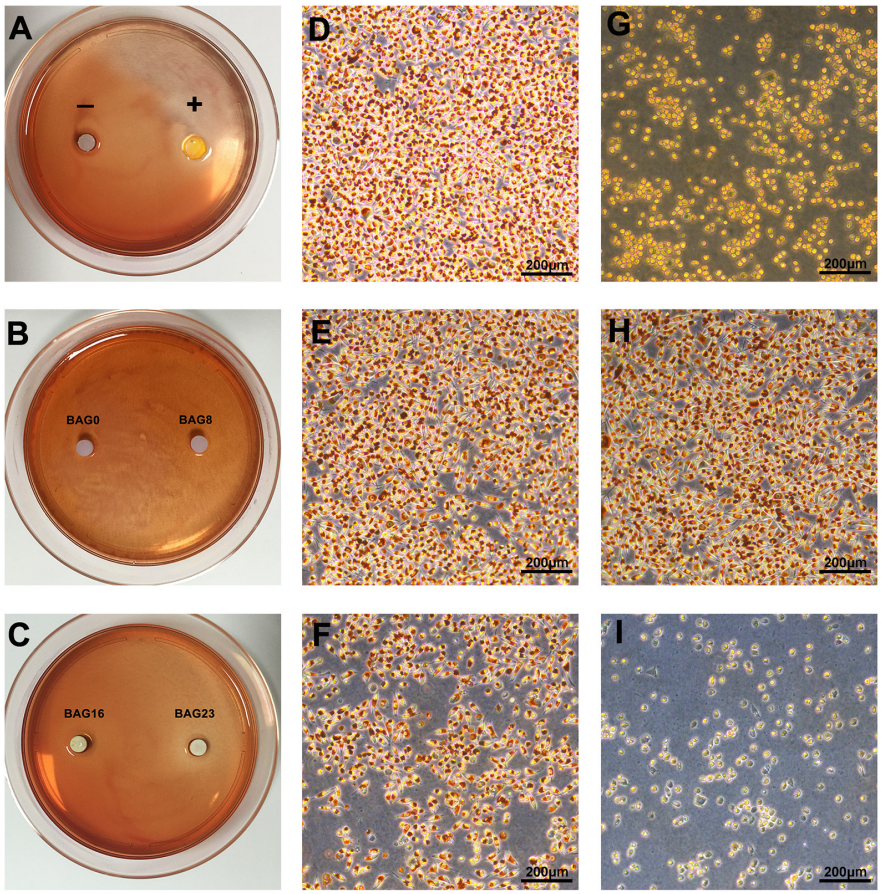

FIGURE 3 | Cytotoxicity determined by agar diffusion test. **(A–C)** Representative gross images of decolorization zones in the agar diffusion test. **(D–I)** Representative microscope images of cellular decolorization and lysis in the agar diffusion test. Bar = 200 μm. **(D)** The negative control. **(E)** BAG0 group. **(F)** BAG16. **(G)** The positive control. **(H)** BAG8 group. **(I)** BAG23 group. "–" indicates the negative control (high-density polytetrafluoroethylene sheet); "+" indicates the positive control (polyvinylchloride containing organotin additives sheet); BAG0 indicates composite resin without BAG; BAG8 indicates composite resin with 8 wt% BAG; BAG16 indicates composite resin with 16 wt% BAG; BAG23 indicates composite resin with 23 wt% BAG.

TABLE 5 | Results of the agar diffusion test.

Test materials	The decolorization index	The cell lysis index	Cell response	Cytotoxicity scoring grade	Interpretation
BAG0	0	0	0	0	Non-cytotoxic
BAG8	0	0	0	0	Non-cytotoxic
BAG16	1	0	1	1	Slightly cytotoxic
BAG23	3	3	3	2	Moderately cytotoxic
Negative control	0	0	0	0	Non-cytotoxic
Positive control	4	5	4	3	Severely cytotoxic

4049 for a minimum flexural strength of 80 MPa (**Figure 2A**; Standardization IOF, 2019). Moreover, our findings further showed that increasing the amount of BAG particles did not affect the short-term compressive and flexural strengths of the composite resin and resulted in only a slight decline in microhardness (**Figures 2A–C**), which is consistent with other previous studies reporting that the mechanical properties did not differ among various composite resins containing BAG particles with 0–15 wt % (Khvostenko et al., 2013). Moreover, a previous study also reported that dental resins containing biostable glass filler (SiO_2, Ba_2O_3, and Al_2O_3) had higher hardness than the dental resins containing BAG filler due to their higher resistance to wear (Proença et al., 2020), suggesting that the decrease in microhardness of BAG-modified composite resins might be attributed to a lower ratio of barium glass filler. By contrast, a continuous reduction in the flexural strength and modulus of the composite resin was observed with increasing BAG content and aging (Yang et al., 2013; Par et al., 2019b). Generally, the mechanical properties of composite resins were largely dependent on polymerization of the resinous matrix, inorganic

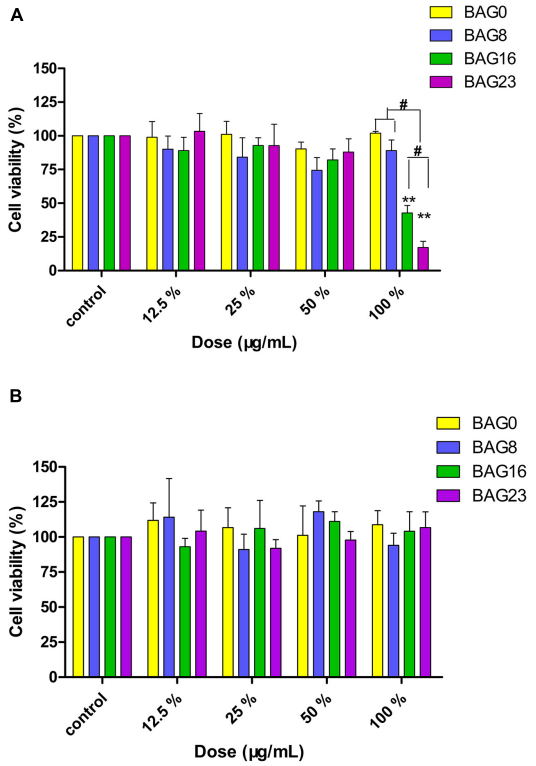

FIGURE 4 | Cytotoxicity determined by MTT assay. **(A)** Cytotoxic effects of the extracts of BAG-modified composite resins after 24-h exposure. **(B)** Effects of pH adjustment of the extracts on cell viability. Results are presented in mean ± SEM of three independent experiments. $^{**}p < 0.01$ vs. control. $^{\#}p < 0.05$ significant difference as compared groups. BAG0: the extracts of the composite resin without BAG; BAG8: the extracts of the composite resin with 8 wt% BAG; BAG16: the extracts of the composite resin with 16 wt% BAG; BAG23: the extracts of the composite resin with 23 wt% BAG.

fillers and filler/matrix interface (Par et al., 2019b). BAG fillers have been reported to have a direct inhibitory effect on the polymerization of Bis-GMA resin systems because of surface oxides (Par et al., 2019a,b), but our data showed that the DC for the as-prepared resin system was not compromised by the addition of BAG fillers up to 23 wt % (**Figure 2F**). A possible explanation is that the larger BAG microparticles used in our study had fewer surface oxides than the smaller BAG particles in other studies (Par et al., 2019b). Moreover, incorporating a low content of larger BAG microparticles (∼7.26 μm) and a high content of smaller barium glass microparticles (∼0.7 μm) might increase the fracture toughness of the composite resin by crack deflection or bridging (Khvostenko et al., 2013; Kundie et al., 2018). Thus, the mechanism underlying the negligible effect of BAG incorporation on compressive and flexural strengths might be attributed to a higher content of hybrid inorganic fillers and a higher DC of resin matrix.

Investigation of the biocompatibility of the novel composite resin is a pre-requisite before clinical use. In compliance with the ISO standards (Standardization IOF, 2009, 2011), both the agar diffusion test and MTT assay were selected to evaluate the cytotoxicity of dental composite resins based on different endpoints in this study. Specifically, the agar diffusion test, as a well-established cytotoxicity barrier test in dentistry, is commonly used to determine cell membrane integrity by mimicking the penetration of leachable substances released from dental materials through the dentin/mucosal membrane barrier. The MTT assay was used to detect mitochondrial activity by simulating the leachable constituents extracted from dental materials (Kilic et al., 2012). The agar diffusion test results showed that the cytotoxicity score of the experimental composite resins with a low (8–16 wt %) mass fraction of BAG filler was grade 0–1, which falls within the acceptable range for medical devices (Standardization IOF, 2009, 2011), but when the mass ratio of BAG filler increased up to 23%, the cytotoxicity score was grade 2, indicating increasing cell membrane permeability with increasing BAG incorporation (**Table 5**). Additionally, the cell metabolic activity could be reduced significantly by exposure to the extracts of composite resins with 16–23 wt % BAG fillers (**Figure 4A**). In other previous studies, the major reason for cytotoxicity was

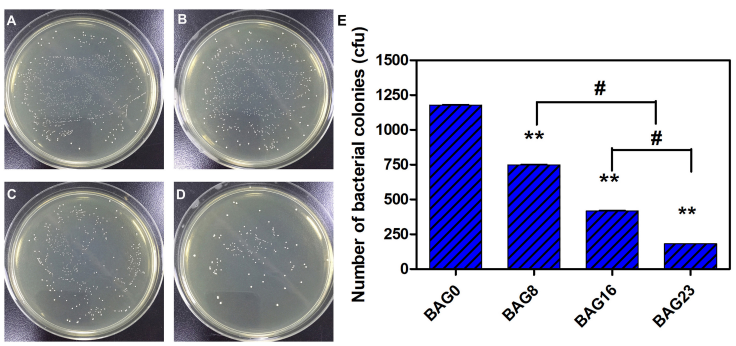

FIGURE 5 | Direct antibacterial effect of modified composite resin with different mass fractions of BAG particles. **(A–D)** Representative gross images of *S. mutans* seeded on the BHI agar plate. **(A)** BAG0 group. **(B)** BAG8 group. **(C)** BAG16 group. **(D)** BAG23 group. **(E)** Bar graph shows quantification and statistical data of colony-forming units (CFUs) of bacterial colonies after different treatments. Data are shown as mean ± SEM, $n = 3$. BAG0 indicates composite resin without BAG; BAG8 indicates composite resin with 8 wt% BAG; BAG16 indicates composite resin with 16 wt% BAG; BAG23 indicates composite resin with 23 wt% BAG. $^{**}p < 0.01$ vs. control. $^{\#}p < 0.05$ significant difference as compared groups.

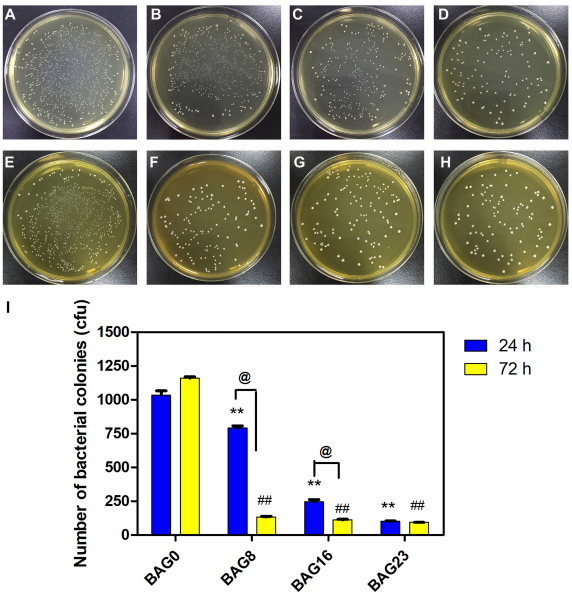

FIGURE 6 | The antibacterial effect of the extracts of modified composite resin with different mass fractions of BAG particles. **(A–H)** Representative gross images of *S. mutans* seeded on the BHI agar plate after exposure to the 24-h extracts of **(A)** BAG0 group, **(B)** BAG8 group, **(C)** BAG16 group, and **(D)** BAG23 group, and the 72-h extracts of **(E)** BAG0 group, **(F)** BAG8 group, **(G)** BAG16 group, and **(H)** BAG23 group. **(I)** Bar graph shows quantification and statistical data of colony-forming units (CFUs) of bacterial colonies after different treatments. Data are shown as mean ± SEM, $n = 3$. BAG0 group as the control. $^{*}p < 0.05$, $^{**}p < 0.01$ vs. the 24 h extracts of BAG0 group, $^{\#}p < 0.05$, $^{\#\#}p < 0.01$ vs. the 72 h extracts of BAG0 group, $^{@}p < 0.05$ significant difference as compared groups. BAG0 indicates composite resin without BAG; BAG8 indicates composite resin with 8 wt% BAG; BAG16 indicates composite resin with 16 wt% BAG; BAG23 indicates composite resin with 23 wt% BAG.

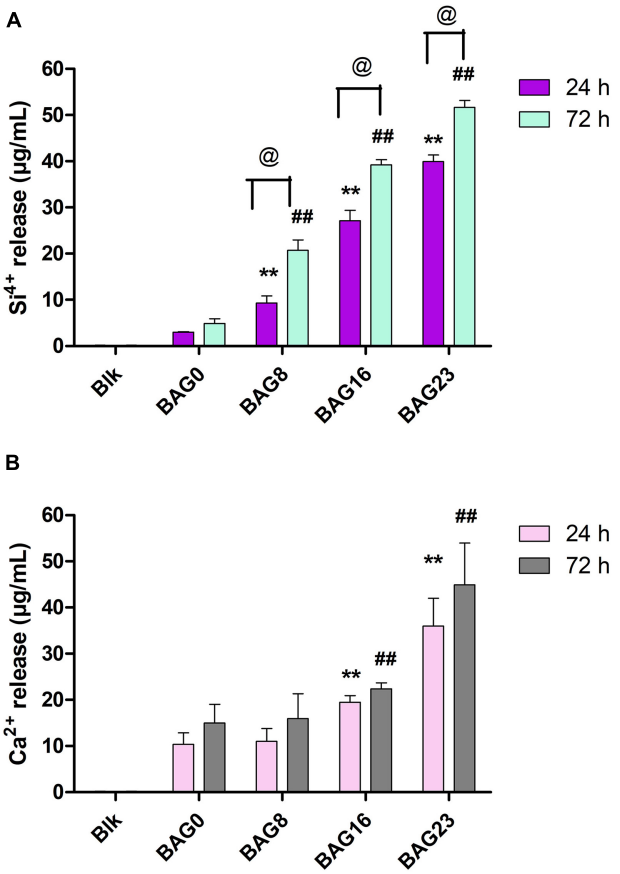

FIGURE 7 | The concentration of Si^{4+} and Ca^{2+} in the BHI extracts of BAG-modified composite resin measured by inductively coupled plasma mass spectrometry (ICP-MS). **(A)** Si^{4+} release. **(B)** Ca^{2+} release. Blk: BHI as blank control; BAG0 indicates composite resin without BAG; BAG8 indicates composite resin with 8 wt% BAG; BAG16 indicates composite resin with 16 wt% BAG; BAG23 indicates composite resin with 23 wt% BAG. $^{**}p < 0.01$ vs. the 24 h extracts of BAG0 group, $^{\#\#}p < 0.01$ vs. the 72 h extracts of BAG0 group, $^{@}p < 0.05$ significant difference as compared groups.

attributed predominantly to the release of residual monomers, not to the presence of the BAG fillers (Salehi et al., 2015; Balhaddad et al., 2019). However, our data showed that neither the unmodified composite resins nor the modified composite resins with 8 wt % BAG exhibited cytotoxicity, reflecting that the level of residual monomers released from our experimental resin matrix would not be sufficient to cause cytotoxic effects. As the degradation of BAG was accompanied by the release of alkali metal ions and an increase in pH in the local microenvironment, a higher pH value might be the prominent factor affecting the cytotoxicity of BAG-modified composite resins. The range of the optimal pH values for cell growth is considered to be between 7.4 and 7.8 (Wang et al., 2015). However, the pH values in the extracts of the four experimental composite resins reached 9.0 when the addition of BAG was 16–23 wt % (**Figure 2D**). Because the *in vitro* cell culture system lacks the buffering capacity of the *in vivo* environment, the pH value of the *in vitro* test system could be adjusted to the normal level to simulate the *in vivo* environment (Wang et al., 2015; Willbold et al., 2017). After adjusting the pH value of the extracts of BAG16 and BAG23 to 7.4, the cell viability recovered significantly up to 100% above (**Figure 4B**).

As composite resins were usually shown to accumulate more biofilms and plaque than other restorative materials (Singh et al., 2009), it is highly desirable to develop composite resins with antibacterial activity to inhibit bacteria and combat secondary caries. Many previous studies, including ours, have found that BAG particles have strong antibacterial effects on a variety of bacteria and biofilms due to ion release (e.g., Ca, P, Na, and Si ions) and the pH elevation of the surrounding environment (Xu et al., 2015; Kargozar et al., 2018; Bauer et al., 2019). BAG particles were also reported to be able to insert into bacterial membranes like a needle, leading to the destruction of the cell walls of bacteria (Hu et al., 2009). However, it is still not clear whether this antibacterial behavior could be affected when the BAG particles were embedded in the composite resin matrix as a filler. In the present study, *S. mutans*, as one of the major caries-related species, was chosen to represent the dominant streptococci genus in dental biofilms. Our data showed that all the composites containing BAG particles significantly reduced

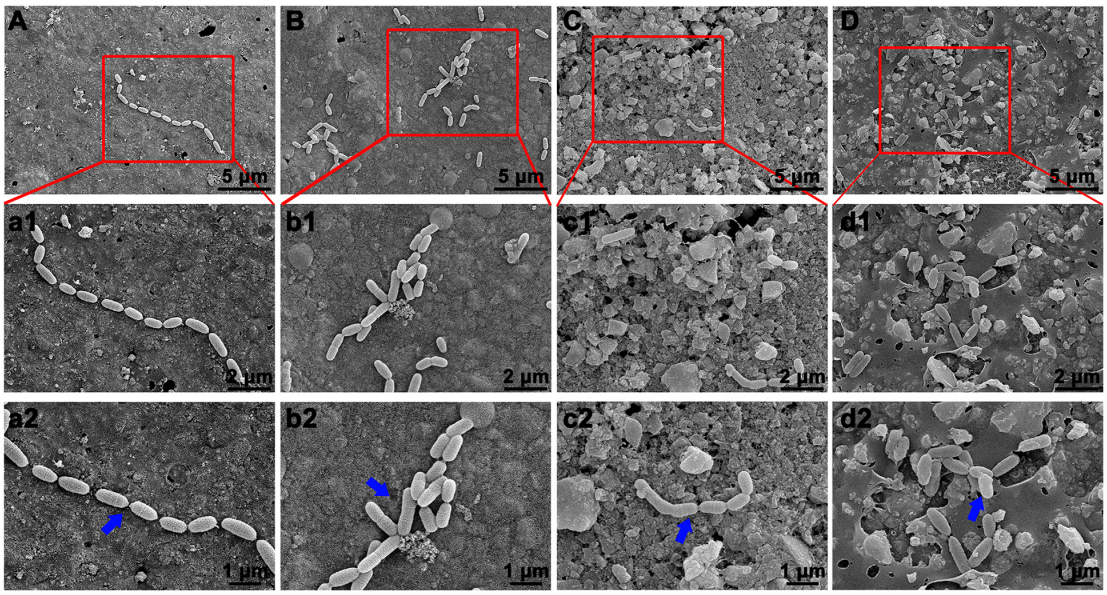

FIGURE 8 | Bacterial morphology of *S. mutans* on surface of BAG-modified composite resin detected by scanning electron microscope (SEM). **(A,a1,a2)** BAG0 group; **(B,b1,b2)** BAG8 group; **(C,c1,c2)** BAG16 group; **(D,d1,d2)** BAG23 group. **(A–D)** Overall bacterial morphology (scale bar: 10 μm). **(a1–d1, a2–d2)** Higher magnification of the red box area in panels **(A–D)** (**a1–d1**, scale bar: 5 μm; **a2–d2**, scale bar: 3 μm). The blue arrow indicates *S. mutans*. BAG0 indicates composite resin without BAG; BAG8 indicates composite resin with 8 wt% BAG; BAG16 indicates composite resin with 16 wt% BAG; BAG23 indicates composite resin with 23 wt% BAG.

the CFU of *S. mutans* and inhibited bacterial growth on the surface of composite resins (**Figure 5**), consistent with other studies, which showed that the addition of BAG particles into composite resins yielded a significant inhibition of *Escherichia coli* and *S. mutans* and reduced the bacterial penetration depth into the interface tooth resins (Khvostenko et al., 2013, 2016; Chatzistavrou et al., 2015). To explore the role of direct surface contact or soluble factor release in its antibacterial action, each composite resin sample with the same specification in the above direct contact antibacterial experiment was extracted in bacterial culture medium for 24 and 72 h, and then the extracts were used to culture *S. mutans* for 24 h. The results showed that the 72-h extracts of various BAG-modified composite resins had better antibacterial effects than the 24-h extract groups with obvious dose- and time-dependent bacterial inhibition (**Figure 6**). Correspondingly, we found that the antibacterial effects of the extracts of BAG-modified composite resins were higher than the antibacterial effects of the direct contact groups at the same aqueous pH value (**Figures 5**, 6), suggesting that the antibacterial mechanism of the BAG-modified composite resin was attributed dominantly to the cumulative effects of ion release, not just the increase in pH value or direct surface contact. This conclusion was further supported by the results from the pH measurements and the ion release in the BHI extracts. **Figure 2E** shows that the pH values in the extracts of BAG-modified composite resin groups were approximately 8.04–8.87, which fell within the *S. mutans*-tolerated pH range of 4–10 described in the literature (Nakajo et al., 2006). Based on ICP-MS analysis, a significant dose-dependent increase in the release of Si^{4+} and Ca^{2+} was observed in the BHI extracts of experimental composite resins with increasing BAG amounts, especially the Si ions released from the composite resin with 23 wt % BAG, which were more than 10 times higher than the Si ions released from the control without BAG (**Figure 7**), suggesting that the combined action of Si^{4+} and Ca^{2+} release is the main factor contributing to the antibacterial properties of BAG-modified composite resin. The release of Si^{4+} or Ca^{2+} from BAG has also been suggested to prohibit bacterial growth by causing perturbations of the membrane potential of bacteria or attacking target sites on the cell membranes of bacteria in many previous studies (Keenan et al., 2017; Drago et al., 2018; Aponso et al., 2019; Dai et al., 2020). Consistently, our SEM data further showed that on the surface of composite resins containing 8 and 16 wt % BAG, the long-chain-like structure of *S. mutans* gradually disintegrated into a short-chain shape. Especially on the surface of composite resins containing 23 wt % BAG, the long-chain structure basically disappeared, indicating that the incorporation of BAG could not only reduce the number of bacteria adhered to the composite resin surface but also disturb the morphology and structure of bacteria (**Figure 8**).

Secondary caries could lead to dentin demineralization by bacterial acids in carious lesions; therefore, in addition to the antibacterial ability, the ideal composite resin should have excellent mineralizing capability to inhibit secondary caries and thus extend the lifetime of restoration. BAG has been proven to promote dentin remineralization in many previous studies (Bakry et al., 2014a,b; Mehta et al., 2014), so BAG has been added to toothpaste, anti-carious gel and dentin desensitizer for clinical use. Once BAG particles were used to modify the composite resin, it was critical that these particles embedded in

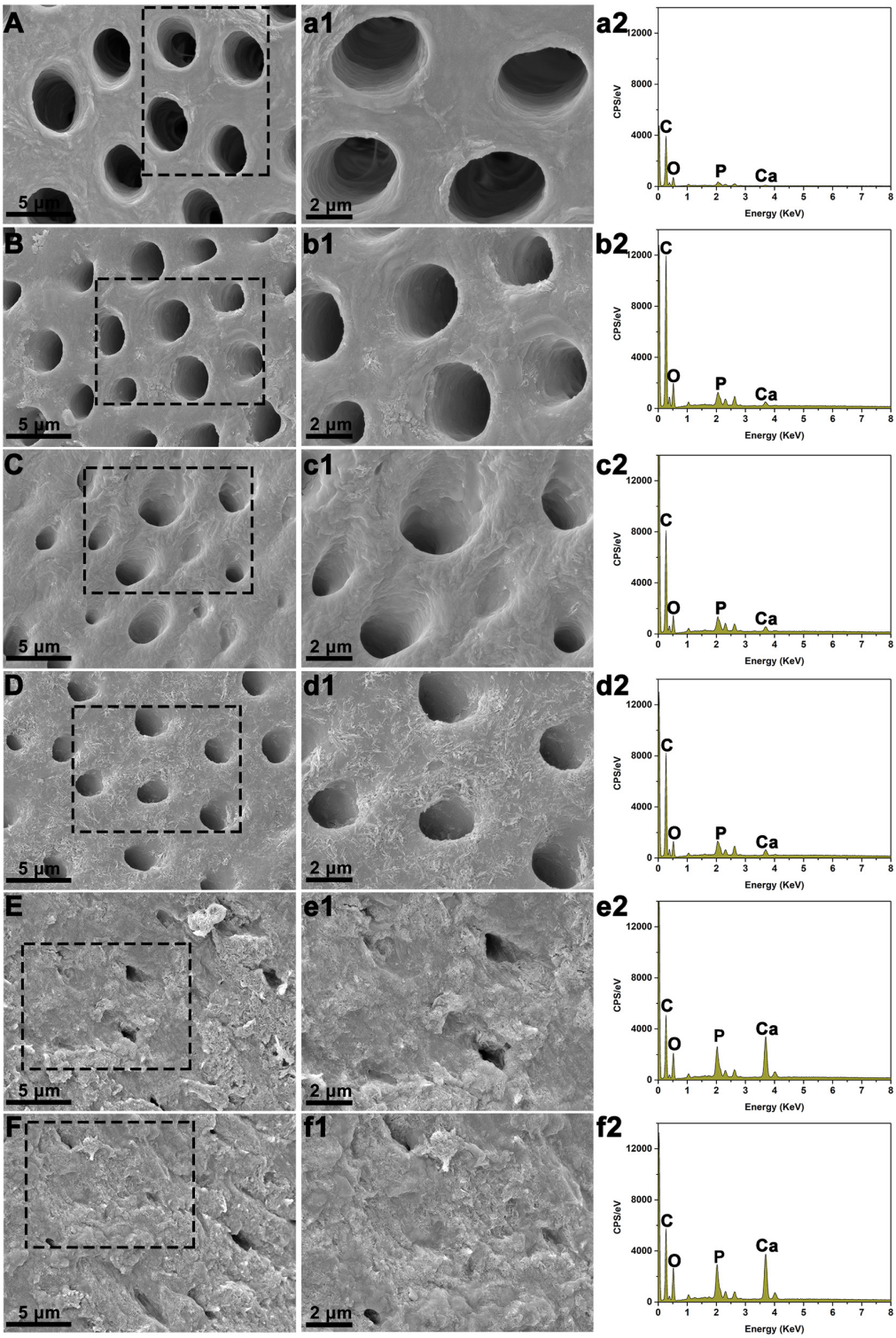

FIGURE 9 | Scanning electron microscopy (SEM) with energy-dispersive X-ray spectroscopy (EDS) analysis of dentin surface morphology following immersion with various BAG-modified composite resins in SBF for 21 days. **(A,a1,a2)** The dentin disks with demineralized treatment immediately. **(B,b1,b2)** The demineralized dentin disks immersed in the blank SBF for 21 days. **(C,c1,c2)** The demineralized dentin disks immersed with BAG0 in the SBF for 21 days. **(D,d1,d2)** The demineralized dentin disks immersed with BAG8 in the SBF for 21 days. **(E,e1,e2)** The demineralized dentin disks immersed with BAG16 in the SBF for 21 days. **(F,f1,f2)** The demineralized dentin disks immersed with BAG23 in the SBF for 21 days. **(A-F)** SEM images (scale bar: 5 μm); **(a1–f1)** Higher magnification of the black box area in panels **(A–F)** (scale bar: 2 μm); **(a2–f2)** EDS analysis. BAG0 indicates composite resin without BAG; BAG8 indicates composite resin with 8 wt% BAG; BAG16 indicates composite resin with 16 wt% BAG; BAG23 indicates composite resin with 23 wt% BAG.

the resin matrix could continue to exert bioactivity. A previous study reported that the hydroxylapatite layer could be formed on the surface of dental adhesive containing 20 wt % BAG particles after immersion in PBS for 21 days (Taubock et al., 2014), but the direct effects of BAG-modified composite resins on dentin remineralization were rarely highlighted. In this study, the capability of inducing remineralization was evaluated by exploring the surface structure and chemical composition of demineralized dentin surfaces of tooth slices mixed with BAG-modified composite resins upon soaking in SBF for 21 days. Our SEM results (**Figure 9**) showed that the demineralized dentin surfaces were covered with a Ca-P-containing layer following immersion with 16–23 wt % BAG-modified composite resins in SBF solutions, while the dentin surfaces showed clearly visible dentin tubules in the control without BAG-modified composite resins. In addition, with increasing amounts of BAG particles within the composite resin, the amounts of Ca and P gradually increased on the demineralized dentin surface, indicating that the incorporation of the BAG particles into the resin matrix could also exert bioactivity and promote dentin remineralization. Materials containing released Ca, P, and Si ions have been widely accepted to be favorable for remineralization (Cheng et al., 2017; Fernando et al., 2017). A previous study focused on the effects of the addition of BAG in polymer constructs on bioactivity and found that the precipitation of mineralized layers on the surface of materials was ascribed to a well-defined ion exchange mechanism between metal cations (Na^+ and Ca^{2+}) in the BAG and hydronium ions (H_3O^+) in the surrounding fluid (Serio et al., 2019). Therefore, in SBF solution, the enhanced remineralization on the demineralized dentin surface was attributed mainly to the release of bioactive ions from BAG and the change in the local microenvironment. Taken together, the above data suggest that the BAG-modified composite resin has both remineralizing and antibacterial capabilities, which could be regulated by the controllable release of bioactive ions (Si^{4+} and Ca^{2+}).

There are several limitations of this study. First, the decline in mechanical properties with aging has been reported in a previous study (Par et al., 2019b); thus, testing the mechanical properties of composite resins immersed in water for a long time (e.g., 30, 60, or 90 days) might be more suitable for the evaluation of the mechanical properties of the material. Second, it would be more appropriate to detect the antibacterial effects of BAG-modified composite resin on biofilms and investigate their remineralization ability using *in situ* or *in vitro* models under clinically relevant conditions, which would make the conclusions on the antibacterial and remineralizing properties more accurate.

CONCLUSION

In summary, a novel BAG-modified hybrid composite resin was developed with excellent biocompatibility and antibacterial and remineralizing capabilities. When the mass fractions of BAG particles were added from 8 to 23 wt %, the original mechanical properties of the composite resin, including flexural strength and compressive strength, were not obviously affected without compromising the DC. Although the BAG incorporation of mass fractions of 16–23 wt % in composite resins reduced cell viability, the cell viability could be recovered by the regulation of pH values. The synthesized BAG-modified composite resins showed good antibacterial effects against *S. mutans* and enhanced remineralization activity on demineralized dentin surfaces in a concentration-dependent manner. The possible mechanisms of antibacterial activity and dentin remineralization might be closely related to the release of bioactive ions, suggesting that the BAG antibacterial and biological properties can be controlled by regulating the amounts of bioactive ions. The capability to balance the mechanical properties, cytotoxicity, antibacterial activity, and bioactivity makes BAG-modified composite resin a promising prospect for clinical application.

DATA AVAILABILITY STATEMENT

The original contributions presented in the study are included in the article/supplementary material, further inquiries can be directed to the corresponding author/s.

ETHICS STATEMENT

The studies involving human participants were reviewed and approved by Ninth People's Hospital, Shanghai Jiao Tong University School of Medicine. The patients/participants provided their written informed consent to participate in this study.

AUTHOR CONTRIBUTIONS

XH: conceptualization, methodology, investigation, and writing – original draft. YC: methodology, investigation, and formal analysis. QJ: methodology, writing – review and editing, and funding acquisition. XL: conceptualization, project administration, and funding acquisition. YmC: supervision, resources, project administration, and funding acquisition. All authors contributed to the article and approved the submitted version.

FUNDING

This work was supported by the National Natural Science Foundation of China (No. 81971751 and No. 31800816) and the Innovative research team of high-level local universities in Shanghai, Oral and maxillofacial regeneration and functional restoration (SSMU-ZDCX20180900).

ACKNOWLEDGMENTS

The authors thank Felix Wöhrle and DMG Dental Material Gesellschaft mbH for their help on the preparation of BAG-modified hybrid composite resin.

REFERENCES

Al-Eesa, N. A., Karpukhina, N., Hill, R. G., Johal, A., and Wong, F. S. L. (2019). Bioactive glass composite for orthodontic adhesives–formation and characterisation of apatites using MAS-NMR and SEM. *Dent. Mater.* 35, 597–605. doi: 10.1016/j.dental.2019.02.010

Aponso, S., Ummadi, J. G., Davis, H., Ferracane, J., and Koley, D. (2019). A chemical approach to optimizing bioactive glass dental composites. *J. Dent. Res.* 98, 194–199. doi: 10.1177/0022034518809086

Arun, D., Adikari Mudiyanselage, D., Gulam Mohamed, R., Liddell, M., Monsur Hassan, N. M., and Sharma, D. (2021). Does the addition of zinc oxide nanoparticles improve the antibacterial properties of direct dental composite resins? A systematic review. *Materials* 14:40. doi: 10.3390/ma14010040

Astvaldsdottir, A., Dagerhamn, J., Van Dijken, J. W., Naimi-Akbar, A., Sandborgh-Englund, G., Tranaeus, S., et al. (2015). Longevity of posterior resin composite restorations in adults–a systematic review. *J. Dent.* 43, 934–954. doi: 10.1016/j.jdent.2015.05.001

Bakry, A. S, Takahashi, H., Otsuki, M., and Tagami, J. (2014a). Evaluation of new treatment for incipient enamel demineralization using 45S5 bioglass. *Dent. Mater.* 30, 314–320. doi: 10.1016/j.dental.2013.12.002

Bakry, A. S., Marghalani, H. Y., Amin, O. A., and Tagami, J. (2014b). The effect of a bioglass paste on enamel exposed to erosive challenge. *J. Dent.* 42, 1458–1463. doi: 10.1016/j.jdent.2014.05.014

Balhaddad, A. A., Kansara, A. A., Hidan, D., Weir, M. D., Xu, H. H. K., and Melo, M.a.S (2019). Toward dental caries: exploring nanoparticle-based platforms and calcium phosphate compounds for dental restorative materials. *Bioact. Mater.* 4, 43–55. doi: 10.1016/j.bioactmat.2018.12.002

Bauer, J., Silva, E. S. A., Carvalho, E. M., Ferreira, P. V. C., Carvalho, C. N., Manso, A. P., et al. (2019). Dentin pretreatment with 45S5 and niobophosphate bioactive glass: effects on pH, antibacterial, mechanical properties of the interface and microtensile bond strength. *J. Mech. Behav. Biomed. Mater.* 90, 374–380. doi: 10.1016/j.jmbbm.2018.10.029

Bhadila, G., Wang, X., Zhou, W., Menon, D., Melo, M.a.S, Montaner, S., et al. (2020). Novel low-shrinkage-stress nanocomposite with remineralization and antibacterial abilities to protect marginal enamel under biofilm. *J. Dent.* 99:103406. doi: 10.1016/j.jdent.2020.103406

Chatzistavrou, X., Velamakanni, S., Direnzo, K., Lefkelidou, A., Fenno, J. C., Kasuga, T., et al. (2015). Designing dental composites with bioactive and bactericidal properties. *Mater. Sci. Eng. C Mater. Biol. Appl.* 52, 267–272. doi: 10.1016/j.msec.2015.03.062

Cheng, L., Weir, M. D., Xu, H. H., Antonucci, J. M., Kraigsley, A. M., Lin, N. J., et al. (2012). Antibacterial amorphous calcium phosphate nanocomposites with a quaternary ammonium dimethacrylate and silver nanoparticles. *Dent. Mater.* 28, 561–572. doi: 10.1016/j.dental.2012.01.005

Cheng, L., Zhang, K., Zhang, N., Melo, M.a.S, Weir, M. D., Zhou, X. D., et al. (2017). Developing a new generation of antimicrobial and bioactive dental resins. *J. Dent. Res.* 96, 855–863. doi: 10.1177/0022034517709739

Cocco, A. R., Da Rosa, W. L. D. O., Da Silva, A. F., Lund, R. G., and Piva, E. (2015). A systematic review about antibacterial monomers used in dental adhesive systems: current status and further prospects. *Dent. Mater.* 31, 1345–1362. doi: 10.1016/j.dental.2015.08.155

Dai, L. L., Mei, M. L., Chu, C. H., and Lo, E. C. M. (2020). Antibacterial effect of a new bioactive glass on cariogenic bacteria. *Arch. Oral Biol.* 117:104833. doi: 10.1016/j.archoralbio.2020.104833

Drago, L., Toscano, M., and Bottagisio, M. (2018). Recent evidence on bioactive glass antimicrobial and antibiofilm activity: a mini-review. *Materials (Basel)* 11:326. doi: 10.3390/ma11020326

Farrugia, C., and Camilleri, J. (2015). Antimicrobial properties of conventional restorative filling materials and advances in antimicrobial properties of composite resins and glass ionomer cements-A literature review. *Dent. Mater.* 31, e89–e99.

Fernando, D., Attik, N., Pradelle-Plasse, N., Jackson, P., Grosgogeat, B., and Colon, P. (2017). Bioactive glass for dentin remineralization: a systematic review. *Mater. Sci. Eng. C Mater. Biol. Appl.* 76, 1369–1377. doi: 10.1016/j.msec.2017.03.083

He, J., Zhu, X., Qi, Z., Wang, C., Mao, X., Zhu, C., et al. (2015). Killing dental pathogens using antibacterial graphene oxide. *ACS Appl. Mater. Interfaces* 7, 5605–5611. doi: 10.1021/acsami.5b01069

Hu, S., Chang, J., Liu, M., and Ning, C. (2009). Study on antibacterial effect of 45S5 Bioglass. *J. Mater. Sci. Mater. Med.* 20, 281–286. doi: 10.1007/s10856-008-3564-5

Kargozar, S., Montazerian, M., Hamzehlou, S., Kim, H. W., and Baino, F. (2018). Mesoporous bioactive glasses: promising platforms for antibacterial strategies. *Acta Biomater.* 81, 1–19. doi: 10.1016/j.actbio.2018.09.052

Keenan, T. J., Placek, L. M., Hall, M. M., and Wren, A. W. (2017). Antibacterial and antifungal potential of Ga-bioactive glass and Ga-bioactive glass/polymeric hydrogel composites. *J. Biomed. Mater. Res. B Appl. Biomater.* 105, 1102–1113. doi: 10.1002/jbm.b.33655

Khvostenko, D., Hilton, T., Ferracane, J., Mitchell, J., and Kruzic, J. (2016). Bioactive glass fillers reduce bacterial penetration into marginal gaps for composite restorations. *Dent. Mater.* 32, 73–81. doi: 10.1016/j.dental.2015.10.007

Khvostenko, D., Mitchell, J., Hilton, T., Ferracane, J., and Kruzic, J. (2013). Mechanical performance of novel bioactive glass containing dental restorative composites. *Dent. Mater.* 29, 1139–1148. doi: 10.1016/j.dental.2013.08.207

Kilic, D., Kesim, S., Liman, N., Sumer, Z., Ozturk, A. J. B., and Equipment, B. (2012). In vitro comparison of the effects of dental filling materials on mouse fibroblasts. *Biotechnol. Biotechnol. Equip.* 26, 3155–3162. doi: 10.5504/bbeq.2012.0030

Kopperud, S. E., Tveit, A. B., Gaarden, T., Sandvik, L., and Espelid, I. (2012). Longevity of posterior dental restorations and reasons for failure. *Eur. J. Oral Sci.* 120, 539–548. doi: 10.1111/eos.12004

Korkut, E., Torlak, E., and Altunsoy, M. (2016). Antimicrobial and mechanical properties of dental resin composite containing bioactive glass. *J. Appl. Biomater. Funct. Mater.* 14, e296–e301.

Kundie, F., Azhari, C. H., Muchtar, A., and Ahmad, Z.a (2018). Effects of filler size on the mechanical properties of polymer-filled dental composites: a review of recent developments. *J. Phys. Sci.* 29, 141–165.

Kurata, S., Hamada, N., Kanazawa, A., and Endo, T. (2011). Study on antibacterial dental resin using tri-n-butyl (4-vinylbenzyl) phosphonium chloride. *Dent. Mater. J.* 30, 960–966. doi: 10.4012/dmj.2011-157

Lee, M. J., Seo, Y. B., Seo, J. Y., Ryu, J. H., Ahn, H. J., Kim, K. M., et al. (2020). Development of a bioactive flowable resin composite containing a zinc-doped phosphate-based glass. *Nanomaterials (Basel)* 10:2311. doi: 10.3390/nano10112311

Liu, Y., Zhang, L., Niu, L. N., Yu, T., Xu, H. H. K., Weir, M. D., et al. (2018). Antibacterial and remineralizing orthodontic adhesive containing quaternary ammonium resin monomer and amorphous calcium phosphate nanoparticles. *J. Dent.* 72, 53–63. doi: 10.1016/j.jdent.2018.03.004

Mariano, N., Oliveira, R., Fernandes, M., and Rigo, E. J. M. (2009). Corrosion behavior of pure titanium in artificial saliva solution. *Matéria (Rio de Janeiro)* 14, 878–880. doi: 10.1590/s1517-70762009000200010

Mehta, A. B., Kumari, V., Jose, R., and Izadikhah, V. (2014). Remineralization potential of bioactive glass and casein phosphopeptide-amorphous calcium phosphate on initial carious lesion: an in-vitro pH-cycling study. *J. Conserv. Dent.* 17, 3–7. doi: 10.4103/0972-0707.124085

Nakajo, K., Komori, R., Ishikawa, S., Ueno, T., Suzuki, Y., Iwami, Y., et al. (2006). Resistance to acidic and alkaline environments in the endodontic pathogen *Enterococcus faecalis*. *Oral Microbiol. Immunol.* 21, 283–288. doi: 10.1111/j.1399-302x.2006.00289.x

Opdam, N. J., Van De Sande, F. H., Bronkhorst, E., Cenci, M. S., Bottenberg, P., Pallesen, U., et al. (2014). Longevity of posterior composite restorations: a systematic review and meta-analysis. *J. Dent. Res.* 93, 943–949. doi: 10.1177/0022034514544217

Par, M., Spanovic, N., Taubock, T. T., Attin, T., and Tarle, Z. (2019a). Degree of conversion of experimental resin composites containing bioactive glass 45S5: the effect of post-cure heating. *Sci. Rep.* 9:17245.

Par, M., Tarle, Z., Hickel, R., and Ilie, N. (2019b). Mechanical properties of experimental composites containing bioactive glass after artificial aging in water and ethanol. *Clin. Oral Investig.* 23, 2733–2741. doi: 10.1007/s00784-018-2713-6

Proença, M.a.M, Carvalho, E. M., E Silva, A. S., Ribeiro, G.a.C, Ferreira, P. V. C., Carvalho, C. N., et al. (2020). Orthodontic resin containing bioactive glass: preparation, physicochemical characterization, antimicrobial activity, bioactivity and bonding to enamel. *Int. J. Adh. Adh.* 99:102575. doi: 10.1016/j.ijadhadh.2020.102575

Salehi, S., Gwinner, F., Mitchell, J. C., Pfeifer, C., and Ferracane, J. L. (2015). Cytotoxicity of resin composites containing bioactive glass fillers. *Dent. Mater.* 31, 195–203.

Serio, F., Miola, M., Verne, E., Pisignano, D., Boccaccini, A. R., and Liverani, L. (2019). Electrospun filaments embedding bioactive glass particles with ion release and enhanced mineralization. *Nanomaterials (Basel)* 9:182. doi: 10.3390/nano9020182

Singh, J., Khalichi, P., Cvitkovitch, D. G., and Santerre, J. P. (2009). Composite resin degradation products from BisGMA monomer modulate the expression of genes associated with biofilm formation and other virulence factors in *Streptococcus mutans*. *J. Biomed. Mater. Res. A* 88, 551–560. doi: 10.1002/jbm.a.31879

Standardization IOF (2009). *ISO 10993-5: Biological Evaluation of Medical Devices—Part 5: Tests for in Vitro Cytotoxicity*. Geneva: International Organization for Standardization (ISO).

Standardization IOF (2011). *ISO 7045: Pan Head Screws With Type H or Type Z Cross Recess—Product Grade A*. Geneva: International Organization for Standardization (ISO).

Standardization IOF (2012). *ISO 10993-12: Biological Evaluation of Medical Devices—Part 12: Sample Preparation and Reference Materials*. Geneva: International Organization for Standardization (ISO).

Standardization IOF (2019). *ISO 4049: Dentistry—Polymer-Based Restorative Materials*. Geneva: International Organization for Standardization (ISO).

Taubock, T. T., Zehnder, M., Schweizer, T., Stark, W. J., Attin, T., and Mohn, D. (2014). Functionalizing a dentin bonding resin to become bioactive. *Dent. Mater.* 30, 868–875. doi: 10.1016/j.dental.2014.05.029

Tezvergil-Mutluay, A., Seseogullari-Dirihan, R., Feitosa, V. P., Cama, G., Brauer, D. S., and Sauro, S. (2017). Effects of composites containing bioactive glasses on demineralized dentin. *J. Dent. Res.* 96, 999–1005. doi: 10.1177/0022034517709464

Wang, J., Witte, F., Xi, T., Zheng, Y., Yang, K., Yang, Y., et al. (2015). Recommendation for modifying current cytotoxicity testing standards for biodegradable magnesium-based materials. *Acta Biomater.* 21, 237–249. doi: 10.1016/j.actbio.2015.04.011

Wang, Z., Sa, Y., Sauro, S., Chen, H., Xing, W., Ma, X., et al. (2010). Effect of desensitising toothpastes on dentinal tubule occlusion: a dentine permeability measurement and SEM in vitro study. *J. Dent.* 38, 400–410. doi: 10.1016/j.jdent.2010.01.007

Willbold, E., Weizbauer, A., Loos, A., Seitz, J. M., Angrisani, N., Windhagen, H., et al. (2017). Magnesium alloys: a stony pathway from intensive research to clinical reality. Different test methods and approval-related considerations. *J. Biomed. Mater. Res. A* 105, 329–347. doi: 10.1002/jbm.a.35893

Xie, D., Zhao, J., Weng, Y., Park, J. G., Jiang, H., and Platt, J. A. (2008). Bioactive glass-ionomer cement with potential therapeutic function to dentin capping mineralization. *Eur. J. Oral Sci.* 116, 479–487. doi: 10.1111/j.1600-0722.2008.00562.x

Xu, Y. T., Wu, Q., Chen, Y. M., Smales, R. J., Shi, S. Y., and Wang, M. T. (2015). Antimicrobial effects of a bioactive glass combined with fluoride or triclosan on *Streptococcus mutans* biofilm. *Arch. Oral Biol.* 60, 1059–1065. doi: 10.1016/j.archoralbio.2015.03.007

Yang, S.-Y., Kim, S.-H., Choi, S.-Y., and Kim, K.-M. (2016). Acid neutralizing ability and shear bond strength using orthodontic adhesives containing three different types of bioactive glass. *Materials* 9:125. doi: 10.3390/ma9030125

Yang, S.-Y., Piao, Y.-Z., Kim, S.-M., Lee, Y.-K., Kim, K.-N., and Kim, K.-M. (2013). Acid neutralizing, mechanical and physical properties of pit and fissure sealants containing melt-derived 45S5 bioactive glass. *Dent. Mater.* 29, 1228–1235.

Yu, Y., Jin, G., Xue, Y., Wang, D., Liu, X., and Sun, J. (2017). Multifunctions of dual Zn/Mg ion co-implanted titanium on osteogenesis, angiogenesis and bacteria inhibition for dental implants. *Acta Biomater.* 49, 590–603.

Zhang, J. F., Wu, R., Fan, Y., Liao, S., Wang, Y., Wen, Z. T., et al. (2014). Antibacterial dental composites with chlorhexidine and mesoporous silica. *J. Dent. Res.* 93, 1283–1289.

Conflict of Interest: The authors declare that the research was conducted in the absence of any commercial or financial relationships that could be construed as a potential conflict of interest.

frontiers in Bioengineering and Biotechnology

ORIGINAL RESEARCH
published: 09 June 2021
doi: 10.3389/fbioe.2021.630977

Fabrication and Characterization of Collagen/PVA Dual-Layer Membranes for Periodontal Bone Regeneration

Tian Zhou[1,2†], Siwei Chen[3†], Xinxin Ding[2,4], Zhihuan Hu[3], Lian Cen[3] and Xiaomeng Zhang[2,4*]*

[1] Department of Oral Maxillofacial-Head and Neck Oncology, Shanghai Ninth People's Hospital, College of Stomatology, Shanghai Jiao Tong University School of Medicine, Shanghai, China, [2] National Clinical Research Center for Oral Diseases, Shanghai Key Laboratory of Stomatology and Shanghai Research Institute of Stomatology, Shanghai, China, [3] Shanghai Key Laboratory of Multiphase Materials Chemical Engineering, State Key Laboratory of Chemical Engineering, Department of Product Engineering, School of Chemical Engineering, East China University of Science and Technology, Shanghai, China, [4] Department of Implant Dentistry, Shanghai Ninth Peoples' Hospital, College of Stomatology, Shanghai Jiao Tong University School of Medicine, Shanghai, China

OPEN ACCESS

Edited by:
Jonathan Lao,
Université Clermont Auvergne, France

Reviewed by:
Xin Zhao,
Hong Kong Polytechnic University, Hong Kong, China
Hae-Won Kim,
Institute of Tissue Regeneration Engineering (ITREN), South Korea

****Correspondence:***
Xiaomeng Zhang
zhangxiaomengwowo@126.com
Lian Cen
liancen@ecust.edu.cn

[†] These authors have contributed equally to this work

Specialty section:
This article was submitted to Biomaterials, a section of the journal Frontiers in Bioengineering and Biotechnology

Received: *18 November 2020*
Accepted: *05 May 2021*
Published: *09 June 2021*

Citation:
Zhou T, Chen S, Ding X, Hu Z, Cen L and Zhang X (2021) Fabrication and Characterization of Collagen/PVA Dual-Layer Membranes for Periodontal Bone Regeneration. Front. Bioeng. Biotechnol. 9:630977. doi: 10.3389/fbioe.2021.630977

Guided tissue regeneration (GTR) is a promising treatment for periodontal tissue defects, which generally uses a membrane to build a mechanical barrier from the gingival epithelium and hold space for the periodontal regeneration especially the tooth-supporting bone. However, existing membranes possess insufficient mechanical properties and limited bioactivity for periodontal bone regenerate. Herein, fish collagen and polyvinyl alcohol (Col/PVA) dual-layer membrane were developed via a combined freezing/thawing and layer coating method. This dual-layer membrane had a clear but contact boundary line between collagen and PVA layers, which were both hydrophilic. The dual membrane had an elongation at break of 193 ± 27% and would undergo an *in vitro* degradation duration of more than 17 days. Further cell experiments showed that compared with the PVA layer, the collagen layer not only presented good cytocompatibility with rat bone marrow-derived mesenchymal stem cells (BMSCs), but also promoted the osteogenic genes (RUNX2, ALP, OCN, and COL1) and protein (ALP) expression of BMSCs. Hence, the currently developed dual-layer membranes could be used as a stable barrier with a stable degradation rate and selectively favor the bone tissue to repopulate the periodontal defect. The membranes could meet the challenges encountered by GTR for superior defect repair, demonstrating great potential in clinical applications.

Keywords: dual-layer, periodontal, collagen, PVA, GTR

INTRODUCTION

Periodontitis is an infectious disease that causes the detachment of the junctional epithelium from the tooth layer and the disconnection of periodontal ligament fibers, and eventually leads to bone loss (Xu et al., 2012). Guided tissue regeneration (GTR) is an effective treatment to control disease progression and promote the formation of tooth-supporting tissues. Ideal GTR membranes are expected to act as barriers that can prevent the migration of epithelial cells into the

defect areas while hold space to guide the regeneration of impaired tissues including cementum, periodontal ligament, and alveolar bone (Liu X. et al., 2020). Collagen membranes, as conventional bioabsorbable membranes, are mostly used for GTR in clinical practice. However, they degrade and collapse quickly, followed by epithelial ingrowth and compromised bone formation. In addition, collagen membranes are mostly chemically crosslinked and lack osteogenic potential. Therefore, it would be a win–win solution to develop a design of a novel dual-layer GTR membrane, of which one layer could prevent epithelium ingrowth and the other layer could promote selective repopulation of the root surface by multipotent cells (i.e., periodontal ligament cells and osteoblasts).

Polyvinyl alcohol (PVA) is a water-soluble polymer with excellent biocompatibility and easy to process for biomedical applications (Chaudhuri et al., 2016). With tissue-like elasticity and excellent mechanical strength, PVA can be used to improve the mechanical properties of other materials. Lin et al. (2020) have reported that the tensile and compressive properties of bioactive glass crosslinked PVA hydrogel were enhanced with the increase in PVA content. PVA membrane also can act as a physical barrier to prevent adhesion after surgery (Weis et al., 2004). The viability of human gingival fibroblasts (HGFs) was decreased by increasing the ratio of PVA in PVA/collagen composite hydrogels (Zhou et al., 2020), which showed the potential of PVA hydrogel for resisting gingival tissue ingrowth. Hence, PVA was chosen for acting as the outer layer of the current novel GTR membrane for providing mechanical support and preventing the fast attachment of epithelium.

Regarding the inner layer, collagen has been widely used in periodontal tissue regeneration for its excellent biocompatibility, biodegradability, and low antigenicity (Jiang et al., 2017). However, currently available collagen is mainly extracted from mammals such as bovine and porcine, which has religious limitation on Jews, Muslims, and Hindus (Goyal et al., 2013), and also has the risk of the prevalence of transmitting animal diseases (Chuaychan et al., 2015). In recent years, marine collagen has gained increasing attention as a safer alternative source of mammalian collagen (Paradiso et al., 2019). Song et al. (2006) have reported that jellyfish collagen exhibited higher fibroblast viability than other naturally derived biomaterials, including bovine collagen, gelatin, hyaluronic acid, and glucan. Tilapia collagen exhibited the effect of promoting osteogenesis and fibroblast formation and is also beneficial to the proliferation of human vascular endothelial cells (Song et al., 2019). According to these reports, fish collagen might have great potential to be used as the inner layer of the current design of GTR membrane to improve the bioactivity of multipotential cells. Although the inner layer made of collagen has relatively poor mechanical property and rapid degradation rate (Raftery et al., 2016), the outer layer made of PVA could make up for that. However, it is still unknown whether the dual-layer membrane could be tailored by taking advantage of fish collagen and PVA. Besides, whether the mechanical property and the osteogenic bioactivity of this novel dual-layer membrane can be improved as expected also needs to be verified.

Therefore, the main aim of this study was to develop a collagen (Col)/PVA dual-layer membrane and investigate its potential for promoting the desired regeneration of impaired tissue within periodontal defect areas. The PVA layer was first partially pre-set according to a freezing/thawing method, while the collagen layer was initiated by layer coating onto the partially set PVA layer without any chemical crosslinking involved. Cross-sectional morphology of the dual-layer membrane was observed by SEM, while its mechanical strength was represented by tensile strength. *In vitro* degradation performance was further determined. Adhesion and proliferation of rat bone marrow mesenchymal stem cells (BMSCs) on each layer of the membrane, as well as osteogenic-related genes, such as runtrelated gene-2 (RUNX2), alkaline phosphatase (ALP), osteocalcin (OCN), and collagen 1 (COL1) and protein (ALP) expression by the attached BMSCs were assayed with time. This study could provide substantial demonstration to realize such a design and also to verify the feasibility of this dual-layer Col/PVA membrane as a novel GTR membrane, and the controllable methodology also exhibits great potential in clinical applications.

MATERIALS AND METHODS

Preparation of Col/PVA Dual-Layer Membrane

Tilapia scale collagen was provided by Shanghai Fisheries Research Institute. It was first dissolved in 0.1 M acetic acid at room temperature with stirring for 4 h to form a 1.5% collagen solution. At the same time, PVA (AR 1799, General-Reagent) was dissolved in water at 80^{o}C with magnetic stirring for 6 h to prepare an 18% PVA solution. The dispersion of PVA solution of high viscosity required a varying stirring speed of around 150–250 rpm. After that, PVA solution was spread evenly in a petri dish of 60 mm-diameter and placed at room temperature for 24 h to crosslink. The PVA membrane was then pre-frozen at −20^{o}C for 1 h and the above-mentioned collagen solution was spread evenly on the pre-frozen membrane layer. The mixture was then placed at −20^{o}C for 24 h. Finally, the dual-layer membrane was immersed in 0.1 M NaOH solution for 10 s and then rinsed with adequate DI water.

Characterization of Col/PVA Dual-Layer Membrane

The morphology of the Col/PVA dual-layer membrane was observed with a scanning electron microscope (SEM) (Nova SEM 450, FEI, United States) with the platinum spray time of 90 s and the voltage of 10 kV. The weight loss temperature of the dual-layer membrane was determined by a thermogravimetric (TG) analyser (Q500, TA, United States). The membrane sample was heated at the rate of 10^{o}C/min in a temperature range of 30–800^{o}C. The characterization tests for pure collagen membrane and PVA membrane were also conducted as comparison. The wettability data of both sides of the dual-layer membrane was obtained by a contact angle measuring instrument (OCA20,

Dataphysics, Germany). To be specific, 5 μl of water droplets were used for water contact angle (WCA) measurement.

Mechanical Strength

The mechanical strength of the membrane was measured by a universal testing machine (Instron 5542, United States) with a stretching speed of 20 mm/min. The membrane was cut into a dimension of 10 mm × 30 mm for the test. The mechanical test is conducted on wet samples which were pre-immersed in DI water for 30 s. The sample thickness was observed through a microscope (BX51-P, Olympus, Japan). In order to prevent the test sample from sliding or falling off the clamps during stretching processes, medical gauze is added between the sample and the clamp to increase friction. Elongation at break was calculated as $(L_b–L_o)/L_o$, where L_b is the length of samples when the tensile force reaches zero, which means the sample is totally broken, and L_o is the length of an exposed sample between two test clamps before stretching. L_o was measured by a vernier caliper and L_b was determined by the universal testing machine. Tensile strength was calculated as F_{max}/A_o, where F_{max} is the maximum of tensile force during stretching and A_o is the cross-section area of the sample before stretching.

In vitro Degradation Test and Morphology After Immersion in PBS

The membranes were irradiated under ultraviolet light for 12 h to kill bacteria, and all operations were performed on a sterile operating table (Hamanaka et al., 2011). Each membrane was cut into 10 mm × 30 mm samples. Each sample was immersed in 5 ml PBS solution at 37^{o}C for different time durations. The PBS solution was replaced every 4 days. After predetermined time durations, the test samples were withdrawn and lyophilized by a freeze dryer. The remaining weight of each sample was measured. The degradation level was calculated in weight % using the following equation:

$$\text{Degradation } [wt\%] = \frac{\text{Mc}}{\text{Mi}} \times 100$$

in which Mc is the weight at the time of measurement, and Mi corresponds to the initial mass of the sample prior to immersion in PBS. The Cross-section morphology of lyophilized Col/PVA dual-layer membranes after immersion in PBS for 4, 8, 12, and 17 days was also observed by SEM.

Rat BMSCs Culture

Rat BMSCs were obtained from the 4-week-old Sprague-Dawley rats. Approval for bone marrow harvesting was obtained from the Animal Care and Experiment Committee of Ninth People's Hospital affiliated to School of Medicine, Shanghai Jiao Tong University. Rat BMSCs were isolated and harvested as described in the literature (Liu and Sun, 2014). Under aseptic conditions, bilateral tibiae and femora were dissected from the muscle and connective tissue, and the epiphyses were removed. Cells were cultured in Dulbecco's modified eagle medium (DMEM, Hyclone) with10% fetal bovine serum (FBS, Hyclone), 100 U/mL penicillin, and 100 mg/L streptomycin (Hyclone) and incubated at 37°C with 5% CO_2 for 24 h. The BMSCs were used for the experiments in passage 2–3.

Cell Viability and Proliferation Assay

BMSCs viability and proliferation were evaluated by the Cell Counting Kit-8 (CCK-8, Dojindo, Japan) assay. Briefly, BMSCs were seeded, respectively, on the collagen layer of the Col /PVA dual-layer membrane and pure PVA membrane in 96-well plates at a cell density of 5×10^3 cells per well for 1, 3, and 5 days. The optical density (OD) of formazan at 450 nm was measured using a Multiskan GO microplate photometer (Thermo Scientific, United States). At 1 day, hochest and EdU staining (Beyotime, Shanghai, China) was performed to detect the DNA duplicate activity and the cells were examined collagen using the fluorescence microscope.

Osteogenic Genes Expression

Expression of marker genes of osteoblasts, such as RUNX2, ALP, OCN, and COL1 was detected by real-time polymerase chain reaction (PCR), and the housekeeping gene GAPDH was used to normalize results. In brief, BMSCs were seeded, respectively, on the layer of the Col/PVA dual-layer membrane and pure PVA membrane in 6- well plates at a cell density of 1×10^5 cells per well for 7 and 14 days. Total RNA extraction was isolated using TRIZOL (Invitrogen, United States) according to the manufacturer's instructions. Gene expression level was tested by a Bio-Rad sequence detection system (MyiQ2, United States) using a real-time PCR kit (SYBR Premix EX Taq, TaKaRa). The sequences of specific primers for these genes are listed in **Table 1**.

ALP Staining and Activity Assay

ALP staining was performed using a BCIP/NBT ALP kit (Beyotime, Shanghai, China). Briefly, BMSCs were seeded, respectively, on the collagen layer of the Col /PVA dual-layer membrane and pure PVA membrane in 6- well plates at a cell density of 1×10^5 cells per well for 3 days. After washed by PBS, the BMSCs were fixed by 4% paraformaldehyde for 30 min,

TABLE 1 | Primer sequences used for qRT-PCR.

Gene	Forward sequence	Reverse sequence
RUNX2	TCCGCCACCACTCACTACCAC	GGAACTGATAGGACGCTGACGAAG
ALP	GCCTACTTGTGTGGCGTGAA	AGGATGGACGTGACCTCGTT
OCN	GGACCCTCTCTCTGCTCACTCTG	ACCTTACTGCCCTCCTGCTTGG
COL1	CGAGTCACACCGGAACTTGG	CCAATGTCCAAGGGAGCCAC
GAPDH	CTGAACGGGAAGCTCACTGG	TGAGGTCCACCACCCTGTTG

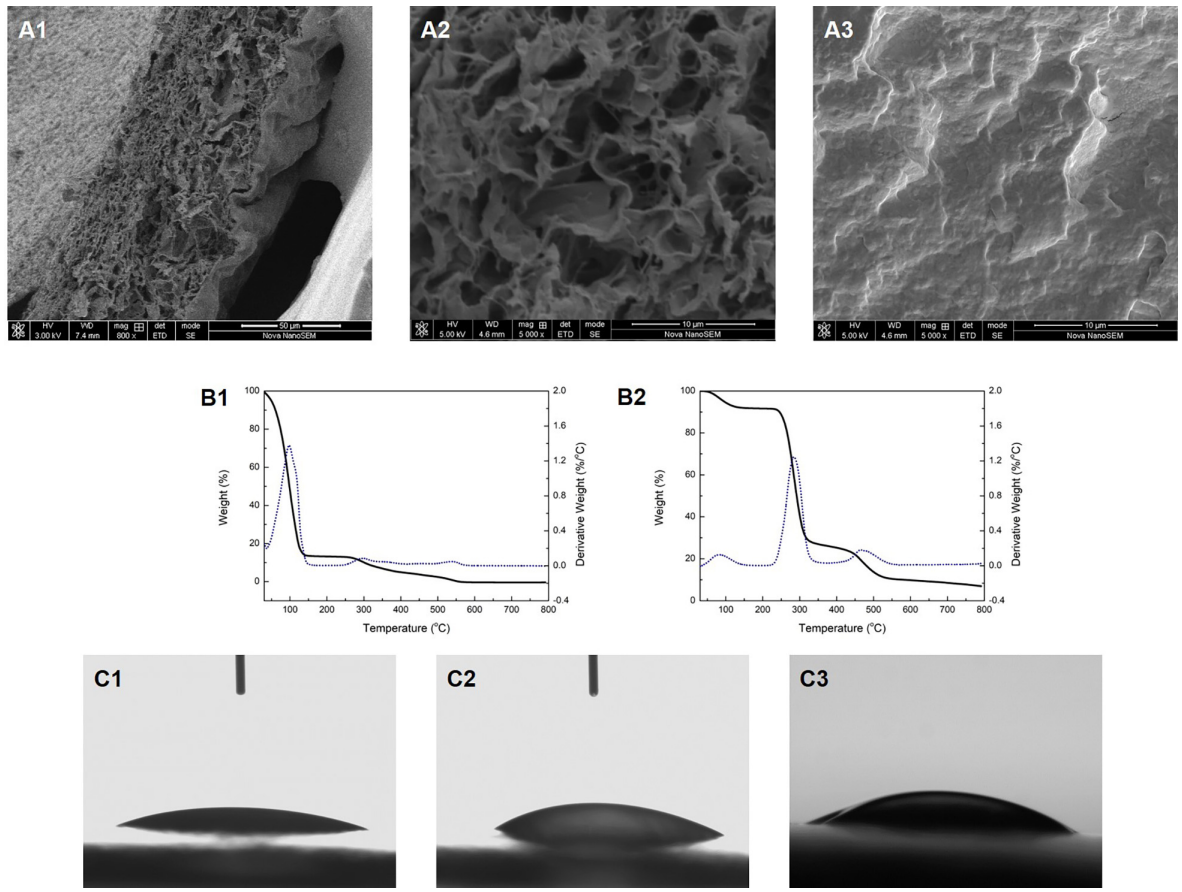

FIGURE 1 | The cross-section morphology of the Col/PVA dual-layer membrane showing **(A1)** both layers, **(A2)** collagen layer, **(A3)** PVA layer. TG analysis of **(B1)** Col/PVA dual-layer membrane, **(B2)** pure PVA membrane. WCA of **(C1)** collagen side, **(C2)** PVA side of the Col/PVA dual-layer membrane, **(C3)** pure PVA membrane.

and were dyed in a mixture of nitro-blue tetrazolium and 5-bromo-4-chloro-3-indolylphosphate (Zhang et al., 2015). Then the cells were observed and photographed by optical microscopy. ALP activity on day 7 was also assessed using ALP detection kit (Beyotime, Shanghai, China) according to the manufacturer's instructions. The ALP activity was normalized to the total protein content measured by BCA method.

Statistical Analysis

Data are expressed as mean ± standard deviation (SD). All statistical analyses were performed using SPSS 20.0 software. Statistically significant differences ($p < 0.05$) between the two groups were evaluated using student's t-test. Data analysis involved the use of Graph Pad Prism 8.2.1 software.

RESULTS AND DISCUSSION

Characterization of the Col/PVA Dual-Layer Membrane

SEM images were taken to reveal the morphology of the membrane. **Figure 1. A1** shows the cross-section of the Col/PVA membrane with a clear dual-layer structure and close connection at the interface. It was shown that the gelation of PVA dissolved in water upon the freezing/thawing cycle is due to partial crystallization of PVA chains that results in hard crystallites serving as physical cross-links of a network structure (Zhang et al., 2012). Moreover, a certain amount of free hydroxyl groups of PVA and enough chain mobility is likely to contributing to the formation of hydrogen bonding between PVA chains. The collagen solution was spread evenly on the pre-frozen PVA membrane layer which was partially set or gelated. It was thus proposed that free hydroxyl groups on PVA chains could lead to the formation of hydrogen bonding across the interface of PVA layer and collagen layer, since extensive hydrogen bonding formation could be expected between PVA chains when the two cut surfaces of PVA are brought into contact. The thickness of each layer could be easily adjusted by changing the amount of PVA solution and collagen solution added to the petri dish. Furthermore, it is obvious that each layer exhibits different morphology. The collagen layer has a loose and porous structure (**Figure 1. A2**), while PVA layer has a dense and highly crosslinked structure (**Figure 1. A3**). The porous network structure of collagen could facilitate new-born cells to migrate

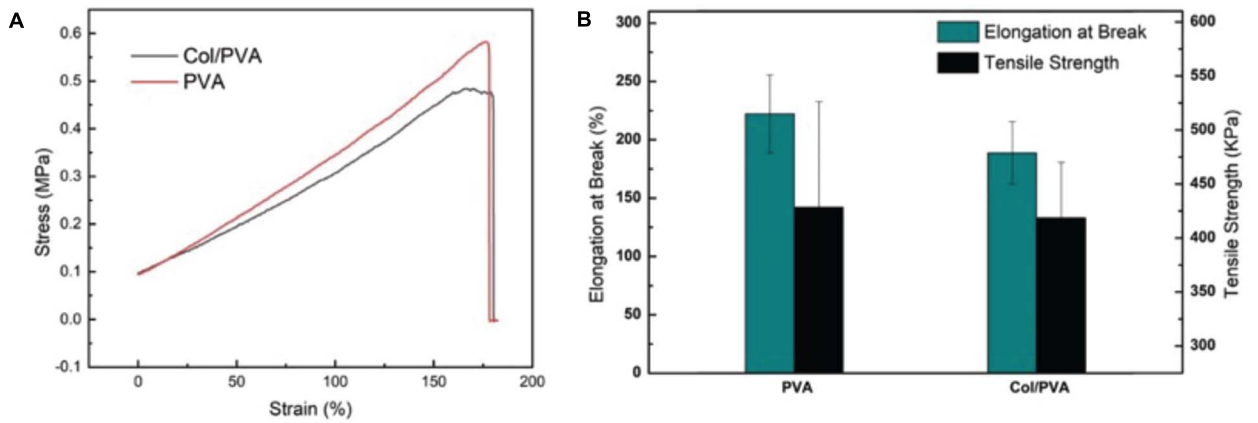

FIGURE 2 | Mechanical properties of the Col/PVA dual-layer membrane and pure PVA membrane **(A)** tensile stress–strain curve **(B)** Elongation at break and tensile strength.

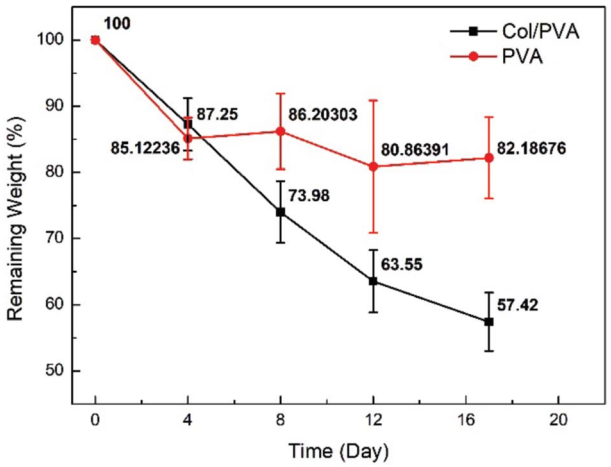

FIGURE 3 | Remaining weight of Col/PVA and PVA membrane after being immersed in PBS for different time durations.

into the scaffold and guide cells to proliferate. The size and porosity of the collagen materials can be effectively controlled by adjusting the freeze-drying rate, where large pore size can permit cell migration and nutrient diffusion and small pore sizes can promote cell adhesion (Sorushanova et al., 2019). However, extremely small pores should also be avoided as cells cannot migrate toward the center of the construct by limiting the diffusion of nutrients and removal of waste products (Murphy and O'Brien, 2010), thus further restricting cell attachment and differentiation potential. In our study, the collagen layer exhibits a microporous structure, which was supposed to permit cell ingrowth. Meanwhile, PVA would act as a barrier with a dense structure that could inhibit other cells from invading the collagen layer. In this way, PVA layer holds adequate space for new-born cells to grow. These properties could be further manipulated with the adjustment of the relative thickness of each layer to achieve the desired biological responses.

The TG analysis and the first derivative to the rate of weight loss are shown in **Figures 1. B1,B2**. The weight loss of the Col/PVA double-layer membrane mainly occurred at 30–147 and 260–575^{o}C (**Figure 1. B1**). The first stage of weight loss was mainly due to the loss of moisture and residual acetic acid (Lewandowska et al., 2016). The second stage might be attributed to the thermal degradation of collagen and PVA. The weight loss of pure collagen solution occurred at 30–163^{o}C, during which the rate of thermal weight loss continued to rise. PVA membrane lost weight at 50–130, 230–340, and 440–540^{o}C, respectively, as shown in **Figure 1. B2**. These three major stages were, respectively, referred to the weakly physisorption of water, the decomposition of PVA side chain, and the decomposition of PVA main chain (Asran et al., 2010). TG analyze indicated that the weight loss behavior of Col/PVA dual-layer membrane was regulated by the properties of collagen and PVA and their relative contents. With the combination of PVA, the weight loss rate of the dual-layer membrane was decreased compared with that of the pure collagen membrane. Therefore, the Col/PVA dual-layer membrane showed thermodynamically stability for application in the human body.

The WCA of both sides of the Col/PVA dual-layer membrane was shown in **Figures 1. C1,C2**. The collagen layer had a WCA of 20^{o} ± 1^{o} (**Figure 1. C1**), and PVA layer had a WCA of 30^{o} ± 1^{o} (**Figure 1. C2**). Pure PVA membrane had a WCA of 33^{o} ± 1^{o} (**Figure 1. C3**). It indicated that both layers have great hydrophilic performance. Hence, the inherent excellent hydrophilicity of both collagen and PVA was preserved. It is known that collagen with amino acid contents is highly hydrophilic and can initiate the release of biological signals to promote cell adhesion and proliferation (Sobhanian et al., 2019). PVA also has good hydrophilicity and is highly soluble in water and environmentally safe, suitable as a component for membrane modification and property enhancement (Park et al., 2018). The manufacturing process of the dual-layer Col/PVA membrane is a purely physical process, which retains both the physical

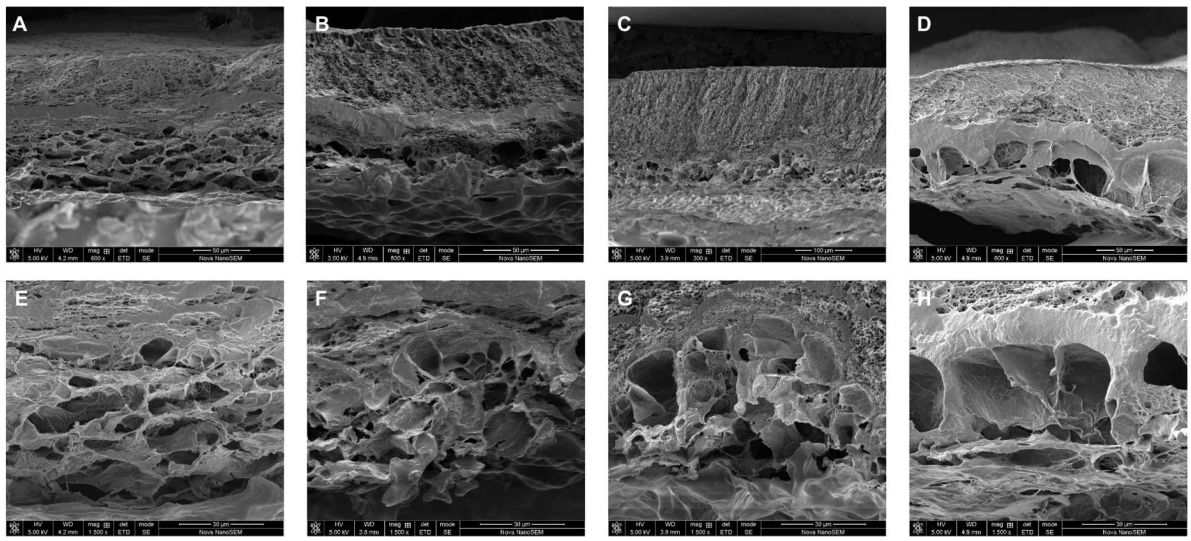

FIGURE 4 | Cross-section morphology of lyophilized Col/PVA dual-layer membranes after being immersed in PBS for **(A)** 4 days, **(B)** 8 days, **(C)** 12 days, **(D)** 17 days, and the corresponding magnified images of collagen layer at **(E)** 4 days, **(F)** 8 days, **(G)** 12 days, **(H)** 17 days.

and chemical properties of collagen and PVA material in each layer, showing superior hydrophilicity as a desirable feature of GTR membranes.

Mechanical Properties of the Col/PVA Dual-Layer Membrane

The mechanical strength of the Col/PVA dual-layer membrane and the pure PVA membrane were compared in **Figure 2**. The PVA membrane has an excellent elasticity with the elongation at break of 222 ± 33% and the tensile strength of 429 ± 98 KPa. After the combination of collagen layer, the Col/PVA dual-layer membrane preserved the close mechanical strength to that of pure PVA membrane. It has an elongation at break of 193 ± 27% and the tensile strength of 419 ± 51 KPa. However, there is no significant difference between the two groups, indicating that the desired mechanical strength from PVA is highly reserved after the addition of collagen layer under the current design and processing conditions.

Guided tissue regeneration membranes need to endure the tensile force from tissue extraction and possess high flexibility to keep structural integrity during the surgical process (Geão et al., 2019). Pure collagen membrane of this our thin-layer scale is too mechanically fragile to test its tensile strength, since it would break when it was placed between testing clamps. PVA is a flexible polymer and can be used to improve the properties of polymers (Aadil et al., 2018). It is robust and has a high strength-to-weight ratio (Chaudhuri et al., 2016). It has been reported that in the process of fabricating collagen/PVA composites patches, the mechanical strength could be increased by increasing the concentration of PVA with a constant collagen amount (Iqbal et al., 2018). Therefore, in our study, adding a PVA layer on the pure collagen membrane is expected to bring adequate mechanical strength. The results showed that the Col/PVA dual-layer membrane is highly flexible with a high elongation, which not only makes the Col/PVA dual-layer membrane easy to operate in clinic, but also provides mechanical support for bone regeneration.

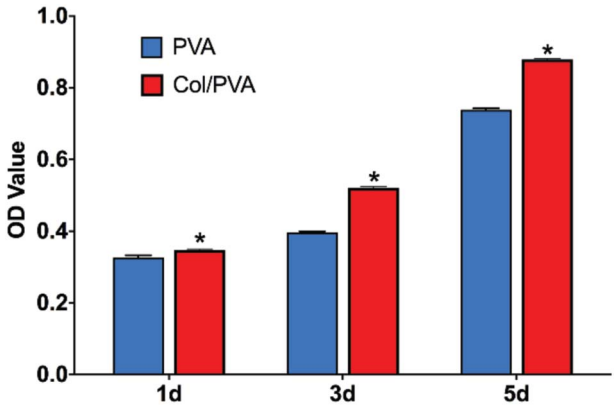

FIGURE 5 | CCK-8 assay results of BMSCs cultured for 1, 3, and 5 days. Data are presented as mean values with standard deviation. *indicates a significant difference between Col/PVA and PVA group with p-value < 0.05.

In vitro Degradation of the Col/PVA Dual-Layer Membrane

The degradation of the Col/PVA dual-layer membranes was evaluated, and it was shown that the weight of the membrane was decreasing when it was immersed in PBS solution as shown in **Figure 3**. The weight of samples decreased with time almost linearly for ∼12 days. The first 4 days had a weight drop of 12.7 ± 4.8%($p < 0.05$, day 0 versus 4), while the second 4 days had a weight drop of 13.3 ± 5.7% ($p < 0.05$, day 4 versus 8) and the third 4 days was 10.4 ± 5.8%($p < 0.1$, day 8

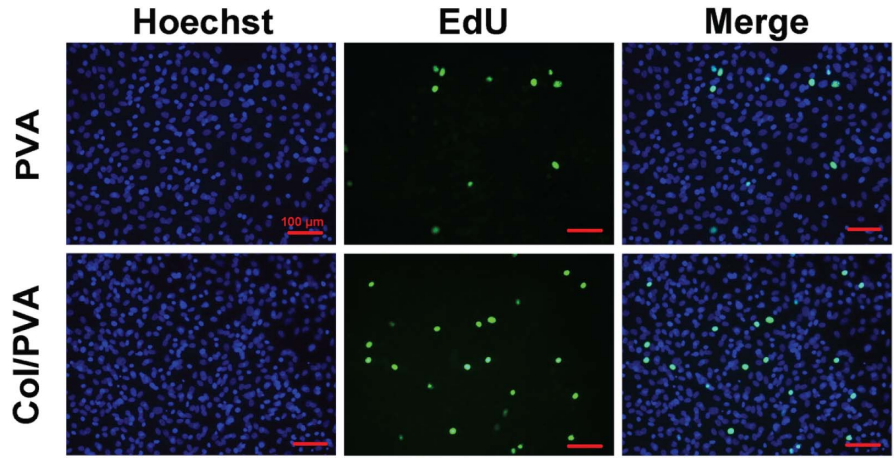

FIGURE 6 | Fluorescence images of BMSCs cultured on the pure PVA membrane and collagen layer of the Col/PVA dual-layer membrane (represented as Col/PVA) for 1 day. Hoechst staining with blue indicated the living cells on two surfaces and EdU staining with green indicated the active DNA duplicate activity of cells. The scale bar was 100 μm.

versus 12). From day 12 on, the degradation was slowed down and the remaining weight was maintained around 58–67% after day 17. The degradation performance of pure PVA membrane was also evaluated, and the remaining weight was maintained around 80–86%. In this study, PVA was used to improve the degradation property of collagen, just as Rebia et al. (2018) reported that the degradation rate of poly (3-hydroxybutyrate-co-3-hydroxyhexanoate) (PHBH) /PVA blend nanofibers could be greatly improved with the increased ratio of PVA polymer.

The morphology of the membrane immersed in PBS at different time points was further observed by SEM. From **Figures 4A–D**, it was obvious that PVA layer remained a dense structure, indicating that PVA degraded slowly and can be a reliable barrier. Meanwhile, the collagen layer exhibited desirable changes to a porous structure. From the images shown in **Figures 4E–H**, the sheet-like porous network of collagen layer was gradually changed with the increase in the pore size and the appearance of local collapse of the microstructure (**Figure 4H**). The increased pore size would be beneficial for new-born cells to grow because the cells need more space to proliferate and spread to the inside of the collagen scaffold. It is normally identified that pore sizes in the 10–150 μm range in scaffolds intended as support for growing cells (Montalbano et al., 2018). Our results showed that the Col/PVA dual-layer membrane could endure immersion in PBS for at least 17 days and kept the desirable porous size on the collagen side, which was advantageous to induce the bone-forming activity of osteoblastic cells.

Viability and Proliferation of BMSCs Cultured With Col/PVA Dual-Layer Membrane

Figure 5 shows the viability of BMSCs cultured on the collagen layer of the Col/PVA dual-layer membrane and pure PVA membrane at 1, 3, and 5 days. Compared to the pure PVA membrane, the collagen layer of the Col/PVA dual-layer membrane had more viable BMSCs at 1, 3, and 5 days. There is a significant difference between the collagen layer and pure PVA membrane ($p < 0.05$). **Figure 6** shows the Hoechst and EdU staining of the BMSCs at 1 day. It was obvious that the collagen layer of the Col/PVA dual-layer membrane had better cell proliferation activity than pure PVA membrane. The fluorescence microscope images were also conformed to the result of CCK-8 assay, indicating that there was a cause-and-effect relationship between the enhanced proliferation activity and cell viability of BMSCs induced by collagen. In our study, the collagen layer used as the inner side of the Col/PVA dual-layer membrane was intended for placing in the bone side of a GTR-treated defect. Therefore, it is advantageous for osteoblastic cells to populate the collagen layer. The results exhibited the improved cell proliferation of BMSCs on the collagen layer, just as many reports also proved that bone tissue-derived cells are able to attach to and to proliferate on different collagen membranes *in vitro* (Behring et al., 2008). The good biocompatibility of the collagen layer was associated with its porous structures and hydrophilicity. Zhang et al. (2017) reported that with the combination of the collagen, poly(L-lactide-co-glycolide)/β-tricalcium phosphate (PLGA/TCP) -collagen materials had the perforative microporous structures and improved hydrophilicity for supporting cell seeding and promoting cell adhesion. **Figures 1**, **4** showed that the collagen layer had a large number of micropores, which can effectively improve the specific surface area of scaffolds to enable their supporting nutrient and oxygen transport during bone regeneration, and to ensure adequate hydrophilicity to allow cells to grow into the scaffolds.

Differentiation of BMSCs Cultured With Col/PVA Dual-Layer Membrane

Figure 7 shows the gene expression analysis of BMSCs cultured on the collagen layer of the Col/PVA dual-layer membrane and pure PVA membrane for 7 and 14 days. The osteoblastic gene

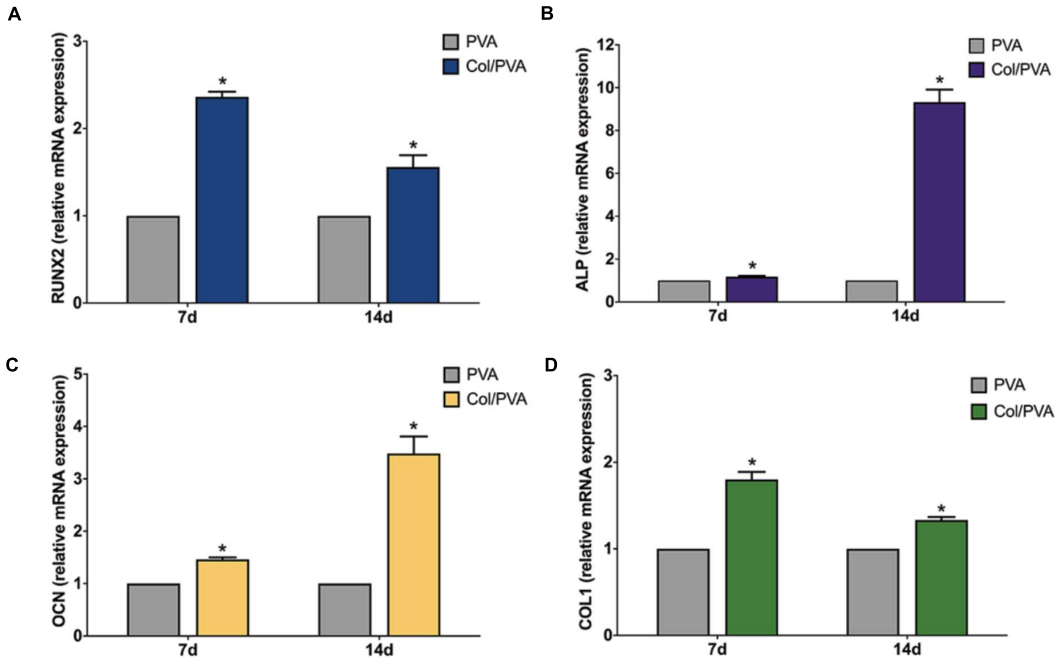

FIGURE 7 | Expression profile of osteogenic differentiation related genes **(A)** RUNX2, **(B)** ALP, **(C)** OCN, **(D)** COL1 of BMSCs cultured on the collagen layer of the Col/PVA dual-layer membrane and pure PVA membrane for 7 and 14 days. *indicates a significant difference between Col/PVA and PVA group with p-value < 0.05.

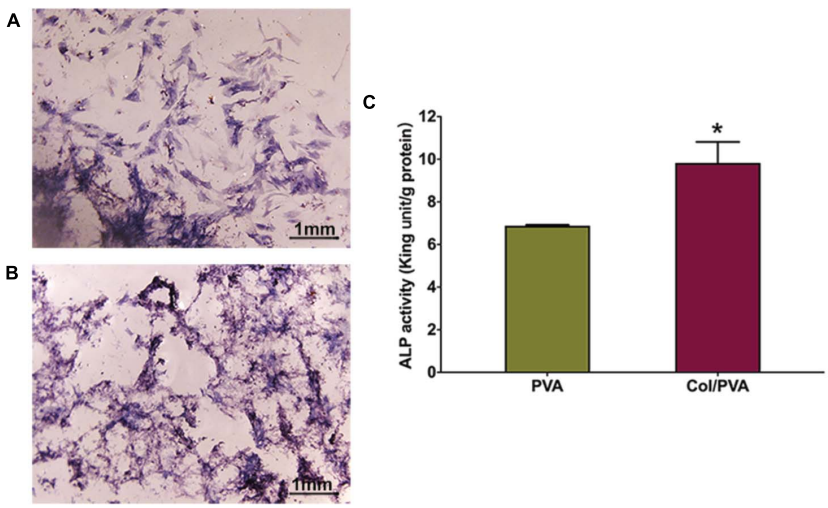

FIGURE 8 | The ALP staining images of BMSCs cultured on the **(A)** pure PVA membrane and **(B)** the collagen layer of the Col/PVA dual-layer membrane for 7 days. **(C)** ALP activity of BMSCs cultured on the different surfaces for 7 days. *indicates a significant difference between PVA and Col/PVA group with p-value < 0.05.

expression of RUNX2, ALP, OCN, and COL1 were significantly upregulated on the collagen layer of the Col/PVA dual-layer membrane at 7 and 14 days as compared to that of the PVA layer ($P < 0.05$). The results demonstrating the expression of osteogenic genes can be induced by the collagen layer of Col/PVA dual-layer membrane. RUNX2 is an essential transcription factor required for osteogenic differentiation. Elango et al. (2019) has reported that collagen peptide (CP) triggered p38MAPK dependent RUNX2 signaling pathway in BMMS cells during osteoblast differentiation. ALP is an early marker for osteogenic differentiation, which can provide the necessary phosphate groups for promoting the formation of bone-like nodules. OCN is a specific marker of mature osteoblasts and is synthesized by fully differentiated osteoblasts. Collagen has outstanding osteoconductive property. It was reported that coating collagen on PLGA fibers could enhance the expression of osteogenic marker genes (RUNX2, ALP, and OCN) of rMSCs (Yang et al., 2018). COL1 gene, a crucial element of connective tissue, is also

a marker of osteogenic differentiation related to bone formation and bone architecture (Hayrapetyan et al., 2016). The data in the present study have confirmed that the RUNX2, ALP, OCN, and COL1 gene expression induced by the collagen layer of Col/PVA dual-layer membrane was significantly higher than that of the pure PVA membrane, which indicated that collagen layer facilitated osteoblastic differentiation of BMSCs and in turn can help to repair the alveolar during periodontal tissue regeneration.

ALP Staining and Activity of BMSCs Cultured With Col/PVA Dual-Layer Membrane

ALP staining was used to detect the differences of the expression on the collagen layer of the Col/PVA dual-layer membrane and pure PVA membrane. As shown in **Figures 8A,B**, the BMSCs cultured on the collagen layer of the Col/PVA dual-layer membrane had enhanced ALP activity compared to the PVA membrane and the at 7 day ($P < 0.05$). ALP staining of BMSCs in **Figure 8C** also indicated that collagen layer of the Col/PVA dual-layer membrane displayed stronger ALP expression. These results indicate that the osteoblastic differentiation of BMSCs was stimulated by the collagen layer of the Col/PVA dual-layer membrane. Collagen is known to be an effective substrate for mineral deposition. Its layer contains sites that can promote osteoblast adsorption and mineral deposition. Volumes of new bone, new cementum and new periodontal ligament were significantly greater in the collagen hydrogel/sponge scaffold (Kosen et al., 2012). Collagen materials had osteogenic effects on human bone marrow-derived mesenchyme stem cells (Li et al., 2019). Montalbano et al. (2018). reported that ALP production in human mesenchymal stem cells increased at higher concentrations of collagen in collagen/alginate/fibrin based hydrogels, indicating their potential for the promotion of osteogenic activity. Moreover, collagen membrane when enriched with human periodontal-ligament stem cells and extracellular vesicles were shown to promote both bone regeneration and vascularization (Pizzicannella et al., 2019a), while bovine pericardium collagen membrane in together with human gingival MSCs and ascorbic acid could further perfect the osteogenic process (Pizzicannella et al., 2019b). In the renewal of bone tissue defects, a suitable scaffold plays a key role for proper bone formation and remodeling (Diomede et al., 2020). All of the above results thus fully substantiate the suitability of current Col/PVA membrane as a promising GTR for dental defects repair. In addition to the collagen based artificial scaffolds or membranes, it is worthy to mention another promising type of scaffold, based more on the extracellular matrix as well as cells, named as "cell sheet" (Chen et al., 2019; Lu et al., 2019). Cell sheet was efficaciously utilized in the regeneration of bone and periodontal ligament-like tissues as shown by recent works (Dong et al., 2020; Liu Y. et al., 2020). Promising as it demonstrated to be, cell sheet manufacture requires high manipulation skills to ensure the quality control (Chen et al., 2019), while the current artificial Col/PVA membrane offers the superiority in relatively easy manufacturing with controllability.

CONCLUSION

The study developed a beneficial Col/PVA dual-layer membrane for periodontal guided bone regeneration. The characterization results suggested that the Col/PVA dual-layer membrane had a clear but contact boundary line between PVA and collagen layers with favorable hydrophilic property. Further research confirms that the collagen layer of the Col/PVA dual-layer membrane can not only enhance BMSCs viability but also induce the osteogenic differentiation of BMSCs by activating expression of RUNX2, ALP, OCN, and COL1. These findings opened up a new way for the application of Col/PVA dual-layer membrane in the field of periodontal regenerative therapy.

DATA AVAILABILITY STATEMENT

The raw data supporting the conclusions of this article will be made available by the authors, without undue reservation.

ETHICS STATEMENT

The animal study was reviewed and approved by The Animal Care and Experiment Committee of Ninth People's Hospital affiliated to School of Medicine, Shanghai Jiao Tong University.

AUTHOR CONTRIBUTIONS

TZ and LC contributed to the study conception and design. SC, XD, and ZH contributed to the fabrication of materials and study conduct. TZ and SC wrote the original manuscript. XZ and LC reviewed and edited the manuscript. XZ contributed to the analysis of data and supervision. All authors contributed to the article and approved the submitted version.

ACKNOWLEDGMENTS

This work was supported by the National Natural Science Foundation of China (No. 81801022).

REFERENCES

Aadil, K. R., Nathani, A., Sharma, C. S., Lenka, N., and Gupta, P. (2018). Fabrication of biocompatible alginate-poly(vinyl alcohol) nanofibers scaffolds for tissue engineering applications. *Mater. Technol.* 33, 507–512. doi: 10.1080/10667857.2018.1473234

Asran, A. S., Henning, S., and Michler, G. H. (2010). Polyvinyl alcohol-collagen-hydroxyapatite biocomposite nanofibrous scaffold: mimicking the key features of natural bone at the nanoscale level. *Polymer (Guildf).* 51, 868–876. doi: 10.1016/j.polymer.2009.12.046

Behring, J., Junker, R., Walboomers, X. F., Chessnut, B., and Jansen, J. A. (2008). Toward guided tissue and bone regeneration: morphology, attachment,

proliferation, and migration of cells cultured on collagen barrier membranes. A systematic review. *Odontology* 96, 1–11. doi: 10.1007/s10266-008-0087-y

Chaudhuri, B., Mondal, B., Ray, S. K., and Sarkar, S. C. (2016). A novel biocompatible conducting polyvinyl alcohol (PVA)-polyvinylpyrrolidone (PVP)-hydroxyapatite (HAP) composite scaffolds for probable biological application. *Colloids Surf. B Biointerfaces* 143, 71–80. doi: 10.1016/j.colsurfb.2016.03.027

Chen, M., Xu, Y., Zhang, T., Ma, Y., Liu, J., Yuan, B., et al. (2019). Mesenchymal stem cell sheets: a new cell-based strategy for bone repair and regeneration. *Biotechnol. Lett.* 41, 305–318. doi: 10.1007/s10529-019-02649-7

Chuaychan, S., Benjakul, S., and Kishimura, H. (2015). Characteristics of acid- and pepsin-soluble collagens from scale of seabass (*Lates calcarifer*). *LWT Food Sci. Technol.* 63, 71–76. doi: 10.1016/j.lwt.2015.03.002

Diomede, F., Marconi, G. D., Fonticoli, L., Pizzicanella, J., Merciaro, I., Bramanti, P., et al. (2020). Functional relationship between osteogenesis and angiogenesis in tissue regeneration. *Int. J. Mol. Sci.* 21, 3242. doi: 10.3390/ijms21093242

Dong, R., Bai, Y., Dai, J., Deng, M., Zhao, C., Tian, Z., et al. (2020). Engineered scaffolds based on mesenchymal stem cells/preosteoclasts extracellular matrix promote bone regeneration. *J. Tissue Eng.* 11, 1–13. doi: 10.1177/2041731420926918

Elango, J., Robinson, J., Zhang, J., Bao, B., Ma, N., de Val, J. E. M. S., et al. (2019). Collagen peptide upregulates osteoblastogenesis from bone marrow mesenchymal stem cells through MAPK- Runx2. *Cells* 8:446. doi: 10.3390/cells8050446

Geão, C., Costa-Pinto, A. R., Cunha-Reis, C., Ribeiro, V. P., Vieira, S., Oliveira, J. M., et al. (2019). Thermal annealed silk fibroin membranes for periodontal guided tissue regeneration. *J. Mater. Sci. Mater. Med.* 30:70. doi: 10.1007/s10856-019-6225-y

Goyal, D., Goyal, A., and Brittberg, M. (2013). Consideration of religious sentiments while selecting a biological product for knee arthroscopy. *Knee Surg. Sports Traumatol. Arthrosc.* 21, 1577–1586. doi: 10.1007/s00167-012-2292-z

Hamanaka, D., Norimura, N., Baba, N., Mano, K., Kakiuchi, M., Tanaka, F., et al. (2011). Surface decontamination of fig fruit by combination of infrared radiation heating with ultraviolet irradiation. *Food Control* 22, 375–380. doi: 10.1016/j.foodcont.2010.09.005

Hayrapetyan, A., Bongio, M., Leeuwenburgh, S. C. G., Jansen, J. A., and van den Beucken, J. J. J. P. (2016). Effect of Nano-HA/collagen composite hydrogels on osteogenic behavior of mesenchymal stromal cells. *Stem Cell Rev. Rep.* 12, 352–364. doi: 10.1007/s12015-016-9644-x

Iqbal, B., Muhammad, N., Rahim, A., Iqbal, F., Sharif, F., Safi, S. Z., et al. (2018). Development of collagen/PVA composites patches for osteochondral defects using a green processing of ionic liquid. *Int. J. Polym. Mater. Polym. Biomater.* 68, 590–596. doi: 10.1080/00914037.2018.1474358

Jiang, X., Wang, Y., Fan, D., Zhu, C., Liu, L., and Duan, Z. (2017). A novel human-like collagen hemostatic sponge with uniform morphology, good biodegradability and biocompatibility. *J. Biomater. Appl.* 31, 1099–1107. doi: 10.1177/0885328216687663

Kosen, Y., Miyaji, H., Kato, A., Sugaya, T., and Kawanami, M. (2012). Application of collagen hydrogel/sponge scaffold facilitates periodontal wound healing in class II furcation defects in beagle dogs. *J. Periodontal Res.* 47, 626–634. doi: 10.1111/j.1600-0765.2012.01475.x

Lewandowska, K., Sionkowska, A., Grabska, S., and Kaczmarek, B. (2016). Surface and thermal properties of collagen/hyaluronic acid blends containing chitosan. *Int. J. Biol. Macromol.* 92, 371–376. doi: 10.1016/j.ijbiomac.2016.07.055

Li, Q., Lei, X., Wang, X., Cai, Z., Lyu, P., and Zhang, G. (2019). Hydroxyapatite/collagen three-dimensional printed scaffolds and their osteogenic effects on human bone marrow-derived mesenchymal stem cells. *Tissue Eng Part A.* 25, 1261–1271. doi: 10.1089/ten.tea.2018.0201

Lin, B., Hu, H., Deng, Z., Pang, L., Jiang, H., Wang, D., et al. (2020). Novel bioactive glass cross-linked PVA hydrogel with enhanced chondrogenesis properties and application in mice chondrocytes for cartilage repair. *J. Non Cryst. Solids* 529:119594. doi: 10.1016/j.jnoncrysol.2019.119594

Liu, C., and Sun, J. (2014). Potential application of hydrolyzed fish collagen for inducing the multidirectional differentiation of rat bone marrow mesenchymal stem cells. *Biomacromolecules* 15, 436–443. doi: 10.1021/bm401780v

Liu, X., He, X., Jin, D., Wu, S., Wang, H., Yin, M., et al. (2020). A biodegradable multifunctional nanofibrous membrane for periodontal tissue regeneration. *Acta Biomater.* 108, 207–222. doi: 10.1016/j.actbio.2020.03.044

Liu, Y., Wang, H., Dou, H., Tian, B., Li, L., Jin, L., et al. (2020). Bone regeneration capacities of alveolar bone mesenchymal stem cells sheet in rabbit calvarial bone defect. *J. Tissue Eng.* 11, 1–12. doi: 10.1177/2041731420930379

Lu, Y., Zhang, W., Wang, J., Yang, G., Yin, S., Tang, T., et al. (2019). Recent advances in cell sheet technology for bone and cartilage regeneration: from preparation to application. *Int. J. Oral Sci.* 11:17. doi: 10.1038/s41368-019-0050-5

Montalbano, G., Toumpaniari, S., Popov, A., Duan, P., Chen, J., Dalgarno, K., et al. (2018). Synthesis of bioinspired collagen/alginate/fibrin based hydrogels for soft tissue engineering. *Mater. Sci. Eng. C* 91, 236–246. doi: 10.1016/j.msec.2018.04.101

Murphy, C. M., and O'Brien, F. J. (2010). Understanding the effect of mean pore size on cell activity in collagen-glycosaminoglycan scaffolds. *Cell Adh. Migr.* 4, 377–381. doi: 10.4161/cam.4.3.11747

Paradiso, F., Fitzgerald, J., Yao, S., Barry, F., Taraballi, F., Gonzalez, D., et al. (2019). Marine collagen substrates for 2D and 3D ovarian cancer cell systems. *Front. Bioeng. Biotechnol.* 7:343. doi: 10.3389/fbioe.2019.00343

Park, M. J., Gonzales, R. R., Abdel-Wahab, A., Phuntsho, S., and Shon, H. K. (2018). Hydrophilic polyvinyl alcohol coating on hydrophobic electrospun nanofiber membrane for high performance thin film composite forward osmosis membrane. *Desalination* 426, 50–59. doi: 10.1016/j.desal.2017.10.042

Pizzicannella, J., Gugliandolo, A., Orsini, T., Fontana, A., Ventrella, A., Mazzon, E., et al. (2019a). Engineered extracellular vesicles from human periodontal-ligament stem cells increase VEGF/VEGFR2 expression during bone regeneration. *Front. Physiol.* 10:512. doi: 10.3389/fphys.2019.00512

Pizzicannella, J., Marconi, G. D., Pierdomenico, S. D., Cavalcanti, M. F. X. B., Diomede, F., and Trubiani, O. (2019b). Bovine pericardium membrane, gingival stem cells, and ascorbic acid: a novel team in regenerative medicine. *Eur. J. Histochem.* 63:3064. doi: 10.4081/ejh.2019.3064

Raftery, R. M., Woods, B., Marques, A. L. P., Moreira-Silva, J., Silva, T. H., Cryan, S. A., et al. (2016). Multifunctional biomaterials from the sea: assessing the effects of chitosan incorporation into collagen scaffolds on mechanical and biological functionality. *Acta Biomater.* 43, 160–169. doi: 10.1016/j.actbio.2016.07.009

Rebia, R. A., Rozet, S., Tamada, Y., and Tanaka, T. (2018). Biodegradable PHBH/PVA blend nanofibers: fabrication, characterization, in vitro degradation, and in vitro biocompatibility. *Polym. Degrad. Stab.* 154, 124–136. doi: 10.1016/j.polymdegradstab.2018.05.018

Sobhanian, P., Khorram, M., Hashemi, S. S., and Mohammadi, A. (2019). Development of nanofibrous collagen-grafted poly (vinyl alcohol)/gelatin/alginate scaffolds as potential skin substitute. *Int. J. Biol. Macromol.* 130, 977–987. doi: 10.1016/j.ijbiomac.2019.03.045

Song, E., Yeon Kim, S., Chun, T., Byun, H. J., and Lee, Y. M. (2006). Collagen scaffolds derived from a marine source and their biocompatibility. *Biomaterials* 27, 2951–2961. doi: 10.1016/j.biomaterials.2006.01.015

Song, W. K., Liu, D., Sun, L. L., Li, B. F., and Hou, H. (2019). Physicochemical and biocompatibility properties of type I collagen from the skin of Nile Tilapia (*Oreochromis niloticus*) for biomedical applications. *Mar. Drugs* 17:137. doi: 10.3390/md17030137

Sorushanova, A., Delgado, L. M., Wu, Z., Shologu, N., Kshirsagar, A., Raghunath, R., et al. (2019). The collagen suprafamily: from biosynthesis to advanced biomaterial development. *Adv. Mater.* 31:e1801651. doi: 10.1002/adma.201801651

Weis, C., Odermatt, E. K., Kressler, J., Funke, Z., Wehner, T., and Freytag, D. (2004). Poly(vinyl alcohol) membranes for adhesion prevention. *J. Biomed. Mater. Res. Part B Appl. Biomater.* 70, 191–202. doi: 10.1002/jbm.b.30007

Xu, C., Lei, C., Meng, L., Wang, C., and Song, Y. (2012). Chitosan as a barrier membrane material in periodontal tissue regeneration. *J. Biomed. Mater. Res. Part B Appl. Biomater* 100 B, 1435–1443. doi: 10.1002/jbm.b.32662

Yang, X., Li, Y., He, W., Huang, Q., Zhang, R., and Feng, Q. (2018). Hydroxyapatite/collagen coating on PLGA electrospun fibers for osteogenic differentiation of bone marrow mesenchymal stem cells. *J. Biomed. Mater. Res. Part A* 106, 2863–2870. doi: 10.1002/jbm.a.36475

Zhang, H., Xia, H., and Zhao, Y. (2012). Poly(vinyl alcohol) hydrogel can autonomously self-heal. *ACS Macro Lett.* 1, 1233–1236. doi: 10.1021/mz300451r

Zhang, T., Zhang, H., Zhang, L., Jia, S., Liu, J., Xiong, Z., et al. (2017). Biomimetic design and fabrication of multilayered osteochondral scaffolds by low-temperature deposition manufacturing and thermal-induced phase-separation

techniques Biomimetic design and fabrication of multilayered osteochondral scaffolds by low-temperat. *Biofabrication* 9:025021. doi: 10.1088/1758-5090/aa7078

Zhang, X., Wu, C., Chang, J., and Sun, J. (2015). Odontogenic differentiation of human dental pulp cells induced by silicate-based bioceramics via activation of P38/MEPE pathway. *RSC Adv.* 5, 72536–72543. doi: 10.1039/c5ra11706b

Zhou, T., Zheng, K., Sui, B., Boccaccini, A. R., and Sun, J. (2020). In vitro evaluation of poly (vinyl alcohol)/collagen blended hydrogels for regulating human periodontal ligament fibroblasts and gingival fibroblasts. *Int. J. Biol. Macromol.* 163, 1938–1946. doi: 10.1016/j.ijbiomac.2020.09.033

Conflict of Interest: The authors declare that the research was conducted in the absence of any commercial or financial relationships that could be construed as a potential conflict of interest.

frontiers in Bioengineering and Biotechnology

ORIGINAL RESEARCH
published: 02 July 2021
doi: 10.3389/fbioe.2021.629270

Effect of Pore Size on Cell Behavior Using Melt Electrowritten Scaffolds

Yu Han[1,2], Meifei Lian[2,3], Qiang Wu[1], Zhiguang Qiao[1,2], Binbin Sun[1,2]* and Kerong Dai[1,2]**

[1] Department of Orthopaedic Surgery, Shanghai Key Laboratory of Orthopaedic Implants, Shanghai Ninth People's Hospital, Shanghai Jiao Tong University School of Medicine, Shanghai, China, [2] Clinical and Translational Research Center for 3D Printing Technology, Shanghai Ninth People's Hospital, Shanghai Jiao Tong University School of Medicine, Shanghai, China, [3] Department of Prosthodontics, Shanghai Ninth People's Hospital, College of Stomatology, Shanghai Jiao Tong University School of Medicine, National Clinical Research Center for Oral Diseases, Shanghai Key Laboratory of Stomatology & Shanghai Research Institute of Stomatology, Shanghai, China

Tissue engineering technology has made major advances with respect to the repair of injured tissues, for which scaffolds and cells are key factors. However, there are still some issues with respect to the relationship between scaffold and cell growth parameters, especially that between the pore size and cells. In this study, we prepared scaffolds with different pore sizes by melt electrowritten (MEW) and used bone marrow mensenchymal stem cells (BMSCs), chondrocytes (CCs), and tendon stem cells (TCs) to study the effect of the scaffold pore size on cell adhesion, proliferation, and differentiation. It was evident that different cells demonstrated different adhesion and proliferation rates on the scaffold. Furthermore, different cell types showed differential preferences for scaffold pore sizes, as evidenced by variations in cell viability. The pore size also affected the differentiation and gene expression pattern of cells. Among the tested cells, BMSCs exhibited the greatest viability on the 200-μm-pore-size scaffold, CCs on the 200- and 100-μm scaffold, and TCs on the 300-μm scaffold. The scaffolds with 100- and 200-μm pore sizes induced a significantly higher proliferation, chondrogenic gene expression, and cartilage-like matrix deposition after *in vitro* culture relative to the scaffolds with smaller or large pore sizes (especially 50 and 400 μm). Taken together, these results show that the architecture of 10 layers of MEW scaffolds for different tissues should be different and that the pore size is critical for the development of advanced tissue engineering strategies for tissue repair.

Keywords: melt electrowritten, pore size, scaffold, cell, PCL

OPEN ACCESS

Edited by:
Jonathan Lao,
Université Clermont Auvergne, France

Reviewed by:
Xiaojun Yu,
Stevens Institute of Technology, United States
Gowsihan Poologasundarampillai,
The University of Manchester, United Kingdom

***Correspondence:**
Binbin Sun
sunbinbin1992@163.com
Zhiguang Qiao
dr_qiaozhiguang@163.com
Kerong Dai
krdai@163.com

Specialty section:
This article was submitted to Biomaterials, a section of the journal Frontiers in Bioengineering and Biotechnology

Received: *14 November 2020*
Accepted: *18 May 2021*
Published: *02 July 2021*

Citation:
Han Y, Lian M, Wu Q, Qiao Z, Sun B and Dai K (2021) Effect of Pore Size on Cell Behavior Using Melt Electrowritten Scaffolds. Front. Bioeng. Biotechnol. 9:629270. doi: 10.3389/fbioe.2021.629270

INTRODUCTION

In recent years, tissue engineering technology has made tremendous contributions to tissue regeneration (Guo et al., 2018; Cunniffe et al., 2019; Ruvinov et al., 2019). Tissue engineering technology simulates the regeneration of tissues and organs by combining elements such as biological materials, cells, and biologically active molecules to mimic the structure and function of native tissues and organs (Kang et al., 2018; Kumai et al., 2019). These studies reveal that tissue engineering scaffolds are vital components, whose composition and structure affect the proliferation, differentiation, and gene expression in cells (Mannoor et al., 2013; Li et al., 2017; Schon et al., 2017; Wang et al., 2018).

In past studies, researchers have gradually found that, although tissue scaffolds made by general manufacturing techniques can alter the extracellular environment, the changes are more uniform and largely uncontrollable (Teimouri et al., 2015; Zhang et al., 2017; Ponce et al., 2018; Li et al., 2019). However, the complex environment in normal tissues is significantly different. While studies have investigated the heterogeneity associated with cellular complexity, the heterogeneity of the natural extracellular environment has not been replicated. This is primarily due to the difficulty of creating a 3D environment. Although we have developed many intricate methods to generate complex 2D models or prototypes with mechanical or chemical gradients, these culture conditions may not apply to many cell types (Karageorgiou and Kaplan, 2005; Tanaka et al., 2010; Panadero et al., 2016). It is difficult to achieve 3D effects with 2D models (Warnecke et al., 2018). The development of 3D printing technology has provided a new method for the production of tissue engineering scaffolds (Hung et al., 2016; Daly et al., 2017, 2018; Kosik-Kozioł et al., 2017; Chen et al., 2018). As an advantage, 3D printing technology can control the shape and size of the scaffold during production and even print different structures in different parts. However, the specific effects of the micro-architecture on cells, especially that of the scaffold pore size, are not completely clear.

Therefore, for tissue scaffolds obtained by printing, a better understanding of the effect of pore size on adhesion, proliferation, and expression is needed. The pores of scaffolds can provide space for cell growth, and the scaffold itself provides support for cell adhesion. However, while the scaffold with small pores provide more adhesion support, they inevitably reduce the cell growth space. Furthermore, pore size can affect cell differentiation and gene expression (Matsiko et al., 2015). Therefore, a balance between the two is crucial (Zhang et al., 2016). The effect of scaffold pores on cell behavior may be due to specific cell–scaffold interactions. In particular, some studies have shown that cell morphology plays an important role in cell differentiation, which is also associated with the scaffolds (Glaeser et al., 2010; Abdeen et al., 2014; Teixeira et al., 2016; Li et al., 2020).

Therefore, it is important to study and understand the mechanisms underlying scaffold–cell interactions and the subsequent cell differentiation. Previous studies have investigated the effects of scaffold pores on cells but reported conflicting findings. For example, some studies suggested that pores were suitable for chondrogenic differentiation at 20–150 μm (Nehrer et al., 1997; Stenhamre et al., 2011), while others suggested that 250–500 μm was suitable for chondrocyte proliferation and gene expression (Griffon et al., 2006; Lien et al., 2009; Nelson et al., 2021). Besides this, different cells have different sizes and shapes so that the optimal pore size may differ for different cell types. Some studies suggested that the optimal pore size should be about 30 times the size of the cell itself (Salem et al., 2002; Oh et al., 2010; Matsiko et al., 2015). Therefore, this study would examine the effects of pore size on the proliferation and differentiation of different cells.

To avoid the effects of other aspects of the scaffold, polycaprolactone (PCL) was chosen by virtue of its excellent thermoplasticity and biocompatibility (Felice et al., 2018; Bahcecioglu et al., 2019). Moreover, PCL has excellent stability as a degradable material and can be mixed with many metals, drugs, biological factors, etc. (Ghorbani et al., 2015). At present, PCL is widely used for printing various organizational structures and is one of the most commonly used materials (Pok et al., 2013; Kundu et al., 2015; Hanas et al., 2016). In this study, we hypothesized that smaller-pore scaffolds provided more adhesion support to the cells, thereby improving cell adhesion, while larger pores provided more space for cells to proliferate, thereby avoiding premature contact inhibition (Woodfield et al., 2005). To verify this, we used melt electrowritten (MEW) printing scaffolds (Hrynevich et al., 2018; Brennan et al., 2019; Youssef et al., 2019). Although humans have large-sized tissues and organs, the size of the smallest functional units of the tissues and organs is often in the micrometer range, potentially giving rise to challenges associated with conducting related research. MEW printing has advantages such as high precision (Castilho et al., 2019; Ye et al., 2019). This technique includes an electric field based on ordinary melt-extrusion printing, which can better control the printing accuracy and increase the porosity (Daly et al., 2017). The printed fiber diameter is about 10 μm, which can give the cell enough mechanical support while avoiding interference from other factors (Zhu et al., 2017; Zamani et al., 2018; Ye et al., 2019; Youssef et al., 2019) (**Figure 1**).

MATERIALS AND METHODS

Materials

The following reagents were used in this study: PCL (average molecular weight Mn = 45.00 kDa; Sigma-Aldrich, CA, United States), a-DMEM, DMEM/F12 (HyClone, UT, United States), fetal bovine serum (FBS; Gibco, NY, United States), TRITC and FITC phalloidin (R415 and A12379, Invitrogen, CA, United States), 4,6-diamidino-2-phenylindole (DAPI, C0060, MaoKang, Shanghai, China), cell counting kit-8 (CCK-8; Dojindo, Kumamoto, Japan), primary antibodies anti-collagen type II (COL II; ab185430), anti-collagen type I (COL I; ab6308), anti-aggrecan (AGC; ab3778), SOX-9 (SOX9; ab76997; Abcam, Cambridge, United Kingdom), Alexa Fluor 555-conjugated anti-mouse antibody (A32727, Invitrogen, CA, United States), RNeasy mini kit (Qiagen, Hilden, Germany), SuperScript^{TM} III Reverse Transcriptase (Bimake, Shanghai, China), and Sirius red solution, Safranin, and fix-green solution (YifanBio, Shanghai, China).

Fabrication of the Scaffold

In this study, PCL was used as the scaffold material that was placed in the charging barrel. The MEW 3D printer (TL-Direct Writing 150) was started, and the barrel temperature was adjusted to 65°C. The distance between the needle and the printing table was about 3 mm, and the printing station had a negative electrical charge. Furthermore, the printing voltage changed as the printing height changed (6 kV, voltage; 1,500 mm/min, printing speed; 22°C, ambient temperature; 35%, humidity). Additionally, the print needle model was 21G, with 100 kPa of air pressure.

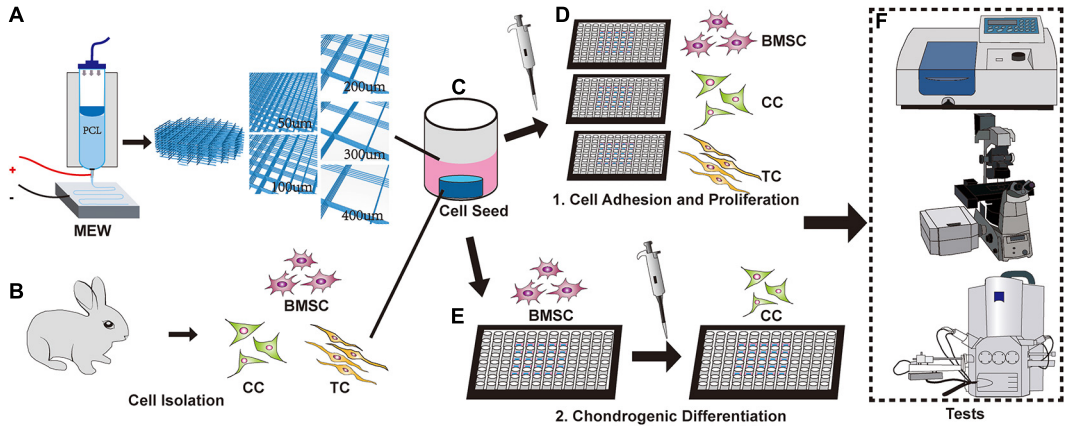

FIGURE 1 | Schematic of the experimental design. **(A)** Melt electrowritten (MEW) printer. The upper part is barreled. The needle is connected to the lower receiving plate to apply an electric field. The pore size of the scaffolds is controlled to 50, 100, 200, 300, and 400 μm, respectively. **(B)** New Zealand white rabbits were used to obtain bone marrow mesenchymal stem cells (BMSCs), chondrocytes, and tendon cells. **(C)** Implantation of different cells on the MEW scaffolds. **(D)** Cultured cells on a scaffold. **(E)** Induction of chondrogenic differentiation of BMSCs on scaffolds. **(F)** Fluorescence staining, microscopy, CCK-8, and other relevant tests were performed.

The conditions remained stable during printing. Different pore supports were fabricated according to the drawing model, and each scaffold was 200 μm in thickness (10 layers).

Cell Isolation and Culture

Three-week-old New Zealand white rabbits were euthanized to extract bone marrow mesenchymal stem cells (BMSCs), chondrocytes (CCs), and tendon stem cells (TCs). For BMSC isolation, both ends of the femur and tibia were removed. Subsequently, 10 ml of high glucose α-DMEM medium containing 10% FBS, 1% penicillin/streptomycin, and 100 U/ml heparin sodium was used to repeatedly rinse the bone marrow cavity and elute the bone marrow. Furthermore, stem cells were collected in a centrifuge tube and centrifuged at 100 × *g* for 5 min. The supernatant was discarded, and the pellet was resuspended in high-glucose α-DMEM medium with 10% FBS and 100 U/ml penicillin/streptomycin. Finally, the cells were incubated in an incubator at 37°C and with 5% CO_2, and the medium was changed every 2–3 days.

For CC isolation, the femur and tibia were removed, and a scalpel and scissors were used to separate the articular cartilage and cut the cartilage into pieces (<0.1 mm). These pieces were suspended in 10 ml DMEM/F12 medium containing 1% collagenase II (2275MG100, Biofroxx, Germany) and mixed. The suspension was then placed in a shaker with 37°C constant temperature and digested at 100 r/min for 2 h. Furthermore, the mixture was centrifuged at 100 × *g* for 5 min, followed by the removal of the supernatant, and cultured in DMEM/F12 medium containing 10% FBS, 50 μg/ml ascorbic acid, and 100 U/ml of penicillin/streptomycin in an incubator at 37°C with 5% CO_2. The medium was changed every 2–3 days.

For TC isolation, the Achilles tendon was removed and cut into pieces (<0.1 mm). Subsequently, the tendon pieces were suspended in 10 ml DMEM/F12 medium containing 1% collagenase I (1904MG100, Biofroxx, Germany), blown, and mixed. The suspension was placed in a constant temperature shaker at 37°C and digested at 100 r/min for 2 h. The mixture was centrifuged at 100 × *g* for 5 min, and the supernatant was discarded. Finally, the cells were cultured in DMEM/F12 medium containing 10% FBS and 100 U/ml of penicillin/streptomycin in an incubator at 37°C with 5% CO_2. The medium was changed every 2–3 days.

The cells were observed daily. The extracted primary cells were marked as P0, and the P2 phase cells were used in the experiments.

Cell Seeding and Culture on Scaffolds

After the scaffolds were printed, they were immersed in 75% alcohol and placed in an ultraviolet disinfection box to be disinfected for about 12 h. After removal, the scaffolds were rinsed with PBS three times (5 min). The scaffolds were then placed in six-well plates or a 96-well plate. Then, P2 BMSCs, CCs, and TCs were adjusted to a density of 3,000 cells/ml; 1 ml of cell suspension/well was added to six-well plates, and 100 μl of cell suspension/well was added to 96-well plates. After a 4-h incubation, the six-well plates were supplemented with 1 ml of medium per well, and the 96-well plates were supplemented with 100 μl of medium per well.

Morphological Characterization of Scaffolds by Scanning Electron Microscope

The pore size and fiber diameter of the scaffold were printed using a pre-designed model. The printed scaffold was mounted on aluminum foil and sprayed with 6-nm-thick platinum (OPC-80T, SPI Supplies, West Chester, PA, United States). The sample with cells was fixed using glutaraldehyde for 4 h and then fixed with citric acid for 2 h. After fixation, it was dehydrated using ethanol (50, 70, 85, 90, and 100%) and then placed in a lyophilizer (Free Zone, Labconco, United States) overnight. The dried sample was

coated with platinum. After coating with a 6-nm-thick layer of platinum, scanning electron microscopy (Leica, Germany) was used to observe the scaffold.

Fluorescence Staining and Microscopy

Scaffolds with cells were fixed using 4% paraformaldehyde. After 1 h, the specimens were removed, washed with PBS three times for 5 min, immersed in Triton X-100 (0.1%) for 5 min, and washed three times with PBS (5 min each). Furthermore, the specimens were incubated with FITC-labeled phalloidin for 45 min at 21°C and then washed with PBS three times (5 min each). Next, the specimens were incubated with DAPI for 10 min at room temperature and then washed with PBS three times (5 min each). Finally, fluorescence microscopy (Leica, Germany) was used to observe the cells after staining.

Cell Counting Kit-8 Test

The CCK-8 test was used to measure the adhesion and proliferation of different cells in various pore scaffolds. After the scaffolds were placed in a 96-well plate, BMSCs, CCs, and TCs were seeded on each of the pore scaffolds. At 4, 7, 14, and 21 days, the cell scaffolds were transferred to another 96-well plate. Then, 10% CCK-8 reagent was added to each well and placed in an incubator at 37°C for 1 h in the dark. Subsequently, 100 μl of each well medium was transferred to a clean 96-well plate. The absorbance of the culture media was measured with a microplate reader (Thermo Fisher Scientific, Inc.) at 450 nm (630 nm as a reference, $n = 4$).

Cell Seeding and Chondrogenic Differentiation on Scaffolds

P2 BMSCs were used to study chondrogenesis, 1 ml of cell suspension (3,000 cells/ml) was added to each well of the six-well plate containing scaffolds. After the cells adhered to the scaffold, the medium was replaced with chondrogenic differentiation medium (DMEM, 1% insulin–transferrin–selenium, 100 μg/ml sodium pyruvate, 40 μg/ml proline, 10^{-7} M dexamethasone, 50 μg/ml ascorbic acid, and 10 ng/ml TGF-β1). The cell condition was closely observed, and the medium was changed every 2 days.

Histological Staining

After 21 days, the specimen were removed, washed two to three times with PBS, and fixed with 4% paraformaldehyde for 1 h. Sirius red, Safranine O, and Fast-Green staining were performed separately. For Sirius red staining, the sample was immersed in PBS and washed. Then, the specimens were stained with Sirius red for 10 min, washed with ethanol, and observed under the stereoscope. For Safranine O and Fast-Green staining, the sample was immersed in PBS and washed. Subsequently, Fast-Green was added for 15 min and washed with PBS, followed by incubation with red dye solution for 5 min and treatment with color separation solution for 20 s. After PBS washing, the specimens were observed under a stereoscope.

Immunofluorescence and Confocal Microscopy

The scaffolds with cells were fixed with 4% paraformaldehyde. After 1 h, the specimens were removed, washed with PBS three times for 5 min, immersed in Triton-X (0.1%) for 5 min, and washed three times with PBS for 5 min each. The specimens were blocked with BSA for 1 h and primary antibody (COL II, COL I, AGC, and SOX9; diluted according to the manufacturer's protocol) for 12 h at 4°C and then washed with PBS three times for 5 min each. Subsequently, they were incubated with the Alexa Fluor 555-conjugated anti-mouse antibody for 1 h at room temperature, washed three times with PBS (5 min each), and then incubated with phalloidin and DAPI as described above in fluorescence staining and microscopy. The specimens were observed by confocal microscopy (Leica, Germany) after staining. ImageJ (National Institutes of Health, Bethesda, MD, United States) was used for quantitative analysis of the image ($n = 4$).

RNA Isolation and Real-Time Quantitative Reverse Transcriptase-Polymerase Chain Reaction

Quantitative reverse transcriptase-polymerase chain reaction (qRT-PCR) was used to detect chondrogenic differentiation-associated gene expression. Cells were seeded and stimulated using the abovementioned methods. After induction culture for 21 days, the medium was discarded, and total RNA was extracted with RNeasy mini kit (Qiagen) according to the instruction manual. The mRNA expression of the cartilage-specific genes (AGC, COL I, COL II, and SOX9) was determined by qRT-PCR using β-actin as an internal reference; the primer sequences are shown in **Supplementary Table 1**. RT-PCR was performed by reverse transcribing 1 mg of RNA with SuperScript^{TM} III Reverse Transcriptase, followed by PCR with SYBR Premix Ex Taq II (2×) on an ABI 7500 Fast machine (Applied Biosystems, Courtaboeuf, France). Gene expression was calculated using the $2^{-\Delta\Delta Ct}$ method, where ΔΔCt = (the average value of the gene Ct to be tested – the average value of the reference gene Ct to be tested) – (the average value of the target gene Ct of the control – the average value of the reference gene Ct of the control) ($n = 5$).

Biochemical Evaluations

All samples were collected and weighed, and then they were tested for total collagen and type II collagen content. Total collagen content was quantified by hydroxyproline assay, and type II collagen content was quantified by sandwich ELISA in accordance with a published method ($n = 5$) (Reddy and Enwemeka, 1996; He et al., 2017, 2018).

Statistical Analysis

Data analysis was performed using SPSS 25.0 software (SPSS Inc., Chicago, IL, United States). Quantitative data are expressed as mean ± standard deviation (mean ± SD). Data were analyzed by independent-sample t-test and one-way analysis of variance. $P < 0.05$ was considered significant.

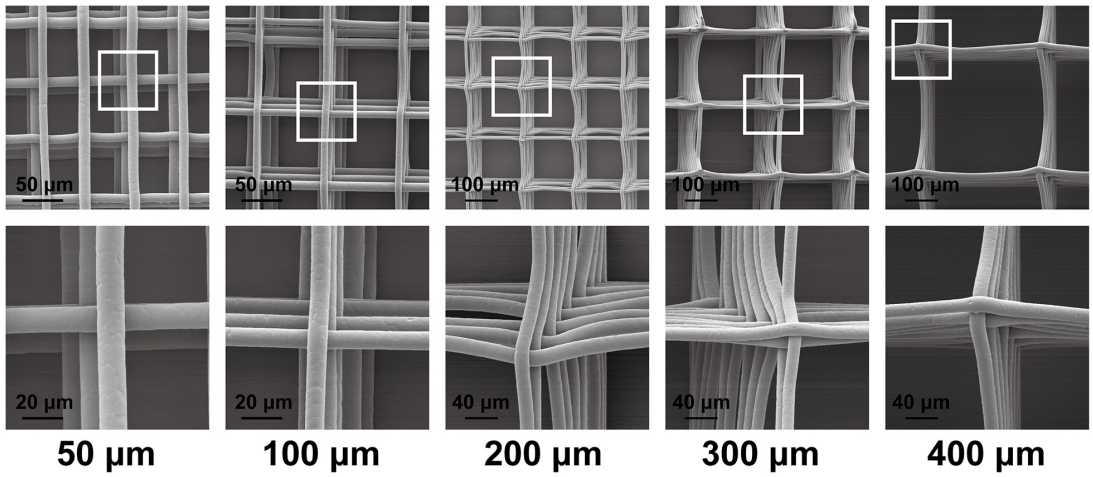

FIGURE 2 | Scanning electron microscopy graphs of the scaffold morphology of 50-, 100-, 200-, 300-, and 400-μm porous scaffolds.

RESULTS AND DISCUSSION

Morphological Characterization of Scaffolds

Figure 2 shows the morphology of the scaffolds under a scanning electron microscope. In this study, we prepared a MEW scaffold with high precision. The surface of the printing fiber is smooth, the diameter of the wire is about 10 μm, and the pore size of the scaffold is controllable. These are conducive to follow-up research.

Comparative Study on Adhesion and Proliferation of Various Cell Types

Bone marrow mesenchymal stem cells, TCs, and CCs were used in a comparative study of the effect of pore size on cell adhesion and proliferation. For different cells, the most suitable pore size for its adhesion and proliferation might be different. **Figure 3A** shows the DAPI-labeled nuclei (blue) and the phalloidin-labeled β-actin (red) in BMSCs under a fluorescence microscope and merged images. **Figure 3B** shows that BMSCs exhibited adhesion and proliferation on 50-, 100-, 200-, 300-, and 400-μm-pore-size scaffolds at 4, 7, and 14 days, respectively. The cell adhesion growth state in each image is significant, indicating that the scaffold has good biocompatibility and is suitable for cell adhesion. At 4 days, the cells in the 50-μm-pore scaffold were almost filled with pores. In the other groups, cell adherence to the surface of each fiber of the scaffold was observed, and there was a tendency to fill the inner pores. At 7 days, the 50- and 100-μm scaffolds were covered and filled by cells; the 200-, 300-, and 400-μm scaffolds also showed a trend of cell ingrowth, which was significantly increased compared with 4 days. At 14 days, the five groups of scaffolds were filled. In each group, compared to 4, 7, and 14 days, the number of cells increased significantly. Among them, the number of cells filled in the 50 μm group increased, and the nuclear field of DAPI significantly increased. **Figure 3C** shows the CCs' adhesion and proliferation on 50-, 100-, 200-, 300-, and 400-μm-pore-size scaffolds at 4, 7, and 14 days. Compared to BMSCs at 4 days, chondrocyte adhesion occurred faster, and the number of adherent cells was higher. At 7 days, the chondrocytes spread to fill the 400-μm pores. At 14 days, the number of cells increased slightly compared to that at 7 days. For TCs, **Figure 3D** shows low cell adhesion and proliferation. Even at 14 days, some of the larger pores were not completely filled. In addition, we found that the cells in the center of the pores are thinner than the cells attached to the fiber due to lack of support. With the completion of filling and further proliferation, the cells and secreted extracellular matrix can gradually fill the entire pore.

Figure 4 shows the results of the CCK-8 tests at 4, 7, 14, and 21 days after transplanting each group of cells on the scaffolds. First, every group showed an increase in measured values over time, indicating cell adhesion and proliferative activity. Among them, the 200 μm group showed the best result at 14 days for BMSCs. At 21 days, there was only little improvement over the 14 days for BMSCs and CCs. Furthermore, the 200 μm group showed the best result at 21 days, indicating that the environment of the 200-μm scaffold was best for BMSC adhesion and proliferation (**Supplementary Figure 1**). In the CC group, similar to the BMSC group, the results in each group improved continuously at 4, 7, and 14 days. However, unlike in the case of BMSCs, the 100 μm group showed similar results to the 200 μm group, considering that chondrocytes are small in size and more suitable for small pores. In the TC group, cell viability was lower than that of BMSCs and CCs at 4, 7, and 14 days but similar at 21 days compared to the other two cell types. At 21 days, the TCs showed best results in 300-μm pores, and the results were similar in 200-μm pores, which were only slightly lower than that in 300-μm pores. By contrast, 50 and 400 μm groups had the lowest values, suggesting that the environment of both 300- and 200-μm scaffolds was suitable for TC adhesion and proliferation. Taken together, the comparison of the three cell types demonstrated the different

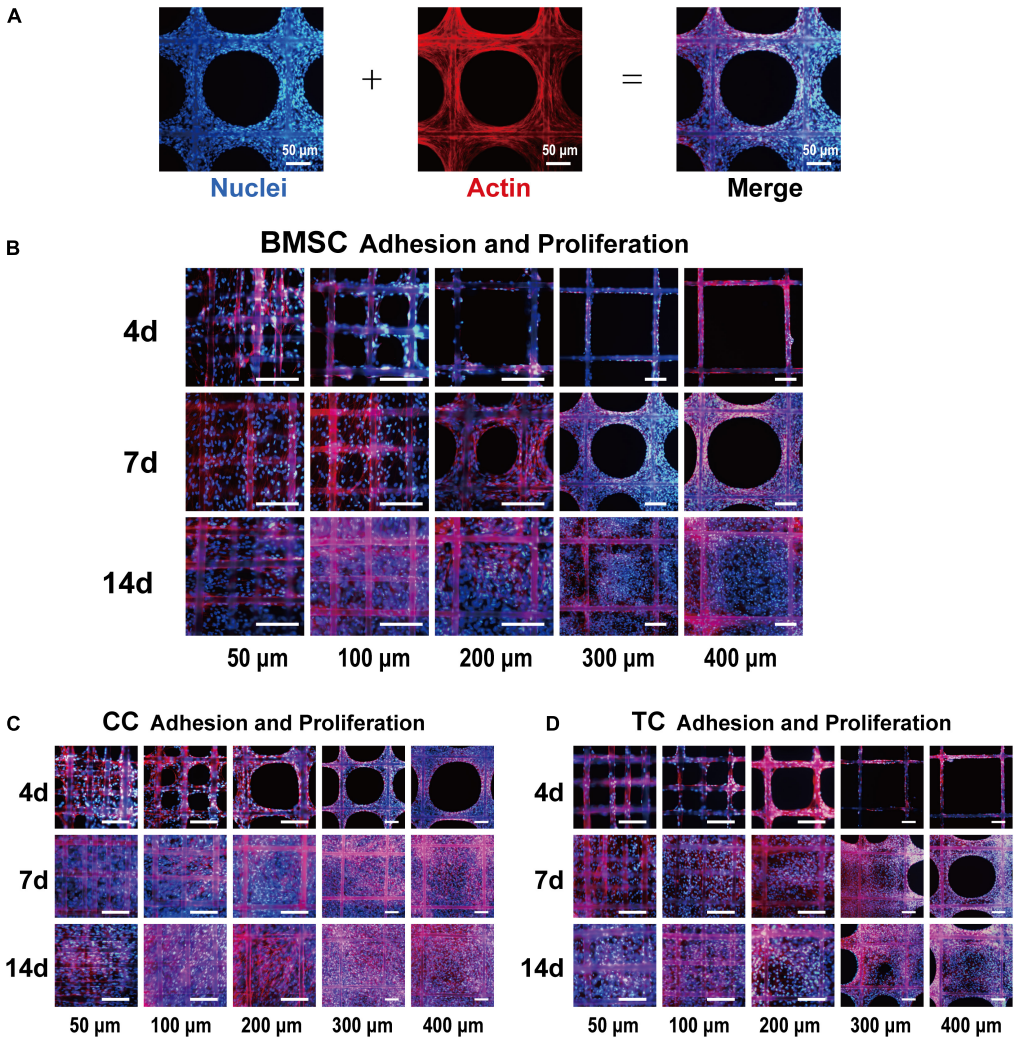

FIGURE 3 | Fluorescence images of bone marrow mesenchymal stem cell (BMSC) adhesion and proliferation. **(A)** Representative example of the cell-loaded scaffold. The left side shows a DAPI (blue)-labeled cell nucleus, the middle shows phalloidin (red)-labeled actin, and the right side shows the merged image. Fluorescence images of BMSCs **(B)**, chondrocytes **(C)**, and tendon cells **(D)** on 50-, 100-, 200-, 300-, and 400-μm porous scaffolds at 4, 7, and 14 days. Scale bar: 100 μm.

preferences of the cells in terms of pore size. Furthermore, all three cell types showed the lowest value in the 50 and 400 μ m groups.

Comparative Study on the Effect of Pore Size on Chondrogenic Differentiation Using BMSCs

To investigate the most appropriate corresponding pore size for cartilage regeneration, BMSCs were implanted on different scaffolds. After cell adherence to the scaffold, the medium was replaced with a chondrogenic differentiation medium. **Figure 5** shows the Sirius red and Safranine O-Fast Green staining stereoscopic images of the groups after chondrogenic differentiation on the scaffolds. In the images of the 50, 100, and 200 μm groups, the cells grew well with strong staining patterns. However, in the 300 and 400 μm groups, the cells did not fully grow and fill up all pores. Moreover, it was observed that collagen (Sirius red) and cartilage (Safranine O) in the 100 and 200 μm groups are more prominent.

The expression of COL II, COL I, AGC, and SOX9 after 21 days of stem cell induction is shown in **Figure 6**. **Figure 6A** shows the DAPI-labeled nuclei (blue), the phalloidin-labeled β-actin (green), the immunofluorescence for proteins (red), and the merged images. After further analysis, we found that the expression in the 100 and 200 μm groups was the best, especially compared to the 50 and 400 μm groups. This indicates that the pore size of chondrogenic differentiation had a clear range; too large or too small pores are not conducive to differentiation. The 100- and 200-μm pores were more suitable, the 50-μm pore was considered to be too small and oxygen and nutrients cannot be transported, while the 400-um pore is too large, such that the cells proliferate too much, and the differentiation ability was inferior.

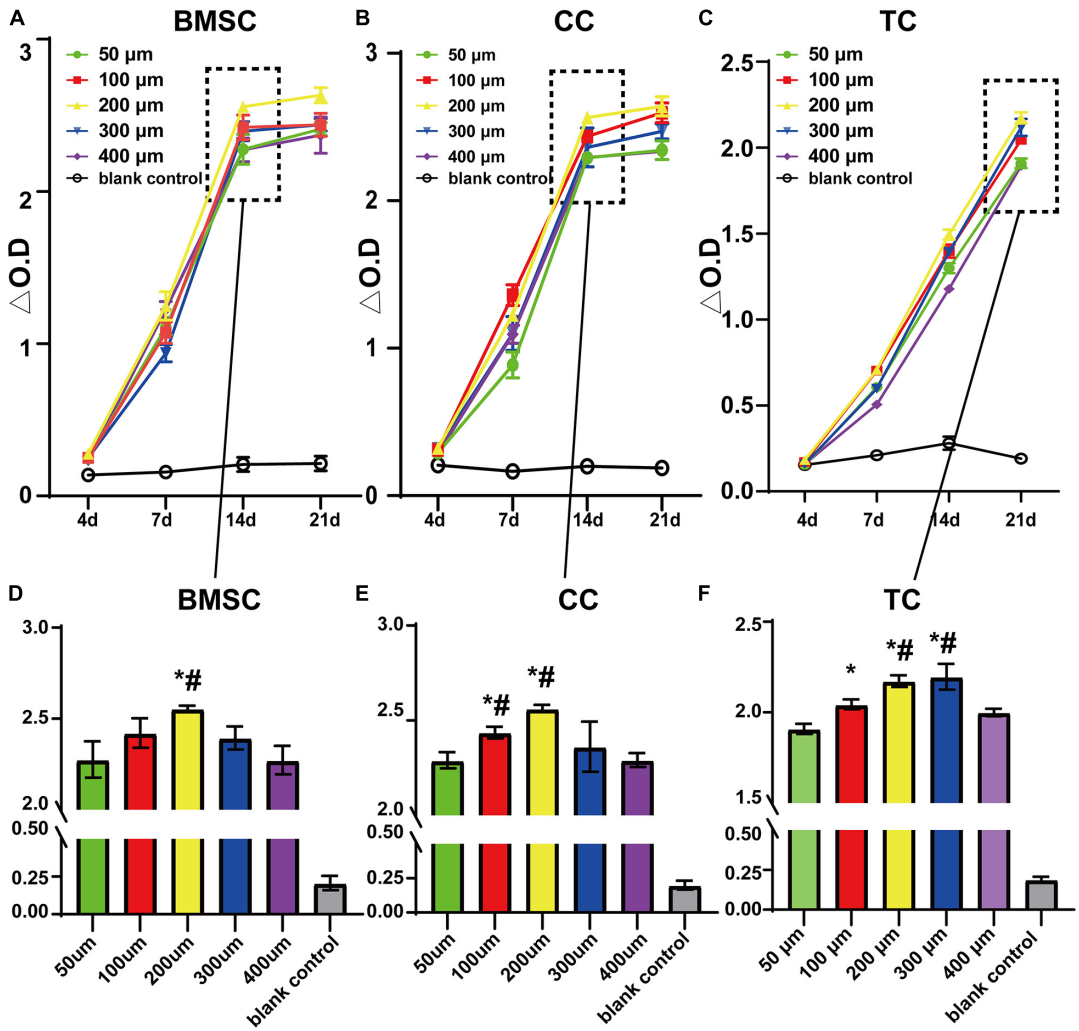

FIGURE 4 | CCK-8 test value for bone marrow mesenchymal stem cells **(A,D)**, chondrocytes **(B,E)**, and tendon cells **(C,F)** in 50-, 100-, 200-, 300-, and 400-μm-pore-size scaffolds at 4, 7, 14, and 21 days. Data represent mean ± standard deviation. $n = 4$; $^{*}p < 0.05$, compared with the 50 μm groups, $^{\#}p < 0.05$, compared with the 400 μm group.

Figures 7A–D show the mRNA expression of the chondrogenic differentiation marker genes (COL II, COL I, AGC, and SOX9) as determined by qRT-PCR using β-actin as an internal reference. The results were calculated by the $2^{-\Delta\Delta Ct}$ method. BMSCs were used as a reference, and the value was 1. We further clarified the effect of pore size on chondrogenic differentiation and further confirmed that too large or too small pores are not suitable for cartilage repair. In this part of the study, the 100 and 200 μm groups still showed good expression, while the 50 and 400 μm groups still had lower expression levels. These are consistent with the previous analysis, but, interestingly, in the previous section, the expression of COL II and AGC in the two groups of 100 and 200 μm showed the opposite results. Even if the difference is not obvious, we think that this small difference may be related to the sub-differentiation, such as superficial or mid-deep chondrocytes. **Figures 7E–G** show the biochemical evaluations after 21 days of stem cell induction. We examined the total weight of each group of scaffolds at 0 and 21 days and finally obtained the weight of the cellular components in the scaffold (**Figure 7F**). As with the previous studies, the 50 μm group had too small pores and low relative porosity. Oxygen and nutrients cannot be transported well, so cell adhesion and expression were the lowest. The 200 μm group was the highest and higher than the 300 and 400 μm groups. In addition, for the analysis of total collagen and type II collagen content, we found that the collagen content in the 50 μm group was not low, but the total amount was low. The collagen content gradually decreased with the increase of pores, being significantly decreased in the 400 μm group. Therefore, it may

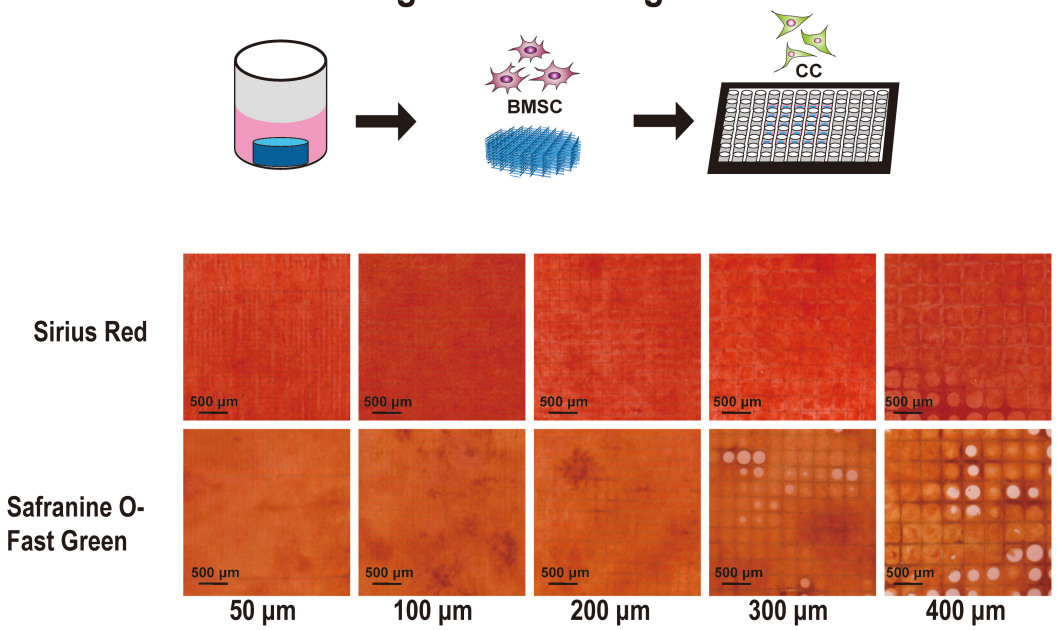

FIGURE 5 | Sirius Red and Safranine O with Fast-green staining of the cell-supported scaffolds. Chondrocyte differentiation from bone marrow mesenchymal stem cells on the 50-, 100-, 200-, 300-, and 400-μm-pore-size scaffolds for 21 days.

be that smaller pores are more capable of promoting collagen production. Thus, we believe that it is more appropriate to use scaffolds with different gradients for cartilage repair. It is more suitable to use smaller pores (such as 100 μm) in the surface layer and larger pores (such as 200 μm) in the middle and deep layers.

Discussion

Although many studies have investigated the effect of scaffold pore size cells (Nehrer et al., 1997; Tanaka et al., 2010; Pok et al., 2013), due to the limitations of the manufacturing process and accuracy, the overall structure cannot be controlled entirely. With MEW technology, we can accurately prepare 50, 100, 200, 300, and 400-μm-pore-size scaffolds. The microstructure of the scaffold is suitable, and the fiber is smooth. At present, for MEW technology, some researchers have been able to control the fiber diameter to the hundred-nanometer level for stable printing. Although the material requirements are higher than other printing methods, it can provide higher printing accuracy (Hochleitner et al., 2015). Moreover, with the continuous development and application of 3D printing technology, it is vital to further study the effect of 3D printing scaffold microstructure on cells.

In our study, we first verified the impact of the difference in scaffold pore size on cell adhesion and proliferation and that the effect on different cells is different. For cell adhesion, we found in our study that pores that were too small (50 μm) may be more suitable for initial cell adhesion, such that this scaffold could provide more support for the cell. Even with very small pores, cells can easily pass through. During subsequent cell proliferation, cells on the small-pore scaffold were more likely to cross each other and fill the pores (Nuernberger et al., 2011). Therefore, in each group, the 50 μm pores were very easily filled with cells. Later, however, because microscopic pores do not provide enough space, cell proliferation is significantly limited in crowded environments, while slightly larger pores provide a broader environment for cells. However, very large pores take more time for the cells to grow and fill (400 μm) (Youssef et al., 2019). Moreover, it can be noticed that due to the lack of support from the scaffold, the cells in the center of the pores are lower than those on the fiber, and the pores are recessed, but with time, the recesses can be gradually filled.

In addition, the ability of different cells to adhere to the scaffold is different. As previously shown, CCs can climb up the scaffold and fill up the smaller pores more quickly. While it takes longer for larger pores, it still fills reasonably quickly (Bhardwaj et al., 2001; Griffon et al., 2006; Brennan et al., 2019). BMSCs have worse adhesion than CCs, with TCs being the worst. The observed phenomenon is the same as in the previous study, such that cells can easily pass through pores slightly larger than themselves, then slowly climb the scaffold at a faster proliferation rate (Tan et al., 2017). Conversely, studies on cell proliferation have shown that, as we have speculated before, different cells do have their optimal pore sizes, such as CCs were suitable for 100 and 200 μm, BMSCs for 200 μm, and TC for 200 and 300 μm. Thus, our findings provide novel insights for subsequent research, such that we can first explore the appropriate parameters before further repair of different tissues to enhance the repair effect (Salifu et al., 2017;

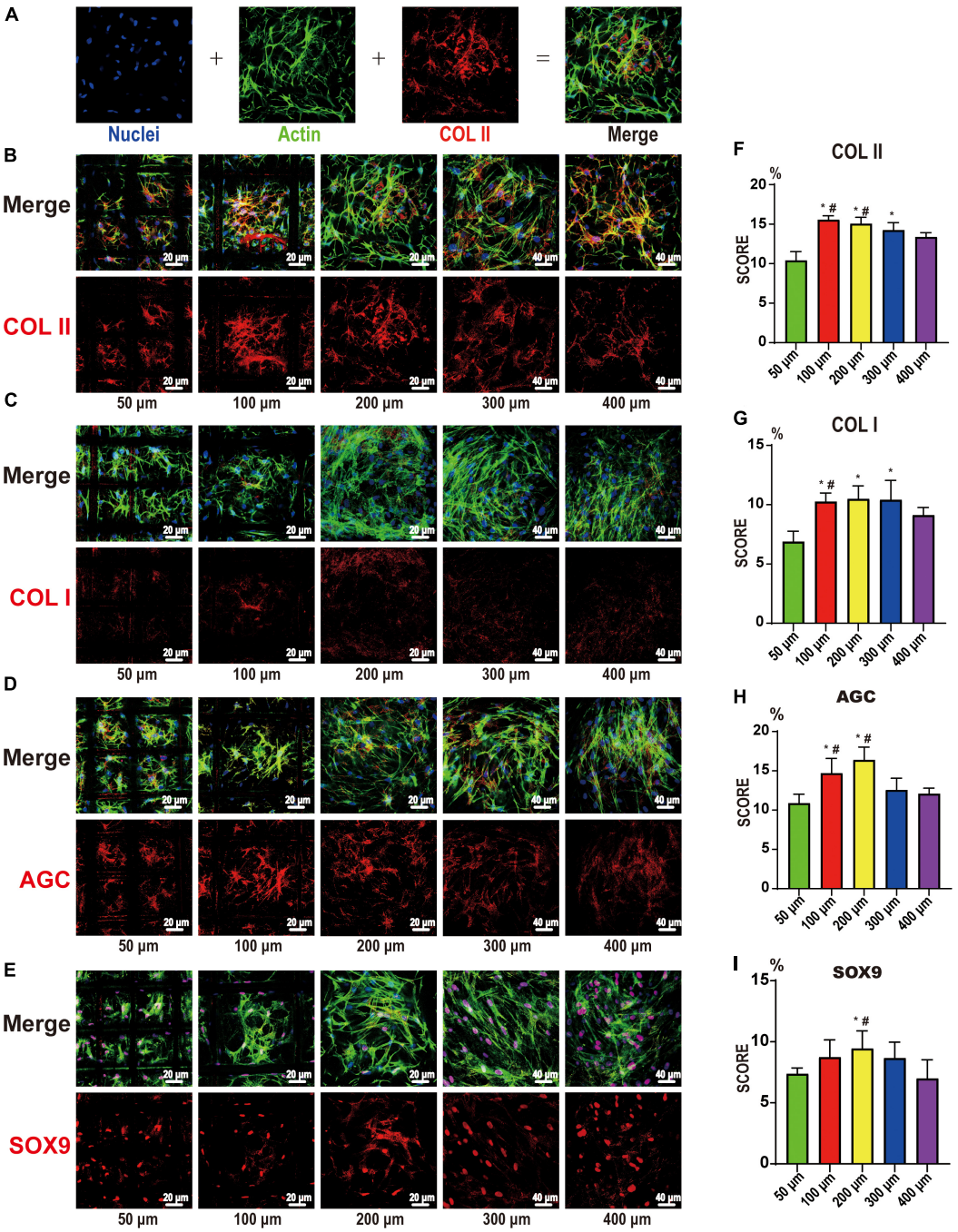

FIGURE 6 | Confocal microscopy for COL I, COL II, AGC, and SOX9. **(A)** Representative example of the confocal microscopy graph of 21-day chondrocyte differentiation from bone marrow mesenchymal stem cells. The first is DAPI (blue)-labeled nuclei, the second is phalloidin (green)-labeled actin, the third is COLII (red), and the fourth is a merged image. COL II **(B)**, COL I **(C)**, AGC **(D)**, and SOX9 **(E)** on the 50-, 100-, 200-, 300-, and 400-μm-pore-size scaffolds. The upper part is the merged image, and the lower part is the protein image (red). Histogram of the results of COL II **(F)**, COL I **(G)**, AGC **(H)**, and SOX9 **(I)** expression in image analysis. Data represent the mean ± standard deviation. $n = 4$; $^{*}p < 0.05$, compared with the 50 μm groups, $^{\#}p < 0.05$, compared with the 400 μm groups.

Kankala et al., 2018). Moreover, although we cannot say that all the scaffolds will have the same trend, this similar trend should exist.

After studying the adhesion and proliferation of several cell types on MEW scaffolds with different pore sizes, we investigated the most appropriate corresponding pore size when BMSCs were induced into cartilage. Therefore, BMSCs were implanted on different scaffolds. Following cell adherence to the scaffold, the medium was replaced with a chondrogenic differentiation medium.

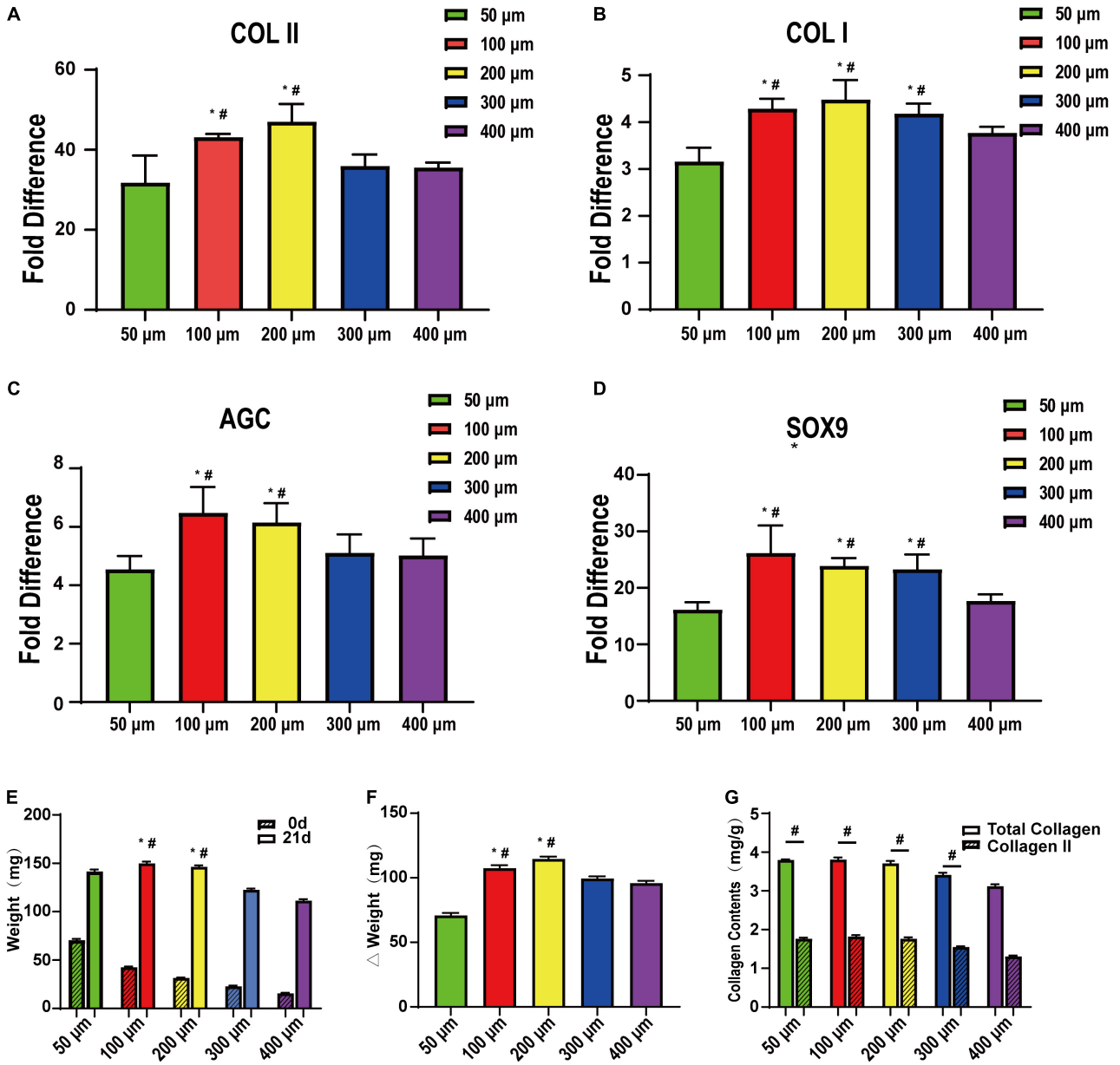

FIGURE 7 | qRT-PCR and quantitative biochemical analysis of bone marrow mesenchymal stem cells on the scaffolds after cartilage induction on 50-, 100-, 200-, 300-, and 400-μm-pore-size scaffolds for 21 days. **(A)** COLII, **(B)** COLI, **(C)** AGC, and **(D)** SOX9 ($n = 5$). **(E)** Simple scaffolds, cell-supported scaffold weight, and **(F)** their gap. **(G)** Total collagen and collagen II content on the scaffolds after cartilage induction on 50-, 100-, 200-, 300-, and 400-μm pore-size scaffolds for 21 days. Data represent the mean ± standard deviation. $n = 4$; $^{*}p < 0.05$, compared with 50 μm groups, $^{\#}p < 0.05$, compared with 400 μm groups.

In our study, the results showed that the 100 and 200 μm groups were the most suitable for cell chondrogenic differentiation and gene expression. In immunofluorescence and qRT-PCR, the two groups exhibited apparent advantages over the other groups. This was significantly less in the 50 μm group, indicating that the smaller pores (50 μm) were not suitable for chondrogenic differentiation of stem cells.

Moreover, in a more in-depth study of chondrogenic differentiation of BMSCs, we found that microscopic pores were not conducive to cell growth and differentiation. For large pores, i.e., >300 μm, although they provided growth space, excessive cell proliferation also caused a decrease in differential expression. As such, completing tissue repair in a short period using tissue engineering scaffolds is desired, providing enough support to the cells without affecting their function (Gotterbarm et al., 2006; Brunger et al., 2014). Although there were no significant differences between the 100 and 200 μm groups in the study, we still have some interesting findings. In general, both groups could provide sufficient adhesion support for the cells, suitable growth space for the cells, and better performance. However,

maybe due to differences in oxygen content or nutrient supply, COL II mRNA expression was higher in the 200 μ m group.

Nevertheless, the total amount of COL II is higher in the 100 μm group. This indicates that pore size is also important for cell sub-differentiation. Therefore, in our study, we believe that the 200-μm-pore scaffold may be more suitable for the mid-layer cartilage scaffold, and a 100-μm-pore scaffold may be more suitable for the surface.

Three-dimensional printing technology can precisely control the geometry, mechanical structure, and spatial distribution of the manufacturing structure to mimic the normal structure (Jose et al., 2014; Thomas et al., 2014). Furthermore, different bioactive materials, cytokines, or cells can be loaded at different locations on a structurally controllable basis (Chang et al., 2015; Teimouri et al., 2015; Daly et al., 2016; Xu et al., 2018). Thus, accurate depictions and better replication of the complexity and heterogeneity of endogenous tissues and organs are expected with the construction of a controllable 3D system in the field of regenerative medicine. Therefore, the application of 3D printing technology in tissue engineering provides a new foundation for subsequent development (Lima et al., 2013).

For a tissue engineering scaffold, the gold standard should be its repair ability (Kang et al., 2016; Shi et al., 2017), for which many factors influence the final effect, such as the type of material, biological activity, printed porosity, and pore size, among others (Abdeen et al., 2014; Ryu et al., 2015; Zhu et al., 2018). However, further elucidation of the impact of these factors on the final repair is needed. To build large organizations, a better understanding of the combined effects of pore size on cell adhesion, differentiation, and secretion capacity is required (Chang et al., 2015; Daly et al., 2018; Prasopthum et al., 2018). Our results show that not all cells behave in the same manner on similar scaffold pores, and the difference in scaffold space is also different for the induction effect and protein expression. In the 3D printing process, the pore size can affect the porosity under other conditions unchanged. This correlation is very close, and because the porosity is not intuitive, the adjustment of the pore size is more direct for 3D printing. Thus, controlling the pore size of the scaffold may enhance tissue repair.

There are many shortcomings in this study. Due to the difficulty of standard setting and PCL material as a relatively inert synthetic material, it has yet to be tested *in vivo*. In addition, the experimental divisions (integer of 100, 200, and 300 μm) are not detailed enough; thus, a more detailed stratification may lead to better results. Considering the thickness of the articular cartilage of small animals in subsequent experiments, we only used 200-μm-thick scaffolds. Whether the increase of thickness has an effect on the results still needs further study. Besides this, the number of cell types and the direction of induction are somewhat insufficient. Therefore, to build a more detailed database, efforts by many researchers are needed.

CONCLUSION

In this study, 10-layer MEW PCL scaffolds with different pore sizes were prepared, and the effect of pore sizes on cell behavior was studied. First, in the study of the effect of pore size on cell adhesion and proliferation, the rate of adhesion and proliferation of different cells on the scaffold differed, along with the suitable pore size. BMSCs performed best on 200 μm, CCs on 200 and 100 μm, and TCs on 200 and 300 μm. Subsequently, in case of chondrogenic differentiation of BMSCs, pore size had an effect on MSC chondrogenic differentiation, in which 200 μm pore size was more suitable for chondrogenic differentiation. In summary, this study verified that the pore size of 3D-printed, 10-layer MEW PCL scaffolds affected cell adhesion, proliferation, and differentiation.

DATA AVAILABILITY STATEMENT

The original contributions presented in the study are included in the article/**Supplementary Material**, further inquiries can be directed to the corresponding author/s.

ETHICS STATEMENT

The animal study was reviewed and approved by 11-20190911 Animal Experimental Ethical Inspection Jiagan Biotchnology Co.

AUTHOR CONTRIBUTIONS

YH: conceptualization, methodology, and writing–original draft preparation. ML: methodology, investigation, formal analysis, and validation. QW: investigation, formal analysis, and data curation. ZQ: methodology, investigation, and supervision. BS: writing–reviewing and editing, and supervision. KD: writing–reviewing and editing, supervision, and funding acquisition. All authors contributed to the article and approved the submitted version.

FUNDING

This work was supported by the National Key R&D Program of China (nos. 2018YFB1105600 and 2018YFA0703000) and Shanghai Ninth People's Hospital (no. XK2019013).

ACKNOWLEDGMENTS

We would like to thank Wenbo Jiang and Shixue Wang from the Clinical and Translational Research Center for the 3D printing technology and Shanghai Ninth People's Hospital, Shanghai Jiao Tong University School of Medicine for their help with the fabrication of the scaffold.

SUPPLEMENTARY MATERIAL

The Supplementary Material for this article can be found online at: https://www.frontiersin.org/articles/10.3389/fbioe.2021.629270/full#supplementary-material

REFERENCES

Abdeen, A. A., Weiss, J. B., Lee, J., and Kilian, K. A. (2014). Matrix composition and mechanics direct proangiogenic signaling from mesenchymal stem cells. *Tissue Eng. Part A* 20, 2737–2745. doi: 10.1089/ten.tea.2013.0661

Bahcecioglu, G., Hasirci, N., Bilgen, B., and Hasirci, V. (2019). A 3D printed PCL/hydrogel construct with zone-specific biochemical composition mimicking that of the meniscus. *Biofabrication* 11:025002. doi: 10.1088/1758-5090/aaf707

Bhardwaj, T., Pilliar, R. M., Grynpas, M. D., and Kandel, R. A. (2001). Effect of material geometry on cartilagenous tissue formation in vitro. *J. Biomed. Mater. Res.* 57, 190–199. doi: 10.1002/1097-4636(200111)57:2<190::aid-jbm1158>3.0.co;2-j

Brennan, C., Eichholz, K., and Hoey, D. (2019). The effect of pore size within fibrous scaffolds fabricated using melt electrowriting on human bone marrow stem cell osteogenesis. *Biomed. Mater.* 14:065016. doi: 10.1088/1748-605x/ab49f2

Brunger, J. M., Huynh, N. P., Guenther, C. M., Perez-Pinera, P., Moutos, F. T., Sanchez-Adams, J., et al. (2014). Scaffold-mediated lentiviral transduction for functional tissue engineering of cartilage. *Proc. Natl. Acad. Sci. U.S.A.* 111, E798–E806.

Castilho, M., Mouser, V., Chen, M., Malda, J., and Ito, K. (2019). Bi-layered micro-fibre reinforced hydrogels for articular cartilage regeneration. *Acta Biomater.* 95, 297–306. doi: 10.1016/j.actbio.2019.06.030

Chang, N. J., Lin, C. C., Shie, M. Y., Yeh, M. L., Li, C. F., Liang, P. I., et al. (2015). Positive effects of cell-free porous PLGA implants and early loading exercise on hyaline cartilage regeneration in rabbits. *Acta Biomater.* 28, 128–137. doi: 10.1016/j.actbio.2015.09.026

Chen, L., Deng, C., Li, J., Yao, Q., Chang, J., Wang, L., et al. (2018). 3D printing of a lithium-calcium-silicate crystal bioscaffold with dual bioactivities for osteochondral interface reconstruction. *Biomaterials* 196, 138–150. doi: 10.1016/j.biomaterials.2018.04.005

Cunniffe, G. M., Diaz-Payno, P. J., Sheehy, E. J., Critchley, S. E., Almeida, H. V., Pitacco, P., et al. (2019). Tissue-specific extracellular matrix scaffolds for the regeneration of spatially complex musculoskeletal tissues. *Biomaterials* 188, 63–73. doi: 10.1016/j.biomaterials.2018.09.044

Daly, A. C., Critchley, S. E., Rencsok, E. M., and Kelly, D. J. (2016). A comparison of different bioinks for 3D bioprinting of fibrocartilage and hyaline cartilage. *Biofabrication* 8:045002. doi: 10.1088/1758-5090/8/4/045002

Daly, A. C., Freeman, F. E., Gonzalez-Fernandez, T., Critchley, S. E., Nulty, J., and Kelly, D. J. (2017). 3D Bioprinting for cartilage and osteochondral tissue engineering. *Adv. Healthc Mater.* 6:1700298. doi: 10.1002/adhm.201700298

Daly, A. C., Pitacco, P., Nulty, J., Cunniffe, G. M., and Kelly, D. J. (2018). 3D printed microchannel networks to direct vascularisation during endochondral bone repair. *Biomaterials* 162, 34–46. doi: 10.1016/j.biomaterials.2018.01.057

Felice, B., Sanchez, M. A., Socci, M. C., Sappia, L. D., Gomez, M. I., Cruz, M. K., et al. (2018). Controlled degradability of PCL-ZnO nanofibrous scaffolds for bone tissue engineering and their antibacterial activity. *Mater. Sci. Eng. C Mater. Biol. Appl.* 93, 724–738. doi: 10.1016/j.msec.2018.08.009

Ghorbani, F. M., Kaffashi, B., Shokrollahi, P., Seyedjafari, E., and Ardeshirylajimi, A. (2015). PCL/chitosan/Zn-doped nHA electrospun nanocomposite scaffold promotes adipose derived stem cells adhesion and proliferation. *Carbohydr. Polym.* 118, 133–142. doi: 10.1016/j.carbpol.2014.10.071

Glaeser, J. D., Geissler, S., Ode, A., Schipp, C. J., Matziolis, G., Taylor, W. R., et al. (2010). Modulation of matrix metalloprotease-2 levels by mechanical loading of three-dimensional mesenchymal stem cell constructs: impact on in vitro tube formation. *Tissue Eng. Part A* 16, 3139–3148. doi: 10.1089/ten.tea.2009.0508

Gotterbarm, T., Richter, W., Jung, M., Berardi Vilei, S., Mainil-Varlet, P., Yamashita, T., et al. (2006). An in vivo study of a growth-factor enhanced, cell free, two-layered collagen-tricalcium phosphate in deep osteochondral defects. *Biomaterials* 27, 3387–3395. doi: 10.1016/j.biomaterials.2006.01.041

Griffon, D. J., Sedighi, M. R., Schaeffer, D. V., Eurell, J. A., and Johnson, A. L. (2006). Chitosan scaffolds: interconnective pore size and cartilage engineering. *Acta Biomater.* 2, 313–320. doi: 10.1016/j.actbio.2005.12.007

Guo, T., Noshin, M., Baker, H. B., Taskoy, E., Meredith, S. J., Tang, Q., et al. (2018). 3D printed biofunctionalized scaffolds for microfracture repair of cartilage defects. *Biomaterials* 185, 219–231. doi: 10.1016/j.biomaterials.2018.09.022

Hanas, T., Sampath Kumar, T. S., Perumal, G., and Doble, M. (2016). Tailoring degradation of AZ31 alloy by surface pre-treatment and electrospun PCL fibrous coating. *Mater. Sci. Eng. C Mater. Biol. Appl.* 65, 43–50. doi: 10.1016/j.msec.2016.04.017

He, A., Liu, L., Luo, X., Liu, Y., Liu, Y., Liu, F., et al. (2017). Repair of osteochondral defects with in vitro engineered cartilage based on autologous bone marrow stromal cells in a swine model. *Sci. Rep.* 7:40489.

He, A., Xia, H., Xiao, K., Wang, T., Liu, Y., Xue, J., et al. (2018). Cell yield, chondrogenic potential, and regenerated cartilage type of chondrocytes derived from ear, nasoseptal, and costal cartilage. *J. Tissue Eng. Regen. Med.* 12, 1123–1132. doi: 10.1002/term.2613

Hochleitner, G., Jungst, T., Brown, T. D., Hahn, K., Moseke, C., Jakob, F., et al. (2015). Additive manufacturing of scaffolds with sub-micron filaments via melt electrospinning writing. *Biofabrication* 7:035002. doi: 10.1088/1758-5090/7/3/035002

Hrynevich, A., Elci, B. S., Haigh, J. N., McMaster, R., Youssef, A., Blum, C., et al. (2018). Dimension-based design of melt electrowritten scaffolds. *Small* 14:e1800232.

Hung, K. C., Tseng, C. S., Dai, L. G., and Hsu, S. H. (2016). Water-based polyurethane 3D printed scaffolds with controlled release function for customized cartilage tissue engineering. *Biomaterials* 83, 156–168. doi: 10.1016/j.biomaterials.2016.01.019

Jose, S., Hughbanks, M. L., Binder, B. Y., Ingavle, G. C., and Leach, J. K. (2014). Enhanced trophic factor secretion by mesenchymal stem/stromal cells with glycine-histidine-lysine (GHK)-modified alginate hydrogels. *Acta Biomater.* 10, 1955–1964. doi: 10.1016/j.actbio.2014.01.020

Kang, H., Zeng, Y., and Varghese, S. (2018). Functionally graded multilayer scaffolds for in vivo osteochondral tissue engineering. *Acta Biomater.* 78, 365–377. doi: 10.1016/j.actbio.2018.07.039

Kang, H. W., Lee, S. J., Ko, I. K., Kengla, C., Yoo, J. J., and Atala, A. (2016). A 3D bioprinting system to produce human-scale tissue constructs with structural integrity. *Nat. Biotechnol.* 34, 312–319. doi: 10.1038/nbt.3413

Kankala, R. K., Xu, X. M., Liu, C. G., Chen, A. Z., and Wang, S. B. (2018). 3D-Printing of microfibrous porous scaffolds based on hybrid approaches for bone tissue engineering. *Polymers* 10:807. doi: 10.3390/polym10070807

Karageorgiou, V., and Kaplan, D. (2005). Porosity of 3D biomaterial scaffolds and osteogenesis. *Biomaterials* 26, 5474–5491. doi: 10.1016/j.biomaterials.2005.02.002

Kosik-Kozioł, A., Costantini, M., Bolek, T., Szöke, K., Barbetta, A., Brinchmann, J., et al. (2017). PLA short sub-micron fiber reinforcement of 3D bioprinted alginate constructs for cartilage regeneration. *Biofabrication* 9:044105. doi: 10.1088/1758-5090/aa90d7

Kumai, T., Yui, N., Yatabe, K., Sasaki, C., Fujii, R., Takenaga, M., et al. (2019). A novel, self-assembled artificial cartilage-hydroxyapatite conjugate for combined articular cartilage and subchondral bone repair: histopathological analysis of cartilage tissue engineering in rat knee joints. *Int. J. Nanomedicine* 14, 1283–1298. doi: 10.2147/ijn.s193963

Kundu, J., Shim, J. H., Jang, J., Kim, S. W., and Cho, D. W. (2015). An additive manufacturing-based PCL-alginate-chondrocyte bioprinted scaffold for cartilage tissue engineering. *J. Tissue Eng. Regen. Med.* 9, 1286–1297. doi: 10.1002/term.1682

Li, D., Yin, Z., Liu, Y., Feng, S., Liu, Y., Lu, F., et al. (2019). Regeneration of trachea graft with cartilage support, vascularization, and epithelization. *Acta Biomater.* 89, 206–216. doi: 10.1016/j.actbio.2019.03.003

Li, L., Yu, F., Shi, J., Shen, S., Teng, H., Yang, J., et al. (2017). In situ repair of bone and cartilage defects using 3D scanning and 3D printing. *Sci. Rep.* 7:9416.

Li, S., Tallia, F., Mohammed, A. A., Stevens, M. M., and Jones, J. R. (2020). Scaffold channel size influences stem cell differentiation pathway in 3-D printed silica hybrid scaffolds for cartilage regeneration. *Biomater. Sci.* 8, 4458–4466. doi: 10.1039/c9bm01829h

Lien, S. M., Ko, L. Y., and Huang, T. J. (2009). Effect of pore size on ECM secretion and cell growth in gelatin scaffold for articular cartilage tissue engineering. *Acta Biomater.* 5, 670–679. doi: 10.1016/j.actbio.2008.09.020

Lima, P. A., Resende, C. X., Soares, G. D., Anselme, K., and Almeida, L. E. (2013). Preparation, characterization and biological test of 3D-scaffolds based on chitosan, fibroin and hydroxyapatite for bone tissue engineering. *Mater. Sci. Eng. C Mater. Biol. Appl.* 33, 3389–3395. doi: 10.1016/j.msec.2013.04.026

Mannoor, M. S., Jiang, Z., James, T., Kong, Y. L., Malatesta, K. A., Soboyejo, W. O., et al. (2013). 3D printed bionic ears. *Nano Lett.* 13, 2634–2639. doi: 10.1021/nl4007744

Matsiko, A., Gleeson, J. P., and O'Brien, F. J. (2015). Scaffold mean pore size influences mesenchymal stem cell chondrogenic differentiation and matrix deposition. *Tissue Eng. Part A* 21, 486–497. doi: 10.1089/ten.tea.2013.0545

Nehrer, S., Breinan, H. A., Ramappa, A., Young, G., Shortkroff, S., Louie, L. K., et al. (1997). Matrix collagen type and pore size influence behaviour of seeded canine chondrocytes. *Biomaterials* 18, 769–776. doi: 10.1016/s0142-9612(97)00001-x

Nelson, M., Li, S., Page, S. J., Shi, X., Lee, P. D., Stevens, M. M., et al. (2021). 3D printed silica-gelatin hybrid scaffolds of specific channel sizes promote collagen Type II, Sox9 and Aggrecan production from chondrocytes. *Mater. Sci. Eng. C Mater. Biol. Appl.* 123:111964. doi: 10.1016/j.msec.2021.111964

Nuernberger, S., Cyran, N., Albrecht, C., Redl, H., Vecsei, V., and Marlovits, S. (2011). The influence of scaffold architecture on chondrocyte distribution and behavior in matrix-associated chondrocyte transplantation grafts. *Biomaterials* 32, 1032–1040. doi: 10.1016/j.biomaterials.2010.08.100

Oh, S. H., Kim, T. H., Im, G. I., and Lee, J. H. (2010). Investigation of pore size effect on chondrogenic differentiation of adipose stem cells using a pore size gradient scaffold. *Biomacromolecules* 11, 1948–1955. doi: 10.1021/bm100199m

Panadero, J. A., Lanceros-Mendez, S., and Ribelles, J. L. (2016). Differentiation of mesenchymal stem cells for cartilage tissue engineering: individual and synergetic effects of three-dimensional environment and mechanical loading. *Acta Biomater.* 33, 1–12. doi: 10.1016/j.actbio.2016.01.037

Pok, S., Myers, J. D., Madihally, S. V., and Jacot, J. G. (2013). A multilayered scaffold of a chitosan and gelatin hydrogel supported by a PCL core for cardiac tissue engineering. *Acta Biomater.* 9, 5630–5642. doi: 10.1016/j.actbio.2012.10.032

Ponce, M. C., Zorzi, A. R., Miranda, J. B., and Amstalden, E. M. I. (2018). Proposal for a new histological scoring system for cartilage repair. *Clinics* 73:e562.

Prasopthum, A., Shakesheff, K. M., and Yang, J. (2018). Direct three-dimensional printing of polymeric scaffolds with nanofibrous topography. *Biofabrication* 10:025002. doi: 10.1088/1758-5090/aaa15b

Reddy, G. K., and Enwemeka, C. S. (1996). A simplified method for the analysis of hydroxyproline in biological tissues. *Clin. Biochem.* 29, 225–229. doi: 10.1016/0009-9120(96)00003-6

Ruvinov, E., Tavor Re'em, T., Witte, F., and Cohen, S. (2019). Articular cartilage regeneration using acellular bioactive affinity-binding alginate hydrogel: a 6-month study in a mini-pig model of osteochondral defects. *J. Orthop. Translat* 16, 40–52. doi: 10.1016/j.jot.2018.08.003

Ryu, S., Yoo, J., Jang, Y., Han, J., Yu, S. J., Park, J., et al. (2015). Nanothin coculture membranes with tunable pore architecture and thermoresponsive functionality for transfer-printable stem cell-derived cardiac sheets. *ACS Nano* 9, 10186–10202. doi: 10.1021/acsnano.5b03823

Salem, A. K., Stevens, R., Pearson, R. G., Davies, M. C., Tendler, S. J., Roberts, C. J., et al. (2002). Interactions of 3T3 fibroblasts and endothelial cells with defined pore features. *J. Biomed. Mater. Res.* 61, 212–217. doi: 10.1002/jbm.10195

Salifu, A. A., Lekakou, C., and Labeed, F. H. (2017). Electrospun oriented gelatin-hydroxyapatite fiber scaffolds for bone tissue engineering. *J. Biomed. Mater. Res. A* 105, 1911–1926. doi: 10.1002/jbm.a.36058

Schon, B. S., Hooper, G. J., and Woodfield, T. B. (2017). Modular tissue assembly strategies for biofabrication of engineered cartilage. *Ann. Biomed. Eng.* 45, 100–114. doi: 10.1007/s10439-016-1609-3

Shi, W., Sun, M., Hu, X., Ren, B., Cheng, J., Li, C., et al. (2017). Structurally and functionally optimized silk-fibroin-gelatin scaffold using 3D printing to repair cartilage injury in vitro and in vivo. *Adv. Mater.* 29:1701089. doi: 10.1002/adma.201701089

Stenhamre, H., Nannmark, U., Lindahl, A., Gatenholm, P., and Brittberg, M. (2011). Influence of pore size on the redifferentiation potential of human articular chondrocytes in poly(urethane urea) scaffolds. *J. Tissue Eng. Regen. Med.* 5, 578–588. doi: 10.1002/term.350

Tan, Z., Liu, T., Zhong, J., Yang, Y., and Tan, W. (2017). Control of cell growth on 3D-printed cell culture platforms for tissue engineering. *J. Biomed. Mater. Res. A* 105, 3281–3292. doi: 10.1002/jbm.a.36188

Tanaka, Y., Yamaoka, H., Nishizawa, S., Nagata, S., Ogasawara, T., Asawa, Y., et al. (2010). The optimization of porous polymeric scaffolds for chondrocyte/atelocollagen based tissue-engineered cartilage. *Biomaterials* 31, 4506–4516. doi: 10.1016/j.biomaterials.2010.02.028

Teimouri, A., Ebrahimi, R., Emadi, R., Beni, B. H., and Chermahini, A. N. (2015). Nano-composite of silk fibroin-chitosan/Nano ZrO2 for tissue engineering applications: fabrication and morphology. *Int. J. Biol. Macromol.* 76, 292–302. doi: 10.1016/j.ijbiomac.2015.02.023

Teixeira, F. G., Panchalingam, K. M., Assuncao-Silva, R., Serra, S. C., Mendes-Pinheiro, B., Patricio, P., et al. (2016). Modulation of the mesenchymal stem cell secretome using computer-controlled bioreactors: impact on neuronal cell proliferation, survival and differentiation. *Sci. Rep.* 6:27791.

Thomas, D., Fontana, G., Chen, X., Sanz-Nogues, C., Zeugolis, D. I., Dockery, P., et al. (2014). A shape-controlled tuneable microgel platform to modulate angiogenic paracrine responses in stem cells. *Biomaterials* 35, 8757–8766. doi: 10.1016/j.biomaterials.2014.06.053

Wang, X., Wei, C., Cao, B., Jiang, L., Hou, Y., and Chang, J. (2018). Fabrication of multiple-layered hydrogel scaffolds with elaborate structure and good mechanical properties via 3D printing and ionic reinforcement. *ACS Appl. Mater. Interfaces* 10, 18338–18350. doi: 10.1021/acsami.8b04116

Warnecke, D., Stein, S., Haffner-Luntzer, M., de Roy, L., Skaer, N., Walker, R., et al. (2018). Biomechanical, structural and biological characterisation of a new silk fibroin scaffold for meniscal repair. *J. Mech. Behav. Biomed. Mater.* 86, 314–324. doi: 10.1016/j.jmbbm.2018.06.041

Woodfield, T. B., Van Blitterswijk, C. A., De Wijn, J., Sims, T. J., Hollander, A. P., and Riesle, J. (2005). Polymer scaffolds fabricated with pore-size gradients as a model for studying the zonal organization within tissue-engineered cartilage constructs. *Tissue Eng.* 11, 1297–1311. doi: 10.1089/ten.2005.11.1297

Xu, W., Wang, X., Sandler, N., Willfor, S., and Xu, C. (2018). Three-dimensional printing of wood-derived biopolymers: a review focused on biomedical applications. *ACS Sustain. Chem. Eng.* 6, 5663–5680. doi: 10.1021/acssuschemeng.7b03924

Ye, K., Kuang, H., You, Z., Morsi, Y., and Mo, X. (2019). Electrospun nanofibers for tissue engineering with drug loading and release. *Pharmaceutics* 11:182. doi: 10.3390/pharmaceutics11040182

Youssef, A., Hrynevich, A., Fladeland, L., Balles, A., Groll, J., Dalton, P. D., et al. (2019). The impact of melt electrowritten scaffold design on porosity determined by X-Ray microtomography. *Tissue Eng. Part C Methods* 25, 367–379. doi: 10.1089/ten.tec.2018.0373

Zamani, R., Aval, S. F., Pilehvar-Soltanahmadi, Y., Nejati-Koshki, K., and Zarghami, N. (2018). Recent advances in cell electrospining of natural and synthetic nanofibers for regenerative medicine. *Drug Res.* 68, 425–435. doi: 10.1055/s-0043-125314

Zhang, Y. S., Yue, K., Aleman, J., Moghaddam, K. M., Bakht, S. M., Yang, J., et al. (2017). 3D Bioprinting for tissue and organ fabrication. *Ann. Biomed. Eng.* 45, 148–163.

Zhang, Z. Z., Jiang, D., Ding, J. X., Wang, S. J., Zhang, L., Zhang, J. Y., et al. (2016). Role of scaffold mean pore size in meniscus regeneration. *Acta Biomater.* 43, 314–326. doi: 10.1016/j.actbio.2016.07.050

Zhu, T., Yu, K., Bhutto, M. A., Guo, X., Shen, W., Wang, J., et al. (2017). Synthesis of RGD-peptide modified poly(ester-urethane) urea electrospun nanofibers as a potential application for vascular tissue engineering. *Chem. Engi. J.* 315, 177–190. doi: 10.1016/j.cej.2016.12.134

Zhu, W., Cui, H., Boualam, B., Masood, F., Flynn, E., Rao, R. D., et al. (2018). 3D bioprinting mesenchymal stem cell-laden construct with core-shell nanospheres for cartilage tissue engineering. *Nanotechnology* 29:185101. doi: 10.1088/1361-6528/aaafa1

Conflict of Interest: The authors declare that the research was conducted in the absence of any commercial or financial relationships that could be construed as a potential conflict of interest.

Advantages of publishing in Frontiers

OPEN ACCESS
Articles are free to read for greatest visibility and readership

FAST PUBLICATION
Around 90 days from submission to decision

HIGH QUALITY PEER-REVIEW
Rigorous, collaborative, and constructive peer-review

TRANSPARENT PEER-REVIEW
Editors and reviewers acknowledged by name on published articles

Frontiers
Avenue du Tribunal-Fédéral 34
1005 Lausanne | Switzerland

Visit us: www.frontiersin.org
Contact us: frontiersin.org/about/contact

REPRODUCIBILITY OF RESEARCH
Support open data and methods to enhance research reproducibility

DIGITAL PUBLISHING
Articles designed for optimal readership across devices

FOLLOW US
@frontiersin

IMPACT METRICS
Advanced article metrics track visibility across digital media

EXTENSIVE PROMOTION
Marketing and promotion of impactful research

LOOP RESEARCH NETWORK
Our network increases your article's readership